NTNU
Norwegian University of
Science and Technology

Detection of Landslides

Using Optical Satellite Remote Sensing

Mads Brandt Fjeld

Geotechnics and Geohazards
Submission date: June 2018
Supervisor: Steinar Nordal, IBM

Norwegian University of Science and Technology
Department of Civil and Environmental Engineering

Detection of Landslides

Using Optical Satellite Remote Sensing

Trondheim 2018

TBA 4900 – Geotechnical Engineering, Master's Thesis
Mads Fjeld

Main supervisor: Steinar Nordal
Co-supervisor: Erin Lindsay

Department of Civil and Environmental Engineering
Norwegian University of Science and Technology (NTNU)

NTNU
Norwegian University of
Science and Technology

ABSTRACT

Norway is exposed to frequent landslide activity. A large number of landslides occur in Norway each year, causing damage to infrastructure, or even loss of lives. Due to the changing climate and more extreme weather patterns, the landslide activity in Norway is expected to increase.

Different approaches and characteristics of satellite remote sensing data are evaluated for the purpose of detecting landslide activity in Norway. The goal is to detect known landslide activity caused (partly) by an excess of water, using the optical satellite Sentinel-2.

A total of 25 landslides classified as either debris avalanches or debris flows have been identified from the Norwegian national landslide inventory. Sentinel-2 data have been acquired from the areas of the landslides, at times before and prior to the events, to investigate if the landslides are detectable in the satellite data.

11/25 of the investigated events are deemed *detected* in the acquired Sentinel-2 data, 3/25 are *possibly detected* and 11/25 are *not detected*. Landslide characteristics, spectral characteristics, and change detection methods are evaluated for all detected landslides.

The boundary of which an event can be deemed *detected* or *not detected* with high certainty is believed to be around 2000-2500 m^2, corresponding to 20-25 pixels.

The spectral characteristics of the investigated landslides are found to have large variability. No unique signature is obtained from the examined

A change detection approach is found to have better accuracy with respect to automatic classification of landslide affected pixels based on spectral characteristics. S2-data acquired with similar lighting- and seasonal conditions are found to yield best results.

The S2-satellites are operational in Norwegian conditions but are limited by climatic conditions and large seasonal variations. Year-round coverage of satellite data to be used for landslide detection purposes is not available using Sentinel-2. S2-data acquired from the summer-season are found to have the best prerequisites for detecting debris avalanches and debris flow, due to the lighting- and vegetative conditions.

PREFACE

The following master thesis marks my final work of the study programme MSc. Geotechnics and Geohazards. The work has been conducted for the Department of Civil and Environmental Engineering at NTNU.

The topic of this study was proposed by Ph.D. candidate Erin Lindsay, working with the Klima 2050 project. The topics of satellite remote sensing, climate change, and geohazards bring together several interested parties, from many of whom I have had interesting feedback, suggestions or comments during the process of putting this report together.

A special thank you is given to Regula Frauenfelder at NGI and Erin Lindsay for helpful meetings and discussions. Steinar Nordal and the institute is given my gratitude for providing the necessary equipment. Martine Holm Frekhaug and Statens Vegvesen for providing landslide-documentation, Gro Sandøy and NGU for landslide classification and map data, and Andreas Kääb at UiO for technical feedback that has also been of great help.

Table of Contents

ABBREVIATIONS

CRS	Coordinate Reference System
ESA	European Space Agency
FCC	False Color Composite
IR	Infrared
MIR	Mid Infrared
NCC	Natural Color Composite
NDR	Normalized Difference Index
NDSI	Normalized Difference Snow Index
NDVI	Normalized Difference Vegetation Index
NDWI	Normalized Difference Water Index
NIR	Near Infrared
NVE	The Norwegian Water Resources and Energy Directorate
S2	Sentinel-2
SWIR	Short Wave Infrared
TIR	Thermal Infrared
UV	Ultraviolet
VNIR	Visible- and Near Infrared

LIST OF FIGURES

LIST OF TABLES

1 Introduction

A large part of the globe experiences some level of landslide activity. On average, about 1000 human lives, and hundreds of millions of dollars of damage per year are lost due to landslides worldwide (Clague and Stead, 2012).

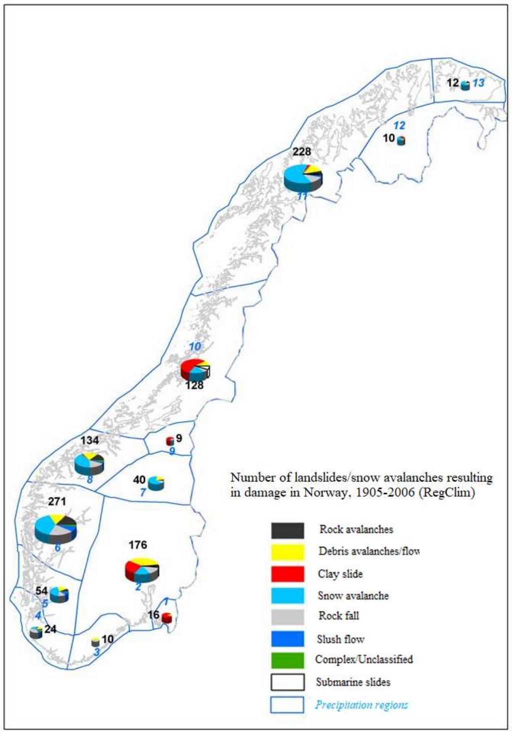

Figure 1.1 – Damage statistics in Norway. Modified from (Hovelsrud et al., 2007).

In Norway, the topography and morphology, together with the climatic conditions contribute to frequent landslide activity. Debris avalanches, rock falls, and snow avalanches are all common hazards that cause monetary losses, sometimes even loss of life. Along the Norwegian road network, 1 500 – 2 000 incidents of sliding activity were recorded per year in the period between 2000 and 2009 (Bjordal et al., 2011). Between 2004 - 2016, there have been five fatalities due to landslides in soils, and it is estimated that about 125 fatalities have occurred over the past 150 years (Colleuille et al., 2017). Landslides causing damage to housing, infrastructure, vehicles, livestock etc. occur nationwide, as illustrated in Figure 1.1.

The changing climate will most likely affect the frequency of landslides in Norway. The precipitation in the country has increased by 20 % in the last century, with the short-term precipitation increasing the most (Metereologisk Institutt, 2017). Short-term intense precipitation events, considered the country's most significant triggering condition for water-related landslides, are also likely to increase (Hovelsrud et al., 2007). If the predictions of climate change are correct, increased landslide activity is expected in large parts of Norway (Bargel et al., 2011).

As part of the research program "KLIMA 2050", research is being conducted to address the problem of rainfall induced landslides, for the purpose of building resilience to the adverse effects of climate change in Norway. With a higher frequency of extreme weather events, Early Warning Systems (EWS) are a possible cost effective approach for risk mitigation. A key aspect of a landslide EWS is accurate forecasting, which involves identifying locations vulnerable to landslide activity and understanding the conditions in which landslides are triggered. Freely available satellite imagery may be a useful source of information to complement ground-based instrumentations to understand more about the occurrence of landslides, particularly in a country with low population density, such as Norway.

1.1 Background

The national Norwegian landslide inventory (available from i.e. www.skrednett.no or www.xgeo.no) is maintained by NVE - the Norwegian Water Resources and Energy Directorate (Devoli, 2017). The documentation and registration of landslide events is mainly completed by the road- and railroad authorities which supervise and report incidents occurring along their respective networks. Consequently, the national database is considered biased towards the Norwegian rail- and road infrastructure.

For the purposes of identifying locations vulnerable to landslide activity and predicting future landslides, one could look to a record of historic events to find potential correlations. The Norwegian landslide inventory has few recorded events away from the road- and railroad network. Additionally, the information about the events is rather limited; the landslide type may be misclassified (e.g. debris flows recorded as rock fall), and little or no information is provided about the timing of initiation or potential causes. Therefore, much filtering is needed in order to complete significant statistical analyses using this database (Devoli, 2017). A more complete database would possibly be a basis for obtaining more knowledge about the causes, distribution and mechanisms of landslides, and ultimately contribute to more accurate forecasting.

The current operational forecasting system in Norway defines hazard levels based on hydrological thresholds which have led to landslide activity in the past (Colleuille et al., 2017). It can be hypothesized that remote sensing techniques and satellite data can be used in combination with ground-based observations to detect landslides, by providing supplementary information about the earth's surface. The European Space Agency (ESA) is developing and operating a series of public satellites, which are designed to monitor different aspects of our planet; atmospheric, oceanic and land monitoring (ESA, 2010). The satellites improved technical specifications, wider spatial coverage and publicly available data, may provide valuable information regarding natural hazards and landslide activity that was not freely available previously. The ability to detect landslides using optical satellite remote sensing data has the potential to assist in building up databases of past events, undiscovered events, poorly documented events, or events occurring in unsupervised/inaccessible areas.

1.2 Problem Description

The main objective of this work is to investigate the possibility of using optical satellite data for detecting landslide activity in Norway. More specifically, to investigate the feasibility of using ESAs satellite mission *Sentinel-2* to detect landslides which have occurred on the Norwegian mainland.

The primary question this report aims to answer: “Is Sentinel-2 a viable option for a landslide monitoring service in Norway?” The paramount agenda is to develop an automated detection system for such a purpose, which possibly can be based on satellite remote sensing data from the Sentinel satellites.

1.2.1 Scope

Monitoring landslide activity using satellites is a complex task. Knowledge of remote sensing fundamentals and techniques, data processing, and geohazards must all intertwine for such a system to function. This report aims to cover parts of all the said topics, as this is considered a requisite for investigating the feasibility of landslide detection by satellite remote sensing. In-depth studies of single methods and techniques will not be given, rather an insight of relevant theory and key techniques. The intention of this thesis is to see what data can be correlated to landslide activity, given Norwegian conditions.

This report focuses solely on remote sensing data acquired by the Sentinel-2 satellites. The satellites have improved technical specifications compared to their predecessors and freely available alternatives. Another incentive is the data availability, which is freely available for public use. As far as the author knows, no similar studies have been conducted using Sentinel-2 as a basis for an operational landslide monitoring service.

The thesis focuses on landslide activity which is believed to (at least partly) be triggered by a surplus of water. In the Norwegian literature, these events are referred to as *jord- og flomskred.* Other landslide types known to occur in Norway, such as snow avalanches, rock avalanches and debris avalanches in clay are not considered. The mechanics of landslides with respect to morphological conditions are of focus, as this possibly can be correlated to satellite data.

The analysis of satellite data characteristics will mainly focus on reflectance properties of landslides and surrounding features. Different image-analysis techniques and their efficiency with respect to this topic is not part of this work. The report does not intend to develop an algorithm for automatic landslide detection, merely to investigate different approaches which possibly can be included in an automated system, and evaluate how well they perform based on tests.

1.2.2 Objectives

Based on the outline and scope above, the following objectives have been established:

- Identify the key-characteristics of detectable landslides vs. non-detectable landslides
    - Size
    - Topography and morphology
    - Soil cover
    - Geological conditions
- Assess aspects of using Sentinel-2 for landslide detection in Norway

- Identify the spectral characteristics of detected landslides
- Evaluate spectral characteristics and change detection approaches with respect to an automated system

1.2.3 Strategy

The approach to evaluate the above objectives, is to examine known landslide events. Landslides registered in the national inventory are documented with a time of occurrence, and coordinate reference, which enables satellite data to be acquired for specific known events.

Sentinel-2 satellite data is acquired from prior to, and after, the reported time of occurrence. The datasets are acquired as close to the landslide's date of occurrence as possible. Datasets acquired prior to the event in this report are referred to as *pre-event* data. Datasets acquired subsequent to the date of occurrence are referred to as *post-event* data.

As the data is acquired at different times of the year and may be subject to seasonal variations, it could be of interest to investigate data acquired with as similar conditions as possible. Data acquired prior to the pre-event data is referred to as *previsit* data. Data acquired after the post-event data is referred to as *revisit* data.

1.3 Structure of report

The report is divided into the following sections:

- Theory
- Method
- Results
- Discussions and conclusions
- Appendices

The theory section covers general theory on landslides and remote sensing fundamentals, as well as a definition of Norwegian conditions with respect to factors influencing geohazards and satellite remote sensing. The chapter is meant to present the theoretical basis in which is needed to evaluate the main objective.

The background and procedures used for data acquisition and analysis are described in the methods section. This chapter is meant to describe how, and what work has been conducted. The essential findings are presented in the results chapter. Explanations and reasons for the different approaches used in the data-analysis are further explained in this chapter.

The discussions and conclusion sections aim to shed light on the results through discussion with respect to the main objectives of this thesis.

The appendicies contains detailed descriptions of all landslide events, and all processed data, used in the report.

2 Theory

Relevant theory regarding landslide processes and remote sensing is presented in the following chapter.

2.1 Landslide classification

Landslide is a broad term which describes a variety of processes. A common definition is *"the failure and movement of a mass of rock, sediment, soil, or artificial fill, under the influence of gravity"* (Clague, 2013). More specific definitions may be used to communicate the characteristics of different types of landslides. These definitions and classifications are mainly based on how the displaced mass is moving, and/or what type of material the displaced mass is comprised of. For remote sensing purposes, one must understand the processes and mechanisms behind landslides to know where, and what to look for.

2.1.1 Type of landslides

Landslides can be classified into different types, dependent on their characteristics. A widely used classification system is the system proposed by (Varnes, 1978), which divides the type of mass movement into five classes, and the type of mass into three materials; rock, debris, and earth. (Varnes, 1978) refers to definitions by (Shroder, 1971) whereas *debris* is defined as a material in which 20-80 % of the grains are larger than 2 mm, with the remainder of the fragments less than 2 mm in size. *Earth* is defined as a material in which at least 80 % of fragments are smaller than 2 mm. Although not a geotechnical term, debris has been established and is widely used as a term for current events. As (Hungr et al., 2014) describes it "*From a geotechnical point of view, debris is a mixture of sand, gravel, cobbles, and boulders. The mix often also contains varying portions of the smaller fractions such as clay and silt*". (Hungr et al., 2014) proposed an updated version of the Varnes classification system, to make the characterizations up to date, and compatible with geotechnical terminology. The type of movement is categorized into five categories, as shown in Figures 2.1 – 2.7.

Fall

The detachment of a mass of soil or rock from a steep slope is considered a *fall.* There is little or no shear displacement along the failure surface before the detachment. The material will mainly descend by falling, bouncing or rolling (Highland and Bobrowsky, 2008).

Topple

A mass of soil or rock, forward rotating around a point or axis below its center of gravity describes a *topple*-like movement type (Highland and Bobrowsky, 2008).

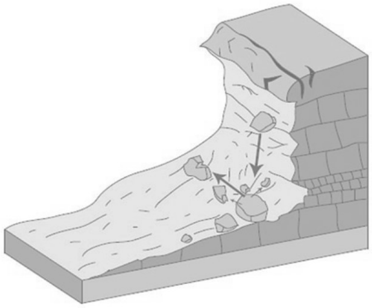

Figure 2.1 – Fall

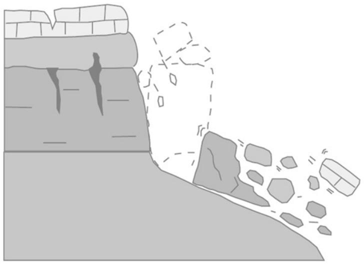

Figure 2.2 – Topple

Slide

A mass of soil or rock moving downslope on surfaces of rupture, or thin regions of intense shear displacement depict a *slide*-like event. The movement of the entire mass does not occur simultaneously, but enlarges from its local point of origin, mobilizing a larger volume along its path (Highland and Bobrowsky, 2008). The slide is *rotational* if it has a curved surface of rupture, where the displaced mass has rotated about an axis at a right angle to its vertical cross-section. If the displaced mass follows a relatively planar surface, with little rotational movement, it is characterized as a *translational* slide (Highland and Bobrowsky, 2008) or *planar* slide (Hungr et al., 2014).

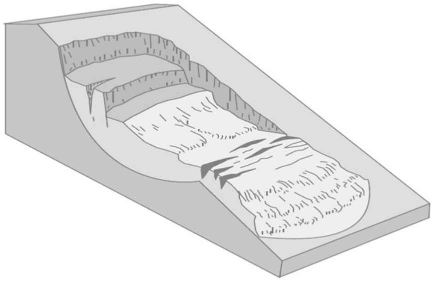

Figure 2.3 - Rotational slide

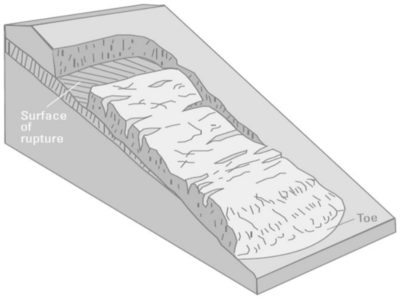

Figure 2.4 – Translational/Planar slide

Flow

A continuously moving mass, behaving like a viscous liquid characterizes the *flow*-like movement types. The shear surfaces are closely spaced, short lived and usually not preserved (Highland and Bobrowsky, 2008). Flows can take on several modes – if the displaced mass follows a channel it is commonly termed a *debris flow*, while open-slope flows characterize *debris avalanches* (Hungr et al., 2014).

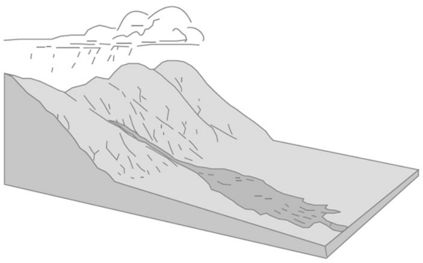

Figure 2.5 – Debris flow

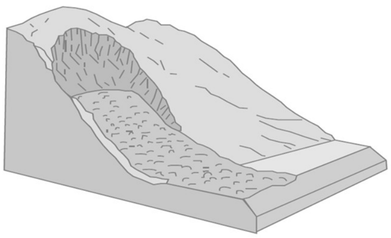

Figure 2.6 – Debris avalanche

Slope deformation

Slope deformation includes processes that cause slow to extremely slow deformation of valley or hill slopes. (Hungr et al., 2014). The processes may be gravity-driven, or a result of climate-driven cycles such as wetting and drying, as well as freeze and thaw (Hungr et al., 2014).

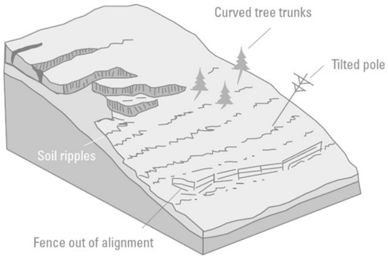

Figure 2.7 - Creep

The material type is divided into two main categories; *rock* and *soil*. Geotechnical terminology is for the most part used for the subdivision of the soil-category; Boulders, gravel, sand, silt, clay, peat, ice, debris, and mud. Debris and mud categorize mixed materials, whereas *debris* is a mixture of sand, gravel, cobbles, and boulders, with varying proportions of silt and clay (Hungr et al., 2014). Mud is termed for a material with similar properties, but with significant plasticity due to higher moisture and a higher content of silt and clay (Hungr et al., 2014). A summary of the updated classification is given in Table 2.1. It should be noted that established term "earthflow" is included in the classification system, referring to cohesive, plastic, clayey soil, often mixed and remolded, whose liquidity index is below 0.5 (Hungr et al., 2014).

Table 2.1 - The updated Varnes classification system, reproduced from (Hungr et al., 2014).

TYPE OF MOVEMENT	ROCK	SOIL
FALL	Rock/Ice-fall	Boulder/Debris/Silt fall
TOPPLE	Rock block topple	Gravel/Sand/Silt topple
	Rock flexural topple	
SLIDE	Rock rotational slide	Clay/Silt rotational slide
	Rock planar slide	Clay/Silt planar slide
	Rock wedge slide	Gravel/Sand/Debris slide
	Rock compound slide	Clay/Silt compound slide
	Rock irregular slide	
FLOW	Rock/Ice avalanche	Sand/Silt/Debris dry flow
		Sand/Silt/Debris flowslide
		Sensitive clay flowslide
		Debris flow
		Mud flow
		Debris flood
		Debris avalanche
		Earth flow
		Peat flow
SLOPE DEFORMATION	Mountain slope deformation	Soil slope deformation
	Rock slope deformation	Soil creep
		Solifluction

2.1.2 Alternative classifications

Multiple landslide classifications systems exist in the literature. These systems may be based on different factors related to the landslide, or the authors' objective. (Dikau et al., 1996) refers amongst other to the comprehensive system by (Hutchinson, 1988), which classify slope movement into eight categories, each divided into several subdivisions, based on morphology, mechanism, type of material and rate of movement. (Dikau et al., 1996) themselves use the European classification developed by (Casale et al., 1994). (Myrabø et al., 2014) presents a system illustrated by a ternary plot, where the classification is based on material and water content:

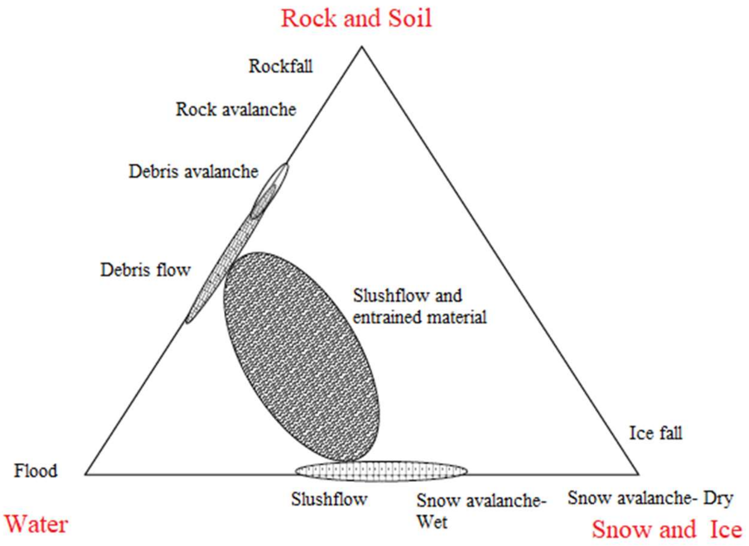

Figure 2.8 – Classification based on the amounts of water and material. Modified from (Myrabø et al., 2014).

The landslide terminology used in the Norwegian national landslide database differs somewhat from that of the international literature. In general, the events are differentiated by their material; rock, snow or soil. NVE and the Norwegian Landslide Forecasting Service – *Jordskredvarslingen* – define the terms:

Table 2.2 – Terminology by NVE, as described by (Colleuille et al., 2017)

Norwegian term	Description
Jordskred	Rapid displacements of saturated soils in steep slopes, with no clearly defined water channel. May be directly translated as "jord = soil", "skred = avalanche" **Coincides with the English terms:** Debris avalanches, debris slides, soil slides, translational slides, shallow slides.
Flomskred	High velocity flow-like slides along defined channels and streams. Can occur in channels where it normally is no running water. The moving mass can entrain large amounts of sediments, boulders, trees, and vegetation. May be directly translated as "flom = flood", "skred = avalanche". **Coincides with the English terms:** Debris flows, debris floods.

2.2 Landslide processes and causes

The cause of a landslide is a result of complex processes. Natural and man-made processes can both contribute to the triggering of a landslide event. (Brunsden, 1993) has classified generalized processes causing landslides:

Table 2.3 - Classification of contributing processes to the triggering of a landslide. Modified from (Brunsden, 1993)

External process	Causal process	Description
Weathering ***(Physical, chemical and biological)***	Physical properties	Changes in particle size
	Chemical properties	Cation exchange, cementation
	Horizonation	Internal layers, ripening, weaker discontinuities
	Regolith thickness	Often determined by slope shape
Erosion *(Fluvial, glacial, coastal etc.) Material removal from face or base of slope.*	Geometrical change	Relief, height, length, angle, aspect
	Unloading	Removal of lateral support, expansion, swelling, fissuring, strain softening, stress concentration
Ground subsidence	Undermining	Mechanical eluviation of fines, leaching, removal of cement, seepage erosion
Deposition *(Fluvial, glacial, mass movement etc.) New material added to face or top of the slope.*	(Undrained) Loading	Landslide activity, deltaic addition, talus accumulation
Shocks and vibration	Vertical and horizontal movement	Varying frequency, magnitude, intensity, duration, disturbance to intergranular bonds and cement, water table change
Air fall *Wind-blown sediments, loess* *Volcanic sediments, tephra*	Addition of fine components to the soil. Mantling with fine regolith.	Producing a new slope with the old surface as possible shear zone
Water regime change *(Geomorphological or meteorological)*	Surface saturation.	Flooding, lake bursts, etc.
	Water-table, and pressure change.	“Wet” rainfall years, intense precipitation, snow and ice melt, drawdown
Compound *Possible "follow-on" or run out processes after initial failure, e.g. after bank collapse, etc.*	Liquefaction, remolding, cohesionless grain flow, heat generation, rate effects, chemical effects.	

(Brunsden, 1993) relates these generalized processes to examples of specific effects on the stability of a slope system; Different weathering and erosion processes can affect material properties such as density, strength, internal friction, and permeability. Local variations may arise within a slope system, causing varying spatial conditions due to weathering and erosion. Alterations in the terrain due to erosion, undermining and depositions affect the stress conditions in the slope system, e.g. with added stress, rapid undrained loading, and pore pressure changes. All water regime changes, related to geomorphological or meteorological conditions affect water pressures, both external and internal, and may influence stability by affecting the stress condition.

2.2.1 General slope stability

To assess the stability of a slope, the *factor of safety* is established. The factor, given in eq. 2.1, is the ratio between *stabilizing* and *driving* forces, where a number larger than 1.0 represents a stable slope, and values below 1.0 represent an unstable slope (Emdal et al., 2014).

$$F = \frac{Stabilizing\ forces}{Driving\ forces} \tag{2.1}$$

The stabilizing forces can comprise both of internal material properties, such as friction between the grains or cohesion. External measures, such as counter-fills, or unloading by removing material from the top of the slope may also contribute to the stabilizing forces. The driving forces are mainly gravity driven, water-pressures, external loads or similar. Different approaches may be used to assess the factor of safety i.e. by limit equilibrium methods or probabilistic approaches. A much used material model applied for soils, is the *Mohr-Coulomb* model. The Mohr-Coulomb failure line governs the strength of the material and is given by the equation below (Nordal, 2017).

$$\tau_f = c + \sigma' tan\varphi = (a + \sigma')tan\varphi \tag{2.2}$$

$where$

$\tau_f = Shear\ strength$

$c = Cohesion$

$\sigma' = Effective\ normal\ stresses = Total\ stresses - pore\ pressure = \mathrm{\sigma} - \mathrm{u}$

$a = Attraction$

$tan\varphi = Friction\ coefficient$

The factor of safety may then be expressed as a function of shear strength:

$$F = \frac{\tau_f}{\tau} \tag{2.3}$$

where

$\tau = Mobilized\ shear\ strength$

2.2.2 Water regimes

Water is a major component of landslide processes. Intense precipitation, prolonged rainfall, and snowmelt affect the soil and its natural condition. The soil is a three-phase element, were water influences the soil's internal stresses.

In susceptible materials, water infiltration may cause pore pressure build-ups. Low permeability materials, typically with high contents of silt and clay, are prone to these pore pressure build ups, which decreases the stability (Myrabø et al., 2014). Illustrated by equation 3.2, an increase in pore pressure will cause reduced effective stresses, resulting in decreased strength. (Dikau et al., 1996) describes a debris avalanche occurring on a slope inclined 43°. The slope had a factor of safety of 1.49 under dry conditions, but became unstable after a rainfall event which caused the pore pressure to increase by 2 kPa. This case indicates how steep slopes with certain preconditions can be very sensitive to pore pressure changes.

Materials with a high content of silt and clay may have added strength due to capillary forces. Capillary rise, referred to as the *capillary fringe* in Figure 2.9, occur just above the groundwater-table. This effect causes a negative pore pressure in the unsaturated zone, effectively increasing the cohesion (Høeg et al., 2014). A fully saturated material will lose this effect, weakening and destabilizing the layer.

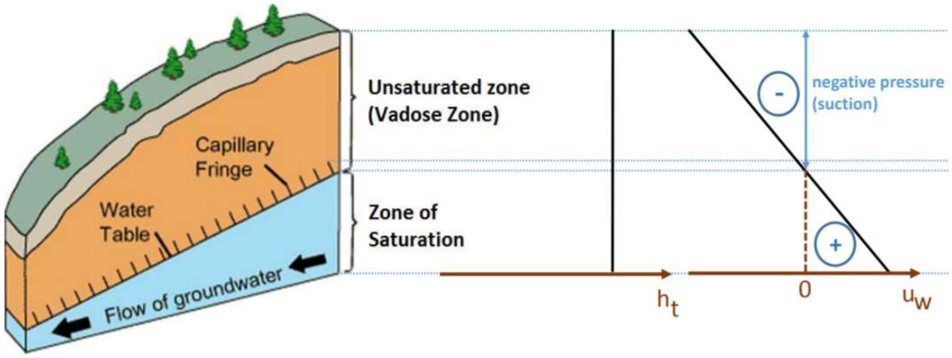

Figure 2.9 - Capillary suction, from (Ghoreishian Amiri, 2017)

Large water input events will increase river flows, which increases the sediment transport. Ultimately, this may initiate debris flows if the river erosion becomes sufficiently large. Over time, the riverbed naturally develops a stronger surface layer, with a higher resilience against erosion (Myrabø et al., 2014). The riverbed adapts to the prevailing climatic conditions, and is sensitive to events beyond normal. Figure 2.10 shows a diagram of velocities critical for erosion, suspension of material and sedimentation of material as a function of particle size. The conditions given in the blue area are prone to erosion, while the areas below represents conditions needed for material- suspension and sedimentation. The silt and sand fraction are more exposed to erosion than the finer and coarser materials. The finer fractions are more resilient due to cohesion, while the coarser fractions require a larger magnitude of stress to be put in suspension, thus a higher water velocity (Myrabø et al., 2014).

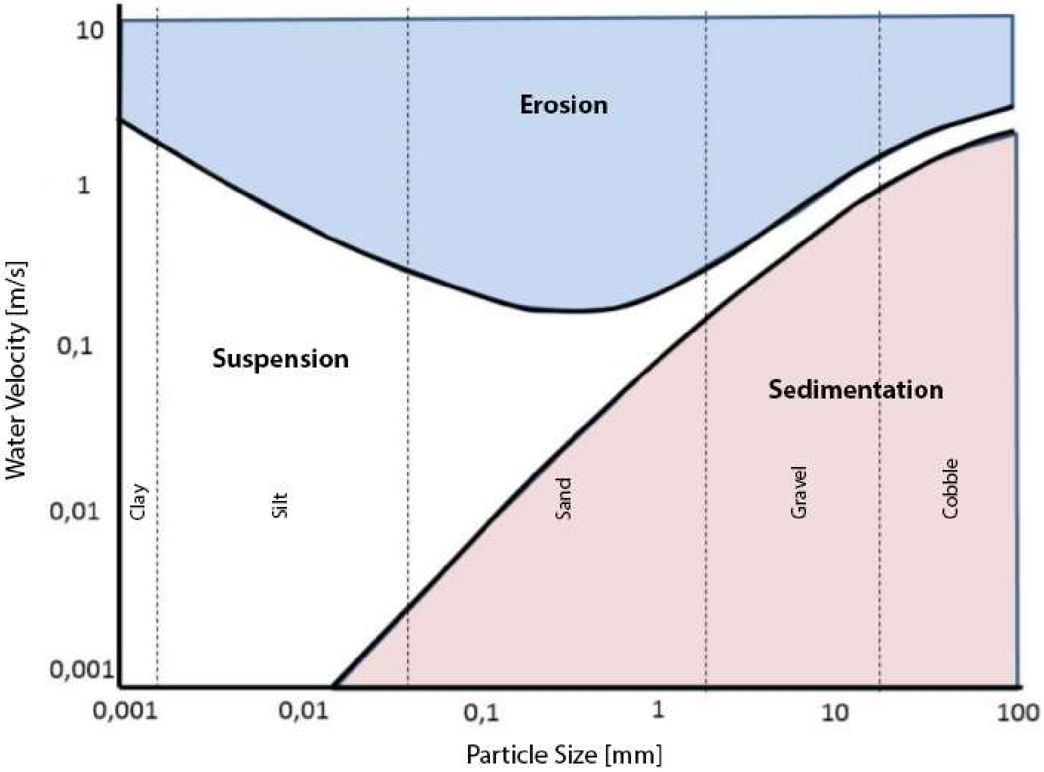

Figure 2.10 – Suspension, erosion, and sedimentation of soil particles as a function of size and stream velocity. Modified from (Norem et al., 2016).

Temporary blockage of channels and streams may occur, damming up water. A sudden burst of a natural dam may initiate landslide events, as a large volume of water is introduced into the surroundings. Glacial melt water can similarly be dammed by ice, and result in the same effect (Colleuille et al., 2017).

2.2.3 Natural and artificial factors

Artificial changes that alter the normal conditions of slopes may cause instabilities. Human activity, buildings, and constructions may possibly change the natural surrounding waterways. Forest roads, cutting through the terrain is a common construction which can function as a gutter. Rerouting of water into slopes may cause pore pressure build-ups and erosion, ultimately triggering landslides (Høeg et al., 2014). Poorly designed or clogged drainage systems in these types of constructions may have a similar effect, rerouting natural water-ways.

Deforestation by logging or forest fires affects the stability of a slope. For comparison, in an event of shallow landslides triggered by a heavy rainfall in Andorra, densely forested slopes had a landslide frequency of 16 % compared to 47 % for grassland slopes (Dikau et al., 1996). The roots in the soil have a binding effect, so act as reinforcement. In addition, root-uptake reduces the available water in the soil, effectively reducing excess pore pressures (Myrabø et al., 2014). The effect of vegetation's binding effect vs. time can be seen in Figure 2.11. The red solid line represents the time of deforestation in a densely forested area. As the roots decay, the relative strength of the soil will gradually decrease due to the decreased binding effect, and emerging cavities where there used to be roots. The increased void ratio may result in even larger pore pressure build-ups (Myrabø et al., 2014). Re-vegetation will gradually re-strengthen the soil due to added root-binding.

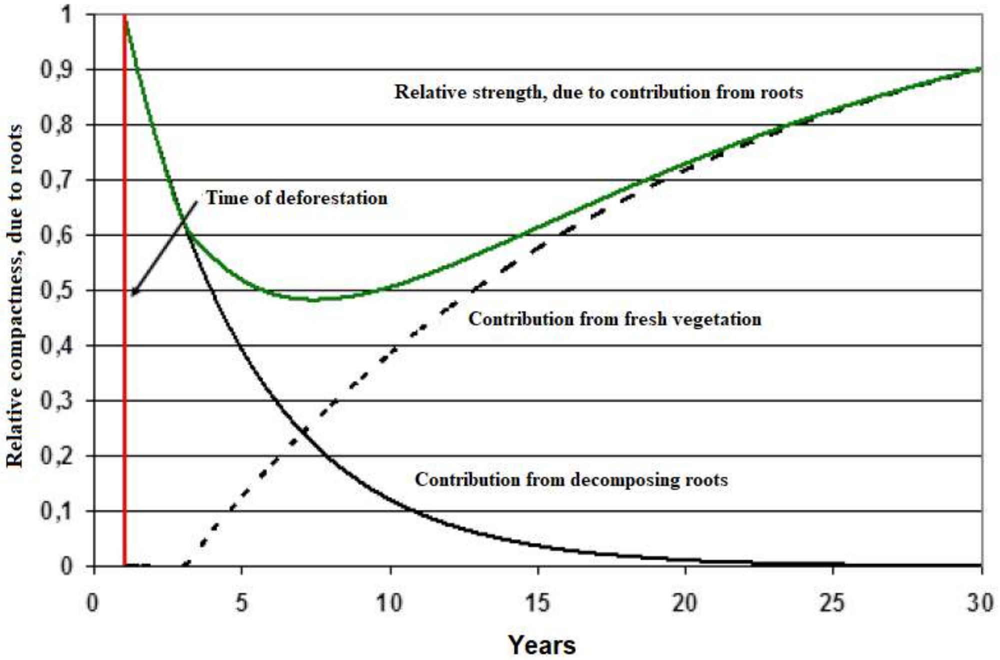

Figure 2.11 - Influence of vegetation on slope stability vs. time. Modified from (Myrabø et al., 2014).

Earthquakes of a certain magnitude will initiate landslide activity. In Norway, this is generally not a problem, due to the low magnitudes of earthquakes that occur (Høeg et al., 2014). External loads and other avalanche activity, from e.g. rockfalls may initiate landslides. The falling material can hit saturated material, causing a sudden increase in pore pressure and initiate a successive slide in underlying soil material (Høeg et al., 2014).

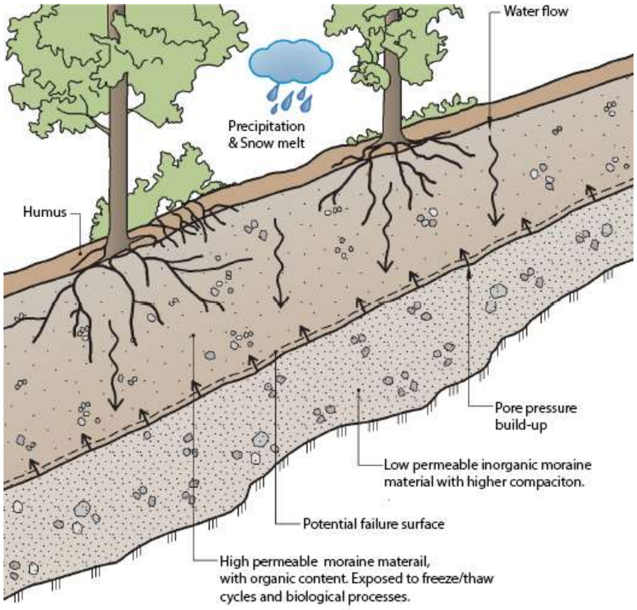

Figure 2.12 – Typical Norwegian soil profile. Courtesy of Byggforskserien 311.137 (Skoglund, 2016).

A typical Norwegian soil profile of moraine-like material is shown in Figure 2.12. The top layer is exposed to frequent biological processes, erosion, and freeze-thaw processes, which increase the permeability of the layer. The depth of this layer usually corresponds to the frost depth of the area (Skoglund, 2016). The layer below the frost depth is less permeable. The interface between these two layers may readily be subjected to pore pressure build-ups due to the difference in permeability, resulting in instability. In coarser material, the critical failure surface is normally in the interface between soil and bedrock, as the groundwater flow follows the underlying rock.

2.3 Terrain Features

Terrain features are essential for the purpose of identifying possible unstable landforms and predicting where one can expect to encounter landslide activity.

2.3.1 Slope characteristics

Some slope configurations are more prone to landslides than others. Three major slope forms can be categorized from most stable to least stable; divergent, planar and convergent (Sidle and Ochiai, 2006). The divergent shape will disperse water while it will be concentrated on planar and convergent landforms. Landslides, creep, or other processes may further add unconsolidated material which concentrates in the convergent landforms, adding more potentially unstable material. Convergent slopes are often found where translational debris avalanches turn into debris flows – typically occurring if there are a large amount of water available, and the slope converges into channels (Dikau et al., 1996).

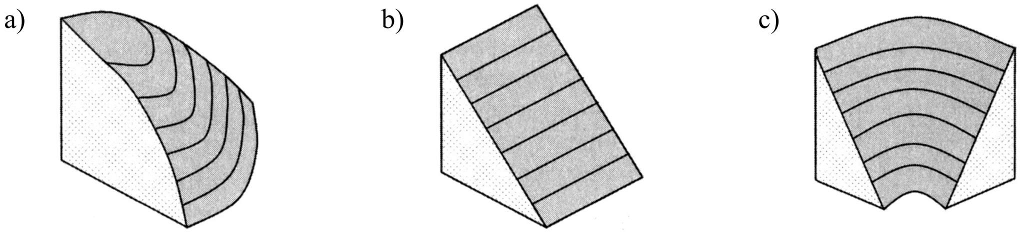

Figure 2.13 – Schematics of a) divergent, b) planar, and c) convergent slopes. From (Sidle and Ochiai, 2006).

Flow-like landslides in soil occur typically in slopes steeper than 25°. They may also occur in gentler slopes if sufficient pore pressures are able to build up. In high permeability soils, there is normally no danger of excess pore pressures. Slopes of this kind of material are usually stable at inclinations lower than 37°, unless they are influenced by external forces from an earthquake or intense rainfall (Høeg et al., 2014)

The inclination required for a debris flow to develop varies, depending on the hydrological conditions. A slope steeper than 15° is normally required for the water to reach high enough velocities to erode and entrain material along its channel (Myrabø et al., 2014). At intense periods of rainfall, debris flows may occur in slopes with inclinations down to 10° (Høeg et al., 2014). The available material the water can entrain along its channel, is a precondition for a debris flow to develop. Channels along bedrock will be less prone to developing debris flows due to the lack of loose material. Steep slopes leading into the debris flow channel may add material by separate sliding events, adding large volumes of water and material to the debris flow. The characteristics of the watershed is also a factor, as debris flows are more prone to occur in steep watersheds, with relatively thin soil cover and a quick response to water inflow (Myrabø et al., 2014).

Layers with differing permeability may destabilize a slope. Wetting/drying processes, roots, freeze-thaw cycles and biological activity affect the upper part of the soil, giving it a porous and permeable structure. Underlying layers with low permeability may cause a pore pressure build-up, and destabilize the soil (Høeg et al., 2014).

2.3.2 Topographic characteristics

Debris flows are distinguishable by their characteristic source area, main track, and depositional toe. Erosion along the main track may remove all overlying material, exposing the underlying bedrock (Høeg et al., 2014). The coarser portions of the displaced material may accumulate along the gullies forming lateral ridges before the deposits are left where the channel gradient decrease at the foot of the slope (Dikau et al., 1996). Debris avalanches are typically characterized by the low depth to length ratio, due to a relatively thin layer of unconsolidated material being mobilized and a high length to width ratio, typically > 5-10 (Dikau et al., 1996). Debris avalanches have a tendency to spread out into a pear-shaped deposit, with a thickness of 0.5 – 1.0 m (Høeg et al., 2014). The source area of the slope will typically have an inclination of 30-40°, the main track 20-30° and the depositional area <15-20° (Høeg et al., 2014).

Traditional mapping of landslides is may be conducted using aerial photographs. Terrain features and their photographic characteristics visible in aerial photography are listed in Table 2.4 below, reproduced from (Jakob and Hungr, 2005).

Table 2.4 - Topographic features of debris avalanches and debris flows, and their photographic characteristics

Terrain feature	Relation to slope stability	Photographic characteristics
Semicircular backscarp and steps	Head part of slide with outcrop of failure plane	Light-toned scarp, associated with small slightly curved lineaments
Hummocky and irregular slope morphology	Microrelief associated with shallow movements or small retrogressive slide blocks	Coarse surface texture, contrasting with smooth surroundings
Berms or levees parallel to a stream channel in a gully or canyon	Microrelief associated with the deposition of debris during a debris flow.	Raised ridges immediately adjacent to and on one or both sides of a stream
Concave/convex slope features	Landslide scar and associated deposit	Concave/convex anomalies in stereo-model
Lack of vegetation immediately below breaks in slope	Removal of vegetation by translational sliding at debris avalanche headscarps	Light-toned elongated areas at the head of gullies or just below breaks in slope
Irregular linear swaths of denuded vegetation or new regrowth	Slips surface of debris avalanches and the path of debris flows	Light toned elongated areas at the head of gullies or just below breaks in slope
Areas of stagnated drainage	Landslide hollow, back-tilting landslide blocks, and hummocky landslide topography	Tonal differences and darker tones associated with ponds of wet areas
Seepage and springs in hillslope hollows	Naturally wet areas on slopes sometimes naturally occur at debris slide headscarps	Dark patches in hollows sometimes enhanced by differential vegetation
Interruption in drainage lines	Drainage anomaly caused by a headscarp	Drainage line abruptly broken by a break in slope
Anomalous drainage pattern	Streams curing around the lobe of a debris deposit	Stream disruption by a debris fan deposit

2.4 Norwegian conditions

The Norwegian landscape is characterized by large u-shaped valleys, fjords, and alpine relief – shaped by glacial variations throughout history. Norway's geographical location, geomorphology, and land-use are interesting to characterize with respect to the processes and conditions that affect landslide activity. In assessing the potential of remote sensing methods, the prevailing atmospheric conditions and the surface characteristics are essential considerations.

2.4.1 Norwegian geography and soil cover

Over the past 2.6 million years, Norway has been subjected to more than 40 glaciations (Ramberg et al., 2008), resulting in a large number of glacial processes influencing the Norwegian geography. The last glacial maximum was reached between 18 000 - 25 000 years ago, covering a large part of the Nordic countries (Ramberg et al., 2008)

The ice sheet thickness is estimated to have been around 3000 m at its greatest (Jørgensen et al., 2013). The ice sheet exerted immense loads on the underlying crust, causing an isostatic depression amounting to several hundred meters (Ramberg et al., 2008). When the overburden ice disappeared, the underlying crust began to rise by the means of isostatic uplift. The shoreline raised and the seabed was progressively exposed. The highest recorded sea level after the last glaciation is known as the *marine limit.* The present-day marine limit is generally lowest in the western coastal regions of Norway, whilst the eastern part and mid-part of Norway have the highest. Oslo and Trondheim have a marine limit 222 m.a.s.l. and 175 m.a.s.l. respectively (Ramberg et al., 2008). Scandinavia is still rising at present-day. The Oslofjord- and Trondheim area has risen 36 cm the past century, while the Gulf of Bothnia has the greatest rate, rising 9mm/year (Ramberg et al., 2008).

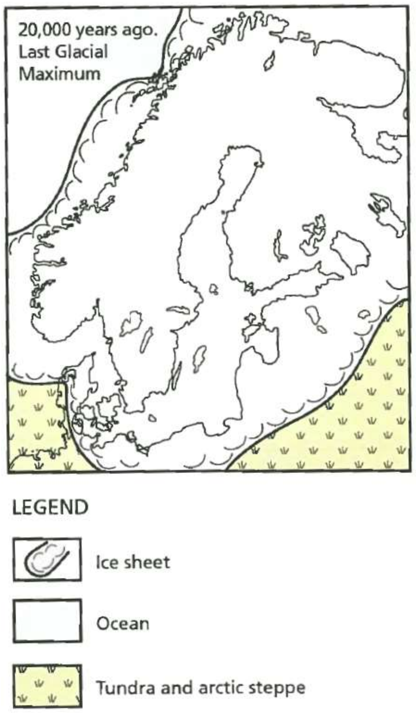

Figure 2.14 – Ice sheet extent, 20 000 years ago. Courtesy of (Ramberg et al., 2008).

The soil cover in Norway predominantly originates from the last glaciation, ending some 11,500 years ago (Ramberg et al., 2008). Several effects of the dynamics between the ice and the earth's crust can be observed in present day soil- cover and layering. Denudation and weathering processes from the retreating ice upon the underlying crust formed loose material in all fractions (Emdal et al., 2014). Climatic variations during the deglaciation made the ice-front advance and retreat, causing a redistribution of sediments and complex layering of different soil types (Emdal et al., 2014).

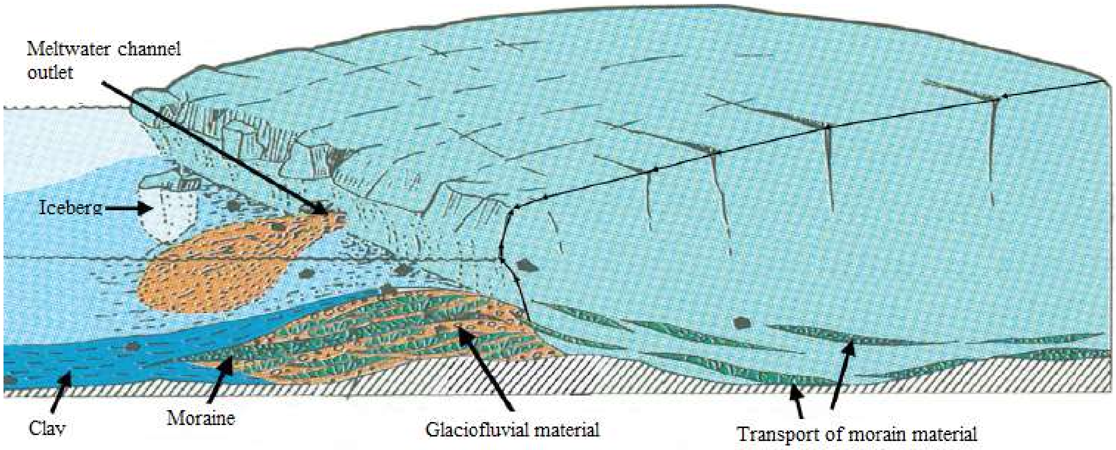

Figure 2.15 - Formation of sediments through glacial processes. Modified from (Jørgensen et al., 2013).

Generally, Norway has large areas of exposed bedrock or bedrock with a thin cover of quaternary sediments. Finnmarksvidda in northern Norway, Jæren in the southwest, and southeastern parts of Norway have large areas with continuous soil cover. The average sediment thickness of these areas are ca. 6 m, but can commonly be thicker than 10 m, and occasionally range in the hundreds of meters (Olsen et al., 2013). The different types of soil in Norway are often classified by the processes by which they were formed, and deposited. (Høeg et al., 2014) has summarized the most common:

Marine deposits

Sediments originally deposited in seawater are known as marine deposits. Areas of marine deposits can be found in Norway above the current sea level, due to the isostatic uplift. The marine sediments are mostly in the clay fraction and can exhibit quick behavior.

Glaciofluvial deposits

Water from the melting glacier would cause erosion. The ice melt resulted in rivers, which transported material. The rivers mostly deposited material in the gravel and sand fractions, as well as some silt. Above the marine limit, the deposits may be formed as long ridges or step-like terraces. Large deposits of gravel may occur below the marine limit, typically at river deltas, where the river emerged into the ocean.

Glaciolacustrine and lacustrine deposits

Sediments deposited in lakes, naturally formed or formed by melting glaciers. Sediments which are transported by rivers into lakes may form deltas close to the river mouth, where the coarser portions of the material are deposited. The finer material, such as the clay and silt fragments, will be transported further out. Large lakes were formed from the melting glaciers towards the end of the deglaciation, where large amounts of silty material were deposited. After the lakes drained, portions of this material remained as large terrace features.

Moraine

The sediments deposited directly by the retreating glaciers are known as moraine. Moraine is typically poorly graded, with a clay/silt content in the range of 5-15 %. The moraine thickness is generally relatively thin, typically in the range of a few meters, but can locally be of greater thickness-.

Colluvium (slide material)

Colluvium refers to sediments originating from landslide and avalanche activity. It is typically seen at the foot of steep mountains, where repeated rock falls and avalanches have deposited large amounts of scree. Deposits of finer material are found in steep valleys, where there might have been high landslide activity after the ice retreated and before vegetation became established.

Weathered material

Sediments originating from weathered bedrock are formed as the gradual disintegration of bedrock leads to new soil particles. A major component of weathering in Norway is the freeze-thaw cycle, in highly jointed rocks, where ice can burst the rock mass. The rock mass in Norway generally has low weathering, due to glaciers shaving the bedrock and removing the pre-glacial weathered material.

Organic material

The top layer of the soil cover typically consists of organic matter, originating from decayed vegetation. Marsh material will typically stem from this organic matter, deposited in water.

2.4.2 Land cover in Norway

The surface characteristics of mainland Norway can be categorized with respect to its land-use. Norway can be considered a barren country, with only 0.71 % of its roughly 324 000 km^2 utilized as built-up or industrial areas (Bryn et al., 2018). According to (Bryn et al., 2018) 38 % of Norway is forested, 43 % is classified as open areas, including areas such as alpine and coastal heaths, non-forested areas and similar. Wetlands and agricultural areas account for 9 % and 4 % respectively, while glaciers, snow, and freshwater account for the remainder.

2.4.3 Climatic conditions and triggers in Norway

One of the most widely used climate classification systems is the *Köppen climate classification* (Mamen, 2017). In this system, the earth is divided into five main climate groups, as described in Table 2.5 below.

Table 2.5 - Köppens main climate groups. Modified from (Mamen, 2017).

Category		Definition
A	Tropical	The annual avg. temperature is larger than 18° C.
B	Arid	One of three criterions must be fulfilled: R < 2T If at least 70 % of the precipitation comes during the winter season. R < 2T + 14 If the precipitation is equally distributed across the summer- and winter seasons. R < 2T + 28 If at least 70 % of the precipitation comes during the summer season. R = Annual precipitation [cm] T = Annual avg. temperature [° C]
C	Tempered	The temperature of the coldest month of the year is between +18 and -3°C, and R > than criterions given in category B.
D	Cold (Continental)	The temperature of the coldest month of the year is below -3°C, and the temperature of the warmest month of the year is above +10°C.
E	Polar	The average temperature of the warmest month of the year is below +10°C.

Norway is characterized by climatic variations, with three of Köppens climatic zone found in Norway; t*empered, cold* and *polar* (Metereologisk Institutt, 2009) as shown in Figure 2.16. The coastal regions of Norway are characterized by mild winters and wet summers. Valleys and mountains in central Norway have a shielding effect, making the south- and north-eastern part of the country subject to a more continental climate, with dryer summers and cold winters. As a result, the west coast is the wettest region, with areas averaging more than 3000 mm of annual precipitation. The spatial distribution of annual avg. precipitation in Norway is shown in Figure 2.17. The larger part of the precipitation comes in general during the fall, with the least in late winter and spring. Inland Norway will typically have most precipitation during July-August (Dannevig and Harstveit, 2013). The average days of precipitation are ca. 100 in Inland Norway, 150 days inland of the coast and some areas along the coast more than 200 (Dannevig and Harstveit, 2013). Debris- avalanches and flows are most frequent in the period October-January along the coastal regions of Norway, while they are more frequent in spring in the regions with a *continental* climate when the thaw and snowmelt sets in (Høeg et al., 2014).

Norway is, in other words, a country with large seasonal variations and frequent cloud cover. The annual average cloud cover percentage varies between 60 – 75 % (Sivle, 2009). Areas along the west coast have the most cloud cover, while the coastal region towards Skagerrak has the least. The cloud cover percentage is also influenced by seasonal- and spatial variations. In southern Norway, the maximum cloud cover percentage reaches typically 75-80 % in October-November while reaching as low as 50 % around May (Sivle, 2009).

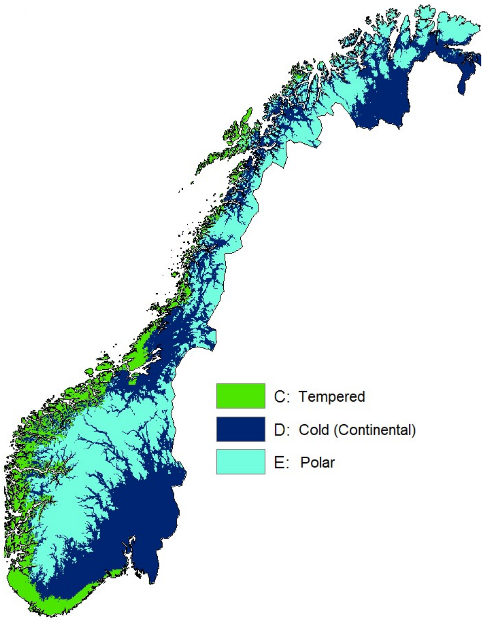

Figure 2.16 -Climate zones in Norway. Modified from (Metereologisk Institutt, 2009), CC BY-SA 3.0

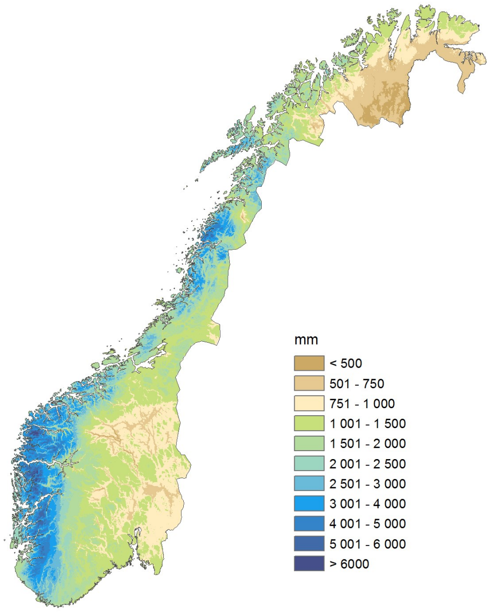

Figure 2.17 – Annual avg. precipitation in Norway (1985-2014). From (Norsk Klimaservicesenter, 2018) with permission.

2.5 Remote Sensing

The basic principle behind remote sensing is to obtain data of the earth's surface, without being in contact with it. In general, the term implies that the measurements are conducted indirectly. When done by satellites, the concept relies on emitted or reflected electromagnetic radiation. Other types of measurements may also qualify as remote sensing techniques. For instance geophysical investigations utilizing sonic waves, or laser scanning techniques such as LiDAR are considered as remote sensing. Over the past few decades, satellite and aircraft data analyses are more closely associated with the term (Emery et al., 2017). Some knowledge about the fundamentals of remote sensing and its physical concepts is necessary for understanding its functionality.

2.5.1 Electromagnetic Radiation

Electromagnetic radiation is a form of energy which can be described with characteristic physical properties. As illustrated in Figure 2.18, electromagnetic radiation consists of an electric and magnetic field, propagating as waves. The electromagnetic field varies in magnitude, in a direction perpendicular to the direction in which the radiation is traveling. The magnetic field behaves in the same manner and is oriented at right angles to the electrical field. Both these fields travel at the speed of light (Lillesand et al., 2004).

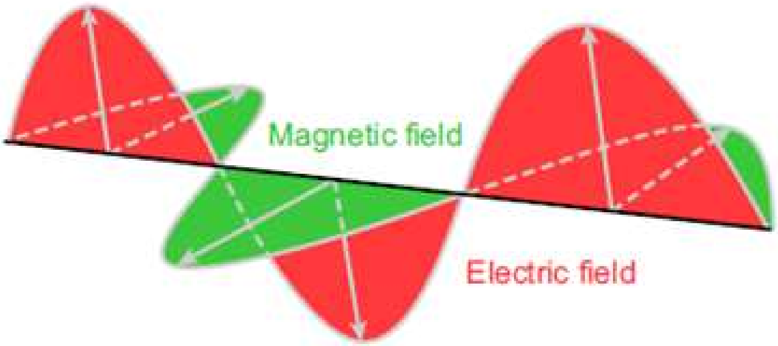

Figure 2.18 - Electric and magnetic fields (Emery et al., 2017).

The fundamental characteristics of electromagnetic waves are described by two principle measures; wavelength and frequency (Emery et al., 2017), as illustrated in Figure 2.19. Wavelength, typically denoted as λ, has a unit of distance. Frequency is measured in cycles per second - Hertz (Hz) and is typically denoted ν.

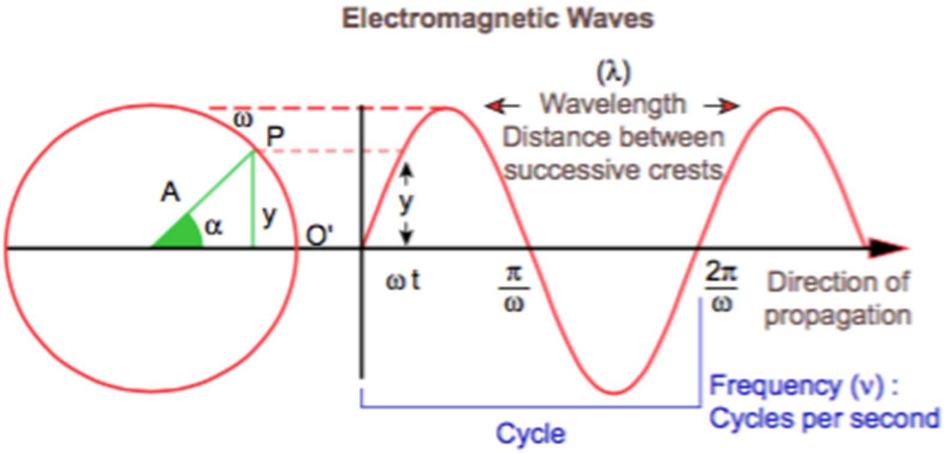

Figure 2.19 - Electromagnetic waves (Emery et al., 2017).

Wavelength and frequency are related by the basic equation:

$$c = \lambda v \tag{2.4}$$

$where$

$\lambda = Wavelength\ [m]$

$v = Freqency\ [Hz]$

$c = Speed\ of\ light\ \approx 3.0\ x\ 10^8\ [m/s]$

The speed of light is essentially a constant, making wavelength and frequency inversely related. The longer wavelengths have lower frequencies, whilst shortwave radiation has high frequencies.

2.5.2 The Electromagnetic Spectrum

Electromagnetic radiation is arranged according to its characteristics, in what is known as *the electromagnetic spectrum*. The total range of wavelengths extends from the longest radio waves to the shortest known cosmic rays. The electromagnetic spectrum is normally divided into seven sections: radio, microwave, infrared (IR), visible, ultraviolet (UV), X-rays and gamma rays (Strozzi, 2014). Their approximate frequencies and wavelengths are illustrated in Figure 2.20.

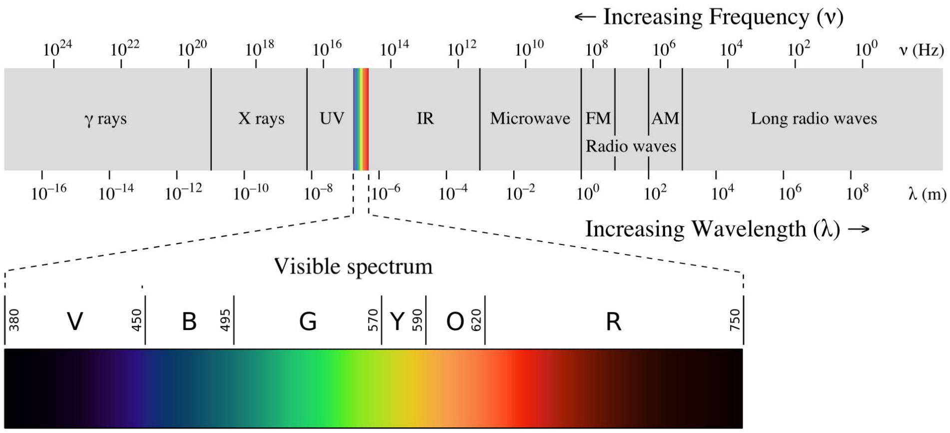

Figure 2.20 - The Electromagnetic Spectrum (Phillip Ronan, 2013).

Radiofrequency wavelengths range from many kilometers to approximately 0.3 m, and the higher end of the frequency is often associated with television and radio broadcasting. The microwave region extends from about 30 cm to 1.0 mm, and are of particular interest in spaceborne communication due to good transmissivity through the atmosphere (Hecht, 1998).

The infrared (IR) section is often subdivided into three regions: Close to the visible portion, the *near* IR (NIR), ranging from about 700 – 1300 nm. The *mid*-IR (MIR) from 1300 to 3000 nm, and the *thermal* IR (TIR) spanning from 3000 – 14 000 nm (Lillesand et al., 2004). It should be noted that there is no standardized division, and variations may be found in the literature. (Hecht, 1998) divides the section into *near* IR (780 – 3000 nm), *intermediate* IR (3000 – 6000 nm), *far* IR (6000 – 15 000 nm) and *extreme* IR (15 000 nm – 1.0 mm). (Drusch et al., 2012) use the term *shortwave* IR (SWIR) for the higher bands of Sentinel-2 (1375 – 2190 nm).

Our human senses are adapted to detect a tiny portion of the electromagnetic spectrum through our eyes – known as visible light. Ordinary white light is a mixture of all the wavelengths in the visible portion of the spectrum, which ranges from approximately 380 – 750 nm (Young et al., 2012). The different wavelengths in the visible range are what we perceive as color, and their approximate wavelengths according to (Young et al., 2012) are:

Violet	380 – 450 nm
Blue	450 – 495 nm
Green	495 – 570 nm
Yellow	570 – 590 nm
Orange	590 – 620 nm
Red	620 - 750 nm

Ultraviolet radiation (UV) ranges from about 400-100 nm. Although not visible to the human eye, the sensation of sunburn is associated with UV-rays. Some UV applications have also been used in aerial photography for detecting oil spills, although these are limited due to strong atmospheric scattering (Lillesand et al., 2004). X-Rays and Gamma rays are the shortest and most energetic wavelengths in the electromagnetic spectrum. X-rays have amongst many applications been utilized in orbiting telescopes for investigating the universe, while gamma rays are mostly associated with reactions in atomic nuclei (Hecht, 1998).

2.5.3 Radiation Principles

Electromagnetic energy is transported through units called *quanta* or *photons*. In quantum physics, electromagnetic radiation consists of photons; the elementary particles responsible for all electromagnetic interactions (Emery et al., 2017). Electromagnetic radiation can hence be described with both wave theory and particle theory. The energy of a single photon is given by Planck's equation:

$$E = hv \tag{2.5}$$

$where$

$E = Energy\ of\ a\ photon\ [J]$

$h = Planck's\ constant = 6.6261\ x\ 10^{-34}\ J\ sec$

$v = Freqency\ [Hz]$

Frequency is thus directly proportional to the energy of the particle. According to Planck's equation, high-frequency gamma-ray radiation is approximately 200 000 times more energetic than visible light. Remote sensing systems operating in the lower end of the spectrum must utilize wider bands to obtain an energy signal, due to the lower energy of the lower wavelengths. (Lillesand et al., 2004).

The molecules of an object with a temperature above absolute zero will continuously emit radiation (Lillesand et al., 2004). The magnitude of energy radiated from an object is related to its surface temperature. A *blackbody* is a theoretical perfect emitter, meaning that the body totally absorbs and reemits all energy incident upon it (Lillesand et al., 2004). Stefan-Boltzmann's law describes how much energy is emitted by a blackbody, at a given surface temperature, integrated over all wavelengths (Rees, 2001) :

$$M = \sigma T^4 \tag{2.6}$$

$where$

$M = Total\ radiant\ exitance\ [Wm^{-2}]$

$\sigma = Stefan - Boltzmann\ constant = 5.6705\ x\ 10^{-8}\ \frac{W}{m^2K^4}$

$T = Temperature\ of\ black\ body\ [K]$

Stefan-Boltzmann’s law describes the emitted radiation integrated across all wavelengths. To find how the energy is emitted in specific wavelengths the distribution can be calculated, as (Rees, 2001) explains, using quantum mechanics: To describe the radiation distribution, *spectral radiance* must be defined. The radiant energy emitted – *radiance*, L –must be modified to include its variation with wavelength. Spectral radiance, L_λ is the differential of radiance L, with respect wavelength λ:

$$L_\lambda = \frac{\Delta L}{\Delta \lambda} \qquad or, \qquad L_\lambda = \left|\frac{\partial L}{\partial \lambda}\right| \ [\frac{W}{m^2 sr\ m}]$$

Which can be solved numerically using the equation:

$$L_\lambda = \frac{2hc^2}{\lambda^5\left(e^{\frac{hc}{kT}} - 1\right)} \tag{2.7}$$

where

$L_\lambda = Spectral\ radiance\ [\frac{W}{m^2 sr\ m}]$

$h = Planck's\ constant = 6.6261\ x\ 10^{-3}\ \ J\ sec$

$c = Speed\ of\ light\ \approx 3.0\ x\ 10^8\ [m/s]$

$\lambda = Wavelength\ [m]$

$k = Boltzmann\ constant = 1.3807\ x\ 10^{-23}\ \frac{J}{K}$

$T = Temperature\ of\ black\ body\ [K]$

Figure 2.21 shows blackbody spectral radiance frequency distributions for different temperatures. The graphs show what Stefan-Boltzmann’s law describes – that the total amount of radiant energy emitted from an object is increasing with higher temperatures. The dominant wavelength, at which a blackbody radiation curve reaches a maximum is found by differentiating eq 2.7, which gives *Wien’s displacement law* (Rees, 2001):

$$\lambda_{max} = \frac{A}{T} \tag{2.8}$$

where

$A = Constant = 2.898 \; x \; 10^{-3} \; K \; m$

$T = Temperature \; of \; black \; body \; [K]$

The sun is a good approximation to a black body at a temperature at 5800 K (Rees, 2001), which as seen in Figure 2.21 yields its dominant wavelength in the visible part of the electromagnetic spectrum. Human vision is sensitive to energy of this magnitude, and we are able to observe objects around us as a result. The earth's ambient temperature is about 300 K (Lillesand et al., 2004), which yields a peak wavelength at roughly 10 000 nm – in the infrared part of the spectrum. Although this radiant energy is not observable by human senses, it can be detected using thermal devices. It is often referred to as *thermal infrared* as the radiance correlates to terrestrial heat (Lillesand et al., 2004).

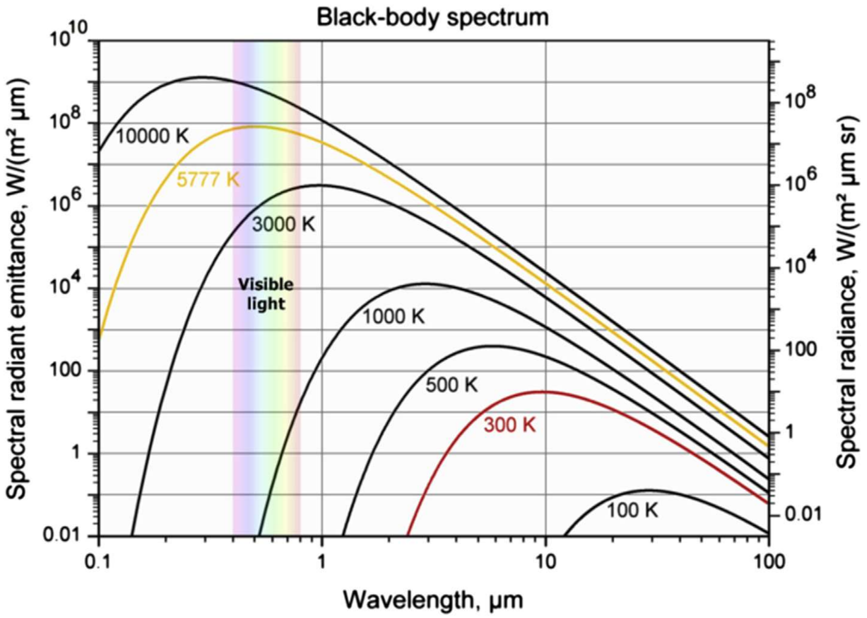

Figure 2.21 - Blackbody emission curves (Emery et al., 2017).

2.5.4 Atmospheric Interactions

All radiant energy detected by a remote sensing system passes some distance through the atmosphere and is influenced by atmospheric effects. The type and amount of atmospheric influence is a function of distance. Energy sensed by terrestrial systems for example, is less influenced than spaceborne systems due to the relative length of atmosphere it encounters. The effect of the atmosphere varies with the magnitude of energy, present atmospheric conditions, and wavelength (Lillesand et al., 2004).

Particles and gases affect the radiation through the mechanisms *scattering* and *absorption.* Scattering occurs when particles or large gas molecules present in the atmosphere interact with and cause the electromagnetic radiation to be redirected from its original path (CCMEO, 2013). The type of scattering mechanism differs depending on the size of the interacting particles, relative to the wavelength of the interacting radiation. The different types of scattering are known as *Rayleigh-, Mie-* and *nonselective* scattering (CCMEO, 2013). *Rayleigh* scattering occurs when the particles are smaller than the interacting wavelength. It is dominant in the upper atmosphere and causes the sky to be perceived as blue. *Mie* scattering occurs when the particles and wavelength are approximately equal. Smoke and water vapor are common causes of this mechanism. When the particles are larger than the interacting wavelengths, it is known as *nonselective* scattering, where all wavelengths are approximately scattered uniformly and cause fog and clouds to appear white. Some of the longer wavelengths utilized in remote sensing systems are very much unaffected by these mechanisms and can penetrate the atmosphere in almost all conditions (Emery et al., 2017), whilst the shorter wavelengths are deemed useless in some atmospheric conditions.

Absorption is a result of molecules in the atmosphere which absorb energy at various wavelengths. Ozone, CO_2 and water vapor are the most efficient constituents which absorb radiation (CCMEO, 2013). The transmission of radiation through the atmosphere is a function of wavelength, as shown in Figure 2.22. The parts of the electromagnetic spectrum in which the atmosphere is transparent are referred to *as atmospheric windows* (Lillesand et al., 2004).

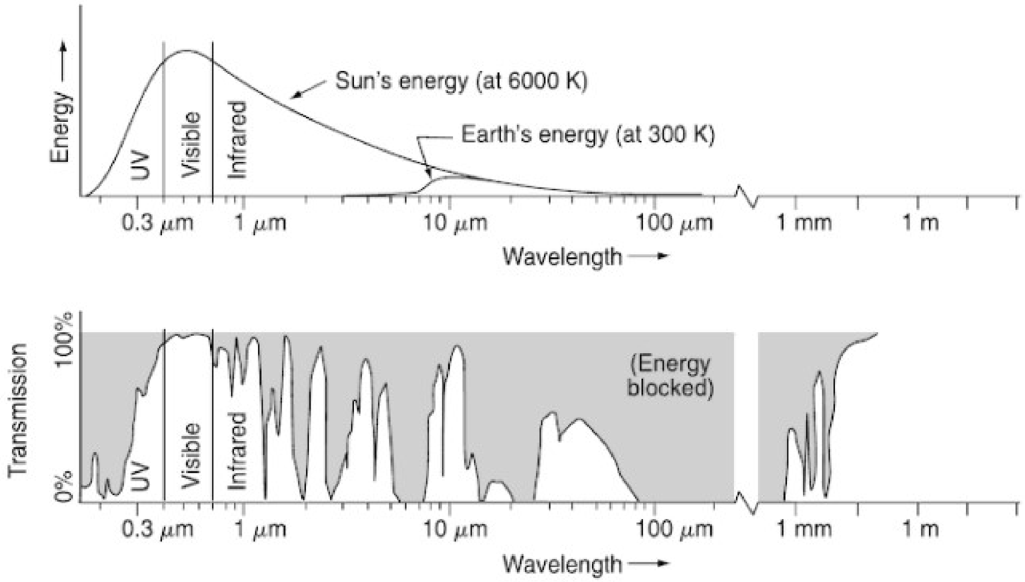

Figure 2.22 – Spectral characteristics of the sun and earth, and atmospheric windows. Courtesy of (Lillesand et al., 2004). (Copyright © John Wiley & Sons, Inc. All rights reserved.)

The dominant wavelengths for the sun and earth correspond to wavelengths with high transmission through the atmosphere. The wavelengths that penetrate the atmosphere is hence the most interesting for satellite remote sensing purposes.

2.5.5 Interactions with earth's surface

Electromagnetic radiation which penetrates the atmosphere will eventually interact with the earth's surface. Three forms of interaction are possible when electromagnetic radiation is incident on a surface: a*bsorption, reflection,* and *transmission* (Lillesand et al., 2004). Many remote sensing systems rely on the reflectance properties of the earth, and hence the reflected radiation. The radiation can be decomposed with respect to reflection, according to the principle of conservation of energy:

$$E_R(\lambda) = E_I(\lambda) - E_A(\lambda) - E_T(\lambda) \tag{2.9}$$

$where$

$E_R(\lambda) = Reflected\ energy$

$E_I(\lambda) = Incident\ energy$

$E_A(\lambda) = Absorbed\ energy$

$E_T(\lambda) = Transmitted\ energy$

The reflected energy off a surface is equal to the incident energy, reduced by any radiation transmitted and/or absorbed through the medium. The effects are illustrated in Figure 2.23. A *specular* reflection is shown in the leftmost illustration - A perfect mirror-like reflection where the incident angle of entry is equal to the output-angle. To the right, a *diffuse* reflector, which scatters the incident radiation uniformly in all directions. These are idealized surfaces, as opposed to real life surfaces on earth which normally behaves somewhat between the two extremes (Lillesand et al., 2004). In addition, as eq.2.9 suggest, the radiation may be transmitted through or absorbed by the medium, as shown by the two rightmost illustrations. Several modes of energy can be utilized by a satellite remote sensing system – In addition to reflected energy, keeping in mind Stefan-Boltzman's law, radiant energy from the sun will heat up the earth, which in turn result in more naturally emitted radiation.

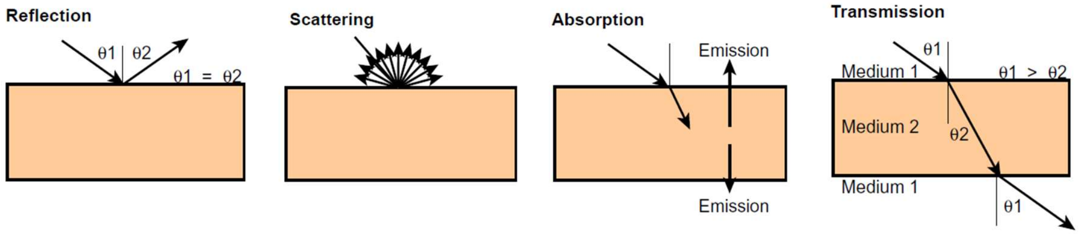

Figure 2.23 - Energy interactions with surface features (Emery et al., 2017).

The reflected energy off a surface is dependent on the material type, its condition and, as indicated in eq. 2.9, wavelength. These characteristics make it possible to distinguish different features and material properties based on its spectral information. A normalized value for the reflectance properties is commonly used for quantification, known as *spectral reflectance* (Lillesand et al., 2004):

$$\rho_\lambda = \frac{E_R(\lambda)}{E_I(\lambda)} \tag{2.10}$$

$where$

$\rho_\lambda \quad = Spectral\ reflectance$
$E_R(\lambda) = Reflected\ energy$
$E_I(\lambda) = Incident\ energy$

The response of a surface to the mechanisms of absorption, transmission, and reflection is known as the *spectral response* (CCMEO, 2013). Figure 2.24 a) shows typical spectral responses for vegetation and soil. Green vegetation has unsurprisingly, a peak reflectance in the green part of the visible wavelengths, but it exhibits relatively low reflectance in this region of the electromagnetic spectrum. It has high reflectance in the NIR-range. It should be noted that the curves represent average reflectance curves derived from a number of measurements. Individual features may have complex spectral signatures and vary considerably. Dependent on the level of detail, the spectral signature of e.g. green vegetation can be further analyzed. The spectra signature of different type of trees may be differed by variations in their specific spectral signatures as shown in Figure 2.24 b). These spectral characteristics are utilized by remote sensing systems for a number of applications, in e.g. forestry management, burn mapping and geology (CCMEO, 2013).

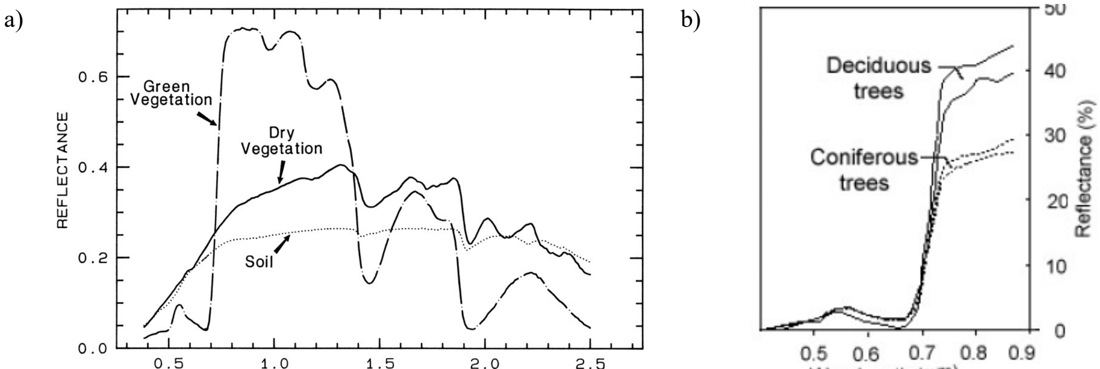

Figure 2.24 – Spectral response from a) different surfaces (Clark, 1999) b) different types of trees (CCMEO, 2013)

2.5.6 Satellite remote sensing systems

The energy from the earth's surface is measured with an instrument, often referred to as a *sensor*. Depending on its purpose and designated target, the sensor can be ground-based, airborne or spaceborne. Satellites are a common platform for spaceborne remote sensing systems, which enables repetitive coverage of large areas of the earth. Earth-mapping satellites commonly follow low earth orbits, typically operating in the 500-900 km range (Emery et al., 2017). A *polar* orbit refers to a satellite orbiting above, or close to the earth's poles. A *sun-synchronous* orbit refers to an orbital period where the satellite follows the sun's westward progress. The satellite will cross the equator and same latitudes at approximately the same time at each passing (Lillesand et al., 2004).

The remote sensing sensor can either be *active* or *passive*. An *active* sensor supplies its own source of energy or illumination (Lillesand et al., 2004), e.g. LiDAR systems which emit their own energy and measure the return signal. *Passive* sensors rely on reflected or emitted energy originating from an external source (Lillesand et al., 2004). The systems operating in the range from approximately 300 nm to 14 000 nm, which includes the UV-, visible-, and IR-wavelengths, are known as optical systems (Lillesand et al., 2004). Optical systems rely on illumination from the sun as their source of energy. For the most part, this is reflected radiation, but natural emitted energy may be detected in the thermal-IR region, if energetic enough (CCMEO, 2013). The term *optical* is coined from the fact that the energy in this part of the spectrum can be refracted and reflected using a system of lenses and mirrors. Spaceborne systems operating in the ~1 mm to 1 m wavelengths are also of substantial use for remote sensing purposes (Lillesand et al., 2004). These are equipped with RADAR-technology – An active system which can penetrate the atmosphere in almost all atmospheric conditions (Emery et al., 2017).

In practice, wavelengths are measured over a small range. The different ranges which are measured are referred to as bands. A *multispectral* (MSI) instrument is a remote sensing system measuring the energy over multiple bands. The MSI operates in the optical range (Lillesand et al., 2004) and is characterized by its technical capabilities; The size of the smallest feature that can be detected and separated from its surroundings is referred to as *spatial resolution* (CCMEO, 2013). The spatial resolution is a good indication of the sensors' ability to extract details, as illustrated in Figure 2.25, showing three images with varying resolution. The range of wavelengths, or *bandwidth,* of which the wavelengths are recorded decides the *spectral resolution*. The narrower the bandwidth, the finer spectral resolution (CCMEO, 2013).

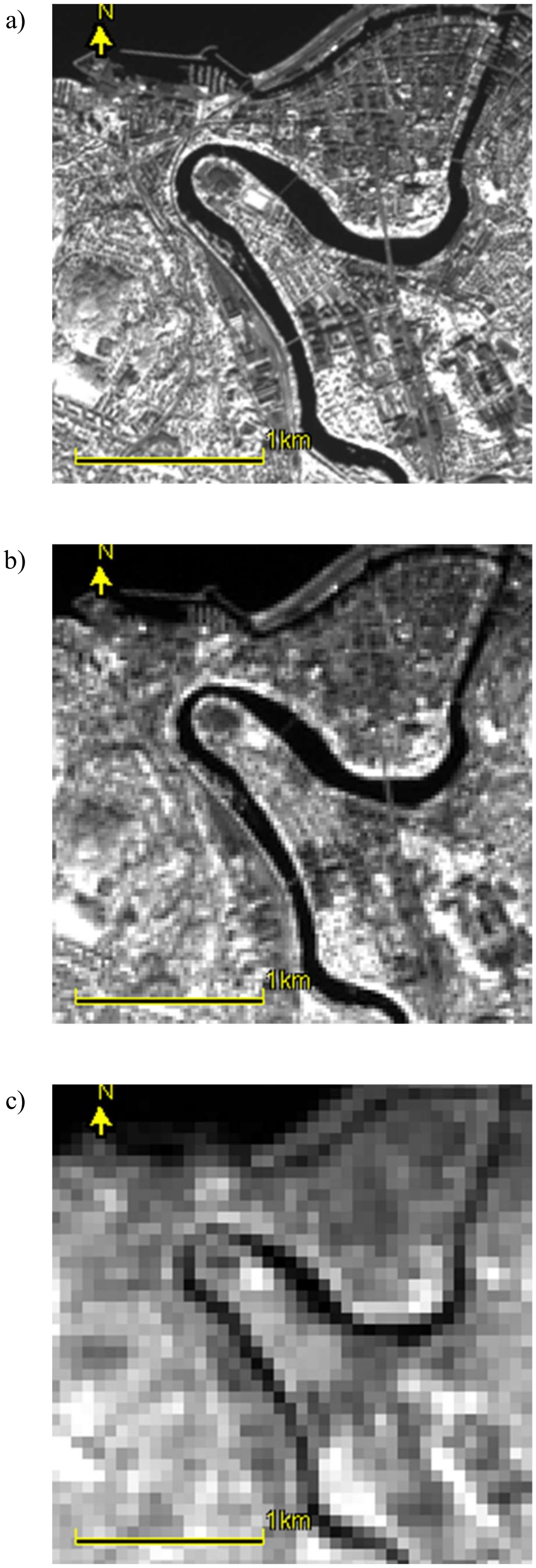

Figure 2.25 – Sentinel 2A scene from Trondheim City center (27.08.17), with resolutions a) 10m, b) 20 m, and c) 60 m.

The sensors ability to discriminate differences in energy determines the *radiometric resolution.* The smaller the differences the sensor is capable to detect, the finer the radiometric resolution (CCMEO, 2013). As satellite remote sensing data commonly is stored in pixels, the radiometric resolution is described by the number of bits used for coding numbers in binary format (CCMEO, 2013) An 8-bit image has 2^8 =256 different intensity values for a pixel, whilst a 12-bit image has 2^{12}=4096 possible values of intensity for a pixel. Although not a technical specification, the *temporal resolution* is used to describe how much time it takes between the data acquisition of the same area.

2.5.7 Data acquisition and processing

An MSI will physically acquire data by scanning the earth's surface, resulting in a raster dataset. The raster dataset is essentially a matrix of cells, where each cell are assigned a value. In the case of raster data derived from an MSI, the cell values correspond to measured reflectance. The components of a raster dataset are illustrated in Figure 2.26 below. The cells, shown to the left, are assigned the values in the corresponding position from the matrix. On the right, a digital image representing the data – Each cell, or *pixel,* is assigned a gray-level intensity based on its value, or a color brightness value.

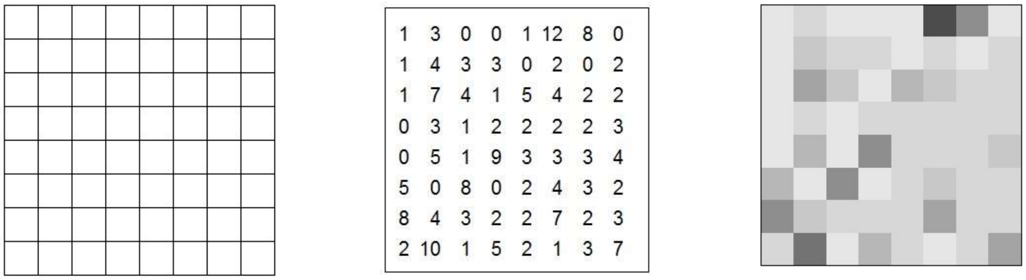

1	3	0	0	1	12	8	0
1	4	3	3	0	2	0	2
1	7	4	1	5	4	2	2
0	3	1	2	2	2	2	3
0	5	1	9	3	3	3	4
5	0	8	0	2	4	3	2
8	4	3	2	2	7	2	3
2	10	1	5	2	1	3	7

Figure 2.26 - Raster data (Cola, 2011).

The raster dataset is geometrically corrected and geocoded so that every pixel is assigned an x-, and y-coordinate in a coordinate reference system. For each band, the result is an orthorectified digital image, representing the magnitude of recorded reflectance for the surface of the earth.

Keeping in mind the fact that different surface features may have distinct spectral signatures, it is possible to calculate and classify the earth's surface features based on these relations. A widely used *band ratio* is the normalized difference vegetation index (NDVI), as described by (CCMEO, 2013):

$$NDVI = \frac{NIR - RED}{NIR + RED} \tag{2.11}$$

As previously shown in Figure 2.24, green vegetation has high reflectance in the NIR wavelengths and low reflectance in the red wavelengths. Soil and water show near equal reflectance both in the red and NIR-portions (CCMEO, 2013). Numerically, the value is normalized, taking on a value between +1.0 and -1.0. Pixels with a high reflectance in the NIR band and low reflectance in the RED band will take on a high value. A pixel with predominantly soil or water will take on values closer to 0, or even negative values. Plank et al. (2016) classifies areas of rock, sand, and snow with an NDVI less than 0.1, waterbodies with negative NDVI values, and an NDVI in the range of 0.1 – 0.7, as a function of vegetation density.

Similar normalized band ratios have been developed for other earth mapping applications. Amongst them the normalized difference water index (NDWI), defined by (McFeeters, 1996):

$$NDWI = \frac{GREEN - NIR}{GREEN + NIR} \tag{2.12}$$

The ratio produces typically positive values representing open water areas, while non-water features are typically taking on negative values. Another index is the normalized difference snow index (NDSI), as described by (Hall et al., 1995):

$$NDSI = \frac{GREEN - SWIR}{GREEN + SWIR} \tag{2.13}$$

The spectral signature of snow reflects visible radiation more strongly than the middle-infrared part. (Hall et al., 1995) found that NDSI values greater than, or equal to 0.4 represent snow cover well.

3 Method

The methods implemented in the preparation of this thesis, and background information on the utilized instruments, are described in the following chapter.

3.1 Literature review

A review of literature concerning the theoretical background of both landslides and satellite remote sensing is given in chapter 2. The literature originates from books, articles, and online content. A complete list of references is given in the final chapter. The purpose of the literature review is to present a relevant theoretical basis of the mechanisms and principles governing landslide processes, and the process of gathering and analyzing satellite remote sensing data.

3.2 Sentinel-2

All remote sensing data used in this thesis is acquired by ESAs Sentinel-2 satellites. The satellites are part of the Global Monitoring for Environment and Security (GMES) initiative. The different missions focus on different aspects of earth observation; atmospheric, oceanic, and land monitoring. The Sentinel-2 mission aims to provide high-resolution multi-spectral remote sensing data for segments such as risk management (floods, forest fires, and landslides), land use- state and changes, forest monitoring, food security, EWS, natural hazards etc. (Drusch et al., 2012).

The Sentinel-2 mission comprises two identical multispectral satellites, in the same orbit, phased 180° to each other. The Sentinel-2A has been in operation since June 2015, while the Sentinel-2B was launched in March 2017. The characteristics of the Sentinel-2 satellites are given in the Tables below. All technical information regarding the Sentinel-2 mission is obtained from (ESA, 2010) and (ESA, 2013).

Table 3.1 – Sentinel-2 characteristics

Bands	13 bands total – Spanning the visible, NIR and SWIR portions of the electromagnetic spectrum.
Temporal resolution	5 days revisit time at the equator. Close to two days at high latitudes (with different viewing angles), depending on location
Spatial resolution	10 m, 20 m or 60 m - Varying with the specific band – The blue (B2), green (B3), red (B4), and one NIR (B8) band have 10 m spatial resolution.
Spectral resolution	Varying with the specific band. See *bandwidth* in Table 3.2.
Radiometric resolution	12 bit – Images can be acquired with up to 4096 different light intensity values.
Orbit	Polar-orbit, sun-synchronous

Table 3.2 - Sentinel-2 band wavelengths (spatial resolution is given in parenthesis)

Band	Central Wavelength [nm]
1 Blue (60 m)	20
2 Blue (10 m)	65
3 Green (10 m)	560
4 Red (10 m)	665
5 NIR (20 m)	705
6 NIR (20 m)	740
7 NIR (20 m)	783
8 NIR (10 m)	842
8a NIR (20 m)	865
9 NIR (60 m)	945
10 SWIR (60 m)	1375
11 SWIR (20 m)	1610
12 SWIR (20 m)	2190

3.3 Data acquisition

The data acquisition is twofold – the first task was to select previously documented landslide events for the study. Secondly, satellite data with adequate quality had to be obtained given the location and timing of the event. A full specification of acquired data is given in Appendix A, Tables A.1-A.3.

3.3.1 Landslide events

Potential landslide events were obtained from the Norwegian national landslide inventory, via the online map services *skredregistrering.no* and *xgeo.no.* Events classified as “landslide in soils” between the period July 2015 and December 2017 were systematically examined. Based on their description, a total of 97 registrations were singled out as “potential events”. The criteria used were events of a certain magnitude – typically specified by *meters of closed road* or *volume of displaced material* – and events with certain interesting characteristics:

- Meters of closed road > 10 m
- Volume of displaced material > 1000 m^3
- Clusters of events – multiple landslide activities occurring at the same time in a small area
- Events related to floods, e.g. the Kristiansand-area flood Oct. 2017.

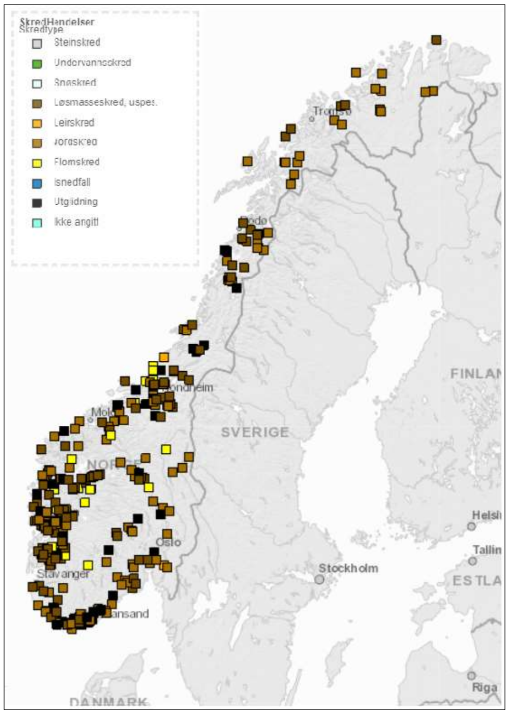

Figure 3.1 – Registered landslides in soils in 2017. (Screenshot from www.skredregistrering.no, captured 29.05.18.)

Further documentation of the events is found through the online service *regObs*. RegObs is an inventory service, containing observations of snow condition and snow avalanches, ice cover conditions, floods, and landslides. The information specified in the registered observations are typically; the date of occurrence/observation, a coordinate reference, pictures of the observation and possibly a link to other sources, e.g. a news report. RegObs has an open data policy, which enables the public to contribute observations, as well as the proper authorities. The regObs observations are linked to the national landslide inventory. If available, regObs links to each investigated event are given in Appendix A, Table A.1.

3.3.2 Sentinel-2 data

The Satellite data was obtained through the online service www.satellittdata.no. The data are downloaded as *tiles*, roughly covering a 100 km x 100 km area (ESA, 2013). Data acquired prior to November 2016 are downloaded as a package of more than 9 tiles, covering a greater area. The provided data are referred to as "Level-1C" products, meaning that the products have undergone a great deal of processing and corrections conducted by the provider. The level-1C products are ready-to-use and orthorectified using the WGS84 datum and UTM projection. The radiometric measurements are provided in *TOA – Top Of Atmosphere Reflectance* (ESA, 2013).

3.3.3 Investigated events

The investigated events are given in Table 3.3 below. A selection of 25 events were picked out of the 97 potential events based on satellite data availability. The table shows the number for each event used for further reference throughout the thesis, the classification of the landslide according to the Norwegian national inventory, and the name of the geographical location, also used for referring to the separate events. The sensing date of the S2-datasets closest to the date of occurrence is given, as well as the coordinate reference reported in the national inventory, given in UTM33N projection. Empty cells indicate no available S2-data.

Table 3.3 – Investigated events

No.	Classified as	Name of location	Date of occurence	UTM 33N		S2 - ACQUISITIONS	
				x	y	Pre-event	Post-event
1	Debris avalanche	Lindelia	03.09.2015	205973	6699030	22.08.2015	04.09.2015
2	Debris flow	Hunnedalen	02.06.2016	4400	6551095	24.05.2016	10.06.2016
3	Debris flow	Kommedal	02.06.2016	2071	6554655	24.05.2016	10.06.2016
4	Debris avalanche	Øksland	03.09.2016	9234	6825644	06.06.2016	04.09.2016
5	Debris avalanche	Slettafossen	19.05.2017	141786	6929661	12.05.2017	28.06.2017
6	Debris flow	Kråkagjelet	19.05.2017	87781	6772220	06.05.2017	22.08.2017
7	Debris avalanche	Spansdalen	15.06.2017	619037	7624840	12.06.2017	22.07.2017
8	Debris flow	Selskreda	24.07.2017	152446	6942625	21.07.2017	26.07.2017
9	Debris flow	Tokke	02.10.2017	94984	6616064	16.09.2017	06.10.2017
10	Debris avalanche	Rødstøl	09.06.2011	142097	6929113	12.05.2017	28.06.2017
11	Debris avalanche	Krundalen	05.07.2015	89269	6857894	-	18.08.2015
12	Debris avalanche	Bjerkadalen	26.01.2017	451347	7337775	25.10.2016	15.02.2017
13	Debris avalanche	Sulitjelma	02.05.2017	545602	7446993	29.04.2017	09.05.2017
14	Debris avalanche	Byrkjedal	02.10.2017	-3207	6549591	23.09.2017	23.10.2017
15	Debris flow	Beiarn	11.07.2015	483056	7406592	-	15.08.2017
16	Debris flow	Raudskredbekken	05.12.2015	32023	6702194	18.08.2015	14.02.2016
17	Debris avalanche	Reinåa	05.12.2016	329768	7040444	07.11.2016	15.02.2017
18	Debris avalanche	Jølster	08.12.2016	31549	6850364	03.11.2016	23.03.2017
19	Debris avalanche	Hyestranda	30.12.2016	30495	6886478	03.11.2016	23.03.2017
20	Debris avalanche	Ommedal	30.12.2016	21026	6874308	03.11.2016	23.03.2017
21	Debris avalanche	Falla	20.01.2017	183744	6978059	17.11.2016	16.04.2017
22	Debris avalanche	Ávžejávri	08.06.2017	825987	7752075	27.05.2017	09.06.2017
23	Debris avalanche	Setesdalsveien	30.09.2017	84709	6473561	22.08.2017	16.10.2017
24	Debris avalanche	Saga	02.10.2017	85672	6475590	12.08.2017	06.10.2017
25	(Multiple) Debris flows	Luster	02.10.2017	104227	6836862	23.09.2017	09.10.2017
				105424	6837850	23.09.2017	09.10.2017
				106008	6838378	23.09.2017	09.10.2017
				112582	6841895	23.09.2017	09.10.2017

3.4 Data analysis

Several aspects of the S2 – datasets and investigated landslide events have been examined. See Appendicies C for landslide characterization, and D, E and F for specifications of spectral reflectance.

3.4.1 GIS-analysis

The surrounding areas of the investigated locations, are all characterized with respect to the quaternary geology, geology, and the terrain inclination. The software ArcGIS Pro was used for the analysis and visualization of geospatial data. The geology and quaternary geology are datasets provided by The Norwegian Geological Survey, NGU. The slope inclination data is provided as a WMS by NVE and is derived from a digital elevation model with 10 m resolution.

3.4.2 Sentinel-2 data analysis

All satellite data have been processed and analyzed in the software "SNAP", provided by ESA. All downloaded datasets were initially visually inspected for traces of any landslide activity at the reported locations. In addition, a simple change detection approach was implemented by simply flicking between the pre-event data and post-event data to visually observe any changes in the area. Natural color composites, false color composites, and NDVI-images were inspected.

The detected landslides were manually lineated, using different feature classes. The surface extent of the landslide area was delimited by a polygon. The length and width were defined with line-features. A transect was defined along the landslide's centerline, and the width taken at two sections; the observed widest and narrowest parts of the detected landslide.

The spectral characteristics of all detected landslides were examined and compared using the S2 bands B2, B3, B4, and B8, which comprise all bands with 10 m resolution. The pixels along the transects were considered the most significant pixels and used in the analysis. Different combinations of the bands are compared; including reflectance of single bands, NDVI, ratios, and NDVI-ratios. See Appendix D.

A change detection approach was applied, using raster calculations. The change of reflectance in landslide pixels was examined between two or more datasets. The pixels along the centerline transects were considered. The difference between single bands and NDVI were used, as well as ratios and a normalized difference ratio. The equations for the calculations are given below – the #-notation refers to the band number, while t_1 and t_2 refer to time 1 and time 2 respectively, where time 1 is the earliest acquisition. See also Appendix E.

Difference

The difference in single bands, and NDVI between time 1 and time 2:

$$B^{\#}_{t_1} - B^{\#}_{t_2} \tag{3.1}$$

$$NDVI_{t_1} - NDVI_{t_2} \tag{3.2}$$

Ratios

The ratio of the spectral reflectance in single bands, and NDVI at time 1 and time 2:

$$\frac{B^{\#}_{t_1}}{B^{\#}_{t_2}} \tag{3.3}$$

$$\frac{NDVI_{t_1}}{NDVI_{t_2}} \tag{3.4}$$

Normalized difference ratios

The normalized difference ratio between single bands, and NDVI at time 1 and time 2:

$$\frac{B^{\#}_{t_1} - B^{\#}_{t_2}}{B^{\#}_{t_1} + B^{\#}_{t_2}} \tag{3.5}$$

$$\frac{NDVI_{t_1} - NDVI_{t_2}}{NDVI_{t_1} + NDVI_{t_2}} \tag{3.6}$$

3.4.3 Automatic classification using thresholds

Based on the spectral reflectance properties and change of spectral reflectance, thresholds were applied to S2-data covering 5 of the detected landslides. The thresholds were used as a mean of classifying pixels into “possible landslide” or “not landslide”.

Multiple thresholds were applied to the same satellite data scene, aiming for higher accuracy than one threshold. Masks were applied to according to the defined thresholds – I.E. NDVI < 0.2 is masked out with a color, indicating “possible landslide”.

4 Results

The findings and characteristics of all examined events, with their belonging satellite data is summarized and presented below.

4.1 Characteristics of investigated events

A total of 25 landslide events were examined. The events have been deemed *"detected", "possibly detected",* and *"undetected"*. Their geographical location and classification are shown in Figure 4.1. Detected events are represented as green circles, possibly detected as yellow circles and the undetected are red. For a full specification of investigated events, and their corresponding remote sensing data, see Tables A.1 - A.3, in Appendix A. A characterization of all investigated locations are summarized in the Tables 4.1 – 4.3. For a more detailed characterization, see Appendix C.

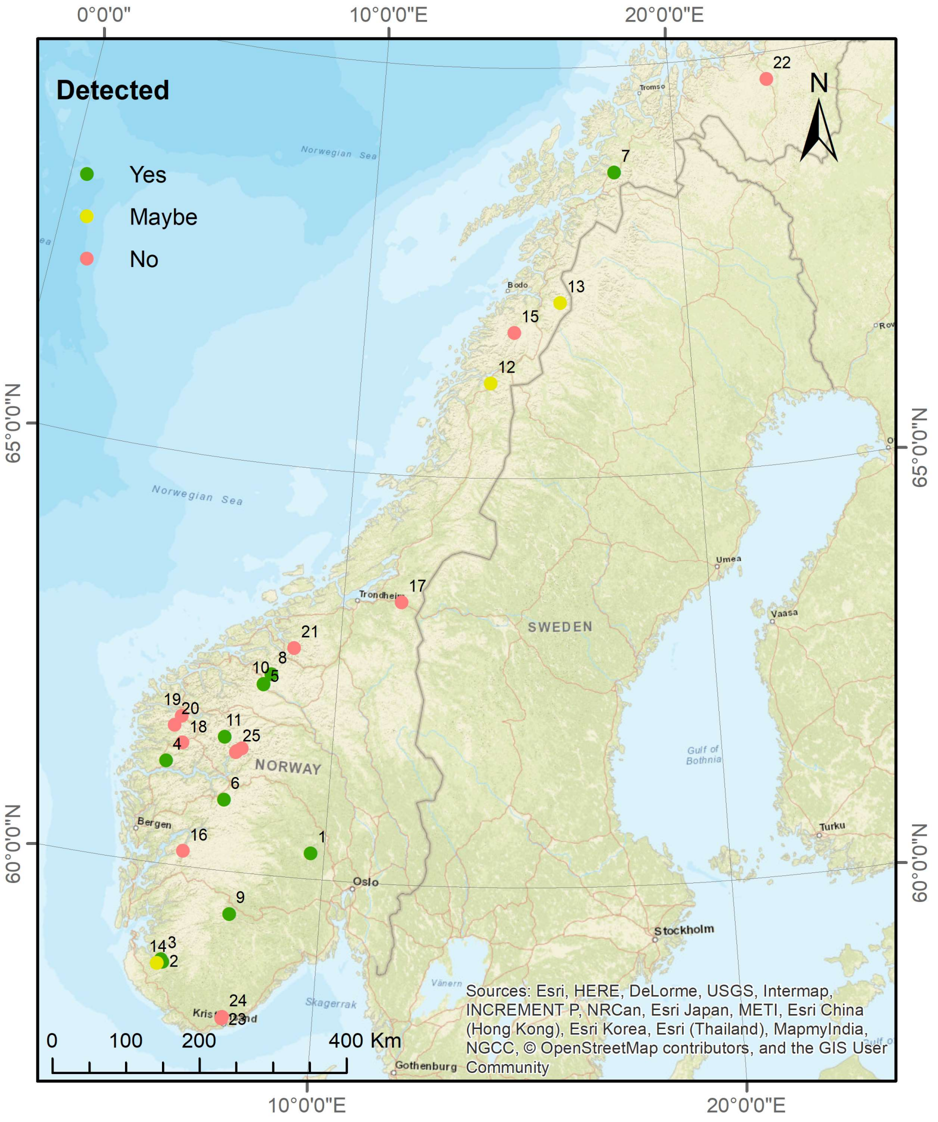

Sources: Esri, HERE, DeLorme, USGS, Intermap, INCREMENT P, NRCan, Esri Japan, METI, Esri China (Hong Kong), Esri Korea, Esri (Thailand), MapmyIndia, NGCC, © OpenStreetMap contributors, and the GIS User Community

Figure 4.1 - Map of investigated events. Courtesy of Erin Lindsay.

A brief summary of the main findings:

- **11/25** of investigated events were deemed *detected*, **3/25** *possibly detected* and **11/25** *undetected.*
- **5/11** of the detected events are classified as debris flows. **6/11** of the detected events are classified as debris avalanches.
- All detected events are obtained from S2-data acquired in summer- or fall season.
- The number of pixels (manually) classified as a "landslide" range from **33 – 1282.**
  - The length of the detected landslides ranges from **172-761 m**.
  - The maximum width of the detected landslides ranges from **42-148 m**.
  - The narrowest width of the detected landslide is **10 m**.
- The quaternary geology at all detected events is classified as till, colluvium or both, **8/11** of the undetected events are classified as till or colluvium.
- The geology at **10/11** detected events are classified as a gneiss-type of bedrock, **8/11** of the undetected events are classified as a gneiss-type of bedrock.
- **23/25** events are found/reported to have occurred in slopes equal to or steeper than 15 degrees.

Table 4.1 below summarizes the characteristics of the detected events. The events are identified by a number and location. The inclination of the slope is given, interpreted as the slopes' dominant inclination. The data is derived from a 10 m DEM. The direction specifies at which orientation the slope inclines (or slope aspect), in compass points. The soil type and geology are obtained from NGUs' geological N250 map and quaternary geology map of the respective areas. Multiple classifications are given if the landslide has occurred on a boundary between multiple types. The *county-* column specifies in which Norwegian county the event has occurred. The *season* specifies in which season the examined S2-data was acquired.

Table 4.1 - Detected events

No.	Name	Slope inc.	Direction	Soil Type	Geology	County	Season
1	Lindelia	15-25	W	Till	Augen-Gneiss	Buskerud	Autumn
2	Hunnedalen	30-40	SSE	Glaciofluvial Exposed bedrock Colluvium	Diorithic to granitic gneiss	Rogaland	Summer
3	Kommedal	15-25	N	Fluvial Exposed-bedrock Colluvium	Diorithic to granitic gneiss	Rogaland	Summer
4	Øksland	15 – 25	W	Till	Diorithic to granitic gneiss	Sogn og Fjordane	Autumn
5	Slettafossen	25-45	NE	Till Fluvial	Diorithic to granitic gneiss	Møre og Romsdal	Summer
6	Kråkagjelet	25-45	S	Weathered material Colluvium	Granite Fyllite	Sogn og Fjordane	Summer
7	Spansdalen	25-45	S	Weathered material Colluvium	Granite and grandiorite	Troms	Summer
8	Selskreda	15-25	NNE	Glaciofluvial Colluvium	Diorithic to granitic gneiss	Møre og Romsdal	Autumn
9	Tokke	5-10	E	Till Glaciofluvial	Granite Metabasalt Quartzite	Telemark	Summer
10	Rødstøl	15-45	NE	Till	Granitic gneiss	Møre og Romsdal	Summer
11	Krundalen	15-25	N	Till Colluvium	Diorithic to granitic gneiss	Sogn og Fjordane	Summer

Table 4.2 - Potentially detected events

No.	Name	Slope inc.	Direction	Soil Type	Geology	County	Season
12	Bjerkadalen	15-25	SE	Fluvial Weathered material	Mica Schist	Nordland	Summer
13	Sulitjelma	25-45	SW	Weathered material Colluvium	Pyhyllite Mica Schist	Nordland	Spring
14	Byrkjedal	25-25	NE	Humus Colluvium	Diorithic to granitic gneiss	Rogaland	Fall

Table 4.3 - Undetected events

No.	Name	Slope inc.	Direction	Soil Type	Geology	County	Season
15	Beiarn	15-25	NNW	Till	Gneisss Biotite shale	Nordland	Summer
16	Raudskredbekken	15-25	E	Fluvial Exposed bedrock Colluvium	Meta-andesite Metadacite	Hordaland	Winter Summer
17	Reinåa	39	WSW	Marine fine grained Fluvial Glaciofluvial	Migmatite gneiss	Trøndelag	Winter
18	Jølster	15-25	N	Till	Diorithic to granitic gneiss	Sogn og Fjordane	Spring
19	Hyestranda	25-45	NNE	Humus	Quartz schist Quartzite	Sogn og Fjordane	Spring
20	Ommedal	25-45	SW	Fluvial Colluvium	Augen gneiss	Sogn og Fjordane	Spring

21	Falla	15-25	NNW	Marine fine grained Fluvial Colluvium	Diorithic to granitic gneiss	Møre og Romsdal	Spring
22	Ávžejávri	25-45	WSW	Till Glaciofluvial	Meta-arkose	Finnmark	Spring
23	Setesdalsvein	15-25	SE	Fluvial Glaciofluvial	Banded gneiss	Aust-Agder	Fall
24	Saga	10-15	NW	Till Fluvial	Banded gneiss	Aust-Agder	Fall
25	Luster	25-90	NW	Colluvium	Gabbroid to quartz dioritc gneiss	Sogn og Fjordane	Fall

4.1.1 Geometry of detected events

The extent and geometrical considerations of the detected landslides are given in the Figures 4.2 – 4.5. All stated values are derived from GIS-system measurements. The surface area and perimeter are generated from the manually delineated polygons, shown in Appendix C. The *transects* are manually delineated line features following the centerline of the landslide. Width 1 refers to the widest observed width of the landslide scar. No polygon was created in event 8, due to its small size/shape. See the Appendix for further description.

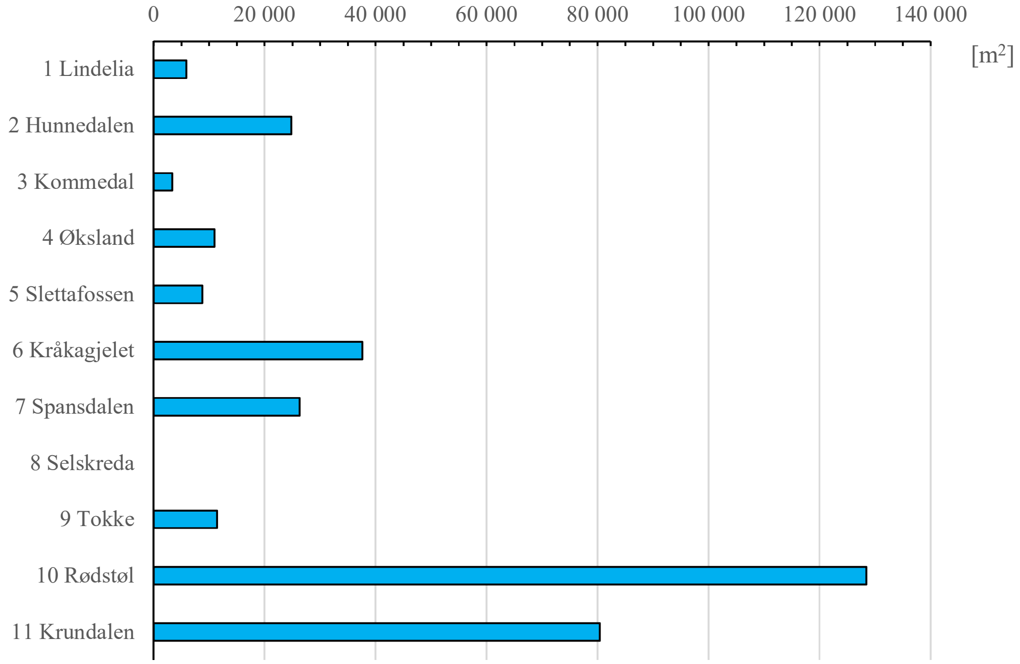

Figure 4.2 - Surface area of detected events

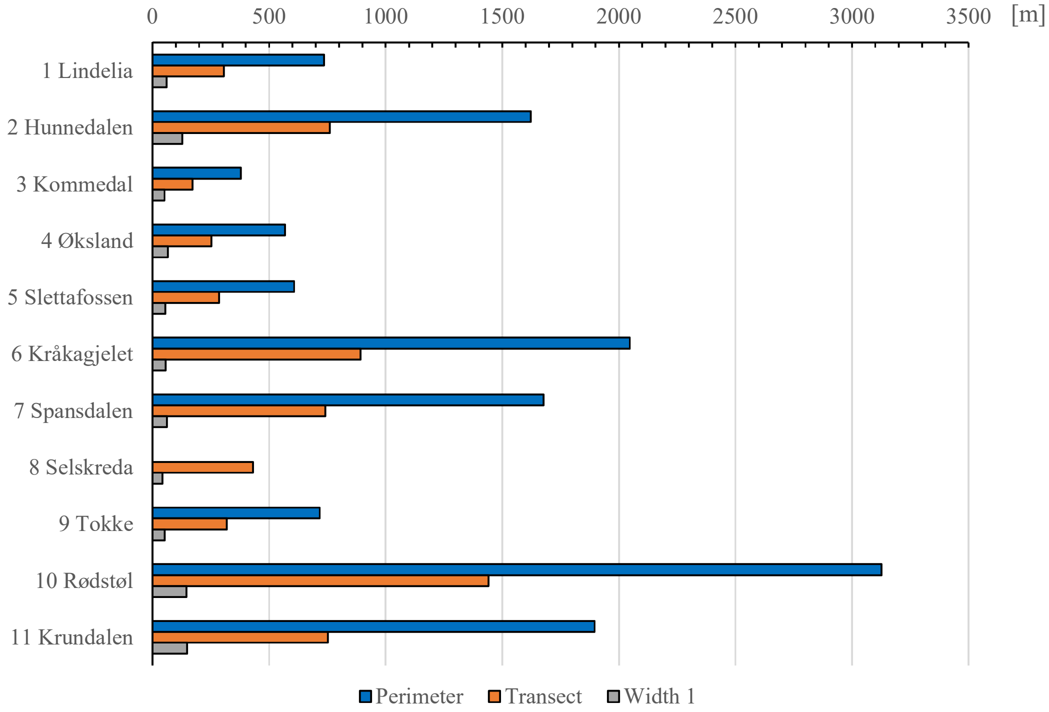

Figure 4.3 - Sizes of the detected landslides

Geometrical ratios related to the shape of the detected landslides are given in Figures 4.4 and 4.5 below. The ratios are calculated based on the values given in the figures above. The blue circles represent the surface area divided by the perimeter and vary between 8.0 and 16.0 for events 1-9. For the two largest events, 10 and 11, the ratios are 41.1 and 42.4 respectively. The orange squares represent the surface area divided by the length of the centerline along the entire detected landslide. It shows the same tendency as the area : perimeter ratio, with values ranging from 19.4 – 43.3 for events 1-9 and 89.1 and 106.1 for events 10 and 11 respectively.

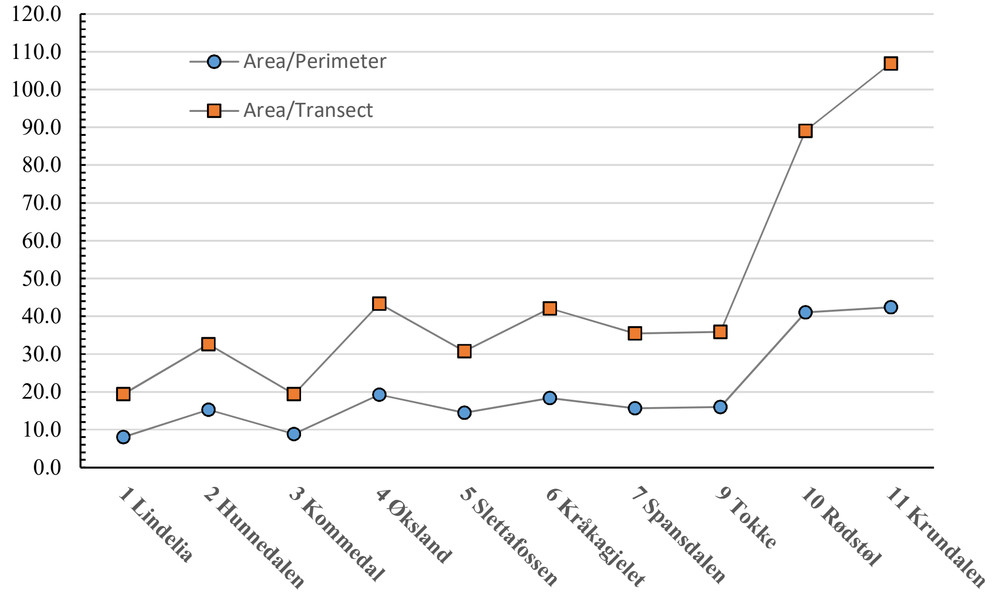

Figure 4.4 - Geometrical ratios

Geometrical ratios are given below, with the square root of the surface area divided by the perimeter and transect. The square root of the area is used to obtain dimensionless factors.

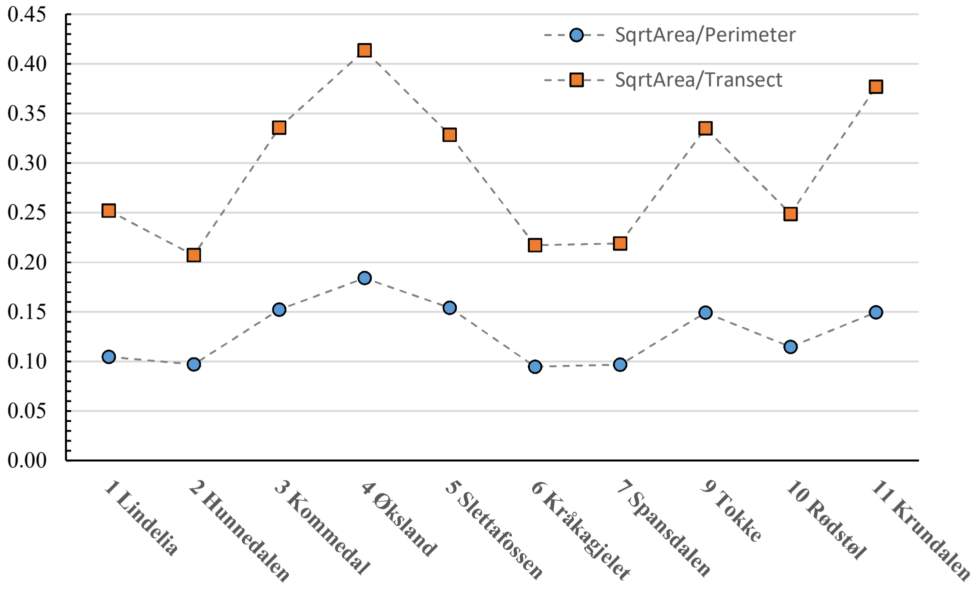

Figure 4.5 - Geometrical considerations using the square root of the surface area

4.2 Spectral reflectance

The spectral characteristics of the detected landslides have been examined along their respective center-line transects. The spectral reflectance is in principle obtained from a row of pixels representing a 10x10m surface area along the length of the detected landslide. The spectral signatures are examined at the centerlines to minimize possible diffuse pixels along the borders of the landslide, which may be influenced by nearby features. The center of the detected landslide is also believed to be least prone to misinterpretation when delineating the "detected landslide"-pixels.

The graphs below show the spectral reflectance of the VNIR-bands along the transects of detected events 1, 7 and 11. For easier comparison between the events, they are normalized with respect to length. The three depicted events show a general pattern of relatively consistent reflectance values between 0.5 and 0.15 for VNIR-bands 2, 3 and 4. Band 8 shows the most variation in reflectance behavior; with strong correlation to the other three bands in event 11, and clear deviance in event 7.

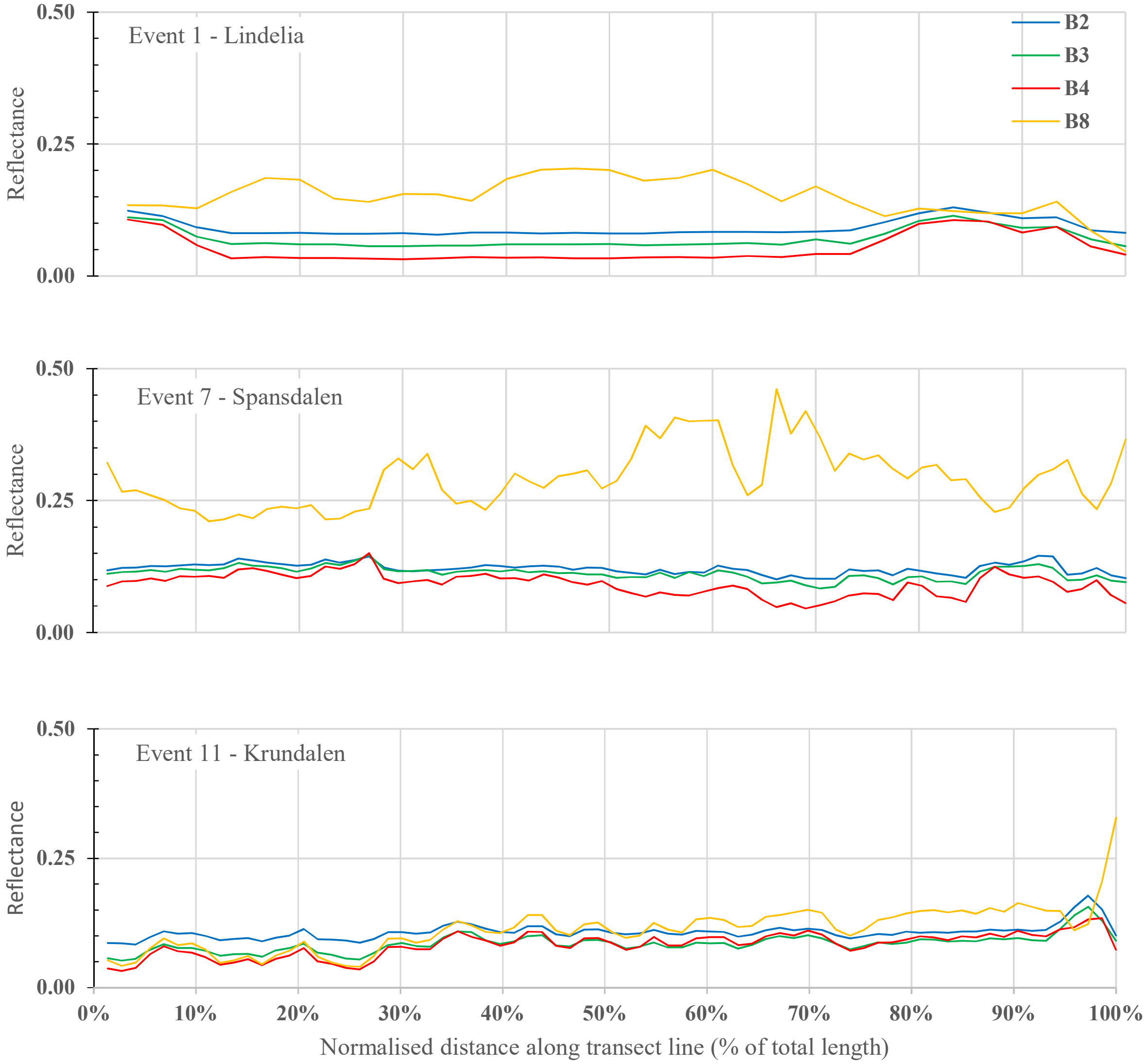

Figure 4.6 – Spectral characteristics of events 1, 7 and 11. The complete set of results is given in Appendix F.

4.2.1 Thresholds

Due to the large observed variations in the spectral characteristics of the detected landslides, illustrated in Figure 4.6, a subset of all the events was used to determine thresholds. Spectral information from the events 2-Hunnedalen, 4-Øksland, 5-Slettafossen, 10-Tokke, and 11-Krundalen were deemed representative for the subset, as they were detected in good quality conditions, and are events of both debris flows and debris avalanches, with varying sizes and soil cover conditions. Large variations in reflectance can still be observed in these events – therefore a portion of the transect which distinctly can be considered as landslide-pixels from each of the five events was used to obtain the upper- and lower limit thresholds.

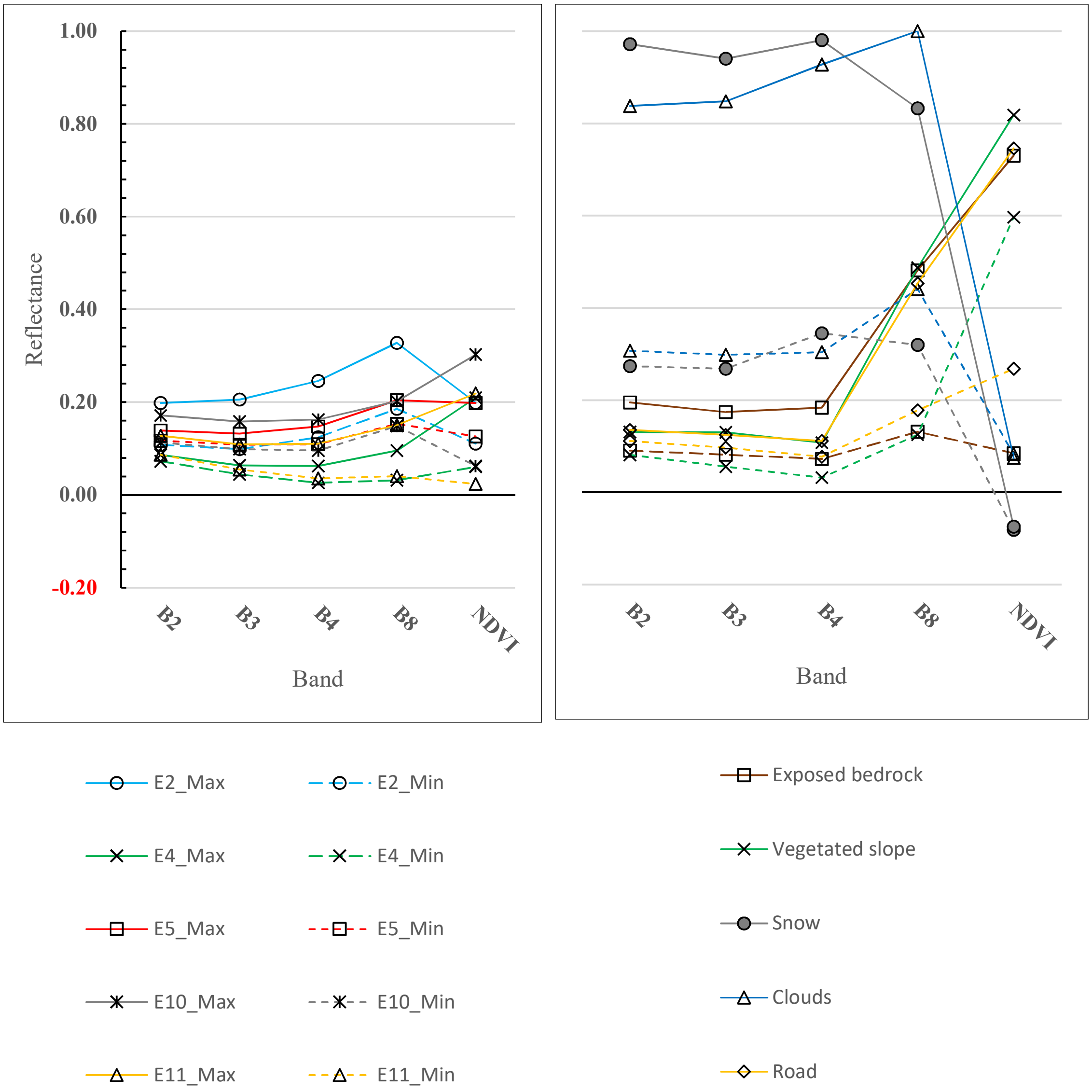

Figure 4.7 – Comparison of simple band thresholds (left) vs. frequent surface features (right)

The subset used to determine the *simple bands* thresholds are given in the figure above. The maximum and minimum reflectance, and maximum and minimum NDVI found from the portion of the transect are plotted for the five events in the leftmost figure. The solid lines represent the maximum values, the dashed lines represent the minimum. The upper- and lower limit thresholds are taken as the highest and lowest values found in each band. The same approach was used to determine the ratio-thresholds, and NDVI ratio-thresholds. The rightmost figure shows the spectral characteristics of typical surface features found in the vicinity of the detected landslides. The spectral reflectance of the surface features is obtained using the same approach as described above. The maximum and minimum spectral reflectance from several transects which distinctively can be perceived as one of the given surface features are the basis for the plot. See Appendix B. for further specification of all selected values. The obtained threshold values for *simple bands,* ratios, and NDVI-ratios are given in the Tables 4.4 – 4.6 below, and their accuracy is tested in the next sections.

In general, using the single bands the range of the thresholds are smallest for the smallest wavelengths. The range of reflectance in the blue band range 13 %, while the NIR-band range 30 %. The NIR-ratios take on larger values than the visible/visible ratios, while the NDVI-ratios yield the largest spread, varying from 0.25 - 5.01.

Table 4.4 – Simple band thresholds

	BLUE	**GREEN**	**RED**	**NIR**	**NDVI**
Max	0.20	0.21	0.25	0.33	0.30
Min	0.07	0.04	0.03	0.03	0.02

Table 4.5 – VNIR-Ratios thresholds

	NIR/ RED	**NIR/ GREEN**	**NIR/ BLUE**	**RED/ GREEN**	**RED/ BLUE**	**GREEN/ BLUE**
Max	1.87	1.91	1.97	1.28	1.31	1.06
Min	0.09	0.70	0.43	0.58	0.36	0.61

Table 4.6 – NDVI-ratios thresholds

	NDVI/ NIR	**NDVI/ RED**	**NDVI/ GREEN**	**NDVI/ BLUE**
Max	3.78	5.01	3.55	2.61
Min	0.34	0.38	0.37	0.25

4.2.2 Automatic classification –Spectral signature, Kråkagjelet

The thresholds given in the section above are applied to three satellite scenes. The spectral characteristics of all pixels in the dataset are compared to the thresholds and are *masked* when having values within the specified values. The total amount of pixels in the satellite data is compared to the total amount of masked pixels. The accuracy of the thresholds with respect to correctly classifying landslide pixels is evaluated using the manually delineated polygons, defining the surface of the detected landslides. The pixels within the polygons are defined as landslide pixels. The number of masked pixels within the polygon is compared with the total number of pixels comprised within the same polygon. The percentage of the correctly classified pixels is given in the *%-of total* column.

The performance of the different thresholds are given in Table 4.7 below and are illustrated in the natural color composite (NCC) images in Figure 4.8. The leftmost images show the entire test area, with masked pixels in red. The yellow square represents the location and extent of the rightmost image - the area of the defined polygon, with the polygon outlined in yellow.

Test area:

Satellite data used	Post-event
Satellite data acquired	22.08.2017
Size of test area	~110 x 110 km^2

Table 4.7 – Results from Kråkagjelet spectral classification

	Number of pixels	% - of total
Total Area	120 560 400	100
Polygon, Kråkagjelet	371	100

Simple Bands	18 814 824	16
Within polygon, Kråkagjelet	237	64

Ratios	24 842 761	21
Within polygon, Kråkagjelet	239	64

NDVI-Ratios	19 363 199	16
Within polygon, Kråkagjelet	251	68

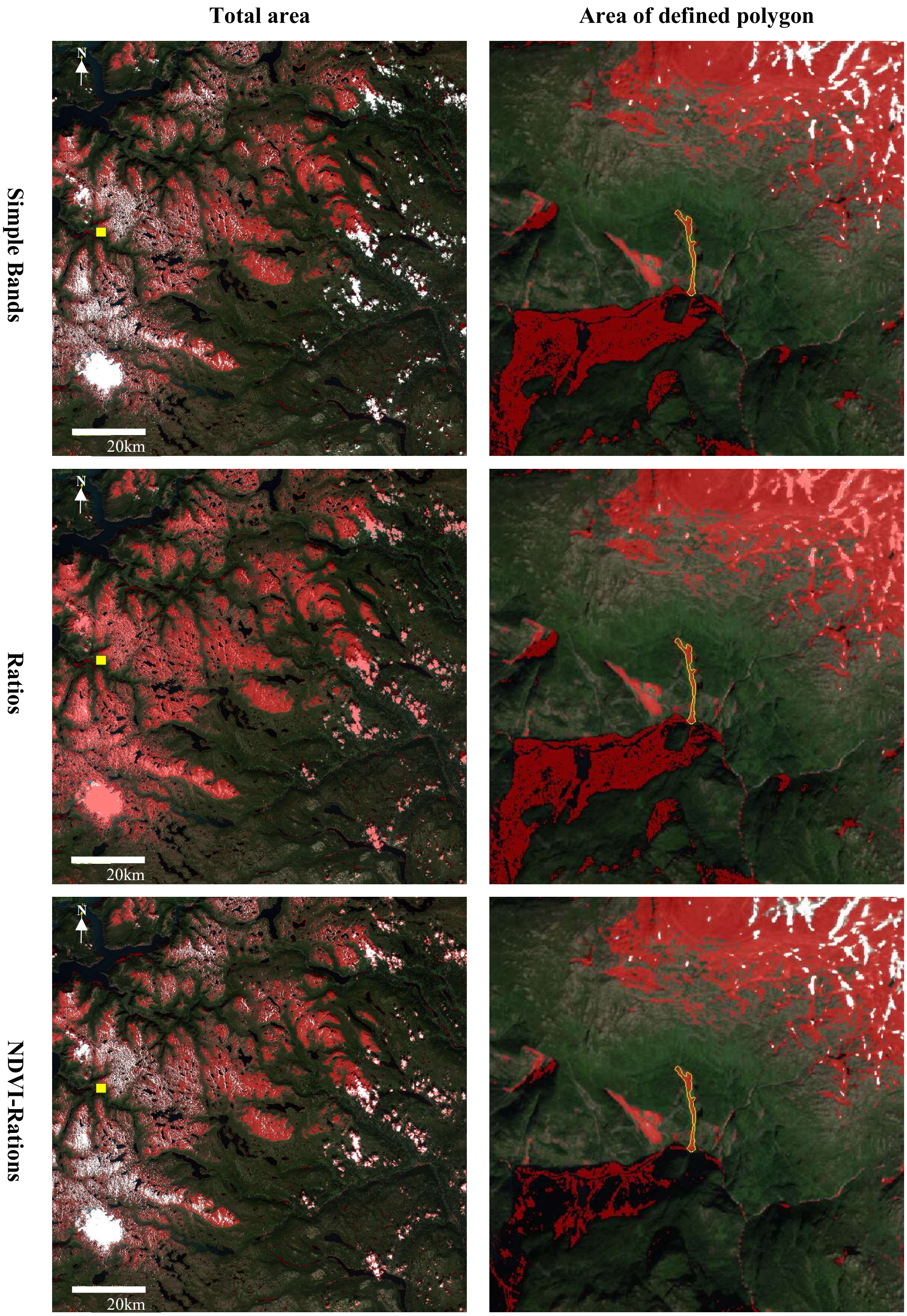

Figure 4.8 – NCC, spectral classification Kråkagjelet.

4.2.3 Automatic classification – Spectral signature, Slettafossen

The performance of the different thresholds are given in the tables below and are illustrated in the false color composite (FCC) images. The leftmost images show the entire test area, with masked pixels in yellow. The yellow square represents the location and extent of the rightmost image - the area of the defined polygon, with the polygon outlined in blue.

Test area:

Satellite data used	Post-event
Satellite data acquired	28.06.17
Size of test area	~110 x 110 km^2

Table 4.8 - Results from Slettafossen spectral classification

	Number of pixels	%-of total
Total Area	120 560 400	100
Polygon, Slettafossen	88	100

Simple Bands	12 130 033	10
Within polygon Slettafossen	58	66

Ratios	36 814 229	31
Within polygon Slettafossen	56	64

NDVI-Ratio	14 276 810	12
Within polygon Slettafossen	42	48

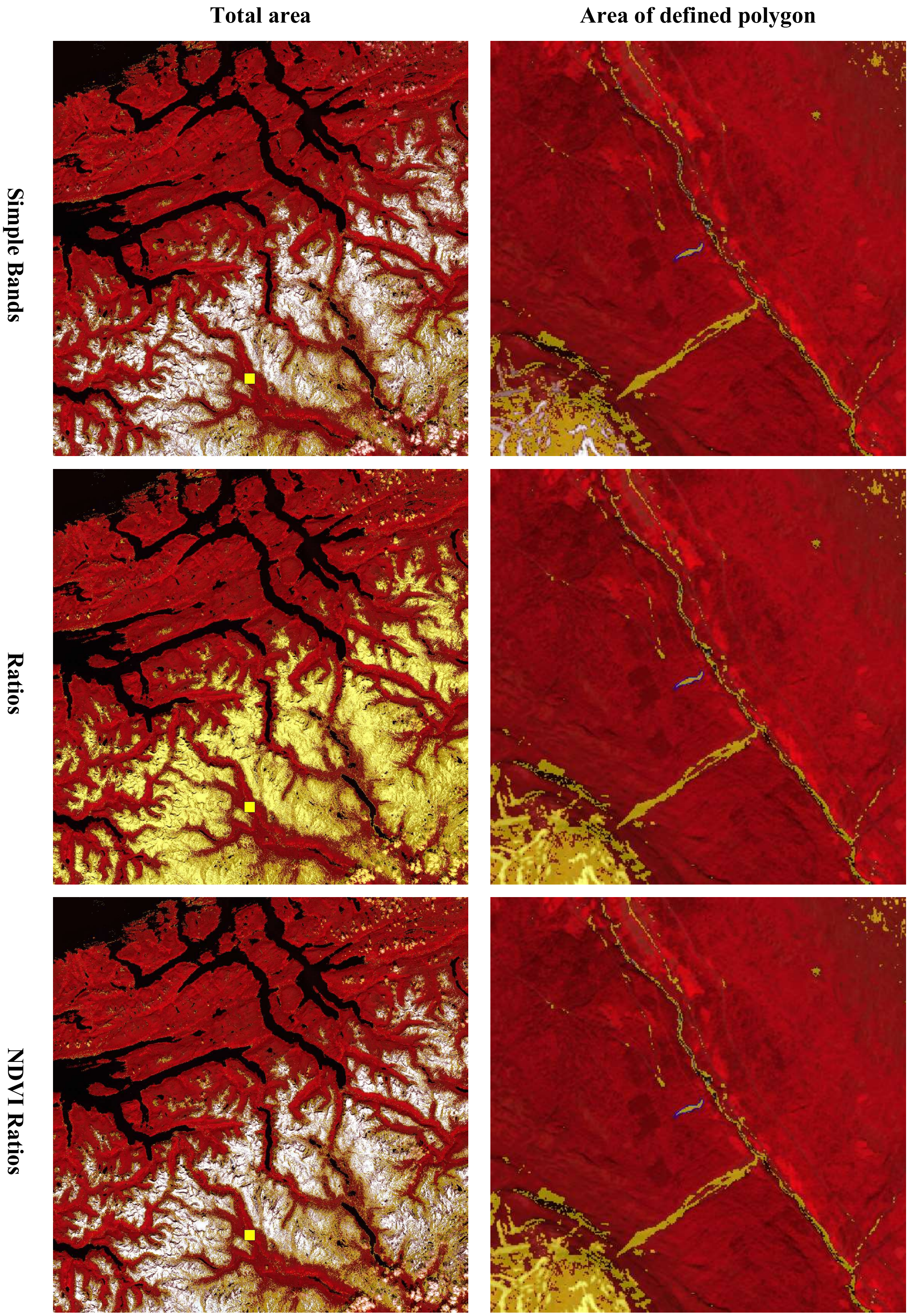

Figure 4.9 - FCC, spectral classification Slettafossen.

4.2.4 Automatic classification – Spectral signature – Hunnedal/Kommedalen

Test area 3 covers both the Hunnedalen and Kommedalen debris flow events. The performance of the different thresholds are given below and illustrated in the natural color composite images. The Hunnedalen event is shown first, secondly the Kommedalen event. The leftmost images show the entire test areas, with red masked out pixels. The area of the defined polygons is shown in the rightmost image, with the polygon outlined in yellow. The extent and position of the areas of the defined polygons are given as a yellow square in the left images.

Test area:

Satellite data used	Revisit-data
Satellite data acquired	28.06.17
Size of test area	~25 x 15km^2

Table 4.9 - Results from Hunnedal/Kommedalen spectral classification

	Number of pixels	% - of total
Total Area	3 885 505	100
Polygon Hunnedal	329	100
Polygon Kommedalen	33	100
Simple Bands	223 190	6
Within polygon Hunnedal	184	56
Within polygon Kommedalen	5	15
Ratios	280 084	7
Within polygon Hunnedal	130	40
Within polygon Kommedalen	5	15
NDVI-Ratios	239 903	6
Within polygon Hunnedal	198	60
Within polygon Kommedalen	5	15

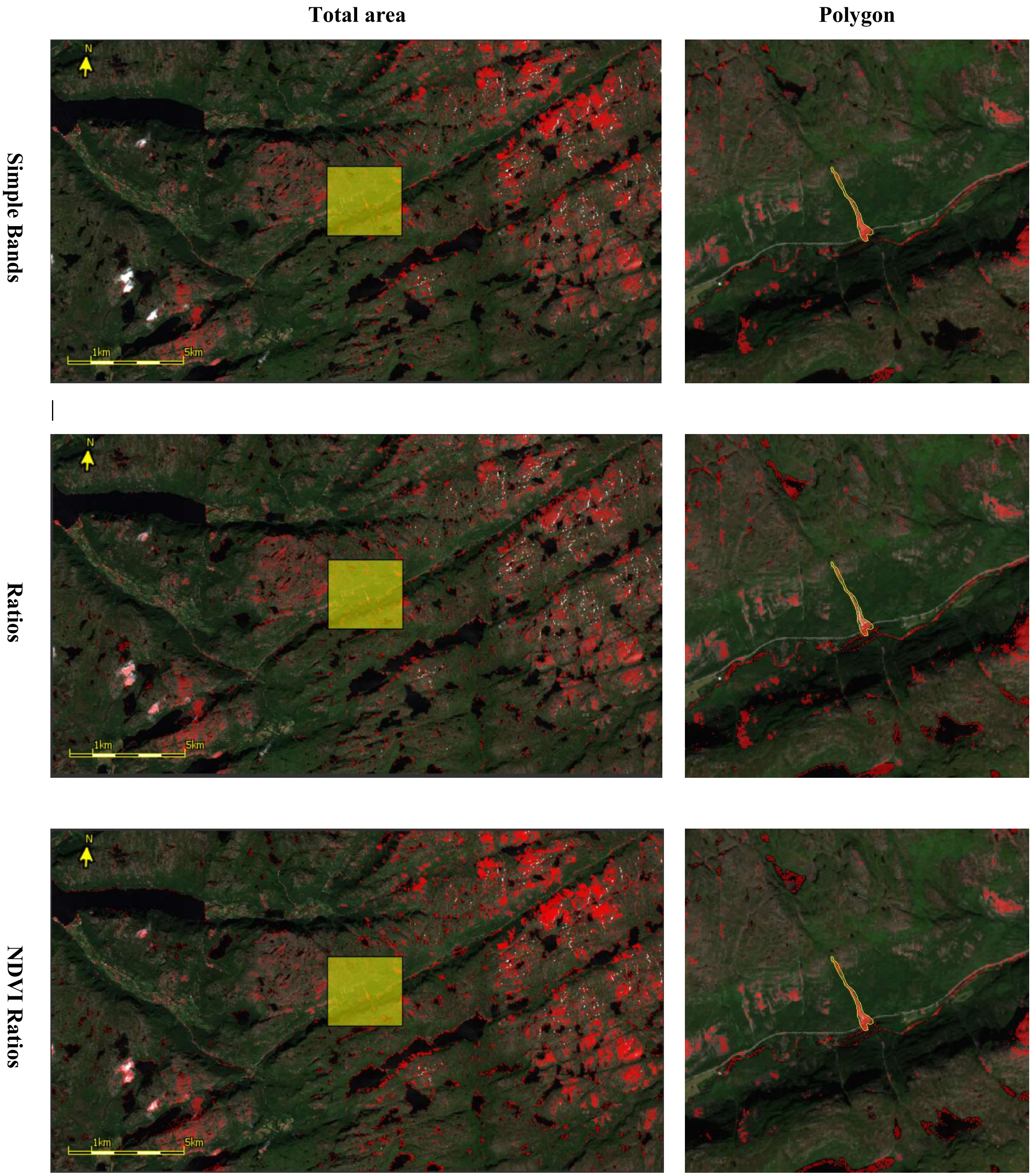

Figure 4.10 - NCC, spectral classification Hunnedalen.

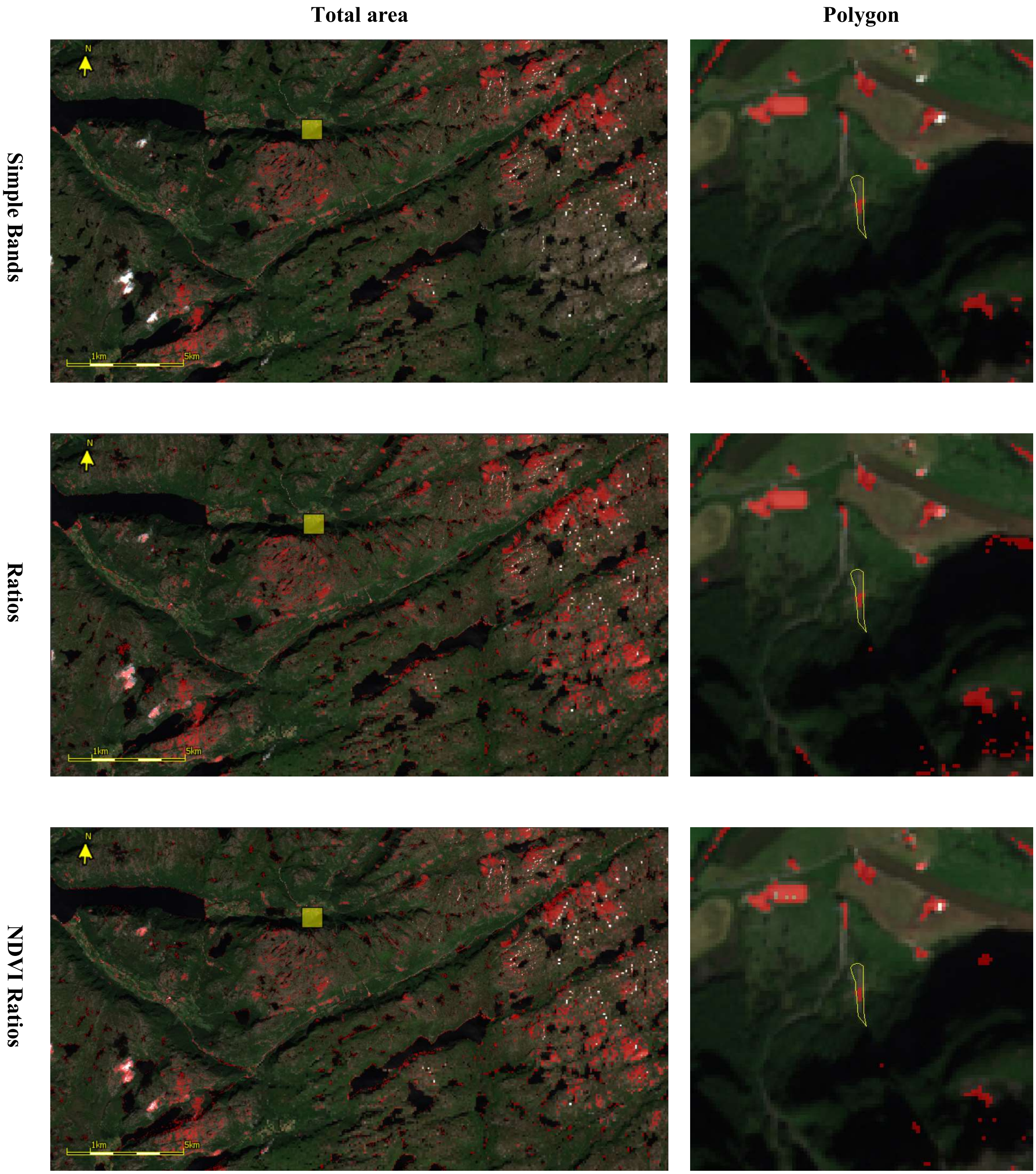

Figure 4.11 - NCC, spectral classification Kommedal.

4.3 Change detection

The change in spectral reflectance of events between pre- and post-event datasets have been examined along with their respective centerline transects. All events with available pre- and post-event data have been examined. If applicable, the change in reflectance has been evaluated with data acquired at times with more similar seasonal conditions.

The graphs given below shows the change in spectral reflectance of the VNIR- along the centerline transects of detected events 1, 7 and 4. The solid lines represent change between two datasets acquired closest to the date of the landslide occurrence. The dashed lines represent the change between two datasets acquired with more similar seasonal conditions. The landslides are normalized with respect to length for easier comparison. The datasets acquired in similar conditions will typically see a positive change in the NIR-band, and a small negative change in the visible bands. The NIR-band has relatively large variation compared to the visible bands, which are showing more consistent values. The data acquired with less similar conditions show a different trend in the event 7-data, while yielding similar characteristics in event 4.

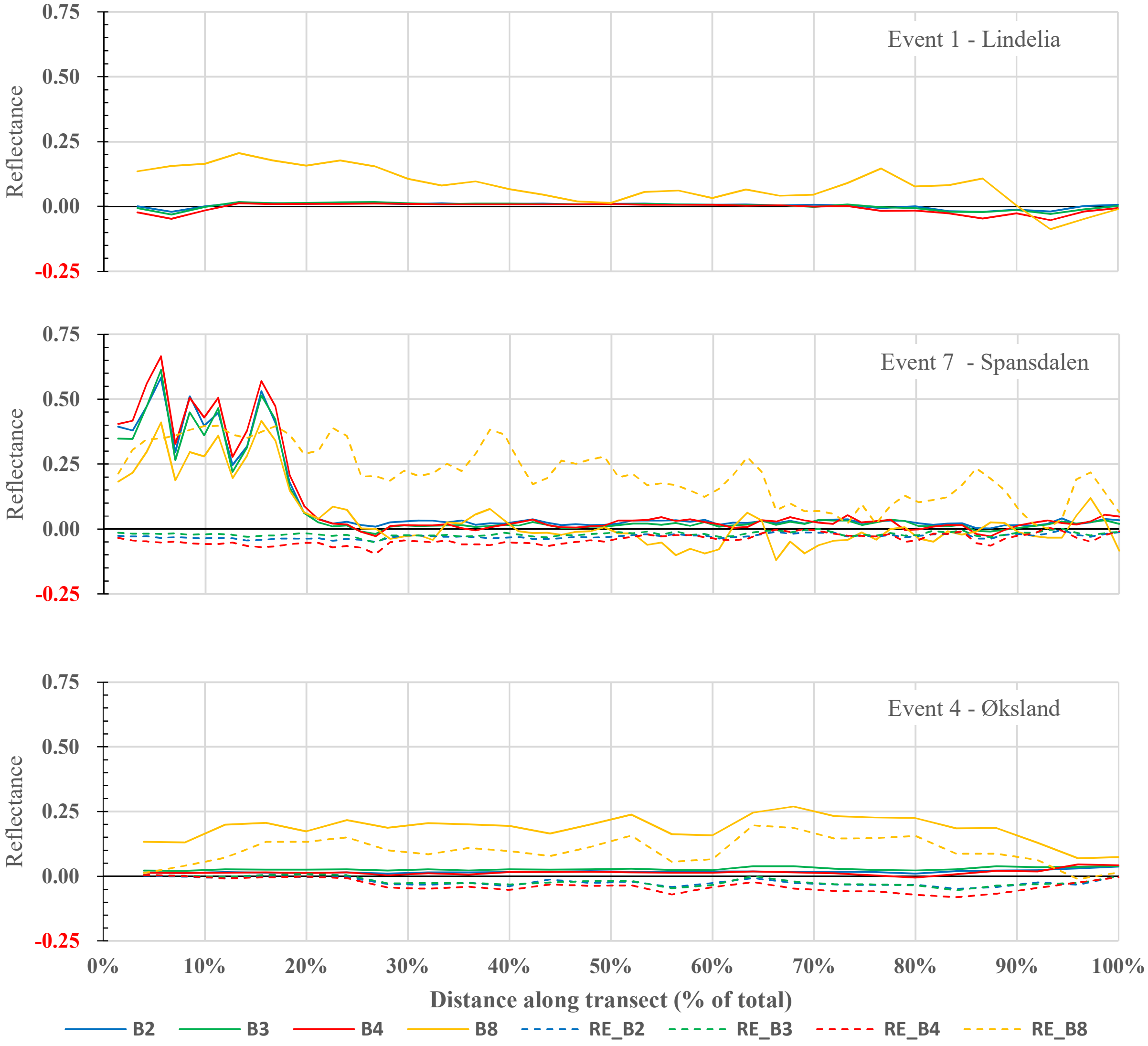

Figure 4.12 – Change in spectral reflectance and NDVI, events1, 4 and 7. Complete results in Appendix F.

4.3.1 Change detection thresholds

A subset of the change detection characteristics from the events 2-Hunnedalen, 4-Øksland, 5-Slettafossen, 7-Spansdalen, and 9-Tokke have been used to determine thresholds. The same approach as described in chapter 1.2.1 has been used.

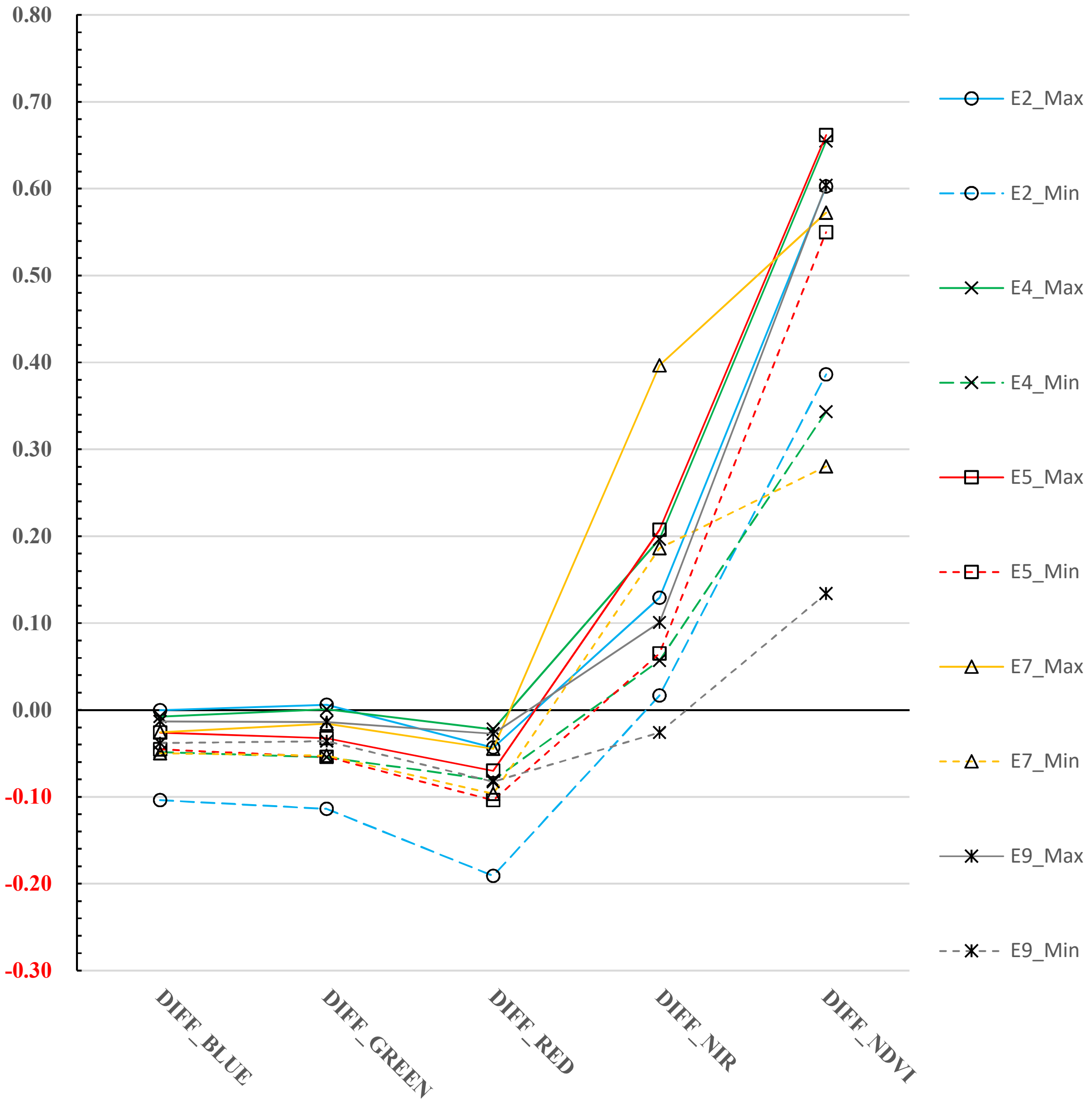

Figure 4.13 – Change in spectral signatures and NDVI from a selection of transects

The subset used to determine the *change in single bands* thresholds are given in the figure above. The maximum and minimum change in reflectance, and maximum and minimum change in NDVI found from the five subsets are plotted. The solid lines represent the maximum values, the dashed lines represent the minimum. The upper- and lower limit thresholds are taken as the highest and lowest values found in each band. The same approach was used to determine the ratio-thresholds, and NDR-thresholds.

The change in spectral signature are all negative in the visible bands, indicating that the reflectance at *time 2* are higher than at *time 1* in the visible region. The difference in the NIR-band and NDVI have a larger spread, ranging from -0.03 to 0.40 and 0.13-0.66 respectively. The blue and green ratio show relatively similar values, while the red ratio yield a bit lower values. The NIR- and NDVI-ratios have the highest spread. The normalized difference ratios in the visible region are mostly on the negative side, while also here the NIR and NDVI ratios show the largest variation.

Table 4.10 - Change in single bands, thresholds

	DIFF_BLUE	DIFF_GREEN	DIFF_RED	DIFF_NIR	DIFF_NDVI
Max	0.00	0.01	-0.02	0.40	0.66
Min	-0.10	-0.11	-0.19	-0.03	0.13

Table 4.11 - Change in ratios, thresholds

	RATIO_NIR	RATIO_RED	RATIO_GREEN	RATIO_BLUE	RATIO_NDVI
Max	3.18	0.69	1.06	1.00	9.73
Min	0.02	0.22	0.45	0.48	1.28

Table 4.12 - Change in NDR, thresholds

	NDR_NIR	NDR_RED	NDR_GREEN	NDR_BLUE	NDR_NDVI
Max	0.52	-0.19	0.03	0.00	0.81
Min	-0.07	-0.64	-0.38	-0.36	0.12

4.3.2 Automatic classification – Change detection, Kråkagjelet

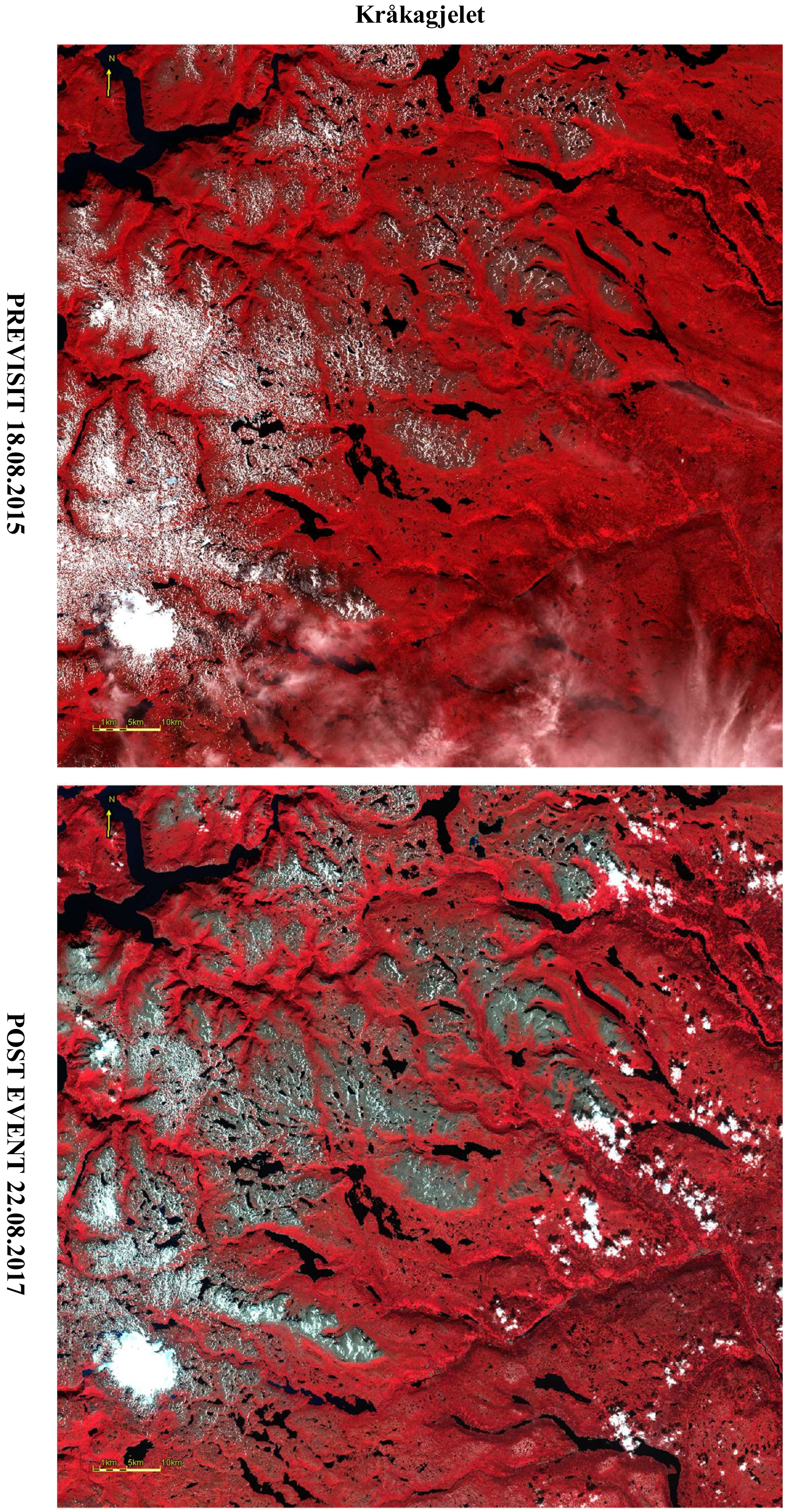

Figure 4.14 – Previsit- and post-event FCC-image of Kråkagjelet area.

The thresholds given in the section above are applied to four satellite scenes. The spectral characteristics of all pixels in the dataset are compared to the thresholds and is *masked* when having values within the specified values. The total amount of pixels in the satellite data is compared to the total amount of masked pixels. The accuracy of the thresholds with respect to correctly classifying landslide pixels are evaluated using the manually delineated polygons, defining the surface of the detected landslides. The pixels within the polygons are defined as landslide pixels. The number of masked pixels within the polygon is compared with the total number of pixels comprised within the same polygon. The percentage of the correctly classified pixels is given in the *%-of total* column.

False color composites of the datasets acquired at time 1 and time 2 are shown in Figure 4.14 to compare the conditions at the time of acquisition. The performance of the different thresholds are given in the Table 4.13 - below and are illustrated in the false color composite images. The leftmost images show the entire test area, from time 2, with masked pixels in yellow. The yellow square represents the location and extent of the rightmost image - the area of the defined polygon, with the polygon outlined in blue.

Test area:

Satellite data, time 1	Pre-visit data 18.08.2015
Satellite data, time 2	Post-event data 22.08.2017
Size of test area	~108 x 108 km^2

Table 4.13 – Results from Kråkagjelet change detection classification

	Number of pixels	%- of total
Total Area	116 639 100	100
Polygon, Kråkagjelet	371	100

Simple Bands	4 776 784	4
Within polygon, Kråkagjelet	229	62

Ratios	2 225 107	2
Within polygon, Kråkagjelt	162	44

NDR	1 073 108	1
Within polygon, Kråkagjelet	147	40

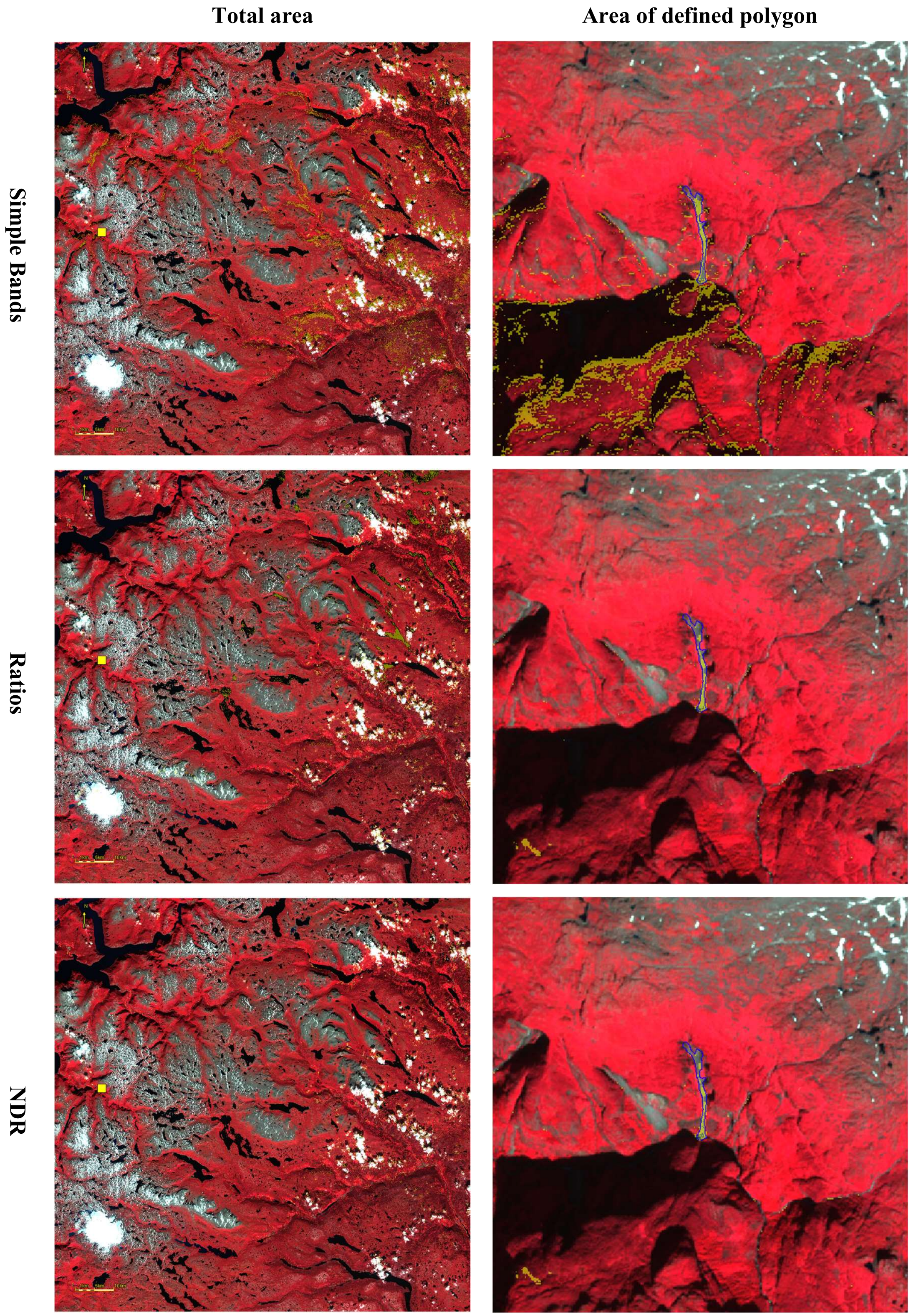

Total area

Area of defined polygon

Simple Bands

Ratios

NDR

Figure 4.15 – FCC, change detection classification, Kråkagjelet.

4.3.3 Automatic classification – Change detection, Slettafossen

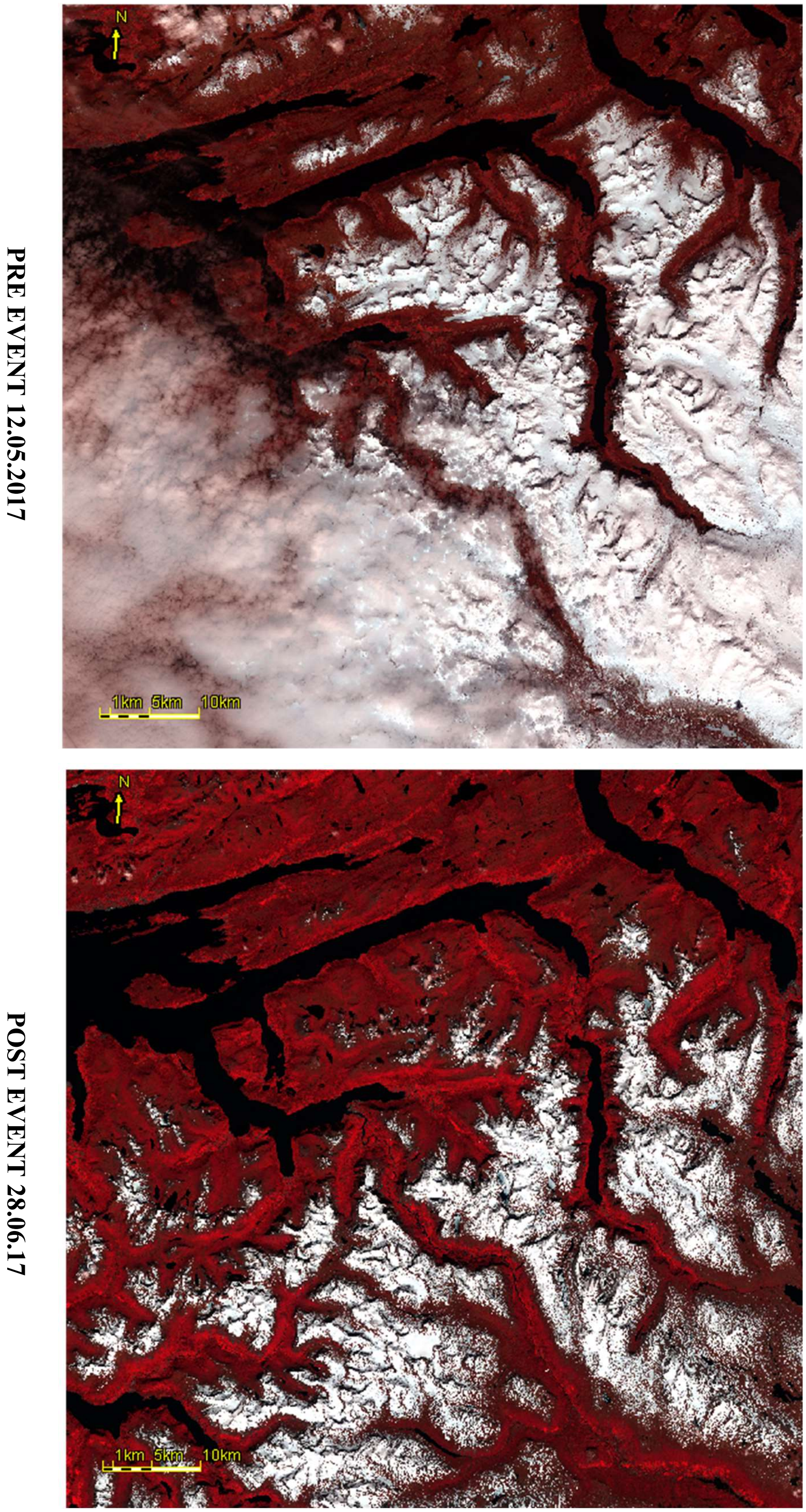

Slettafossen (1)

PRE EVENT 12.05.2017

POST EVENT 28.06.17

Figure 4.16 – Pre-event and post-event data of the Slettafossen area.

Slettafossen (2)

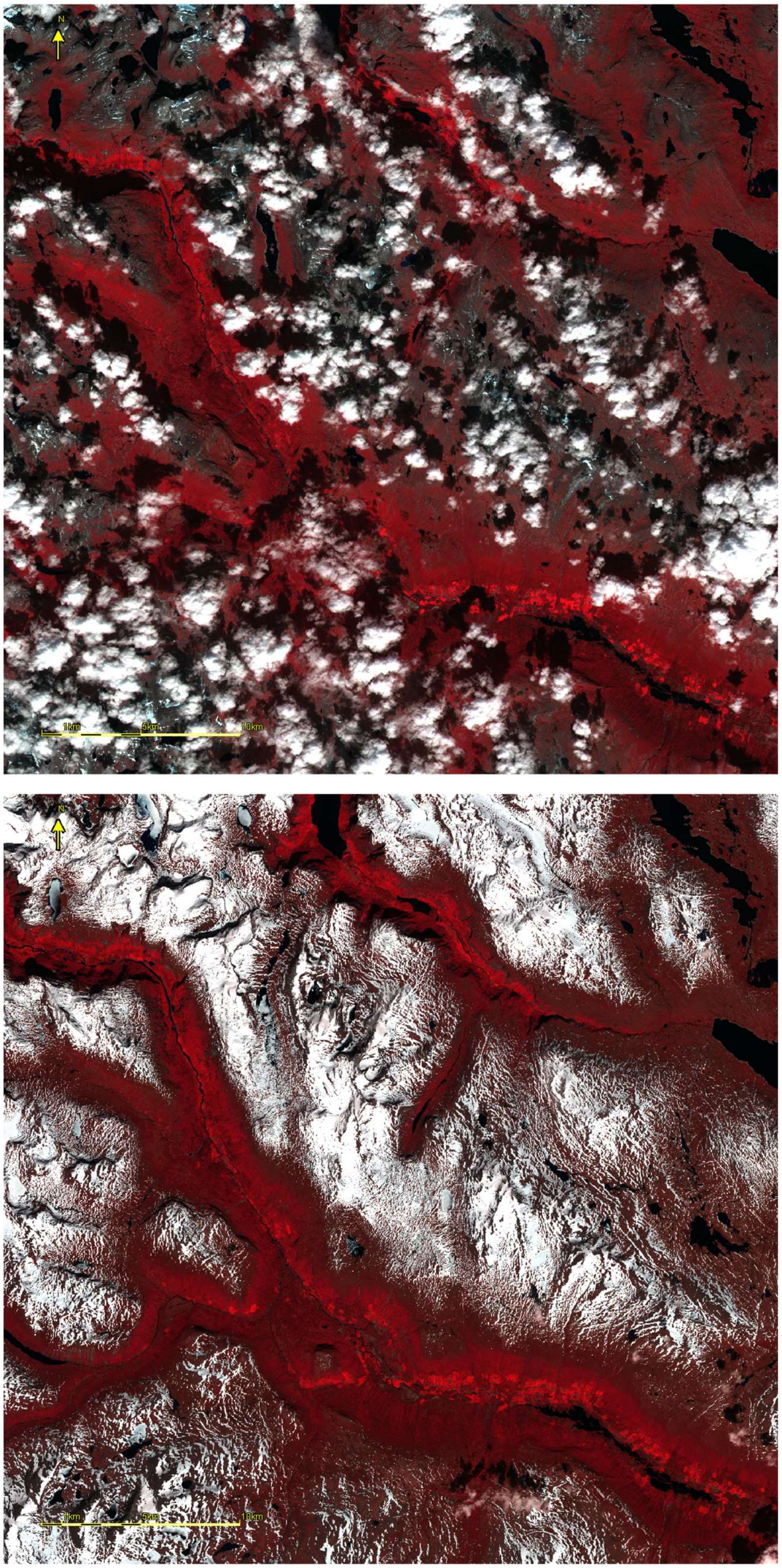

PREVISIT 19.08.2016

POST EVENT 28.06.17

Figure 4.17 – Previsit- and post-event data of the Slettafossen area.

False color composites of the two pairs of datasets are given above. Pair (1) is comprised of pre-event data and post-event data. Pair (2) is comprised of previsit-data and post-event data. The two pairs of datasets have both different conditions at the time of acquisition and have different areas due to satellite data quality. The thresholds were applied on (1) and (2). The performance of the different thresholds are given in the Tables below, and (2) are illustrated in the false color composite images. The leftmost images show the entire test area, from time 2, with masked pixels in yellow. The yellow square represents the location and extent of the rightmost image - the area of the defined polygon, with the polygon outlined in blue. Images of (1) are not included due to unsatisfactory results.

Test area:

(1)Satellite data, time 1	Pre-event data 12.05.2017
(1)Satellite data, time 2	Post-event data 28.06.2017
(1)Size of test area	~75 x 75 km^2
(2)Satellite data, time 1	Pre-visit data 19.08.2016
(2)Satellite data, time 2	Post-event data 28.06.2017
(2)Size of test area	~39 x 39 km^2

Table 4.14 - Results from Slettafossen change detection classification

	Number of pixels	%- of total
Total Area (1)	56 572 542	100
Total Area (2)	15 315 372	100
Polygon, Slettafossen (1)	88	100
Polygon, Slettafossen (2)	88	100

Simple Bands (1)	12 625	0.02
Simple Bands (2)	1 220 010	8
Polygon, Slettafossen (1)	0	0
Polygon, Slettafossen (2)	85	97

Ratios (1)	40 033	0.07
Ratios (2)	710 132	5
Polygon, Slettafossen (1)	3	3
Polygon, Slettafossen (2)	87	99

NDR (1)	8 220	0.01
NDR (2)	346 415	2
Polygon, Slettafossen (1)	0	0
Polygon, Slettafossen (2)	87	99

4.3.4 Automatic classification – Change detection, Hunnedal/Kommedalen

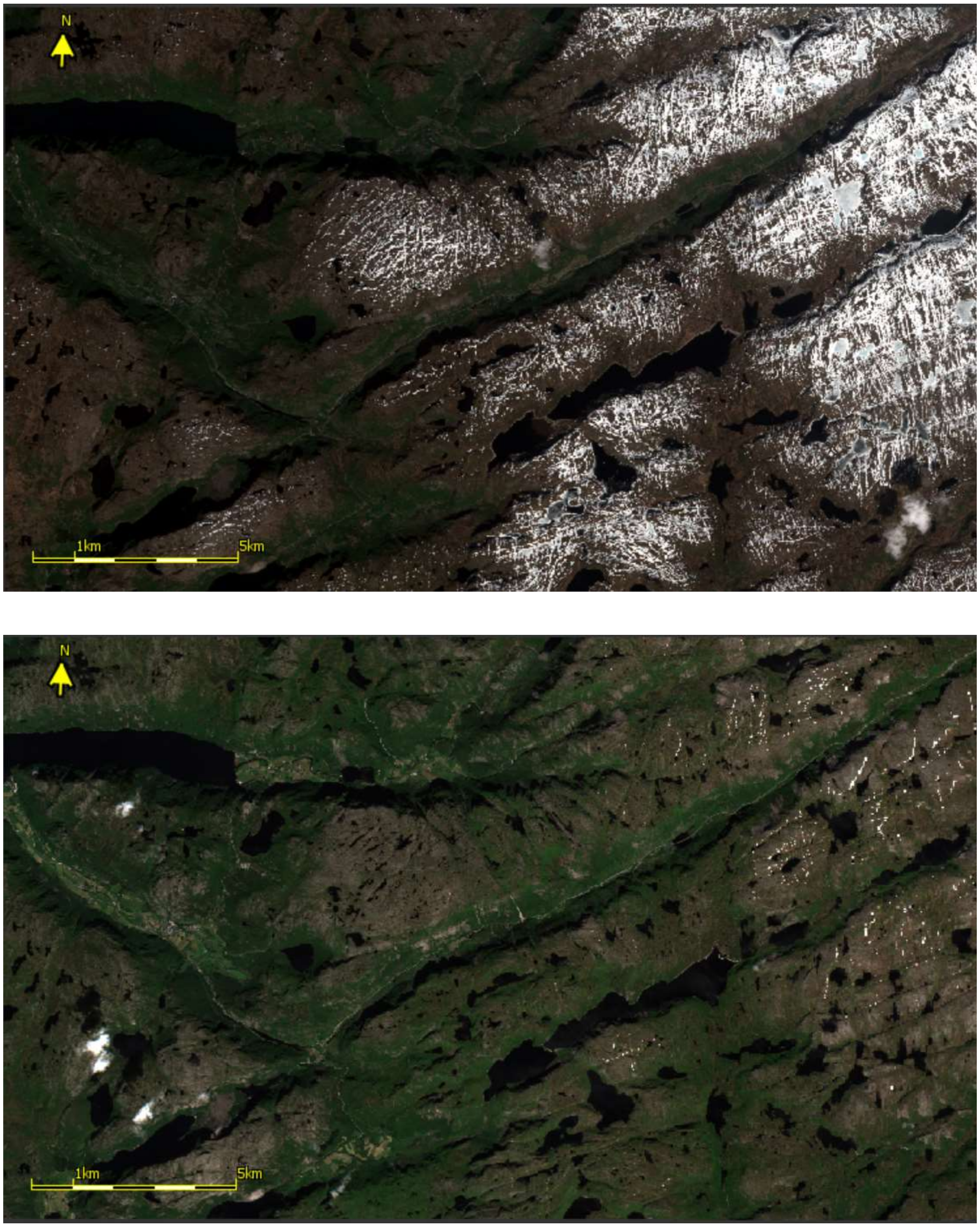
Hunnedal/Kommedalen

PRE EVENT 2705.16

REVISIT 28.06.17

Figure 4.18 - Pre-event and revisit data of the Hunnedalen/Kommedalen area

Natural color composites of the datasets acquired at time 1 and time 2 are given above to compare the conditions at the time of acquisition. The performance of the different thresholds are given in the Tables below and are illustrated in the false color composite images. The Hunnedalen event is presented first, secondly the Kommedalen event. The leftmost images show the entire test area, from time 2, with masked pixels in red. The yellow square represents the location and extent of the rightmost image - the area of the defined polygon, with the polygon outlined in yellow.

Test area:

Satellite data, time 1	Pre-event data 27.05.16
Satellite data, time 2	Revisit data 28.06.17
Size of test area	~25 x 15 km^2

Table 4.15 - Results from Hunnedal/Kommedalen change detection classification

	Number of pixels	%- of total
Total Area	3 495 525	100
Polygon, Hunnedal	329	100
Polygon, Kommedalen	33	100
Simple Bands	20 108	0.6
Within polygon, Hunnedal	221	67
Within polygon, Kommedalen	16	48
Ratios	19 008	0.5
Within polygon, Hunnedal	216	66
Within polygon, Kommedalen	11	33
NDR	17 665	0.5
Within polygon, Hunnedal	208	63
Within polygon, Kommedalen	11	33

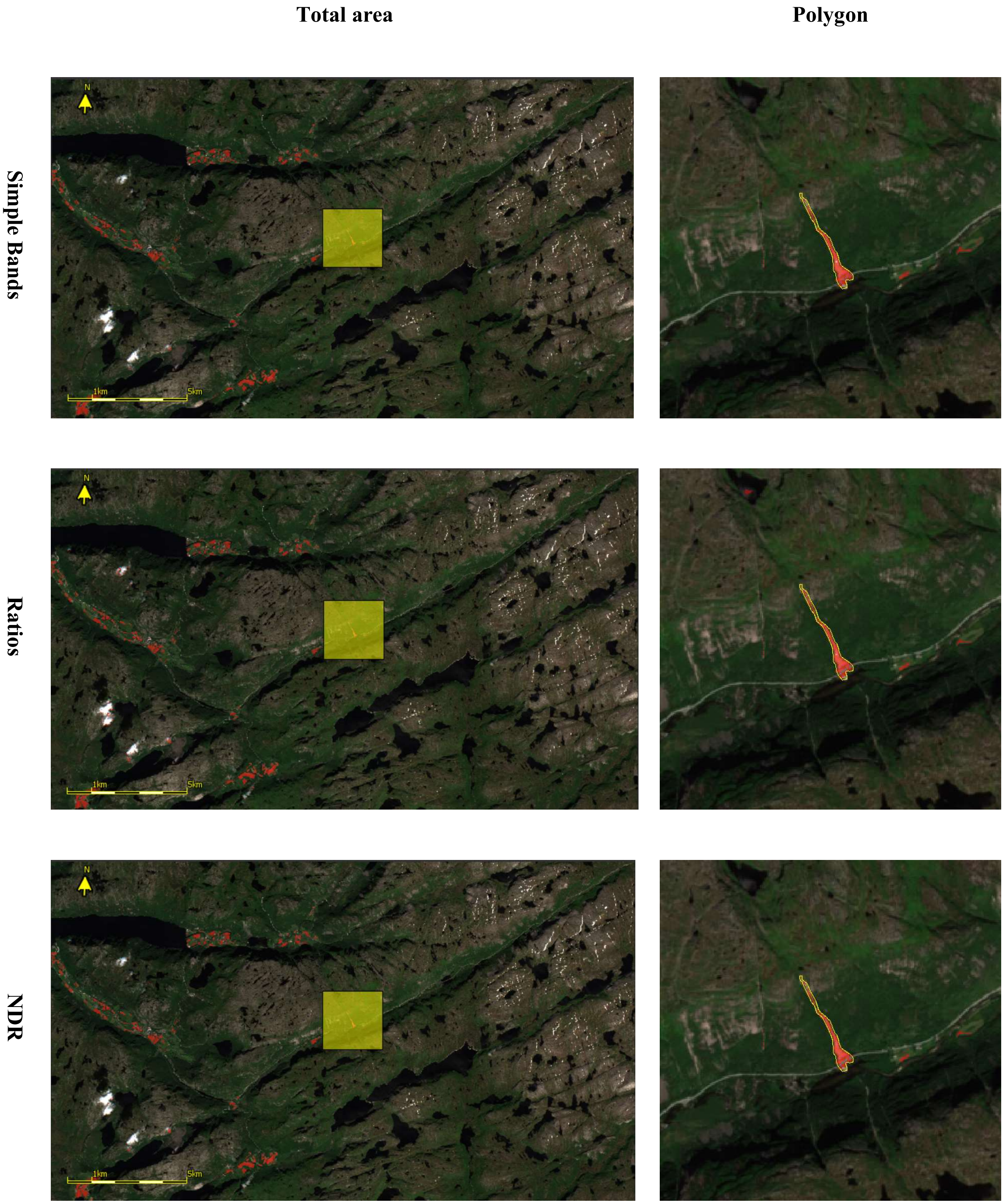

Figure 4.19 – NCC, change detection classification, Hunnedalen.

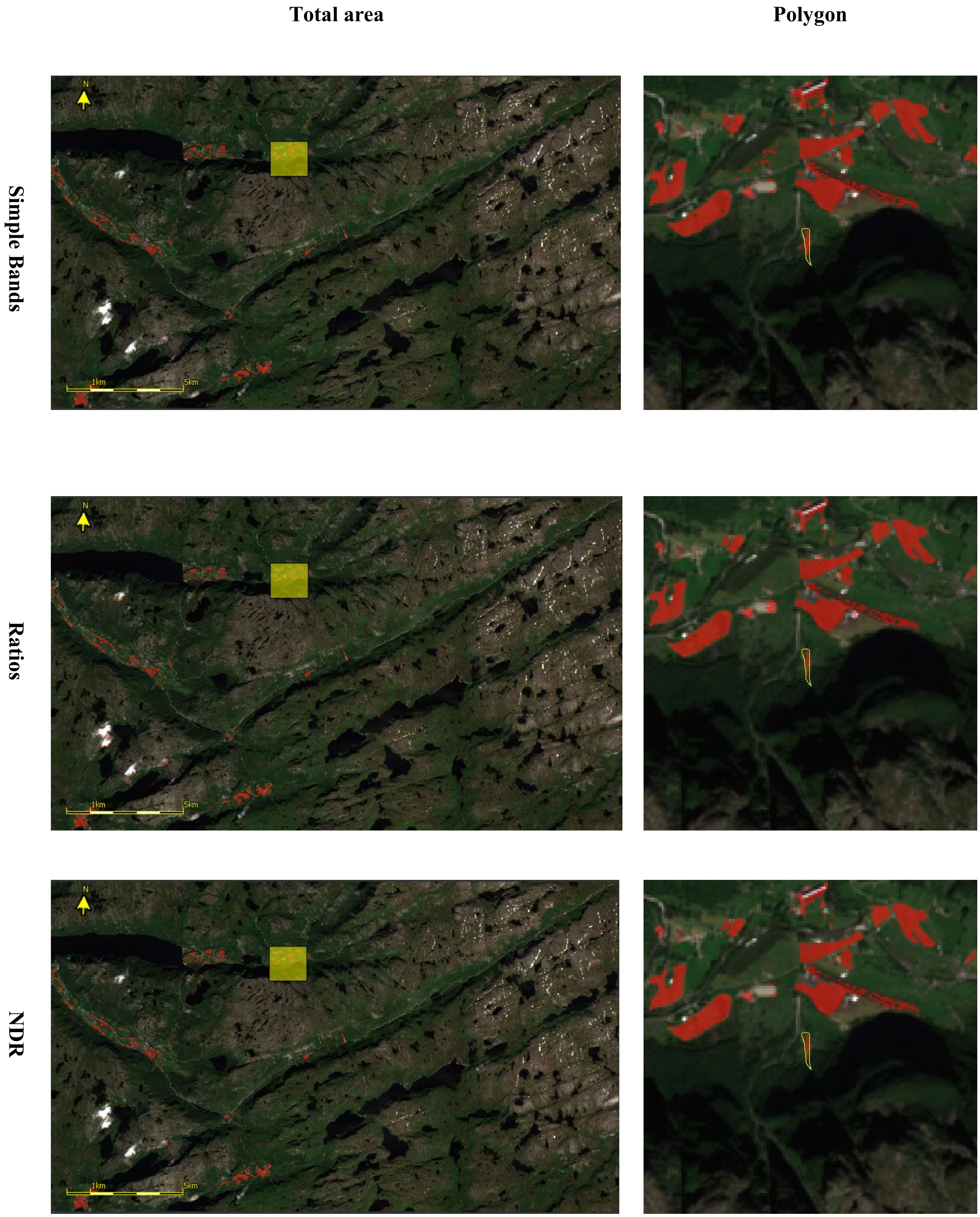

Figure 4.20 - NCC, change detection classification, Hunnedalen.

4.3.5 Automatic classification – Change detection, Spansdalen

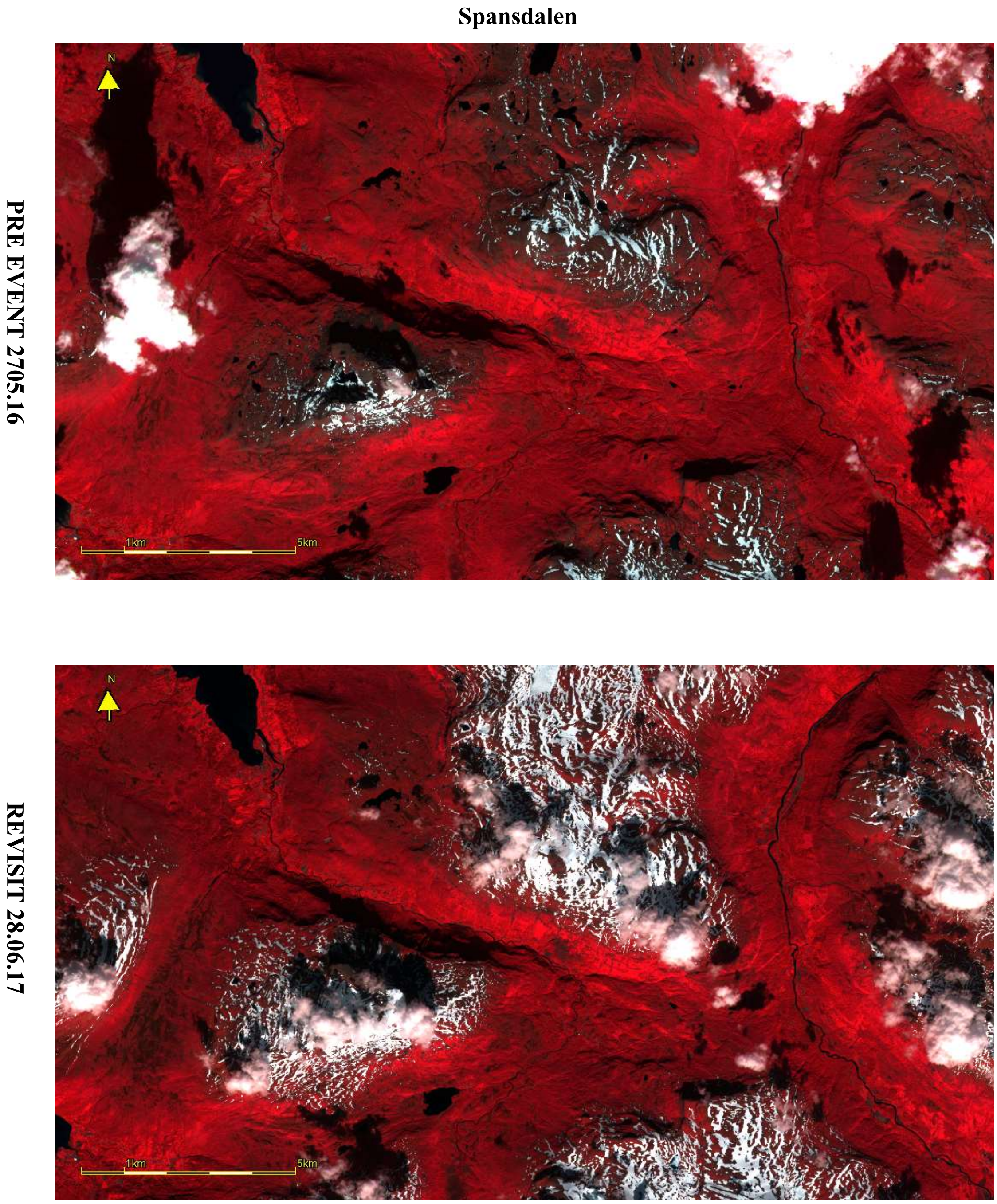

Figure 4.21 - Pre-event and post-event data of the Spansdalen area

False color composites of the datasets acquired at time 1 and time 2 are given above to compare the conditions at the time of acquisition. The performance of the different thresholds are given in the Tables below and are illustrated in the false color composite images. The leftmost images show the entire test area, from time 2, with masked pixels in yellow. The yellow square represents the location and extent of the rightmost image - the area of the defined polygon, with the polygon outlined in blue.

Test area:

Satellite data, time 1	Pre-visit data 23.07.2016
Satellite data, time 2	Revisit data 22.07.2017
Size of test area	~23 x 12 km^2

Table 4.16 - Results from Spansdalen change detection classification

	Number of pixels	%- of total
Total Area	2 807 500	100
Polygon, Spansdalen	258	100
Simple Bands	364 173	13
Within polygon, Spansdalen	194	75
Ratios	216 053	8
Within polygon, Spansdalen	151	59
NDR	151 219	5
Within polygon, Spansdalen	151	59

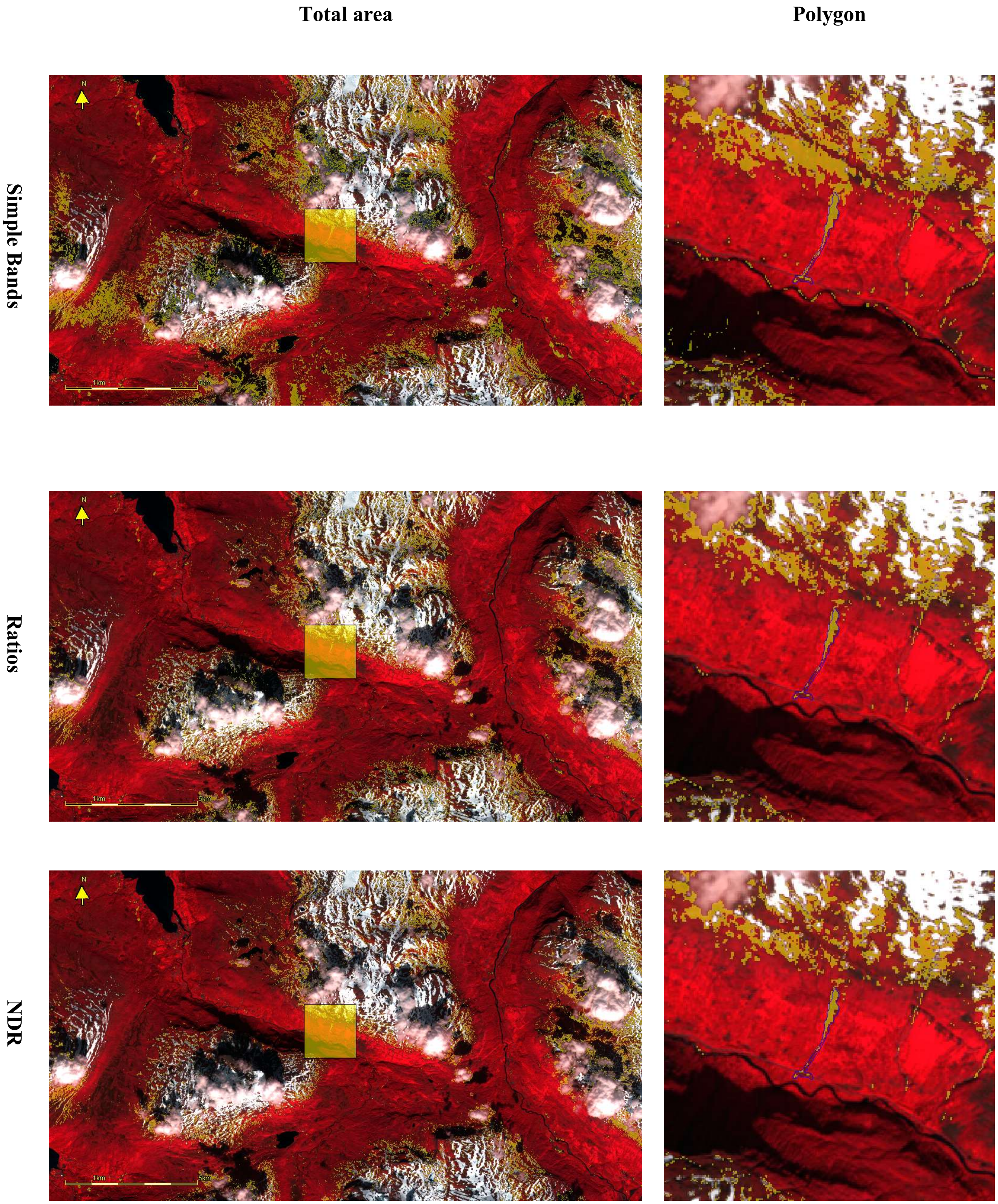

Figure 4.22 – FCC, change detection classification, Spansdalen.

5 Discussion and conclusions

The results and findings of this report are discussed in the following chapter.

5.1 Landslide characteristics

The characteristics of the investigated landslide are expected to show some similarities, as debris avalanches and debris flows are the primary focus. The events are believed to (partly) be triggered due to excess water. The climatic conditions of each event are evaluated in Appendix C, which shows clear signs of wet conditions for the majority of the investigated events. Referring to the Norwegian definitions given in Table 2.2, the investigated landslide types are characterized as water-related events, i.e. the displacement of fully saturated material, or a flow-like displacement of material. For such an event to be detectable by Sentinel-2, some distinct features must be identified to determine if certain areas found in the satellite data can be defined as a landslide. The landslide must sufficiently alter the terrain or its surroundings for it to be recognizable.

5.1.1 Size and geometry

Considering S2-data, the magnitude of the landslide is an obvious characteristic for its detectability. Utilizing only the bands with 10 m spatial resolution features down to 10 meters in size are visually discernable. However, to detect signs of landslide activity extending only a single pixel of 10 x 10 m is not likely. The spectral signature of the single pixel will be that of the landslide, but without any reference of its surface characteristic other than a single pixel, it will most likely be disregarded. The extent of the smallest detected event, given in surface area is roughly 3 000 m^2, which approximates to a cluster of ~30 pixels. Figure C.20 and C.21 show natural color composites of the event, and it is possible to outline a cluster of pixels, of what appears to be a debris fan, based on its shape, and the fact that the event was known on beforehand. Narrow sections of ~10 m in width are observed in several of the detected events, but only as parts of larger areas defined as a landslide. For example, the bottom part of event 7-Spansdalen (Figure C.62) and event 8-Selskreda (Figure C.72), which both extend roughly 10 m in width. The total length of the two events is 741 m and 431 m respectively. The bottom narrow sections of the Spansdalen event correspond to ~25 pixels in length, as seen in Appendix D.7. It is difficult to imagine landslide events extending less than roughly 25 pixels, being defined as a landslide-pixels with high certainty. As the magnitude decreases, its shape and geometrical reference will be more and more diffuse and prone to misclassification, which makes it difficult to distinguish as a landslide from surrounding pixels.

5.1.2 Topography and morphology

Certain areas can be identified as more exposed to landslide activity based on topography. The topography can be visually observed in the S2-datasets or included as digital terrain models, which in principle enables a way of quantifying the topography.

The visual interpretation of landslides may be based on the recognition of certain features in the terrain related to landslide activity. Referring to Table 2.4. by (Jakob and Hungr, 2005) - *Topographic features of debris avalanches and debris flows, and their photographic characteristics* used for the recognition of landslide activity in aerial photography. Aerial photography typically has better spatial resolution than S2, but dependening on the size of the topographic features, some may be applicable for the interpretation of S2-composite imagery;

An exact *backscarp* of a debris avalanche was not observed in any of the detected events from the satellite images. A clear circular backscarp can be seen in the photo documentation of event 1-Lindelia (Figure C.1). The same cannot be observed in the false color composite (Figure C.3), probably due to the size and the nearby railway influencing the area.

*Hummocky and irregular slope morpholog*y may be detected in the S2-data. The photographic characteristics refer to “coarse surface texture contrasting with smooth surroundings”. Different surface textures can be observed on a relatively coarse scale in the S2-data, for example between the surface textures of forested areas vs. farmland. Figure C.29, a natural color composite of the Øksland event, shows a clear difference in the texture between the forested area and the cultivated land. The same can be observed in Figure C.38, a false color composite of the Slettafossen debris avalanche. The surface texture between the adjacent forests appears to have a coarser surface texture than the observed landslide scar.

Lack of vegetation and irregular denuded swaths are probably the most characteristic feature which can be detected in the S2-data. In addition to a visually observable area of denuded vegetation, the vegetation has a significant spectral reflectance which can be detected. The S2 sensor is highly adapted to detect vegetation, and the NDVI is a robust method of evaluating the amount of biomass in optical satellite remote sensing data. All detected events in this report have, in some manner, removed or covered vegetation. Event 8-Selskreda would not have been possible to delineate without an irregular swath of less vegetation, observed in the NDVI-image. The detectability of events occurring in regions with little or no green vegetation appears to be more uncertain. Event 14-Byrkjedal occurred in a location where the spectral signature is strongly influenced by shadows, and the NDVI is not clear. From the documentation, event 22-Ávžejávri would appear to be of a magnitude large enough to be detected. However, the landslide occurred in a low vegetated area, at a time with little green vegetation. Event 13-Sulitjelma is possibly too small for detection, but could possibly have been deemed *detected* or *not detected* with higher certainty if it occurred on a slope with green vegetation.

Distinct b*erms/levees* are not observed in any of the detected events. The features are possibly somewhat detectable in S2-data if they have altered the vegetation along the water channels.

Topographic and morphological characteristics may be used to identify terrain prone to landslide activity. These charracteristics are of aid when manually identifying areas of interest, as well as using satellite remote sensing data. An automated approach could utilize a DTM – Digital Terrain Model, which could be applicable to automatically delimit areas based on given criterias. A minimum slope inclination of 15° could e.g. be defined after (Myrabø et al., 2014) or convergent-formed terrain could be identified automatically be identified.

5.2 Sentinel-2 in Norwegian Conditions

Characteristics of Norway influence S2-data in numerous ways. The geography has a large influence, both directly and indirectly. The mountainous and hilly landscapes create shadows, decreasing the quality of S2-data. The investigated events situated at south-facing slopes have generally been found to have good lighting conditions. North-facing slopes will be more prone to shadows, but also south facing slopes in steep narrow valleys may be subjected to shadows from the opposite sides and poor illumination. The shadows are more pronounced in the late seasons, as the sun is lower on the horizon and casts longer shadows.

The geography also contributes to the varied climate across Norway. Three of Köppens climate regions can be found in the Norwegian mainland, which indicate variable weather conditions depending on location. The average cloud cover in Norway can be as much as 75 % (Sivle, 2009), effectively rendering the acquisition of satellite data useless over large periods. However, Norway's northern latitude results in a high revisit time of the S2-constellation which improves the odds of obtaining cloud free data.

The spectral characteristics of surface features may vary dependent on seasonal variations. As previously mentioned, shadow effects differ during the season, and as Norway has large amounts of vegetation, the time of the growth seasons affect the spectral characteristics of large surface areas. Large areas are snow covered during the winter, and coastal regions may have short periods of snow, causing large variations between acquired datasets. The northernmost part of the country is not subjected to sunlight during large parts of the winter, therefor no optical satellite data is available.

5.3 Spectral Signatures and NDVI

A natural variability is prominent in the investigated spectral signatures. The reflectance of pixels along the centerlines of the detected landslides was examined, with the purpose of disregarding pixels with more diffuse signatures, or misclassified pixels. The pixels around the perimeter of the landslide are believed to be less influenced by the landslide and believed to be prone misclassification by a human operator.

The spectral signature of all detected landslides is characterized by natural variability. Some trends can be observed from the investigated S2-bands; the red, green, blue and NIR. As shown by (Clark, 1999) in Figure 2.24a), the NIR-band is sensitive to green vegetation, and will typically show higher reflectance in the NIR wavelengths than in the visible wavelengths. What can be seen from most of the events is that the vegetation has great influence, even if only considering the centerline pixels. The spectral signatures of each detected event are shown in Appendix D. It should be noted that the NDVI is derived from the NIR and red band, but is shown in the same plots as the VNIR-bands. The NDVI is considered as a reference to the vegetation along the transect, as well as utilized in the threshold techniques.

The beginning section of several transects have a high NDVI-relative to the rest of the landslide, (e.g. event 3-Kommedal, 4-Øksland, 5-Slettafossen, and 6-Kråkagjelet). This may partly be due to in-accuracies in the delineation of the starting point, or due to the fact that several of the debris avalanches have a V-shape (e.g. 4-Øksland, 5-Slettafossen, and 11-Krundalen) with a narrow start. The narrowest sections, typically defined with a width of 1 pixel, are highly influenced by surrounding vegetation yielding a high NDVI. This results in a varying NDVI signature, based on the part of the landslide, and shape. The spectral signature of event 1-Lindelia is given below, which has a narrow section from pixel 4-20. The landslide occurred on a slope with dense vegetation, which can be seen in the NDVI, with values ranging around 0.60-0.70. It can also be seen in the same sections, that the vegetation influence the visible bands more than the soil. In the most vegetated pixels, the NIR-band should in theory have the highest spectral reflectance, followed by the green, red, and blue band, as shown by (CCMEO, 2013) in Figure 2.24b). The parts of the transects which have the highest NDVI values are observed to have the highest reflectance in the NIR-band, then blue, green and red (E.g. event 1,3,4,5,7,10 and 11), which fits with the theoretical spectra signature of coniferous forest.

The theoretical reflectance of soil have according to (Clark, 1999) highest reflectance in the NIR-range, and decreasing in the red, green and blue band respectively. It should be noted that the graph given in Figure 2.24a) is based on average values. The observed spectral signature from the landslide pixels differs somewhat from the theoretical graph. The debris fan of event 2-Hunnedalen is the only event corresponding to the theoretical signature. Most of the events have relatively little sensitivity in the visible bands, but typically the blue band is highest, then the green and the red. The green and red bands are approximately equal in many cases. E.g. events 3, 4, 5, 6, 7, 9, 10 and 11. All visible bands are typically below 0.15, and events 1, 3, 5 and 6, show slightly higher reflectance in the parts of the transect with the lowest NDVI, which is theoretically expected. The remainder of events are more unclear, and this trend isn't observed. Possibly due to the fact that the sensitivity between soil and vegetation is not that large in the visible range.

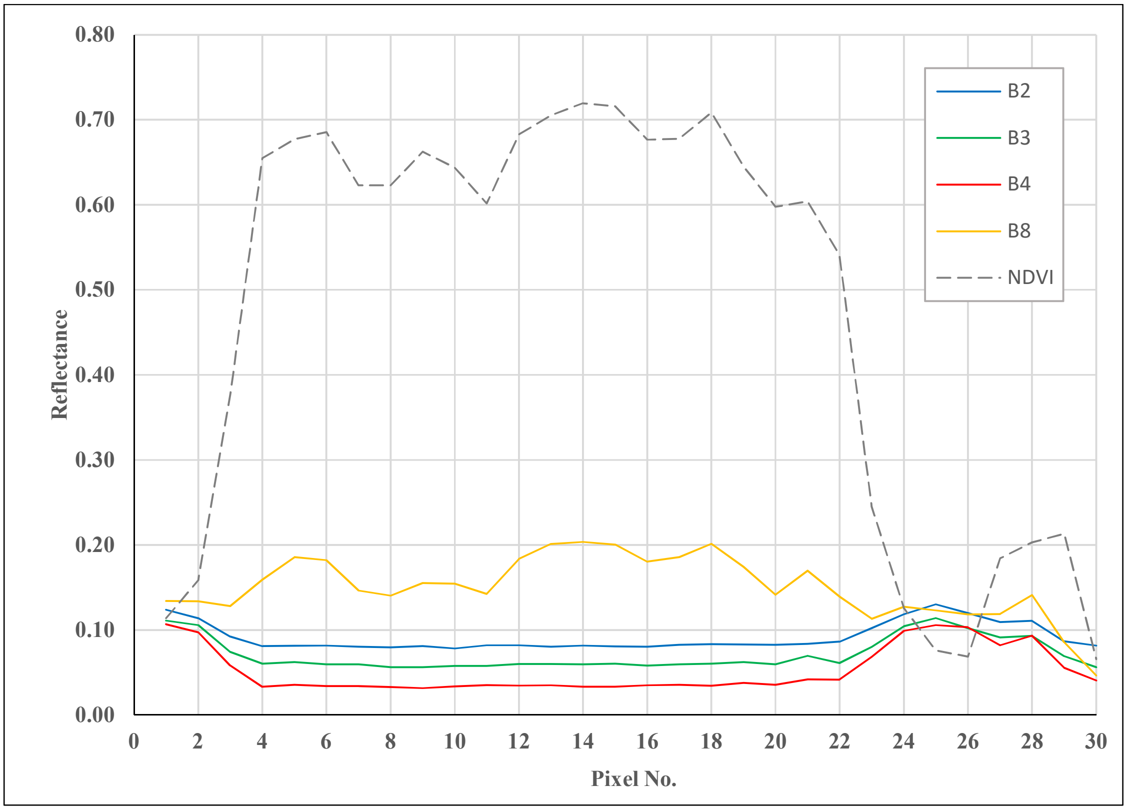

Figure 5.1 – The spectral reflectance of the VNIR-bands and NDVI of event 1-Lindelia.

The most distinct parts of the landslides within the transects, i.e. the wider parts, are less affected by vegetation and has typically an NDVI of less than 0.20. For automatic classification purposes a balance must be obtained, where the denuded vegetation must be taken into account, as well as pixels being influenced by nearby vegetation.

Ratios derived from the single bands are also examined. The NIR/Visible bands ratios are sensitive to vegetation in the same way NDVI is, but it is not normalized. The NIR/red ratio is in principle the NDVI, but with another scale and sensitivity. The NIR/visible ratios show the same trends, but with different magnitudes. The ratios show a large spread, but the high vegetated pixels have NIR/visible-ratios in the range of 2-6. The visible/visible ratios are consistent in their respective transects, and appear to fluctuate around 1.0 on most of the detected events.

Due to the robustness of NDVI, and that it is a good indication of landslide activity, NDVI-ratios has also been investigated. Numerically, the ratios are co-dependent of some of the bands, as it will yield the ratio of a ratio sensitive to the amount of vegetation. E.g. the NDVI/red-ratio – large amounts of vegetation yields a large NDVI and little red reflectance, resulting in the highest observed values. The NDVI/NIR-ratio show the lowest values.

5.3.1 Thresholding based on spectral reflectance

To evaluate if a unique spectral signature could be obtained from the detected landslides, simple thresholding techniques were applied. The strategy was to focus solely on the spectral signature from the detected landslide-pixels, and compare them to the spectral reflectance of the pixels in the rest of the satellite scene. Small amounts of misclassification would indicate that the landslide pixels had a unique signature, while large amounts would indicate the opposite.

Initial testing based on statistical values revealed poor accuracy, as shown in the Figure below. Here the NDVI and VNIR-thresholds are based on average values and standard deviation. The red pixels indicate pixels with a spectral signature within the given thresholds. The red pixels represent *potential landslide*-pixels, based on the thresholds.

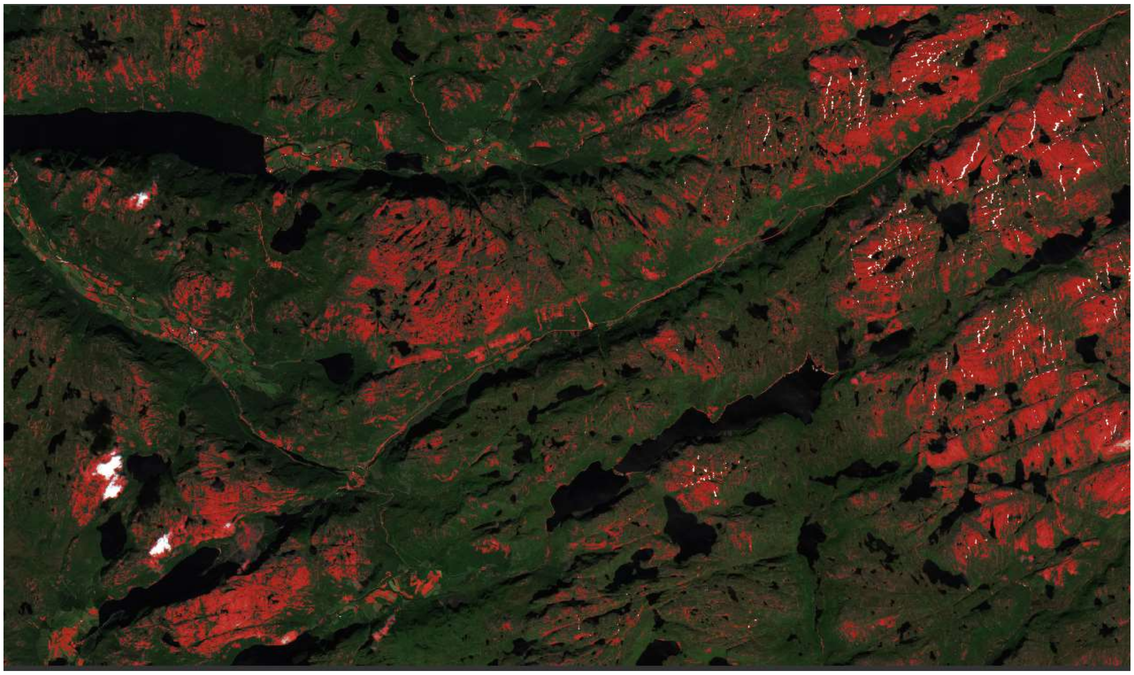

Figure 5.2 - Initial threshold test of the Hunnedalen area

The statistical approach above did produce good results. Instead, a rather crude approach was used to determine the values for thresholds. The approach was to consider only the most distinct pixels, as described in section 4.2, which proved to have better accuracy. A theoretical success criteria could be defined as zero misclassified pixels, and all predefined landslide pixels correctly classified. Some uncertainty is of course associated with the predefined landslide pixels, as they can in principle be misclassified by the operator. The exact border between the outline of the detected landslide and the adjacent terrain can be misinterpreted, but assuming the larger part of the predefined pixels are correctly classified, the results from the different approaches should be representative. Ground truthing the exact extent of the landslide would be the approach to eliminate this uncertainty.

The thresholds applied to the test areas did not show great accuracy. Out of the tested areas, the thresholds based on single bands and NDVI-ratios had the best performance. One of the best accuracies achieved by the simple-band approach classified 10% out of the total amount of pixels as *potential landslide*-pixels, which amounts to ~12 million pixels. The amount of misclassified pixels could possibly be reduced by refining the threshold values, but the spectral signature alone is not likely to produce high accuracies, as there are other features with similar reflectance characteristics. The Figure below shows the maximum and minimum reflectance of some typical features found in the vicinity of the detected landslides. Snow and clouds are for the most part excluded from the *potential landslide*-pixels, except for the *ratio*-approach. The threshold used in the *ratio* approach does not include a threshold specifically connected to the NDVI. The NDVI of snow has negative maximum and minimum value, which is outside the threshold range. Clouds have a high reflectance in the visible region, also outside the threshold ranges. The minimum values of exposed bedrock, roads and vegetated slopes, on the other hand, have values within the ranges, which then can be misclassified.

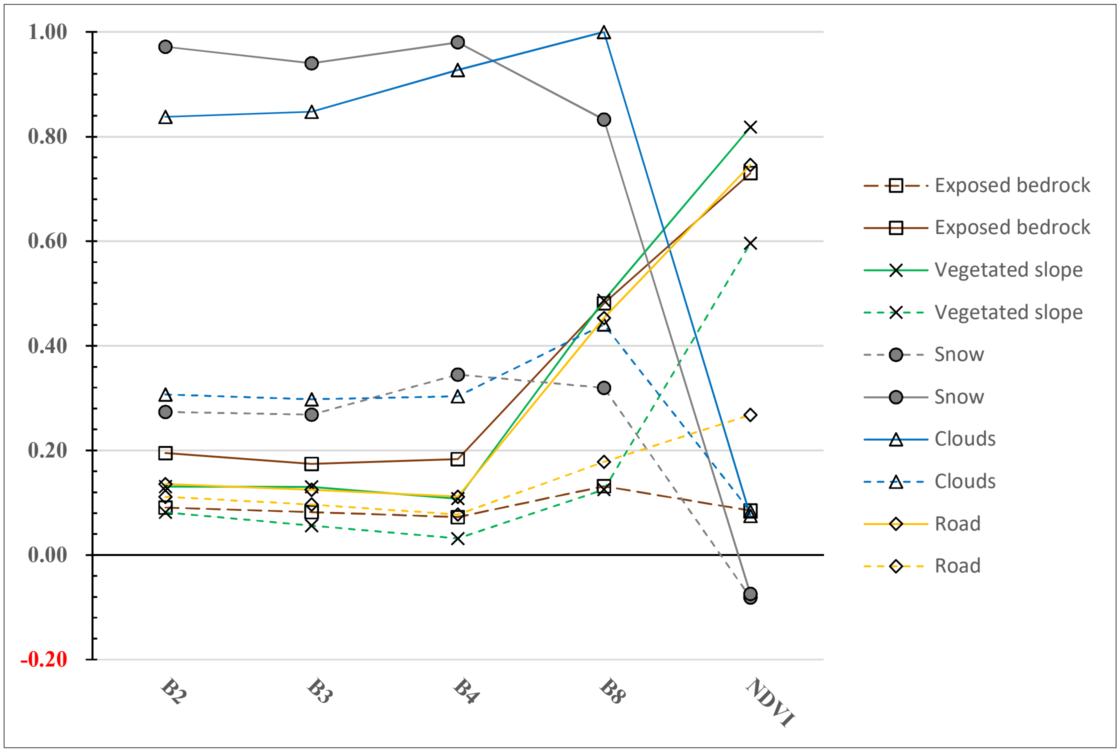

Figure 5.3 - Maximum and minimum reflectance of typical surface features

5.4 Change Detection

The change detection approach looks at the change in a time series of satellite data. No unique spectral reflectance is in principle needed to detect a landslide using this strategy. If two datasets acquired at two different times, in theory, are identical expect for a large landslide occurrence, the difference between the two datasets would be sufficient to identify the landslide. Identical pixels from time 1 to time 2 would yield no change, while pixels affected by terrain alteration from a landslide would show change. In practice, a great deal of variation can be observed from the same area over time. Norway, as previously discussed, is in particular prone to large seasonal variations both with respect to season and lighting conditions.

Transects of the detected landslide are in the same manner examined with respect to change between datasets. Some characteristics are expected. All change detection approaches are in this work calculated as the change from time 1 to time 2, where time 1 occurs first. As previously discussed, a key characteristic of a landslide is the denudation of vegetation. With a high relative vegetation at time 1 and low relative vegetation at time 2, we expect a change in the NIR-band and the NDVI in the potential landslide pixels. This can be observed at many of the investigated transects. This may, of course, be subject to seasonal variations. E.g. a dataset acquired in early spring, and a dataset acquired mid-summer. The vegetation is lusher in the mid-summer, yielding a large difference in the NDVI-values from the early spring compared to the mid-summer. This effect is observed in event 7-Spansdalen, shown in Appendix E.7 – The pre-event data is acquired at early summer and the post-event data one month later. The post-event data contains a much greener landscape, and the transect covering the landslide-pixels show a negative change in NDVI, indicating more vegetation in the area where the landslide has occurred. The same transect is compared to a satellite scene acquired a year before, with similar seasonal conditions, and show a much more expected spectral signature – a positive NDVI difference, indicating a loss of vegetation.

According to the spectral signatures defined by (Clark, 1999), some theoretical characteristics could be expected. Assuming the landslide occurs in a vegetated area and denudes vegetation – In the visible region, vegetation has less reflectance than soil and a higher response in the NIR-region. The soil has a higher reflectance in the visible bands, but significantly less than vegetation in the NIR-regions. This should expect us to obtain a small negative change in the visible bands and a positive change in the NIR-bands. This can be observed in the most distinct parts of all the investigated events, with similar seasonal conditions. The NDR-yields the same trend, but as the values are normalized, the scale is transformed. The ratio-approach gives the quotient of the spectral reflectance prior the landslide and after the landslide. Referring to Clark's spectral characteristics, the ratios should be lower in the visible region and produce higher values in the NIR-band. The NDVI-ratio should be even higher. This response is observed in many of the detected events.

5.4.1 Thresholding based on change detection

Similar threshold-techniques were applied on the test areas, investigating the change in spectral signature over time for the respective areas. Initial observations revealed the great influence of seasonal variation. This can be e.g. be seen in Appendix E.7-Spansdalen, where snow and vegetation cause an unexpected response in the spectral difference. Similar effects are observed in the classification test at event 5-Slettafossen (1) (section 4.3.3), where the change in two datasets with large seasonal variations are used, yielding poor results. It should be noted that the pre-defined thresholds are based on the spectral difference derived from data with similar conditions. If seasonal variations were taken into account in the threshold ranges, it is believed that the accuracy would have decreased because of the spectral indifferences.

The change detection approach works well with regards to cloud and snow variations, as little areas of either seem to be classified as *potential landslide*-pixels. The spectral characteristics of soil and vegetation vs. snow and clouds are different enough to not be classified. The snow has high reflectance in the visible range, and snow yields negative NDVI value, which differs from the landslide pixels with low reflectance in the visible bands, and positive NDVI values.

Some areas observed to typically be misclassified are shown in the figures below. The yellow pixels represent pixels with spectral difference within the defined thresholds. The yellow pixels are considered *potential landslide*-pixels, based on the change detection thresholds. Agricultural areas have been observed to typically be misclassified, especially if the fields are plowed or have matured in between data acquisition. Minor alterations along water channels and rivers are yellow, which possibly are due to river erosion. Interventions in the landscape, due to e.g. construction activity is also found to be misclassified.

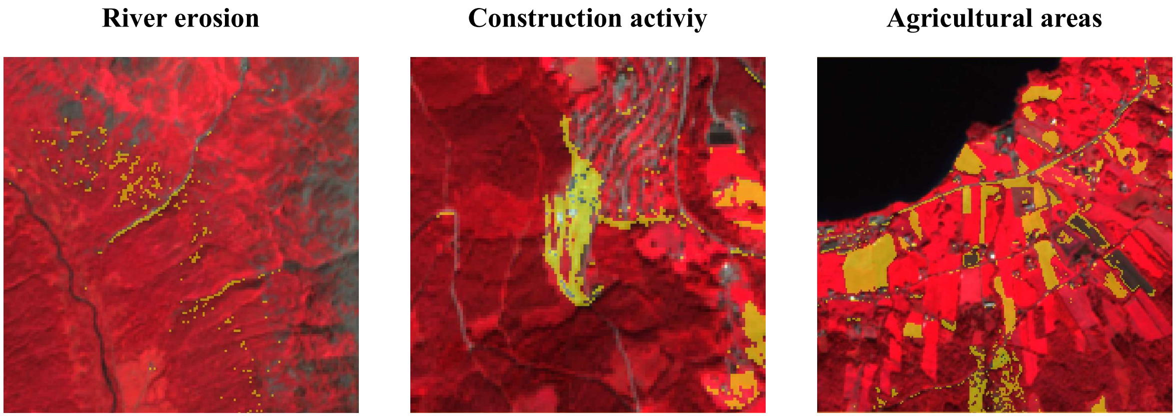

River erosion

Construction activiy

Agricultural areas

Figure 5.4 - Misclassified areas using change detection thresholds

The change detection method proved to detect landslides not found in the Norwegian landslide database. The two events shown below are detected in the Kråkagjelet-area, where satellite data acquired from 2015 and 2017 were used in the calculations. The detected landslide 1 has automatically masked out a larger portion of the landslide scar than detected landslide 2. This is possibly due to the observed difference in the previsist and poste-event images. The slope of landslide 1 appears to have more vegetation, while the slope of landslide 2 appear to have more exposed bedrock. It appears to be the section of denuded vegetation which has been automatically masked out. This also shows that the difference in vegetation is a key factor in the change detection approach.

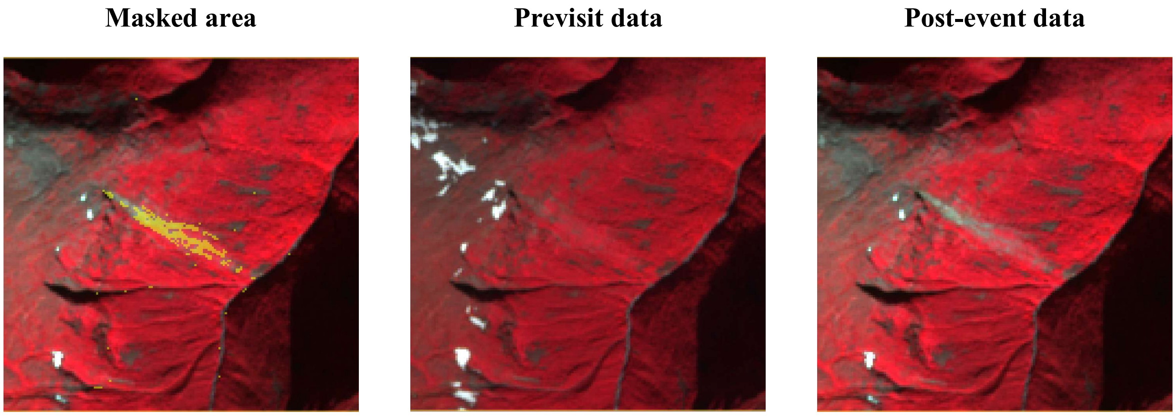

Figure 5.5 - Detected landslide 1

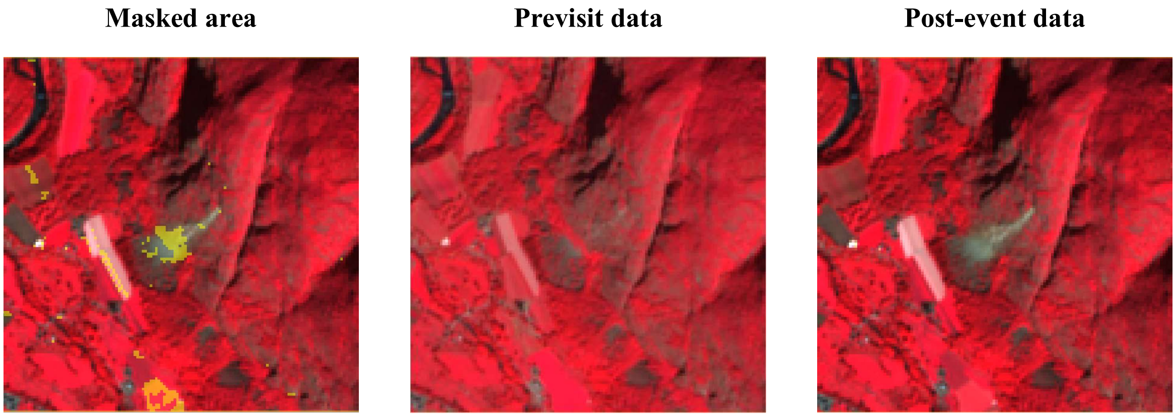

Figure 5.6 - Detected landslide 2

5.5 Spectral Reflectance vs. Change Detection

The threshold approach based on the spectral reflectance and the approach based on change detection managed to classify predefined landslide pixels. For the algorithm to be useful however, the amount of misclassified pixels should be minimized, in addition to a high amount of correctly classified landslide pixels. The different approaches revealed great variations regarding this issues, as shown in the results section. Though, all test areas show unambiguously a better accuracy using the change detection approach. The trend is illustrated in the satellite scene below, where spectral reflectance thresholds and change detection thresholds are applied to the same area. The topmost Figures show the result from the spectral reflectance thresholds, where the red pixels are considered *potential landslide*-pixels. Both approaches are able to correctly classify a large amount of the predefined landslide pixels, as seen in the right excerpt. The change detection approach, however, has a lot less misclassified pixels.

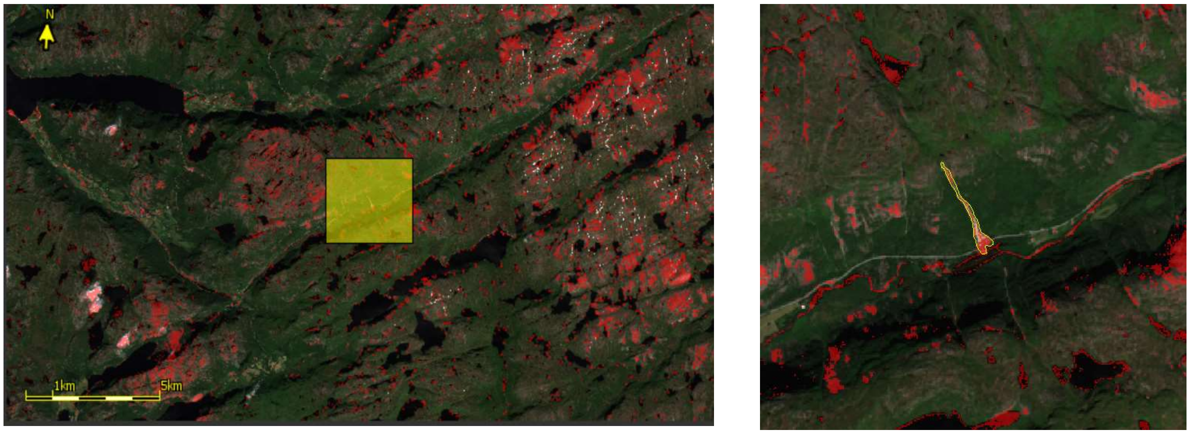

Figure 5.7 - Thresholds based on spectral signature, Hunnedalen

Figure 5.8 - Thresholds based on change detection, Hunnedalen

5.6 Outlook Towards an Operational Landslide Monitoring System

Using Sentinel-2 in an operational landslide monitoring system appear to be possible, but the limitaions of the satellites must be seen against the utilitarian value of such a system. 11 out of the 25 investigated events were detected, showing that it is possible to detect landslides using Sentinel-2. The limitations are connected to the desired accuracy of such a system. An overall goal of detecting all landslide events occurring in Norway is unrealistic. A large amount of the registered landslide events in Norway appear to be too small to be detected by a high resolution sensor such as S2. A sensor with a higher spatial resolution would probably increase the number of detected landslides in such a system, merely because its potential to recognize smaller features at the earth's surface. Based on the findings of this report, three prerequisites can be said to be in place to be able to detect landslides using S2:

- The landslide must be of a certain size.
- The landslide must sufficiently alter the terrain in such a way that makes it identifiable, either by visual inspection or spectral detection.
- Satellite data of sufficient quality must be available from the area, after the landslide has occurred.

The smallest landslide-surface detected in this work consist of 33 pixels – This corresponds to a surface area of roughly 3 300 m^2. It is probable that a large amount of the landslide activity occurring in Norway do not reach this magnitude. However, some landslides do – If the overall goal were to update the national landslide inventory by one event, this can be achieved based on the findings in this report. The realistic goal is probably somewhere in between identifying all landslide activity and identifying some landslide activity.

The identification of *when* a landslide has occurred should also be included in such a system. If the detected landslides are to be correlated to conditions at the time of occurrence, the time must be identified. The S2-sensors are theoretically able to pinpoint the time of occurrence within an interval of 2-3 days in Norway given optimal conditions. In practice, it will not be as frequent. Cloud cover and seasonal variations will strongly influence the satellite data availability, and effectively governing the satellites possibility of identifying the time of occurrence.

The results given in this report are based on spectral signature- and change detection thresholds from a relatively small sample of data. The thresholds approaches are believed to produce better results if their values are further refined. From this work, it is not believed that an operational landslide detection system would be based spectral thresholds alone. A multi-criteria approach, including elements such as slope inclination, terrain shape, and geometrical considerations would possibly produce better results. A large amount of the misclassified pixels from e.g. the agricultural areas could be disregarded by implementing a slope inclination criterion, which excludes pixels in terrain with less inclination than 15 degrees. Geometrical ratios, based on similar values as given in Figure 4.5 could have been used on clusters of pixels, possibly excluding e.g. roads. Divergent terrain forms could e.g. be excluded, to reduce the search area.

5.7 Conclusions

The conclusions which can be drawn from this report is given below.

The size of a landslide corresponding to 33 pixels (~3 300 m^2) are detectable in the 10 m resolution bands of S2. The boundary of which an event can be deemed *detected* or *not detected* with high certainty is believed to be around 2000-2500 m^2, corresponding to 20-25 pixels.

The topography and morphology affect S2-data in various ways. Optical data acquired from steep north-facing slopes are prone to shadow effects. No specific soil cover, or geological setting are found to affect the detectability of the investigated landslides.

The S2-satellites are operational in Norwegian conditions, but are limited by climatic conditions and large seasonal variations. Year-round coverage of satellite data to be used for landslide detection purposes is not available using S2. S2-data acquired from the summer-season are found to have the best prerequisites for detecting debris avalanches and debris flow, due to the lighting- and vegetative conditions.

The spectral characteristics of the investigated landslides are found to have large variability. No unique signature is obtained from the examined datasets, but some characteristics are identified:

- The NDVI is highly applicable for indication of landslide activity
- The landslide affected areas have generally low sensitivity in the visible bands

A change detection approach is found to have better accuracy with respect to automatic classification of landslide affected pixels based on spectral characteristics. S2-data acquired with similar lighting- and seasonal conditions are found to yield best results.

Dependent on the level of accuracy wanted, Senintel-2 may be utilized as part of an automated landslide detection system. The optical satellites operate well in certain Norwegian conditions, but are delimited by climatic conditions and large seasonal variations. Due to a large amount of landslide activity which would go undetected by S2, the frequent cloud cover conditions in Norway, and low data availability in the winter season, using Sentinel-2 alone is probably not a viable option for a landslide detection system. A more realistic option is to use S2-data in combination with other remote sensing systems, I.E in combination with radar satellites, or drones with multispectral instrumentation.

REFERENCES

BARGEL, T. H., FERGUS, T., DEVOLI, G., ORVEDAL, K., PEEREBOM, I., ØYDVIN, E. K., STALSBERG, K., SLETTEN, K., FISCHER, L., RUBENSDOTTER, L. & EILERTSEN, R. 2011. Plan for skredfarekartlegging – Delrapport jordskred og flomskred. *In:* BARGEL, T. H. (ed.) *16/2011.* NVE.

BJORDAL, H., HELLE, T. E., VEGDIREKTORATET. TRAFIKKSIKKERHET, M.-O. T. & STATENS, V. 2011. Skred og flom på veg : statistiske betraktninger. Oslo: Vegdirektoratet.

BRUNSDEN, D. 1993. Mass movement; the research frontier and beyond: a geomorphological approach. *Geomorphology,* 7**,** 85-128.

BRYN, A., STRAND, G.-H., ANGELOFF, M. & REKDAL, Y. 2018. Land cover in Norway based on an area frame survey of vegetation types. *Norsk Geografisk Tidsskrift - Norwegian Journal of Geography,* 72**,** 131-145.

CASALE, R., FANTECHI, R., FLAGEOLLET, J. C. & COMMUNITIES, C. O. T. E. 1994. *Temporal Occurrence and Forecasting of Landslides in the European Community: Final Report. Part 1, Methodology (reviews) for the Temporal Study of Landslides. Part 2, Case Studies of the Temporal Occurrence of Landslides in the European Community*, European Commission.

CCMEO 2013. Remote Sensing Fundamentals. CCMEO - The Canada Centre for Mapping and Earth Observation (formerly Canada Centre for Remote Sensing).

CLAGUE, J. J. 2013. Landslide. *In:* BOBROWSKY, P. T. (ed.) *Encyclopedia of Natural Hazards.* Dordrecht: Springer Netherlands.

CLAGUE, J. J. & STEAD, D. 2012. Landslides : types, mechanisms and modeling. Cambridge: Cambridge Univ. Press.

CLARK, R. N. 1999. Chapter 1: Spectroscopy of Rocks and Minerals, and Principles of Spectroscopy, in Manual of Remote Sensing, Volume 3, Remote Sensing for the Earth Sciences. New York: John Wiley and Sons, Inc.

COLA, L. D. 2011. *The use of a raster data structure to summarize a point pattern* [Online]. Wikimedia Commons. Available: https://commons.wikimedia.org/wiki/File:The_use_of_a_raster_data_structure_to_summarize_a_point_pattern.gif [Accessed 04.04.2018].

COLLEUILLE, H., BOJE, S., DEVOLI, G., KRØGLI, I. K., ENGEN, I. K., SUND, M., SKASLIEN, T., HUMSTAD, T., FREKHAUG, M. & WIRÉHN, P. 2017. Jordskredvarslingen: nasjonal varslingstjeneste for jord-, sørpe- og flomskredfare. *In:* COLLEUILLE, H. (ed.). Oslo: NVE, 2017: Norges vassdrags- og energidirektorat.

DANNEVIG, P. & HARSTVEIT, K. 2013. *Klima i Norge* [Online]. Store Norske Leksikon: Store Norske Leksikon. Available: https://snl.no/Klima_i_Norge [Accessed 12.05.2018].

DEVOLI, G. 2017. Regional early warning systems for rainfall- and snowmeltinduced landslides. Need for an international forum? NVEs hustrykkeri: NVE.

DIKAU, R., BRUNSDEN, D., SCHROTT, L. & IBSEN, M.-L. 1996. *Landslide recognition : identification, movement and causes,* Chichester, Wiley.

DRUSCH, M., DEL BELLO, U., CARLIER, S., COLIN, O., FERNANDEZ, V., GASCON, F., HOERSCH, B., ISOLA, C., LABERINTI, P., MARTIMORT, P., MEYGRET, A., SPOTO, F., SY, O., MARCHESE, F. & BARGELLINI, P. 2012. Sentinel-2: ESA's Optical High-Resolution Mission for GMES Operational Services. *Remote Sensing of Environment,* 120**,** 25-36.

EMDAL, A., FAGGRUPPE FOR GEOTEKNIKK, N. & NORGES TEKNISK-NATURVITENSKAPELIGE UNIVERSITET FAGGRUPPE FOR GEOTEKNIKK 2014. *Introduksjon til geoteknikk,* Trondheim, NTNU, Geoteknikk Tapir akademisk forlag, Kompendieforlaget.

EMERY, W., CAMPS, A. & RODRIGUEZ-CASSOLA, M. 2017. Introduction to Satellite Remote Sensing. Elsevier.

ESA. 2010. *GMES Mission Requirements Document* [Online]. European Space Agency. Available: http://esamultimedia.esa.int/docs/GMES/Sentinel-2_MRD.pdf [Accessed 08.02.2018].

ESA 2013. SENTINEL-2 User Handbook. *In:* HOERSCH, B. (ed.). European Space Agency.

GHOREISHIAN AMIRI, S. A. 2017. "Unsaturated Soils" **-** Lecture notes distributed in TBA5155 Febrary 2017. NTNU.

HALL, D. K., RIGGS, G. A. & SALOMONSON, V. V. 1995. Development of methods for mapping global snow cover using moderate resolution imaging spectroradiometer data. *Remote Sensing of Environment,* 54**,** 127-140.

HECHT, E. 1998. *Optics,* Reading, Mass, Addison-Wesley.

HIGHLAND, L. M. & BOBROWSKY, P. 2008. *The Landslide Handbook - A Guide to Understanding Landslides,* Reston, Virginia, U.S Geological Survey.

HOVELSRUD, G. K., AMUNDSEN, H. & FØRLAND, E. J. 2007. *Utviklingen av naturulykker som følge av klimaendringer : utredning på oppdrag fra Statens Landbruksforvaltning,* Oslo, CICERO.

HUNGR, O., LEROUEIL, S. & PICARELLI, L. 2014. The Varnes classification of landslide types, an update. *Journal of the International Consortium on Landslides,* 11**,** 167-194.

HUTCHINSON, J. Morphological and Geotechnical Parameters of Landslides in Relation to Geology and Hydrogeology, Landslides. Proceedings of the fifth international symposium on landslides, 1988. 3-35.

HØEG, K., LIED, K., KARLSRUD, K., GREGORY, T. & NORGES GEOTEKNISKE, I. 2014. *Skred : skredfare og sikringstiltak : praktiske erfaringer og teoretiske prinsipper,* Oslo, NGI Universitetsforl.

JAKOB, M. & HUNGR, O. 2005. *Debris-flow hazards and related phenomena,* Berlin, Springer published in association with Praxis PUbl.

JØRGENSEN, P., SØRENSEN, R. & PRESTVIK, O. 2013. Norske jordarter. NIBIO.

LILLESAND, T. M., KIEFER, R. W. & CHIPMAN, J. W. 2004. *Remote sensing and image interpretation,* New York, Wiley.

MAMEN, J. 2017. *Köppens klimaklassifikasjon* [Online]. Store Norske Leksikon. Available: https://snl.no/K%C3%B6ppens_klimaklassifikasjon [Accessed 11.05.2018 2018].

MCFEETERS, S. K. 1996. The use of the Normalized Difference Water Index (NDWI) in the delineation of open water features. *International Journal of Remote Sensing,* 17**,** 1425-1432.

METEREOLOGISK INSTITUTT. 2009. *Klimasoner* [Online]. Meteorologileksikon - metlex.met.no. Available: https://web.archive.org/web/20120123185532/http://metlex.met.no/wiki/Fil:Klimasoner.png [Accessed 11.05.2018].

METEREOLOGISK INSTITUTT. 2017. *Det blir våtere* [Online]. Available: https://www.met.no/vaer-og-klima/det-blir-vatere [Accessed 28.05.18].

MYRABØ, S., STALSBERG, K., FERGUS, T., LARSEN, J. O. & BJORDAL, H. 2014. *Håndbok V139 Flom- og Sørpeskred,* Oslo, Vegdirektoratet.

NORDAL, S. 2017. Geotechnical Engineering Advanced Course - Lecture notes and background material. NTNU, Geotechnical Division.

NOREM, H., FLESJØ, K., SELLEVOLD, J., RØDIN LUND, M. & VIRÉHN, P. L. E. 2016. Drenering for veg og jernbane: Naturfareprosjektet Delprosjekt 5 Flom og vann på avveie. *In:* NOREM, H. & SELLEVOLD, J. (eds.). NVE: Norges vassdrags- og energidirektorat.

NORSK KLIMASERVICESENTER. 2018. *Normalkart nedbør 1985-2014* [Online]. klimaservicesenter.no. Available: https://klimaservicesenter.no/faces/desktop/article.xhtml?uri=klimaservicesenteret/Klimanormaler [Accessed 11.05.2018 2018].

OLSEN, L., FREDIN, O. & OLESEN, O. 2013. *Quaternary geology of Norway,* Trondheim, Geological Survey of Norway.

PHILLIP RONAN, G. 2013. *The Electromagnetic Spectrum* [Online]. Wikimedia Commons. Available: https://commons.wikimedia.org/wiki/File:EM_spectrumrevised.png [Accessed].

PLANK, S., TWELE, A. & MARTINIS, S. 2016. Landslide Mapping in Vegetated Areas Using Change Detection Based on Optical and Polarimetric SAR Data. *Remote Sensing,* 8**,** 307.

RAMBERG, I. B., SOLLI, A., NORDGULEN, Ø., BINNS, R., GROGAN, P. & NORSK GEOLOGISK, F. 2008. *The Making of a land : geology of Norway,* Trondheim, The Norwegian Geological Association.

REES, W. G. 2001. *Physical principles of remote sensing,* Cambridge, Cambridge University Press.

SHRODER, J. F. 1971. *Landslides of Utah*, Utah Geological and Mineralogical Survey.

SIDLE, R. C. & OCHIAI, H. 2006. *Landslides : processes, prediction, and land use,* Washington, D.C, American Geophysical Union.

SIVLE, A. D. 2009. *Skydekke* [Online]. Store Norske Leksikon: Store Norske Leksikon. Available: https://snl.no/skydekke [Accessed 12.05.2018].

SKOGLUND, K. A. 2016. 311.137 Løsmasseskred i bratt terreng - Farevurdering og sikringstiltak. Sintef Byggforsk, byggforskserien.

STROZZI, T. 2014. Encyclopedia of Environmental Change. *In:* MATTHEWS, J. A. (ed.) *Electromagnetic Spectrum.*

VARNES, D. J. 1978. Slope movement types and processes. *Special report,* 176**,** 11-33.

YOUNG, H. D., FREEDMAN, R. A., SEARS, F. W., ZEMANSKY, M. W. & FORD, A. L. 2012. *Sears and Zemansky's University physics : with modern physics,* Boston, Addison-Wesley.

APPENDICES

Table of Contents

A. APPENDIX A – Methods

Table A.1 – Documentation of investigated events

No.	Classified as	Name of location	Date of occurence	Documentation
1	Debris avalanche	Lindelia	03.09.2015	http://www.regobs.no/Registration/66293
2	Debris flow	Hunnedalen	02.06.2016	http://www.regobs.no/Registration/99182
3	Debris flow	Kommedal	02.06.2016	http://www.regobs.no/Registration/99185
4	Debris avalanche	Øksland	03.09.2016	http://www.regobs.no/Registration/100133
5	Debris avalanche	Slettafossen	19.05.2017	http://www.regobs.no/Registration/128393
6	Debris flow	Kråkagjelet	19.05.2017	http://www.regobs.no/Registration/128325
7	Debris avalanche	Spansdalen	15.06.2017	http://www.regobs.no/Registration/129347
8	Debris flow	Selskreda	24.07.2017	http://www.regobs.no/Registration/129946
9	Debris flow	Tokke	02.10.2017	http://www.regobs.no/Registration/131387
10	Debris avalanche	Rødstøl	09.06.2011	http://www.andalsnes-avis.no/nyheter/article347475.ece
11	Debris avalanche	Krundalen	05.07.2015	http://www.regobs.no/Registration/65513
12	Debris avalanche	Bjerkadalen	26.01.2017	http://www.regobs.no/Registration/120366
13	Debris avalanche	Sulitjelma	02.05.2017	http://www.regobs.no/Registration/126553
14	Debris avalanche	Byrkjedal	02.10.2017	http://www.regobs.no/Registration/131533
15	Debris flow	Beiarn	11.07.2015	http://www.regobs.no/Registration/65750
16	Debris flow	Raudskredbekken	05.12.2015	http://www.regobs.no/Registration/79791
17	Debris avalanche	Reinåa	05.12.2016	http://www.regobs.no/Registration/104864
18	Debris avalanche	Jølster	08.12.2016	http://www.regobs.no/Registration/105451
19	Debris avalanche	Hyestranda	30.12.2016	http://www.regobs.no/Registration/108564
20	Debris avalanche	Ommedal	30.12.2016	http://www.regobs.no/Registration/108392
21	Debris avalanche	Falla	20.01.2017	http://www.regobs.no/Registration/111478
22	Debris avalanche	Ávžejávri	08.06.2017	http://www.regobs.no/Registration/129415
23	Debris avalanche	Setesdalsveien	30.09.2017	http://www.regobs.no/Registration/130625
24	Debris avalanche	Saga	02.10.2017	http://www.regobs.no/Registration/130656
25	Multiple debris flows	Luster	02.10.2017	http://www.regobs.no/Registration/131049 http://www.regobs.no/Registration/131037 http://www.regobs.no/Registration/131038 http://www.regobs.no/Registration/131530

Table A.2 – Satellite data ID of investigated events

No.	S2 - ACQUISITIONS				Pre-event data ID	Post-event data ID
	Previsit	Pre-event	Post-event	Revisit		
1		22.08.2015	04.09.2015	20.07.2016	S2A_OPER_PRD_MSIL1C_PDMC_20160706T181324_R008_V20150822T104035_20150822T104035	S2A_OPER_PRD_MSIL1C_PDMC_20161010T214744_R051_V20150904T105046_20150904T105042
2		24.05.2016	10.06.2016	28.08.2027	S2A_OPER_PRD_MSIL1C_PDMC_20160527T092044_R094_V20160524T105625_20160524T105625	S2A_OPER_PRD_MSIL1C_PDMC_20160614T210859_R051_V20160610T105030_20160610T105030
3		24.05.2016	10.06.2016	28.08.2027	S2A_OPER_PRD_MSIL1C_PDMC_20160527T092044_R094_V20160524T105625_20160524T105625	S2A_OPER_PRD_MSIL1C_PDMC_20160614T210859_R051_V20160610T105030_20160610T105030
4		06.06.2016	04.09.2016	23.07.2017	S2A_OPER_PRD_MSIL1C_PDMC_20160607T014123_R137_V20160606T110624_20160606T110624	S2A_OPER_PRD_MSIL1C_PDMC_20160905T215913_R137_V20160904T110652_20160904T110817
5	19.08.2016	12.05.2017	28.06.2017		S2A_MSIL1C_20170512T110651_N0205_R137_T32VMQ_20170512T111302	S2A_MSIL1C_20170628T105651_N0205_R094_T32VMQ_20170628T105649
6	18.08.2015	06.05.2017	22.08.2017		S2A_MSIL1C_20170506T105031_N0205_R051_T32VMN_20170506T105029	S2B_MSIL1C_20170822T105649_N0205_R094_T32VMN_20170822T105648
7	23.07.2016	12.06.2017	22.07.2017		S2A_MSIL1C_20170612T104021_N0205_R008_T33WXS_20170612T104023	S2A_MSIL1C_20170722T104021_N0205_R008_T33WXS_20170722T104023
8		21.07.2017	26.07.2017	22.08.2017	S2A_MSIL1C_20170721T110621_N0205_R137_T32VMQ_20170721T110758	S2B_MSIL1C_20170726T110619_N0205_R137_T32VMQ_20170726T110854
9		16.09.2017	06.10.2017		S2A_MSIL1C_20170916T105701_N0205_R094_T32VML_20170916T105658	S2A_MSIL1C_20171006T105941_N0205_R094_T32VML_20171006T105937
10		12.05.2017	28.06.2017		S2A_MSIL1C_20170512T110651_N0205_R137_T32VMQ_20170512T111302	S2A_MSIL1C_20170605T105031_N0205_R051_T32VMQ_20170605T105303
11			18.08.2015	06.06.2016	N.A	S2A_OPER_PRD_MSIL1C_PDMC_20160707T072908_R094_V20150818T110049_20150818T110049
12		25.10.2016	15.02.2017	20.07.2017	S2A_OPER_PRD_MSIL1C_PDMC_20161026T172837_R008_V20161025T104122_20161025T104122	S2A_MSIL1C_20170215T105121_N0204_R051_T33WVP_20170215T105122
13		29.04.2017	09.05.2017		S2A_MSIL1C_20170429T105651_N0205_R094_T33WWQ_20170429T105653	S2A_MSIL1C_20170509T105621_N0205_R094_T33WWQ_20170509T105622
14		23.09.2017	23.10.2017		S2A_MSIL1C_20170923T105021_N0205_R051_T32VLL_20170923T105022	S2A_MSIL1C_20171023T105111_N0206_R051_T32VLL_20171023T131219
15			15.08.2017		N.A	S2A_OPER_PRD_MSIL1C_PDMC_20160705T144751_R051_V20150815T105041_20150815T105041
16		18.08.2015	14.02.2016	13.06.2016	S2A_OPER_PRD_MSIL1C_PDMC_20160707T072908_R094_V20150818T110049_20150818T110049	S2A_OPER_PRD_MSIL1C_PDMC_20160408T225306_R094_V20160214T110150_20160214T110150
17		07.11.2016	15.02.2017		S2A_OPER_PRD_MSIL1C_PDMC_20161108T174957_R051_V20161107T105242_20161107T105242	S2A_MSIL1C_20170215T105121_N0204_R051_T33VUL_20170215T105122
18		03.11.2016	23.03.2017		S2A_OPER_PRD_MSIL1C_PDMC_20161103T181111_R137_V20161103T111222_20161103T111222	S2A_MSIL1C_20170323T110721_N0204_R137_T32VLP_20170323T111323
19		03.11.2016	23.03.2017		S2A_OPER_PRD_MSIL1C_PDMC_20161103T181111_R137_V20161103T111222_20161103T111222	S2A_MSIL1C_20170323T110721_N0204_R137_T32VLP_20170323T111323
20		03.11.2016	23.03.2017		S2A_OPER_PRD_MSIL1C_PDMC_20161103T181111_R137_V20161103T111222_20161103T111222	S2A_MSIL1C_20170323T110721_N0204_R137_T32VLP_20170323T111323
21		17.11.2016	16.04.2017		S2A_OPER_PRD_MSIL1C_PDMC_20161117T193021_R051_V20161117T105322_20161117T105322	S2A_MSIL1C_20170416T105031_N0204_R051_T32VMQ_20170416T105026
22		27.05.2017	09.06.2017		S2A_MSIL1C_20170527T102031_N0205_R065_T34WEC_20170527T102026	S2A_MSIL1C_20170609T103021_N0205_R108_T34WEC_20170609T103023
23		22.08.2017	16.10.2017		S2B_MSIL1C_20170822T105649_N0205_R094_T32VMK_20170822T105648	S2A_MSIL1C_20171016T110031_N0205_R094_T32VMK_20171016T110313
24		12.08.2017	06.10.2017		S2B_MSIL1C_20170812T105619_N0205_R094_T32VMK_20170812T105617	S2A_MSIL1C_20171006T105941_N0205_R094_T32VMK_20171006T105937
25		23.09.2017	09.10.2017		S2A_MSIL1C_20170923T105021_N0205_R051_T32VMP_20170923T105022	S2A_MSIL1C_20171009T110951_N0205_R137_T32VMP_20171009T110946
		23.09.2017	09.10.2017		S2A_MSIL1C_20170923T105021_N0205_R051_T32VMP_20170923T105022	S2A_MSIL1C_20171009T110951_N0205_R137_T32VMP_20171009T110946
		23.09.2017	09.10.2017		S2A_MSIL1C_20170923T105021_N0205_R051_T32VMP_20170923T105022	S2A_MSIL1C_20171009T110951_N0205_R137_T32VMP_20171009T110946
		23.09.2017	09.10.2017		S2A_MSIL1C_20170923T105021_N0205_R051_T32VMP_20170923T105022	S2A_MSIL1C_20171009T110951_N0205_R137_T32VMP_20171009T110946

Table A.3 – Satellite data ID of investigated events

No.	S2 - ACQUISITIONS				Pre-event data ID	Revisit data ID
	Previsit	Pre-event	Post-event	Revisit		
1		22.08.2015	04.09.2015	20.07.2016	-	S2A_OPER_PRD_MSIL1C_PDMC_20160721T161006_R051_V20160720T105030_20160720T105030
2		24.05.2016	10.06.2016	28.08.2027	-	S2A_MSIL1C_20170628T105651_N0205_R094_T32VLL_20170628T105649
3		24.05.2016	10.06.2016	28.08.2027	-	S2A_MSIL1C_20170628T105651_N0205_R094_T32VLL_20170628T105649
4		06.06.2016	04.09.2016	23.07.2017	-	S2B_MSIL1C_20170723T105619_N0205_R094_T32VLN_20170723T105619
5	19.08.2016	12.05.2017	28.06.2017		S2A_OPER_PRD_MSIL1C_PDMC_20160820T180925_R051_V20160819T105032_20160819T105337	-
6	18.08.2015	06.05.2017	22.08.2017		S2A_OPER_PRD_MSIL1C_PDMC_20160707T072908_R094_V20150818T110049_20150818T110049	-
7	23.07.2016	12.06.2017	22.07.2017		S2A_OPER_PRD_MSIL1C_PDMC_20161008T075744_R094_V20160723T105622_20160723T105623	-
8		21.07.2017	26.07.2017	22.08.2017	-	S2B_MSIL1C_20170822T105649_N0205_R094_T32VMQ_20170822T105648
11			18.08.2015	06.06.2016	-	S2A_OPER_PRD_MSIL1C_PDMC_20160607T014123_R137_V20160606T110624_20160606T110624
12		25.10.2016	15.02.2017	20.07.2017	-	S2B_MSIL1C_20170720T105029_N0205_R051_T33WVP_20170720T105026
16		18.08.2015	14.02.2016	13.06.2016	-	S2A_OPER_PRD_MSIL1C_PDMC_20160613T231647_R094_V20160613T105622_20160613T105622

Table A.4 - Sentinel-2 bands specification

Band	**Application** (From http://esamultimedia.esa.int/docs/GMES/Sentinel-2_MRD.pdf)	**Spatial Resolution [m]**	**Central Wavelength [nm]**	**Bandwidth [nm]**
1 – Blue	Atmospheric correction	60	443	20
2 – Blue	Vegetation senescing, carotenoid, browning and soil background. Atmospheric correction.	10	490	65
3 – Green	Green peak, total chlorophyll in vegetation.	10	560	35
4 – Red	Maximum chlorophyll absorption.	10	665	30
5 – NIR	Position of red edge, consolidation of atmospheric corrections / fluorescence baseline.	20	705	15
6 – NIR	Position of red edge, atmospheric correction, retrieval of aerosol load.	20	740	15
7 – NIR	Leaf area index, edge of the NIR plateau.	20	783	20
8 – NIR	Leaf area index	10	842	115
8a – NIR	NIR plateau, sensitive to total chlorophyll, biomass, LAI, and protein; water vapor absorption reference; retrieval of aerosol load and type.	20	865	20
9 – NIR	Water vapor absorption, atmospheric correction.	60	945	20
10 – SWIR	Detection of thin cirrus for atmospheric correction.	60	1375	30
11 – SWIR	Sensitive to lignin, starch, and forest aboveground biomass. Snow/ice/cloud separation.	20	1610	90
12 – SWIR	Assessment of Mediterranean vegetation conditions. Distinction of clay soils for the monitoring of soil erosion. Distinction between live biomass, dead biomass, and soil, e.g. for burn scars mapping.	20	2190	180

B. APPENDIX B – Results

B.1 Characteristics of investigated events

Table B.1 - Geometric characteristics, detected events

No.	Name	Area m^2	Perimeter m^2	Transect m	Width 1 m	Width 2 m	No. of pixels
1	Lindelia	5 908	735	305	60	10	58
2	Hunnedalen	24 823	1 623	761	128	23	329
3	Kommedal	3 332	379	172	51	16	33
4	Øksland	10 962	569	253	65	17	104
8	Slettafossen	8 764	607	285	55	33	88
6	Kråkagjelet	37 569	2 047	893	56	21	371
7	Spansdalen	26 300	1 677	741	62	12	258
8	Selskreda	-	-	431	42	10	40*
9	Tokke	11 437	717	319	53	16	113
10	Rødstøl	128 414	3 126	1 441	146	58	1 282
11	Krundalen	80 417	1 896	752	148	89	805

**From transect*

Table B.2 - Geometrical ratios

No.	Name	Area/ Perimeter	√(Area)/ Perimeter	Area/ Transect	√(Area)/ Transect
1	Lindelia	8.0	0.10	19.4	0.25
2	Hunnedalen	15.3	0.10	32.6	0.21
3	Kommedal	8.8	0.15	19.4	0.34
4	Øksland	19.3	0.18	43.3	0.41
8	Slettafossen	14.4	0.15	30.8	0.33
6	Kråkagjelet	18.4	0.09	42.1	0.22
7	Spansdalen	15.7	0.10	35.5	0.22
8	Selskreda	-	-	-	-
9	Tokke	16.0	0.15	35.9	0.34
10	Rødstøl	41.1	0.11	89.1	0.25
11	Krundalen	42.4	0.15	106.9	0.38

B.2 Spectral reflectance

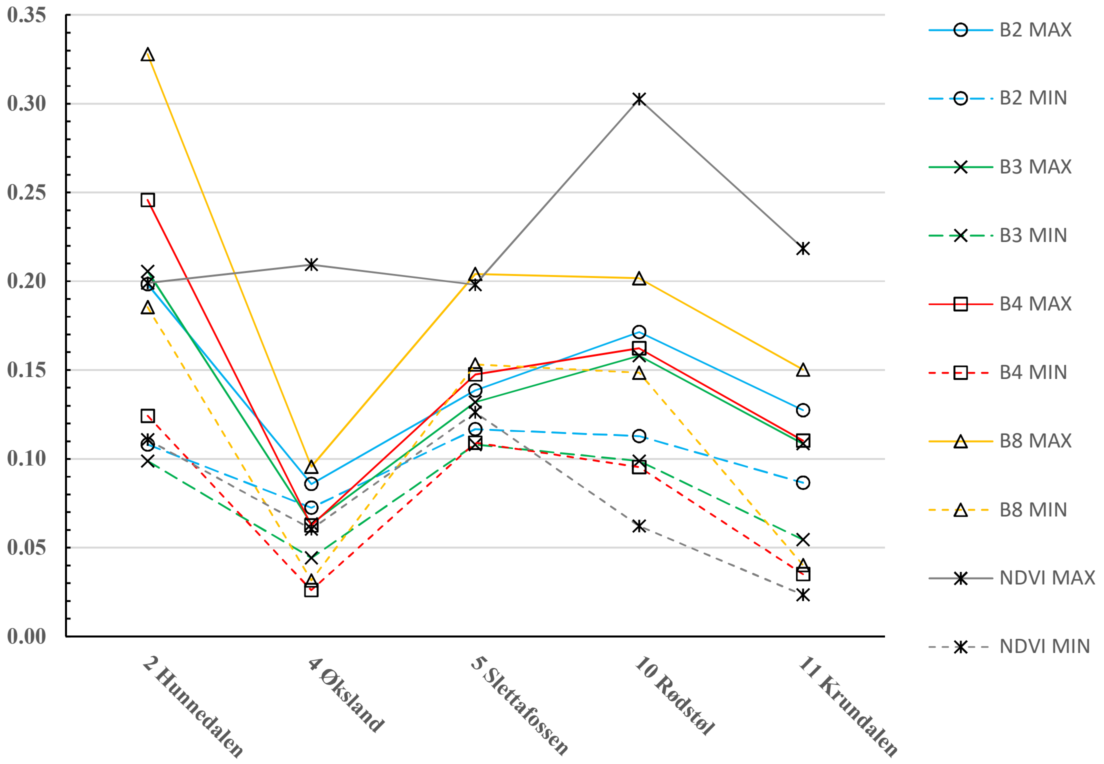

Figure B.1 - Basis for simple bands thresholds

Table B.3 – Basis for simple band thresholds

Event	Pixel no. in transect		B2	B3	B4	B8	NDVI
2 Hunnedalen	45-60	*Max*	0.20	0.21	0.25	0.33	0.20
		Min	0.11	0.10	0.12	0.19	0.11
4 Øksland	10-23	*Max*	0.09	0.06	0.06	0.10	0.21
		Min	0.07	0.04	0.03	0.03	0.06
5 Slettafossen	6-24	*Max*	0.14	0.13	0.15	0.20	0.20
		Min	0.12	0.11	0.11	0.15	0.13
10 Rødstøl	10-50	*Max*	0.17	0.16	0.16	0.20	0.30
		Min	0.11	0.10	0.10	0.15	0.06
11 Krundalen	5-60	*Max*	0.13	0.11	0.11	0.15	0.22
		Min	0.09	0.05	0.04	0.04	0.02

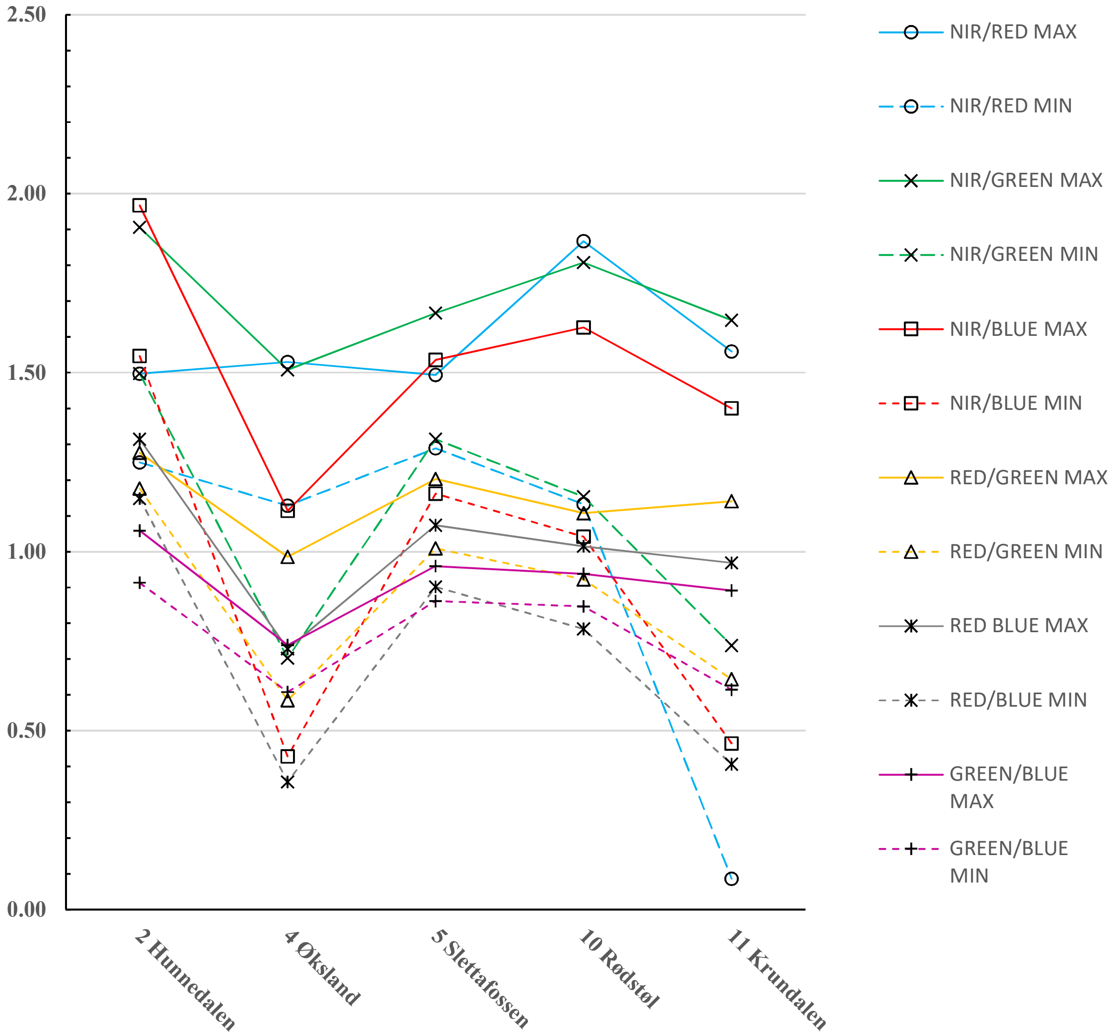

Figure B.2 – Basis for VNIR-Ratios thresholds

Table B.4 - Basis for VNIR-Ratios thresholds

Event	Pixel no. in transect		B8/B4	B8/B3	B8/B2	B4/B4	B4/B2	B3/B2
2 Hunnedalen	45-60	*Max*	1.50	1.91	1.97	1.28	1.31	1.06
		Min	1.25	1.50	1.55	1.18	1.15	0.91
4 Øksland	10-23	*Max*	1.53	1.51	1.11	0.99	0.73	0.74
		Min	1.13	0.70	0.43	0.58	0.36	0.61
5 Slettafossen	6-24	*Max*	1.49	1.67	1.54	1.20	1.07	0.96
		Min	1.29	1.31	1.16	1.01	0.90	0.86
10 Rødstøl	10-50	*Max*	1.87	1.81	1.63	1.11	1.02	0.94
		Min	1.13	1.15	1.04	0.92	0.78	0.85
11 Krundalen	5-60	*Max*	1.56	1.65	1.40	1.14	0.97	0.89
		Min	0.09	0.74	0.46	0.64	0.41	0.61

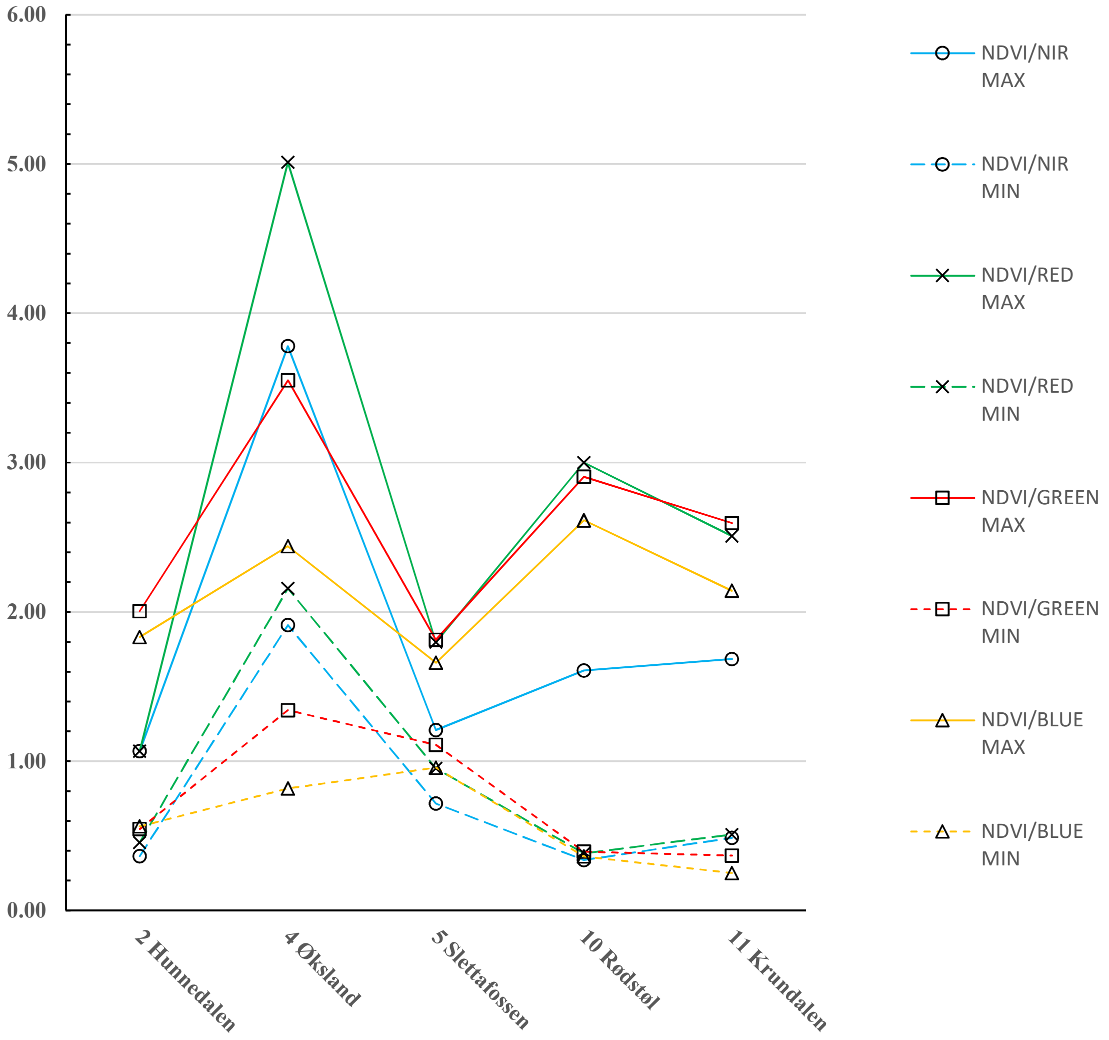

Figure B.3 - Basis for NDVI-ratios thresholds

Table B.5 - Basis for NDVI-ratios thresholds

Event	Pixel no. in transect		NDVI/B8	NDVI/B4	NDVI/B3	NDVI/B2
2 Hunnedalen	45-60	*Max*	1.07	1.07	2.01	1.83
		Min	0.36	0.45	0.55	0.56
4 Øksland	10-23	*Max*	3.78	5.01	3.55	2.44
		Min	1.91	2.16	1.34	0.82
5 Slettafossen	6-24	*Max*	1.21	1.80	1.81	1.66
		Min	0.72	0.95	1.11	0.96
10 Rødstøl	10-50	*Max*	1.61	3.00	2.91	2.61
		Min	0.34	0.38	0.39	0.36
11 Krundalen	5-60	*Max*	1.68	2.51	2.59	2.14
		Min	0.49	0.51	0.37	0.25

B.3 Change detection

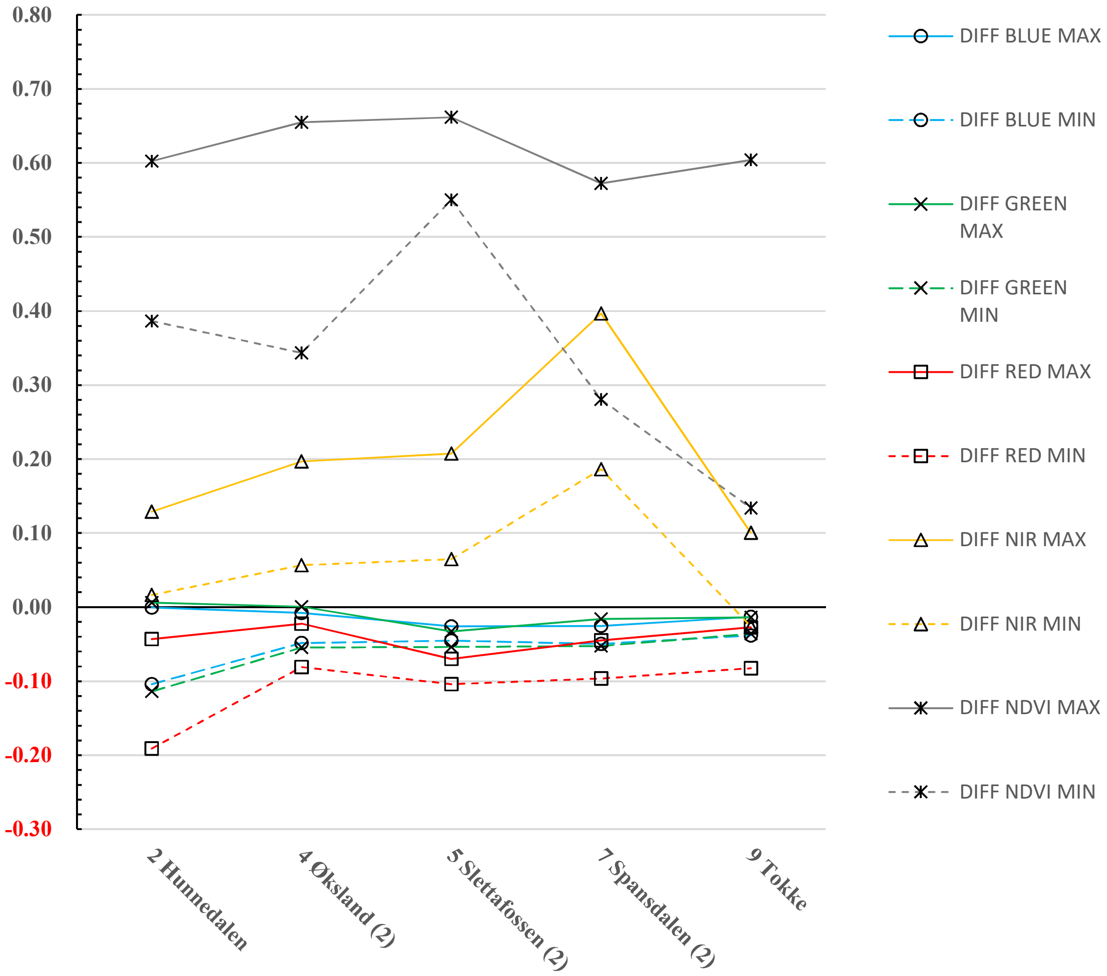

Table B.6 - Basis for simple band change detection thresholds

Event	**Extent of transect**		**DIFF B2**	**DIFF B3**	**DIFF B4**	**DIFF B8**	**DIFF NDVI**
2 Hunnedalen	45-60	*Max*	0.00	0.01	-0.04	0.13	0.60
		Min	-0.10	-0.11	-0.19	0.02	0.39
4 Øksland (2)	10-23	*Max*	-0.01	0.00	-0.02	0.20	0.65
		Min	-0.05	-0.05	-0.08	0.06	0.34
5 Slettafossen (2)	6-24	*Max*	-0.03	-0.03	-0.07	0.21	0.66
		Min	-0.05	-0.05	-0.10	0.07	0.55
7 Spansdalen (2)	10-25	*Max*	-0.03	-0.02	-0.04	0.40	0.57
		Min	-0.05	-0.05	-0.10	0.19	0.28
9 Tokke	15-25	*Max*	-0.01	-0.01	-0.03	0.10	0.60
		Min	-0.04	-0.04	-0.08	-0.03	0.13

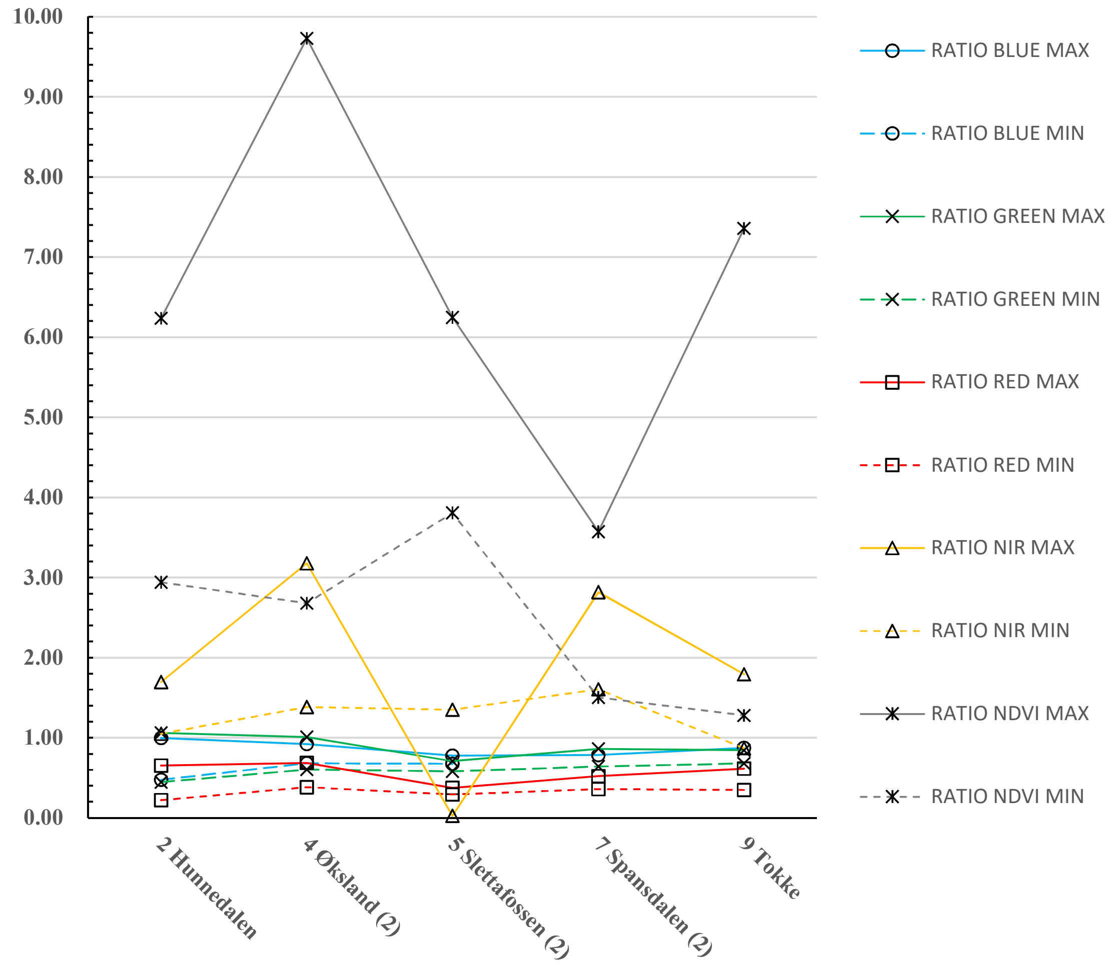

Table B.7 - Basis for ratios change detection thresholds

Event	Extent of transect		RATIO B8	RATIO B4	RATIO B3	RATIO B2	RATIO NDVI
2 Hunnedalen	45-60	*Max*	1.70	0.65	1.06	1.00	6.23
		Min	1.05	0.22	0.45	0.48	2.94
4 Øksland (2)	10-23	*Max*	3.18	0.69	1.01	0.92	9.73
		Min	1.38	0.38	0.60	0.68	2.68
5 Slettafossen (2)	6-24	*Max*	0.02	0.37	0.71	0.78	6.24
		Min	1.35	0.29	0.58	0.67	3.81
7 Spansdalen (2)	10-25	*Max*	2.82	0.52	0.86	0.78	3.57
		Min	1.60	0.36	0.64	0.65	1.50
9 Tokke	15-25	*Max*	1.79	0.61	0.84	0.87	7.36
		Min	0.87	0.35	0.68	0.70	1.28

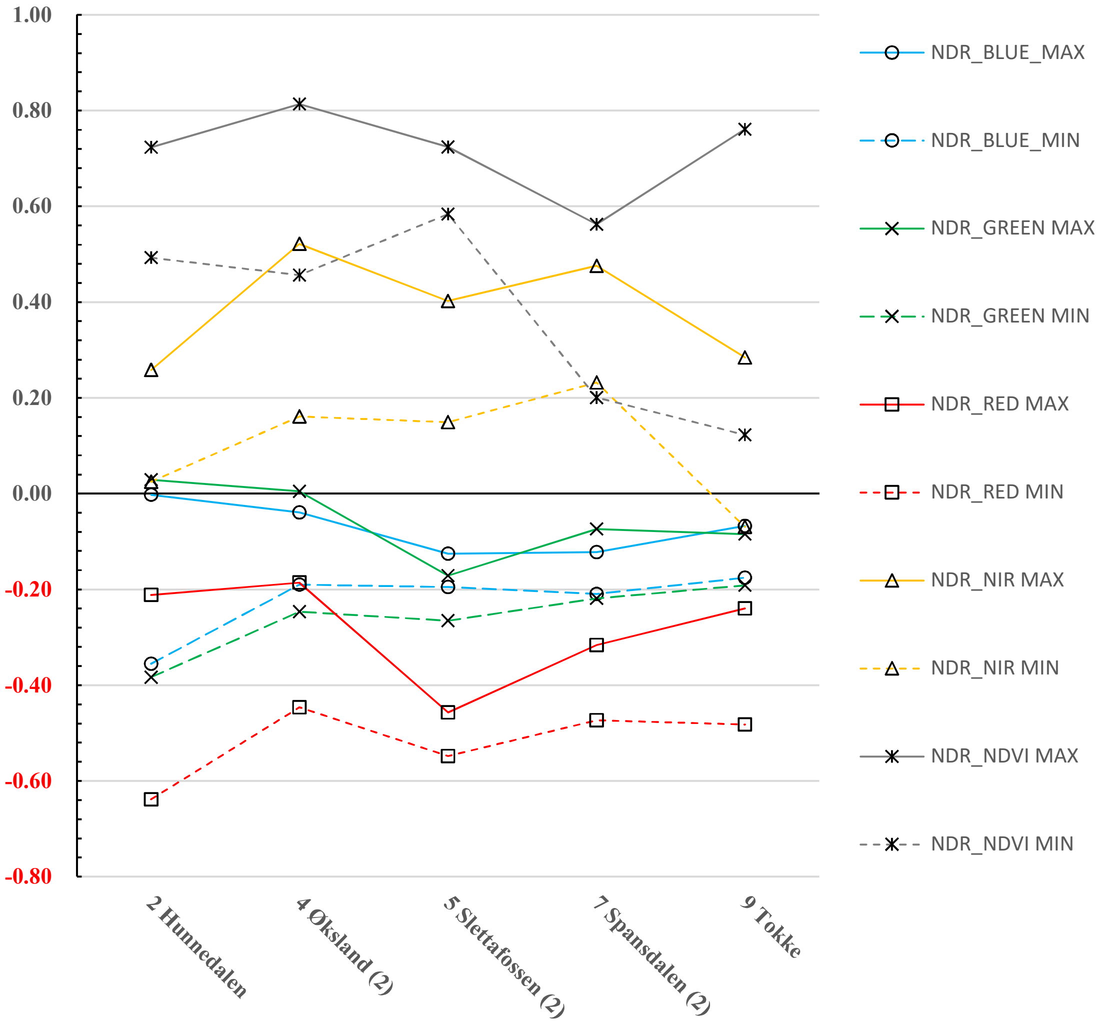

Table B.8 - Basis for NDR change detection thresholds

Event	Extent of transect		NDR B8	NDR B4	NDR B3	NDR B2	NDR NDVI
2 Hunnedalen	45-60	*Max*	0.26	-0.21	0.03	0.00	0.72
		Min	0.02	-0.64	-0.38	-0.36	0.49
4 Øksland (2)	10-23	*Max*	0.52	-0.19	0.00	-0.04	0.81
		Min	0.16	-0.45	-0.25	-0.19	0.46
5 Slettafossen (2)	6-24	*Max*	0.40	-0.46	-0.17	-0.13	0.72
		Min	0.15	-0.55	-0.27	-0.19	0.58
7 Spansdalen (2)	10-25	*Max*	0.48	-0.32	-0.07	-0.12	0.56
		Min	0.23	-0.47	-0.22	-0.21	0.20
9 Tokke	15-25	*Max*	0.28	-0.24	-0.08	-0.07	0.76
		Min	-0.07	-0.48	-0.19	-0.18	0.12

C. APPENDIX C – Characterization of Investigated Events

C.1 Detected Landslides

C.1.1 Event 1 – Lindelia

Type	Debris avalanche			
Date	03.09.2015			
Area	Flå, Buskerud			
Ref. ETRS89, UTM 33N	E: 205973	N: 6699030		
S2-data acquisition dates	Previsit:	Pre event:	Post event:	Revisit:
	-	22.08.2015	04.09.2015	20.07.2016

Figure C.1 – Lindelia debris avalanche, along with the Bergen railway. Photo by Jernbaneverket (Frank et al., 2015).

Figure C.2 – Displaced material, downslope. Photo: Statens Vegvesen, from (Statens Vegvesen, 2015).

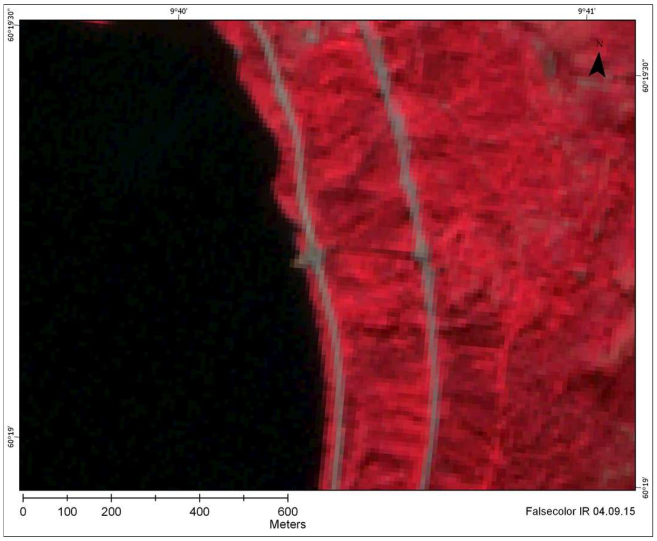

Figure C.3 – False color composite, Lindelia post-event data

The landslide is classified as a debris avalanche. It occurred in autumn, in the eastern part of Norway. The landslide happened in conjunction with intense rainfall and flooding in several places in eastern Norway. The slope is situated along Krøderfjorden. A motorway is situated at the foot of the slope, and the Bergen railroad track is further upslope. The slide initiated at the railroad, possibly with a rotational type of motion. The displaced material followed a thin path downslope hitting the road and ending in the fjord. From the pictures, the displaced material looks to have been fully saturated, and transported with a surcharge of water. The material has covered/shaved some vegetation. The vegetation is observed as dense and green in the pictures. The road authorities report a volume of the displaced mass to be larger than 1000 m^3.

Satellite data is available close to the date of occurrence. The datasets are acquired 12 days before the event, and one day after the event. The post-event data has some scattered clouds, possibly influencing the lighting conditions in the color composite images. Revisit satellite data from 2016 is available, with good lighting conditions, and the landslide scar still detectable.

The weather conditions in the area were wet as previously indicated, in accordance with the data below. Snowmelt, precipitation and temperature time series are shown in figure C.4. Accumulated snowmelt and precipitation for the 7 preceding days are shown in figure C.5. The time series is obtained from www.xgeo.no, with data provided from NVE and met.no. The spatial reference is given in UTM 33N coordinates in the figures.

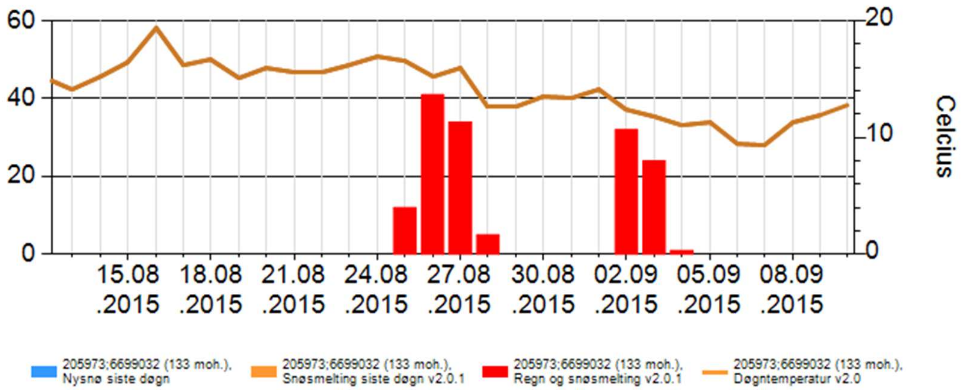

Figure C.4 - Meteorological conditions in the Lindelia area. (Screenshot from xgeo.no, captured 08.04.18)

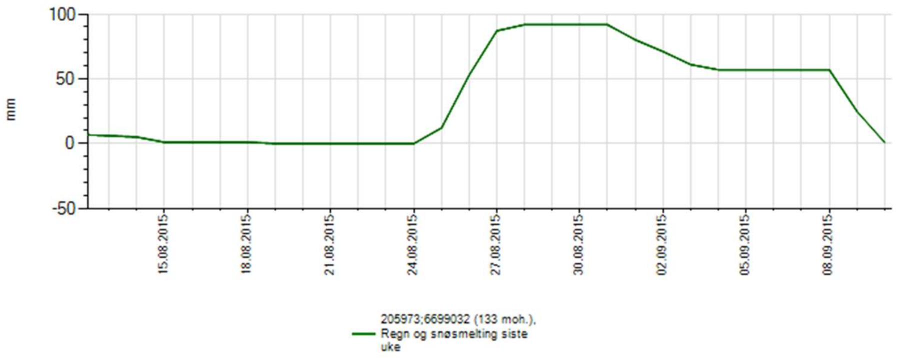

Figure C.5 - Weekly snowmelt & precipitation in the Lindelia area. (Screenshot from xgeo.no, captured 08.04.18)

The slope is facing west and is moderately steep. As seen in the figure below, the upper part of the landslide is inclined with 10-15 degrees, before it steepens downslope.

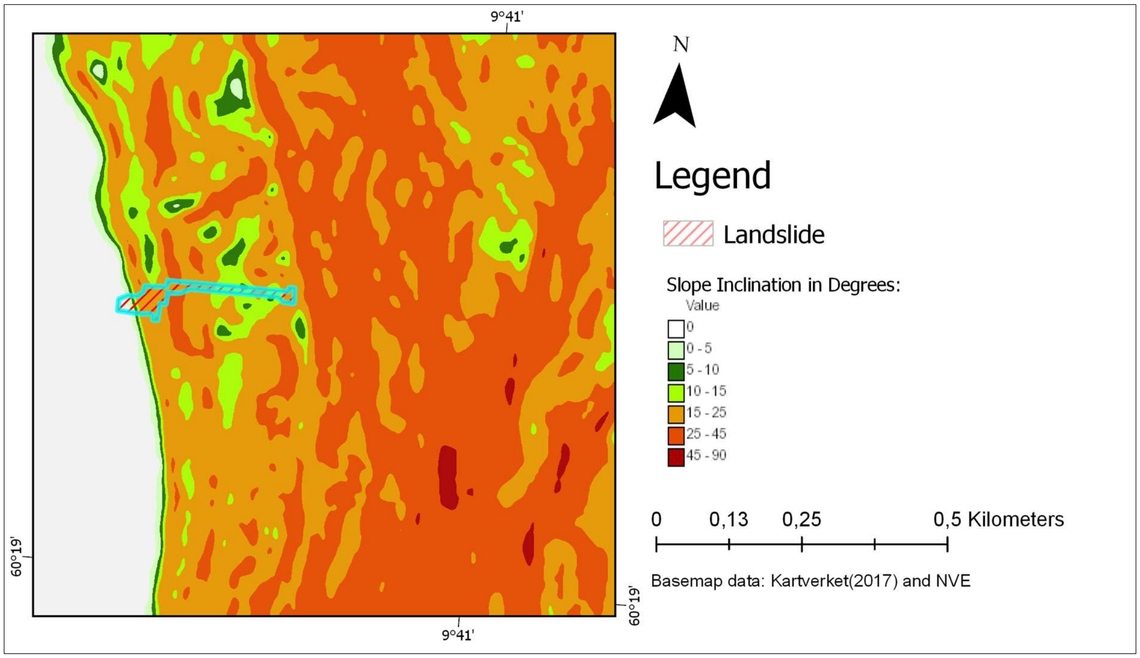

Figure C.6 – Inclination, Lindelia

The soil cover in the area is dominated by moraine material. The slope is classified as a continuous cover of till, very thick in places. The geological conditions in the area are predominantly characterized by banded gneiss. An area along the fjord, where the landslide occurred is classified as *augen gneiss*, *granite* or *foliated granite*.

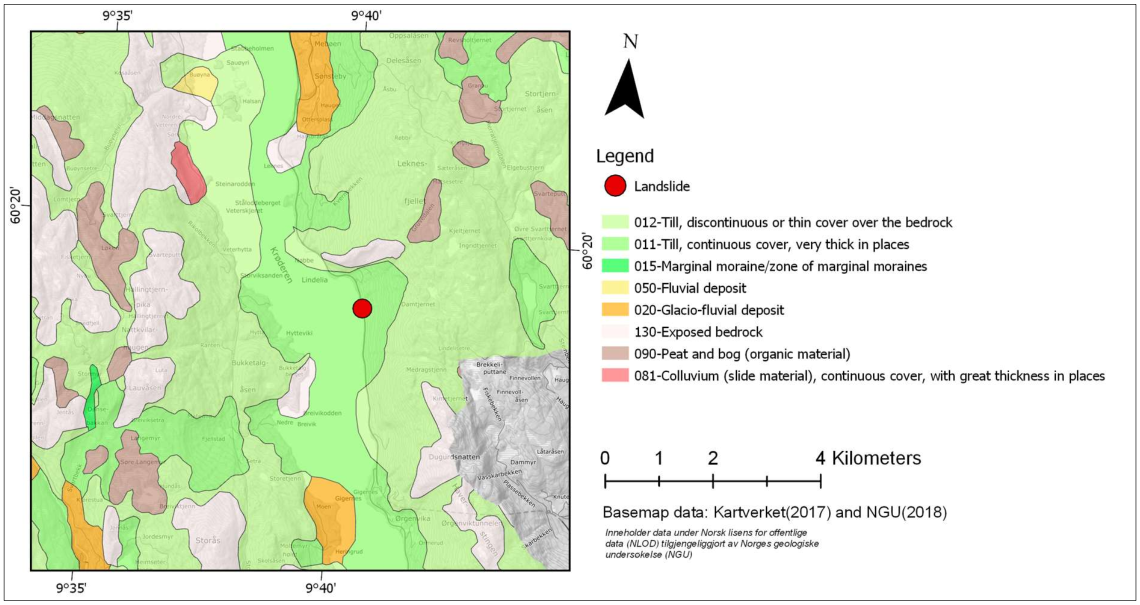

Figure C.7 - Quaternary geology, Lindelia

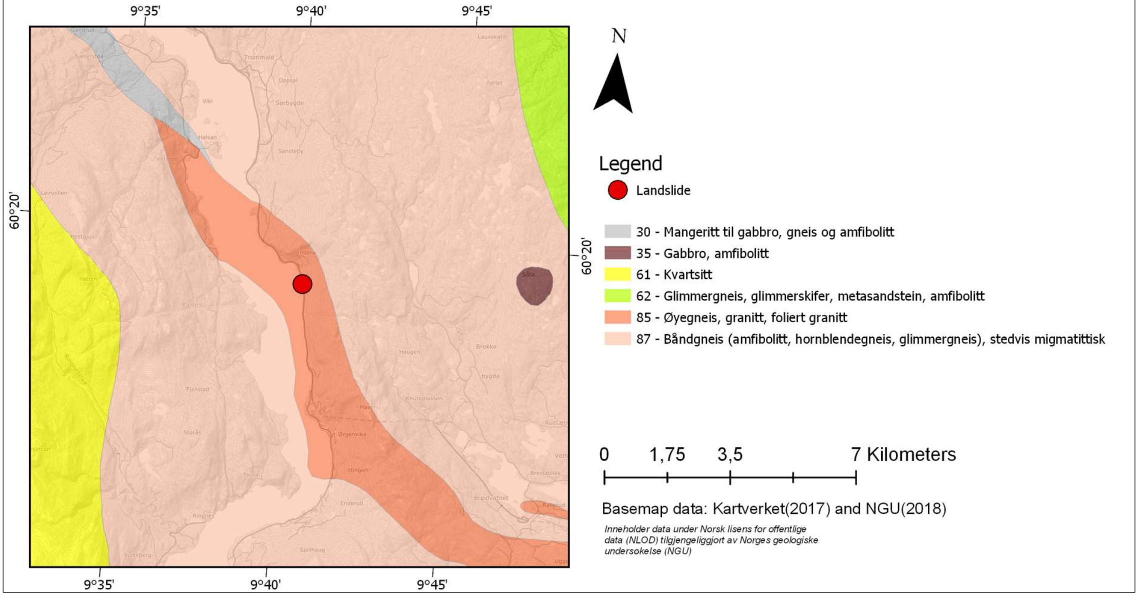

Figure C.8 –Geology, Lindelia

The geometry of landslide scar is compound. The area of initiation has a spoon shaped geometry, before following a possible existing stream, eventually accumulating in a small fan close to the fjord. The size and area of the landslide scar are shown below, calculated from the polygons and lines shown in the figures below in a GIS-system.

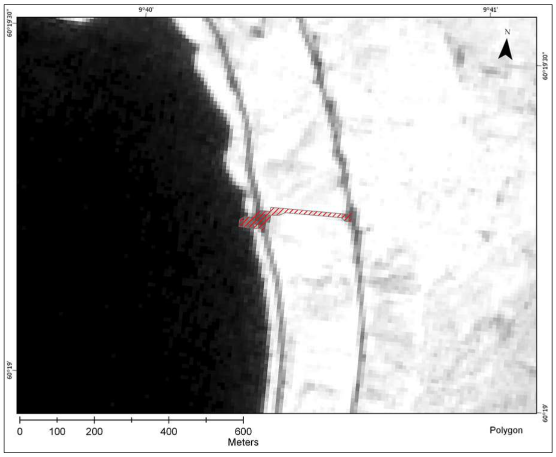

Figure C.9 – Polygon feature, Lindelia

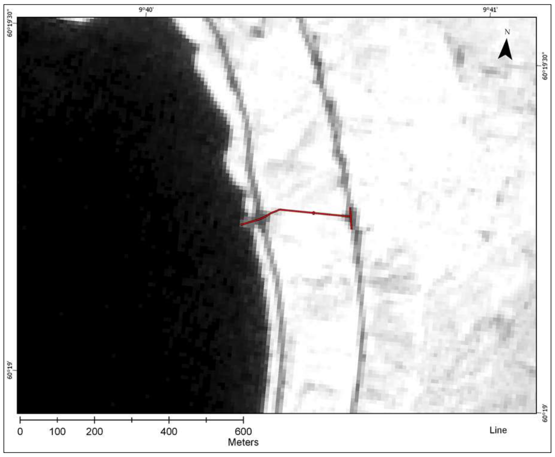

Figure C.10 – Line features, Lindelia

Geometry of landslide

Area of polygon	5 908	m^2	*(1)*
Perimeter of polygon	735	m	*(2)*
Length of centerline	305	m	*(3)*
Length of wide line	60	m	*(4)*
Length of narrow line	10	m	*(5)*
Area/Perimeter	8.0		*(1) / (2)*
Length/Widest width	5.1		*(3) / (4)*
Length/Narrowest width	30.5		*(4) / (5)*

C.1.2 Event 2 – Hunnedalen

Type	Debris flow			
Date	02.06.2016			
Area	Gjesdal, Rogaland			
Ref. ETRS89, UTM 33N	E: 4400	N: 6551095		
S2-data acquisition dates	Previsit:	Pre event:	Post event:	Revisit:
	-	24.05.2016	10.06.2016	28.06.2017

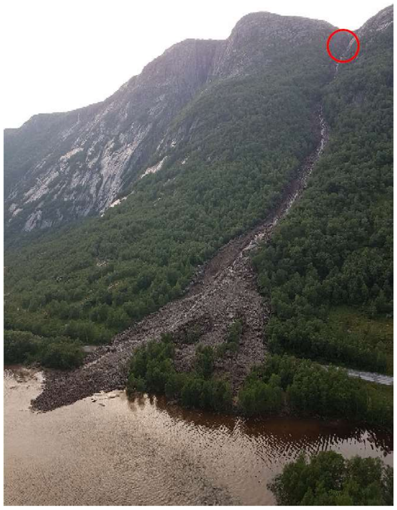

Figure C.11 - Overview of debris flow. Photo from (Rese, 2016), with permission.

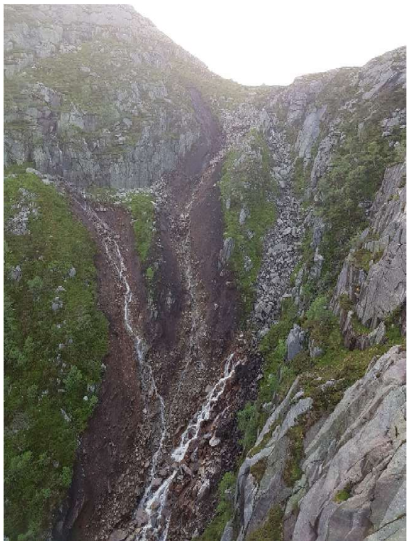

Figure C.12 - Area of initiation. Photo from (Rese, 2016), with permission.

Figure C.13 - Natural color composite, Hunnedalen post-event data

The landslide is classified as a debris flow in regObs. *It* occurred in early summer, in the south-western part of Norway. A motor highway is situated at the foot of the slope. The slide was initiated at the top of the slope, before following a gully, entraining material downslope. The material accumulated in a large debris fan at the foot of the slope, covering the road with displaced material over 2 meters thick as reported by the authorities.

Satellite data is acquired close to the date of occurrence. The pre-event data is acquired 9 days before the debris flow, and the post-event data is acquired 8 days after the debris flow. There is little seasonal variation in the two images, but some snow melt. A small cloud is covering parts of the mid-part of the landslide scar, and will possibly influence the spectral reflectance in this area.

Short periods of intense precipitation is reported at the time of the debris flow (Rese, 2016). Accumulated rain and snowmelt from the 7-days prior to the event is shown below, and has reached the 2-300 mm range in some areas close to the debris flow, as illustrated in figure C.14.

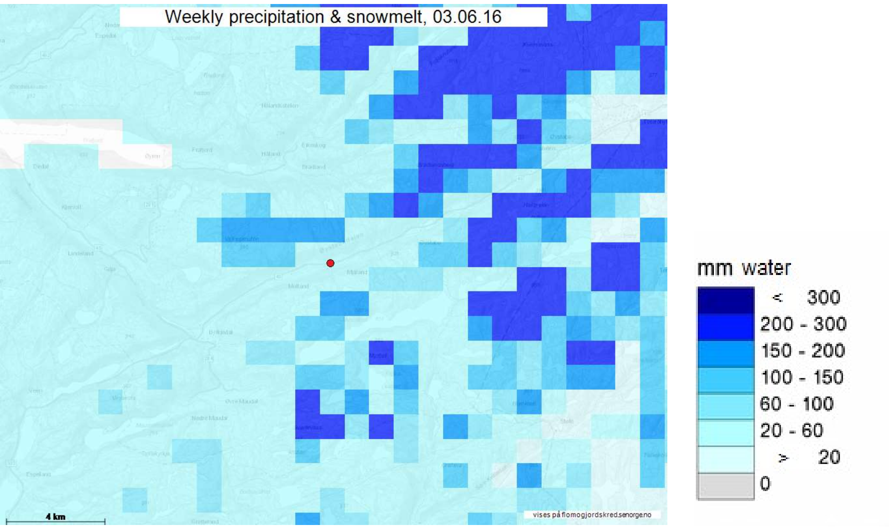

Figure C.14 - Combined precipitation and snowmelt for landslide area (Screenshot from xgeo.no, captured 11.04.2018)

The conditions in the area are described by (Rese, 2016): The slope is facing south-southeast. The major part of the slope inclines around 30-40°, whilst the inclination flattens out to around 20° towards the foot of the slope. The inclination characteristics can be seen in figure C.15.

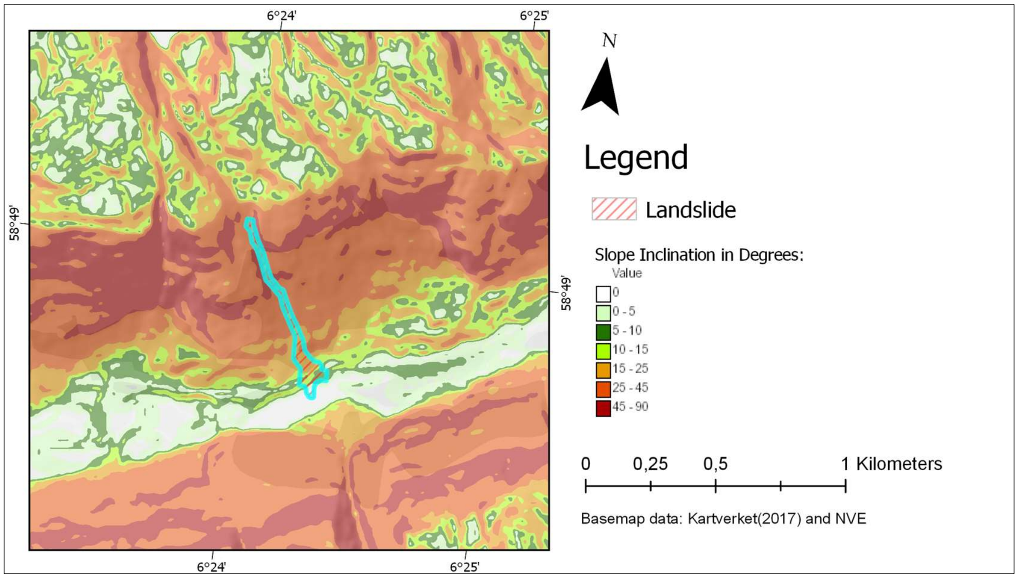

Figure C.15 – Inclination, Hunnedalen

The quaternary geology in the area is predominantly exposed rock. Some glaciofluvial and fluvial deposits are located at valley floors, as well as deposits colluvium, which indicates prior landslide activity in the area. The exact location of the Hunndalen debris flow is classified as exposed bedrock. Deposits of colluvium and a glacio-fluvial deposit are situated at the foot of the slope, as indicated in the figure below.

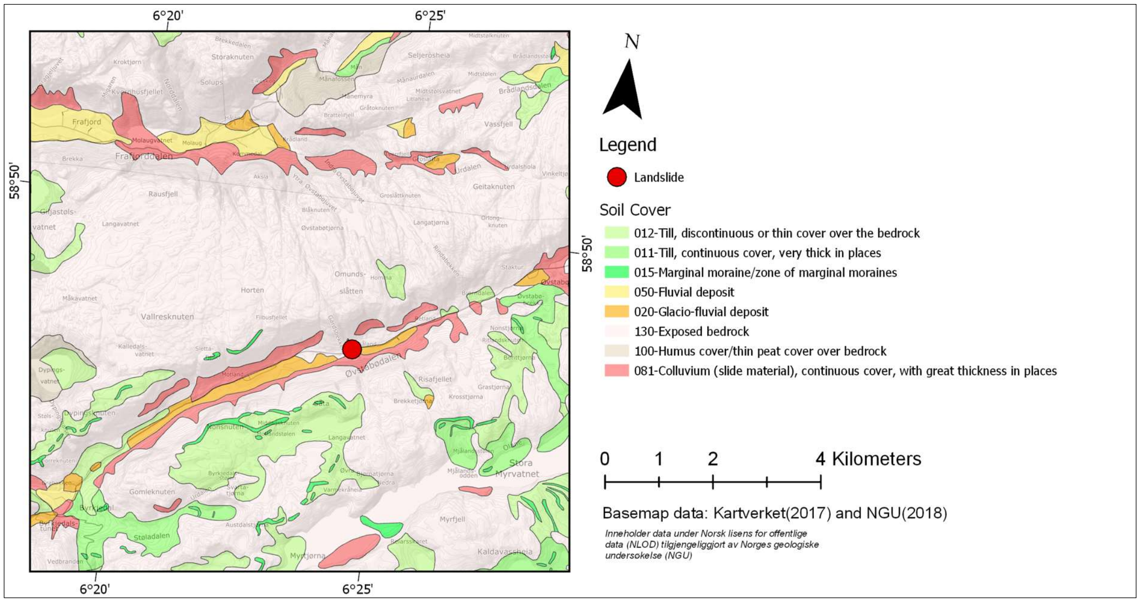

Figure C.16 - Quaternary geology, Hunnedalen

The geological setting of the area is predominated by dioritic to granitic gneiss.

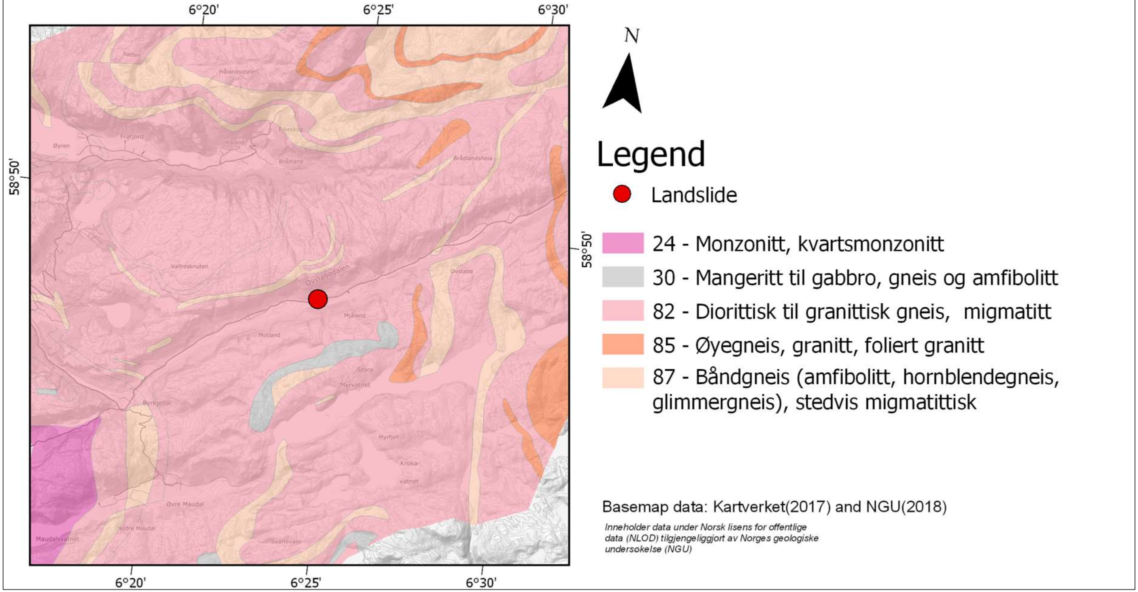

Figure C.17 – Geology, Hunnedalen

The geometry of the landslide is that of a characteristic channelized debris flow. The material has followed a gully stream, before spreading out in a debris fan at the foot of the slope.

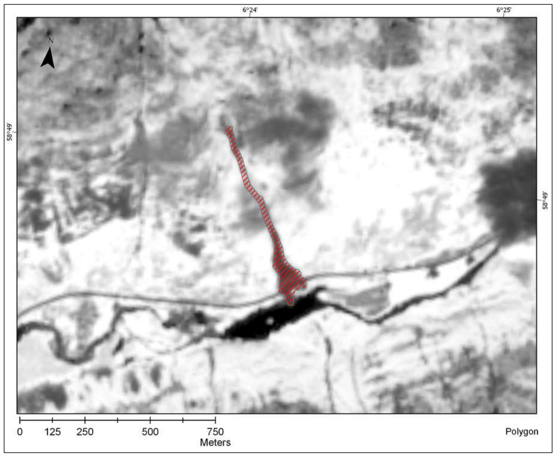

Figure C.18 - Polygon, Hunnedalen

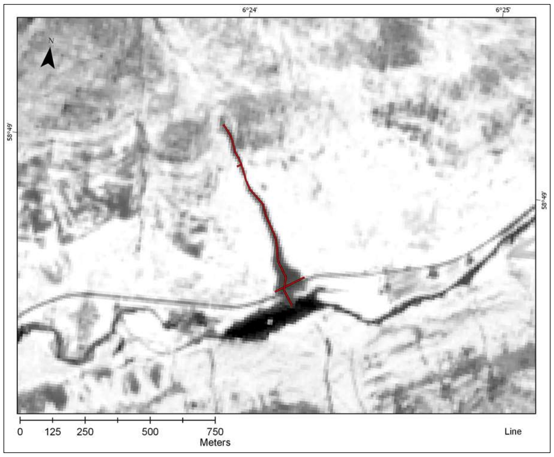

Figure C.19 - Line sections, Hunnedalen

Geometry of landslide

Area of polygon	24 823	m^2	*(1)*
Perimeter of polygon	1 623	m	*(2)*
Length of centerline	761	m	*(3)*
Length of wide line	128	m	*(4)*
Length of narrow line	23	m	*(5)*
Area/Perimeter	15.3		*(1) / (2)*
Length/Widest width	5.9		*(3) / (4)*
Length/Narrowest width	33.1		*(4) / (5)*

C.1.3 Event 3 – Kommedal

Type	Debris flow			
Date	02.06.2016			
Area	Gjesdal, Rogaland			
Ref. ETRS89, UTM 33N	E: 2071	N: 6554655		
S2-data acquisition dates	Previsit:	Pre event:	Post event:	Revisit:
	-	24.05.2016	10.06.2016	28.06.2017

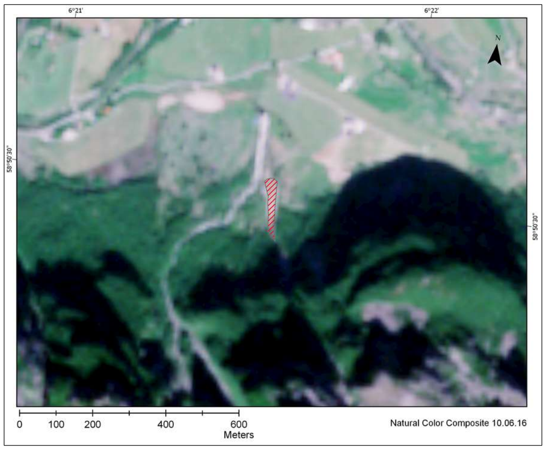

Figure C.20 - Polygon of the Kommdalen debris flow

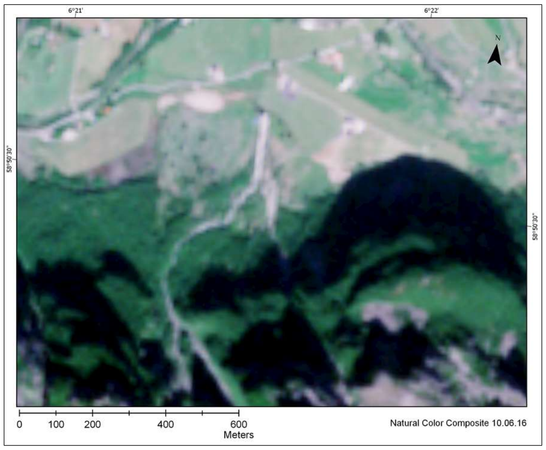

Figure C.21 - Natural color composite of Kommedalen, post-event data

The landslide occurred at the same time, and in the same area as event no. 2 – *The Hunnedalen debris flow*. The event is classified as a debris flow in regObs but poorly documented. It is briefly described in two news reports (Links can be found in regObs-registration 99185): *"A landslide occurred on the other side of the mountain (of the Hunndalen debris flow), 150 meters long x 30 meters wide."* And *"On the Frafjord side of the mountain, large amounts of rock and sand slid down..."*

The landslide is detected in the same satellite data as for the Hunnedalen debris flow. The lighting conditions are generally good, but some shade from surrounding hillsides affect the area of the landslide.

The meteorological conditions for the Kommedal-event are the same as for the Hunndalen debris flow. The kommedal event is marked in red in figure C.22 and the Hunnedalen event in gray.

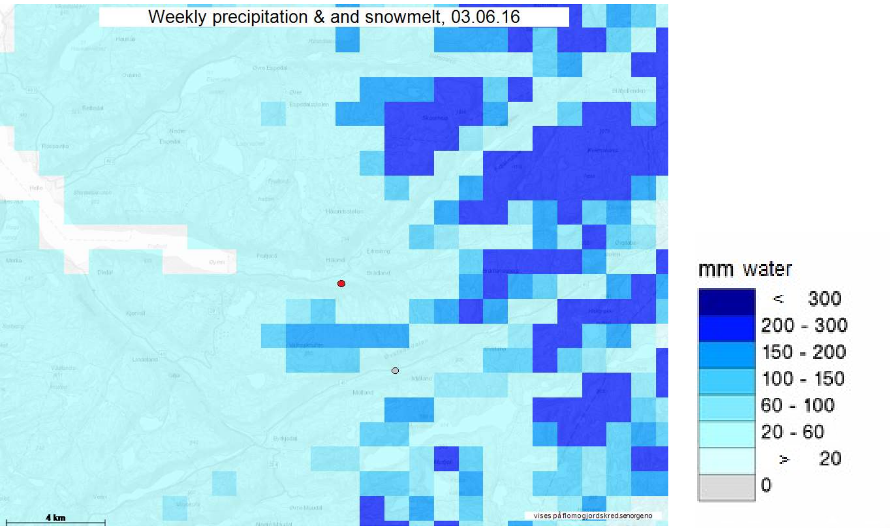

Figure C.22 - Combined precipitation and snowmelt for the landslide area (Screenshot from xgeo.no, captured 12.04.2018)

The event occurred on a steep south-facing slope, as illustrated in figure x.x.

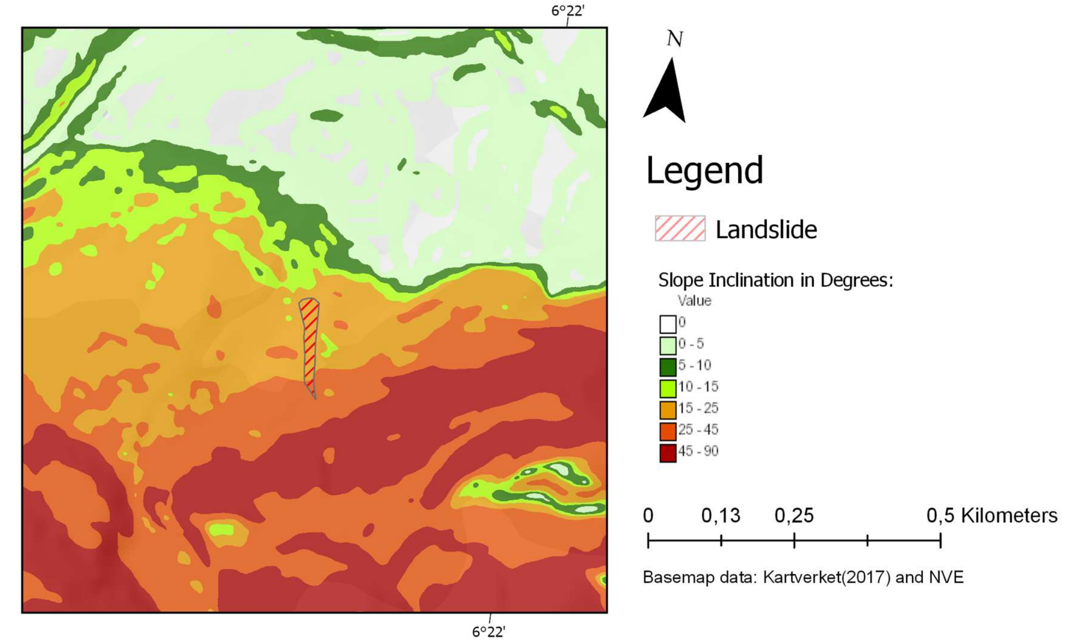

Figure C.23 - Slope inclination, Kommedal

The quaternary geology is similar to that of the Hunnedalen side of the mountain. Colluvium deposits can be found at the foot of the slope, suggesting previous landslide activity. Fluvial deposits can be found on the valley floors, and close to the debris flow. The news article reports "sand"-material, possibly originating from the fluvial deposit.

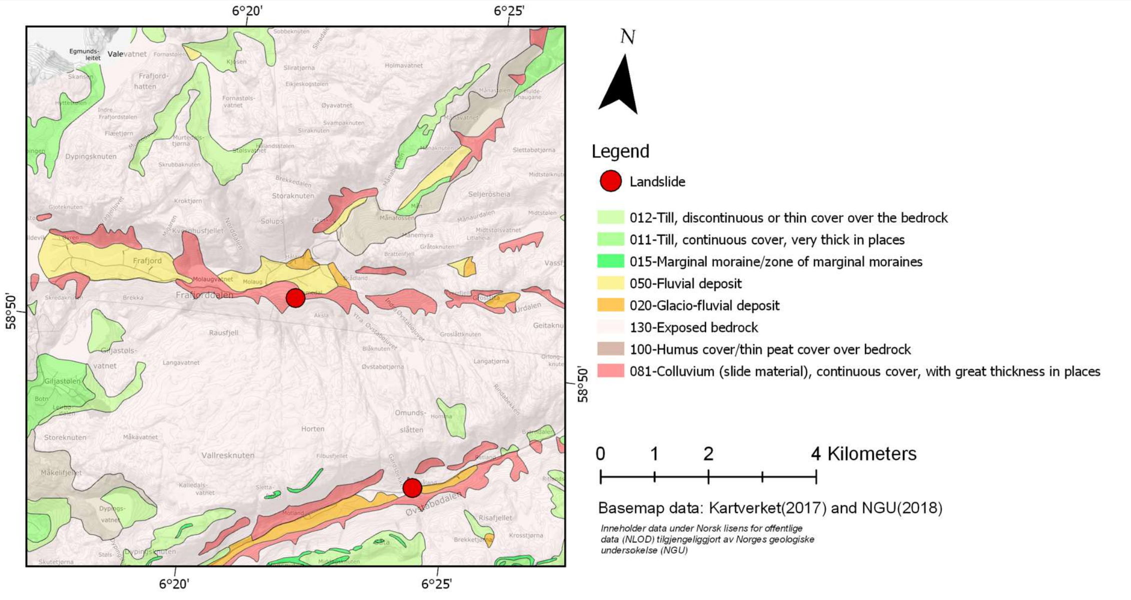

Figure C.24 – Quaternary, Kommedal (uppermost red circle)

The geological setting of the area is predominated by dioritic to granitic gneiss.

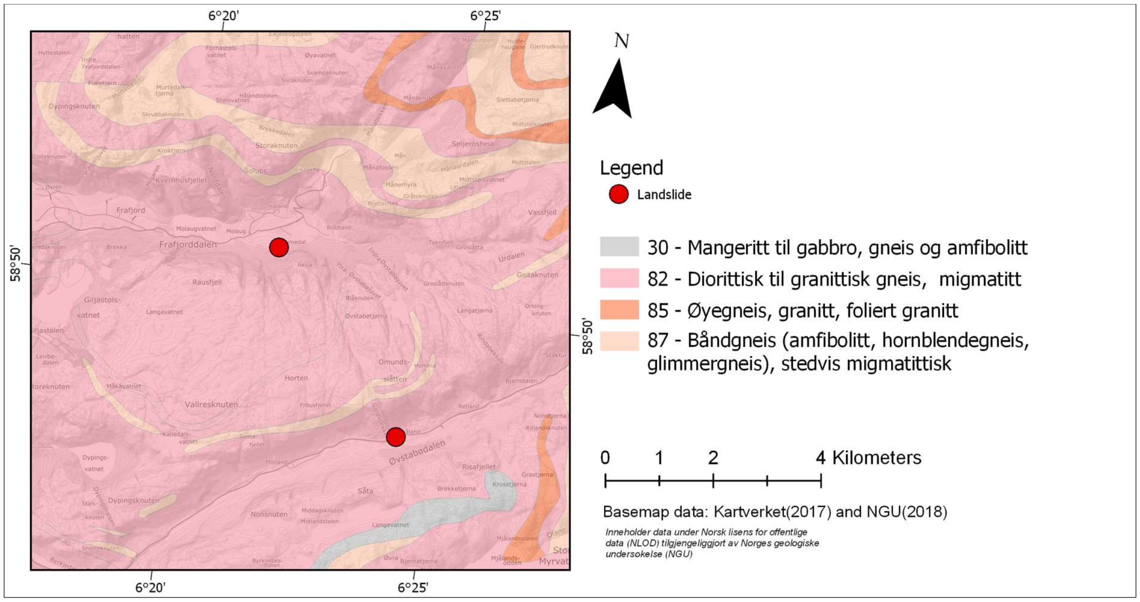

Figure C.25 – Geology, Kommedal (uppermost red circle)

The size and area of the accumulated material are described below. The detected material is possibly the debris fan, which has been transported from a gully stream along the steeper part of the slope.

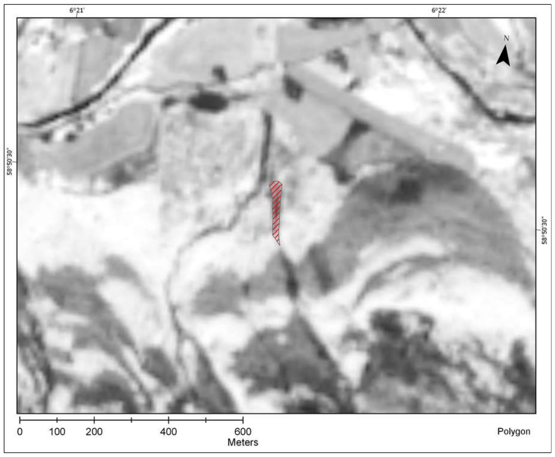

Figure C.26 - Polygon, Kommedal

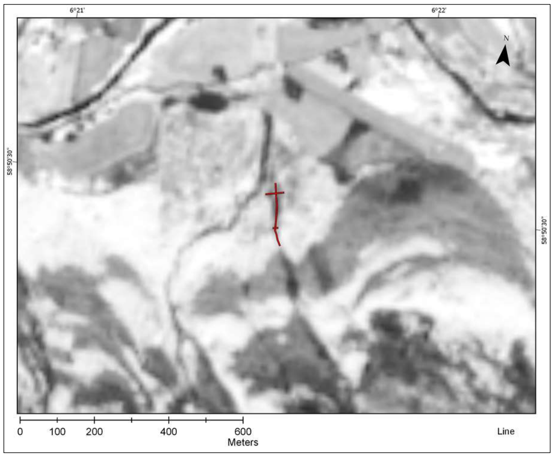

Figure C.27 - Line sections, Kommedal

Geometry of landslide

Area of polygon	3 332	m^2	*(1)*
Perimeter of polygon	379	m	*(2)*
Length of centerline	172	m	*(3)*
Length of wide line	51	m	*(4)*
Length of narrow line	16	m	*(5)*
Area/Perimeter	8.8		*(1) / (2)*
Length/Widest width	2.2		*(3) / (4)*
Length/Narrowest width	23.7		*(4) / (5)*

C.1.4 Event 4 – Øksland

Type	Debris avalanche			
Date	03.09.2016			
Area	Gaular, Sogn og Fjordane			
Ref. ETRS89, UTM 33N	E: 9234	N: 6825644		
S2-data acquisition dates	Previsit:	Pre event:	Post event:	Revisit:
	-	06.06.2016	04.09.2016	23.07.2017

Figure C.28 – Debris avalanche, Øksland. Photo: Statens Vegvesen, from (Statens Vegvesen, 2016)

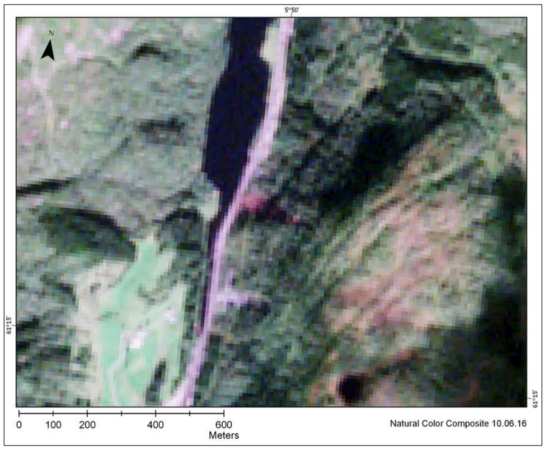

Figure C.29 - Natural color composite. Post-event data, Øksland

Landslide classified as debris avalanche in regObs. Little information is given regarding the debris avalance. It occurred at the start of autumn, and from the pictures, it looks to have removed the vegetation from the slope. The slope is situated next to a motor highway.

Satellite data is available 89 days before the date of occurrence. Post-event data is available one day after the event. There is some seasonal difference between the two datasets, with respect to vegetation greenness and length of shadows. Both datasets have scattered clouds close to the landslide-area.

Weather-data from xgeo suggest wet condtions leading up to the date of occurrence. A snowmelt, precipitation and temperature time series are shown in figure C.30. Accumulated snowmelt and precipitation for the 7 preceding days are shown in figure C.31. The time series is obtained from www.xgeo.no, with data provided from NVE and met.no. The spatial reference is given in UTM 33N coordinates in the figures.

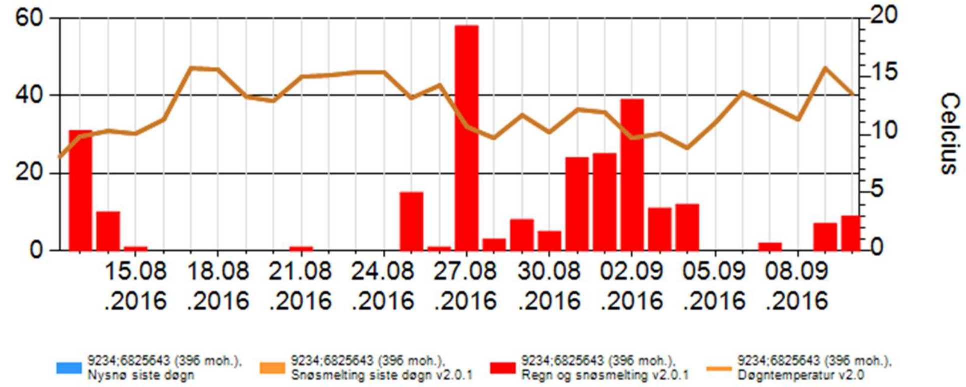

Figure C.30 - Meteorological conditions in the Øksland area. (Screenshot from xgeo.no, captured 12.04.18)

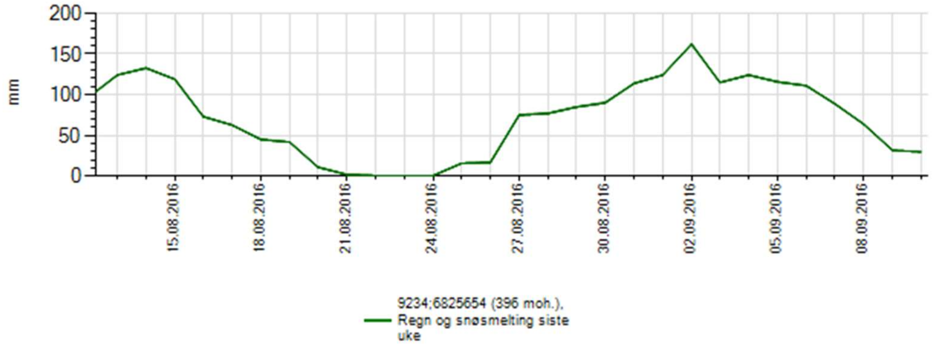

Figure C.31 - Weekly snowmelt & precipitation in the Øksland area. (Screenshot from xgeo.no, captured 12.04.18)

The landslide occurred in a west-facing slope, with an inclination between 15-25 degrees.

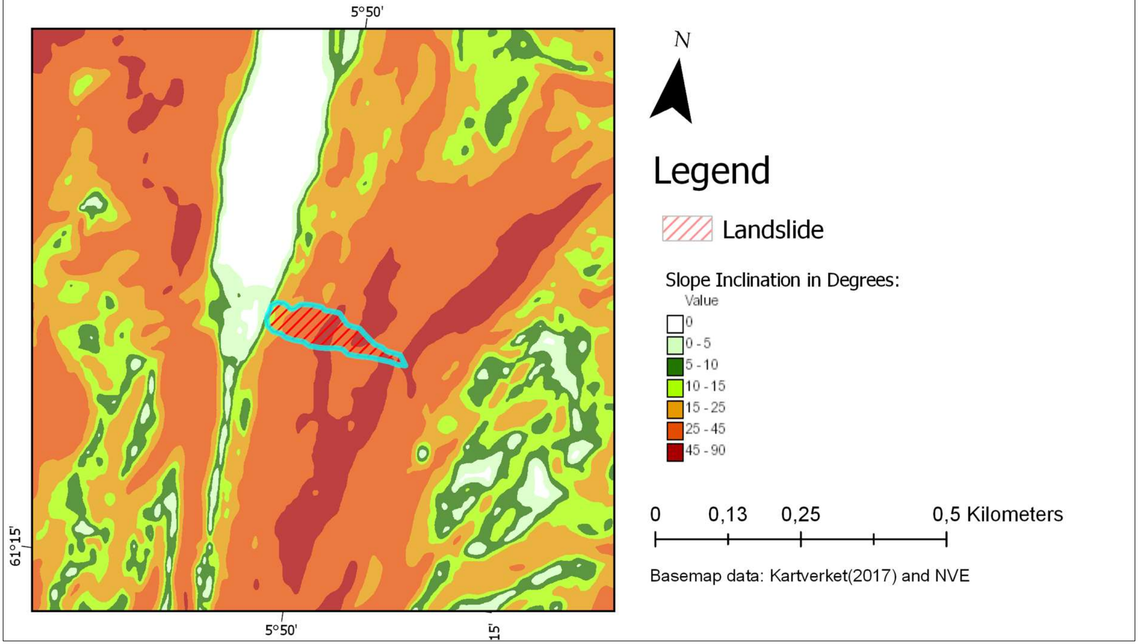

Figure C.32 - Inclination, Øksland

The soil cover in the area is predominated by exposed bedrock and moraine material. There is also deposits of weathered material in the area. The location of the debris avalanche is classified as till, continuous cover, thick in places.

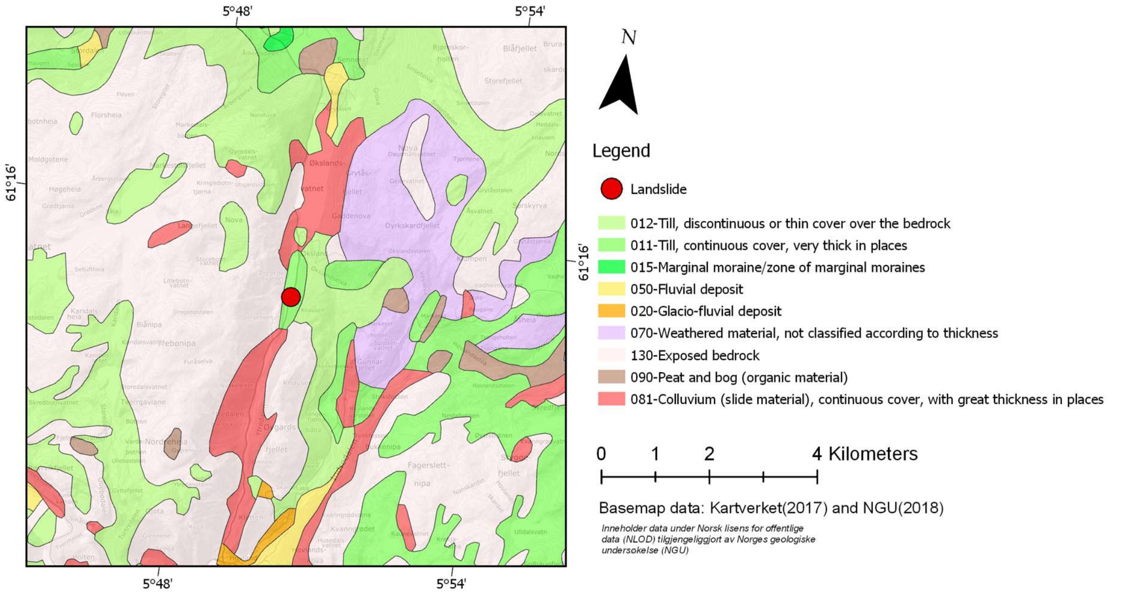

Figure C.33 - Quaternary geology, Øksland

The geological setting of the area is predominated by dioritic to granitic gneiss.

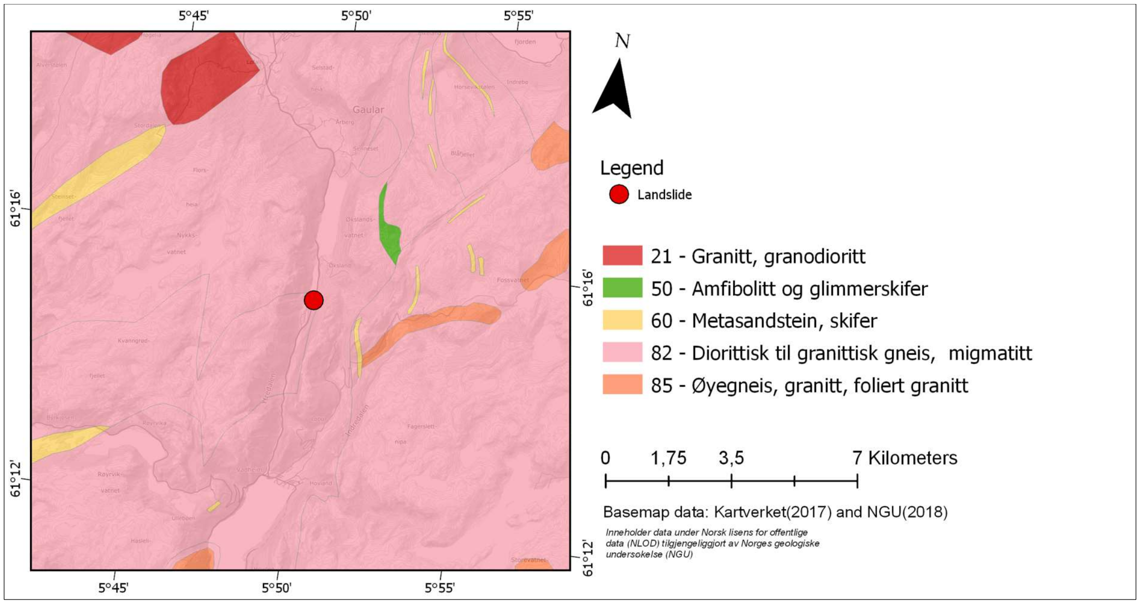

Figure C.34 - Geology of the Øksland area.

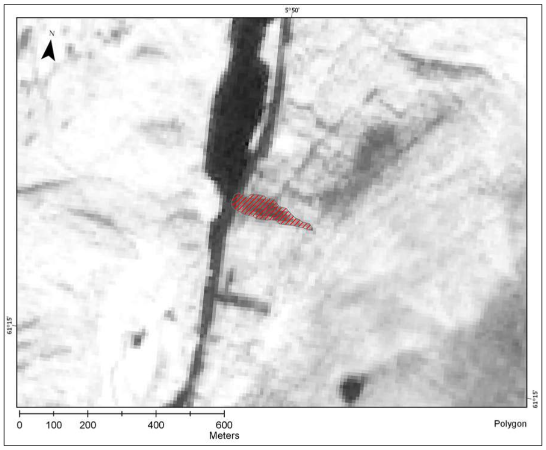

Figure C.35 - Polygon, Øksland

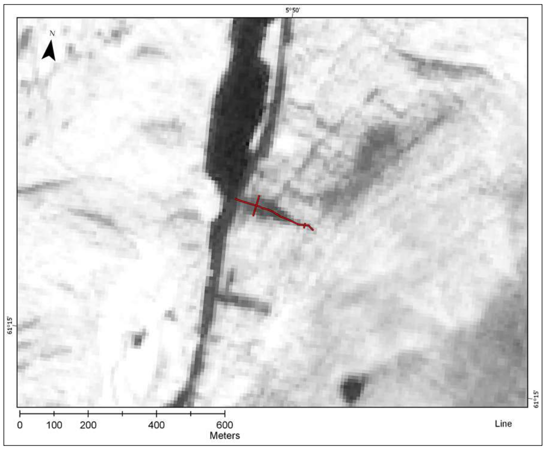

Figure C.36 - Line sections, Øksland

Geometry of landslide

Area of polygon	10 962	m^2	*(1)*
Perimeter of polygon	569	m	*(2)*
Length of centerline	253	m	*(3)*
Length of wide line	65	m	*(4)*
Length of narrow line	17	m	*(5)*

Area/Perimeter	19.3	*(1) / (2)*
Length/Widest width	3.9	*(3) / (4)*
Length/Narrowest width	14.9	*(4) / (5)*

C.1.5 Event 5 and 9 - Slettafossen and Rødstøl

<table>
<tr><td>Type</td><td colspan="4">Debris avalanche</td></tr>
<tr><td>Date</td><td colspan="4">19.05.2017</td></tr>
<tr><td>Area</td><td colspan="4">Rauma, Møre og Romsdal</td></tr>
<tr><td>Ref. ETRS89, UTM 33N</td><td>E: 141786</td><td colspan="3">N: 6929661</td></tr>
<tr><td rowspan="2">S2-data acquisition dates</td><td>Previsit:</td><td>Pre event:</td><td>Post event:</td><td>Revisit:</td></tr>
<tr><td>19.08.2016</td><td>12.05.2017</td><td>28.07.2017</td><td>-</td></tr>
<tr><td colspan="5">


Figure C.37 – Debris avalanche, Slettafossen. Photo: Leif Johnny Olestad/Åndalsnes Avis. From (NVE, 2017c), with permission.

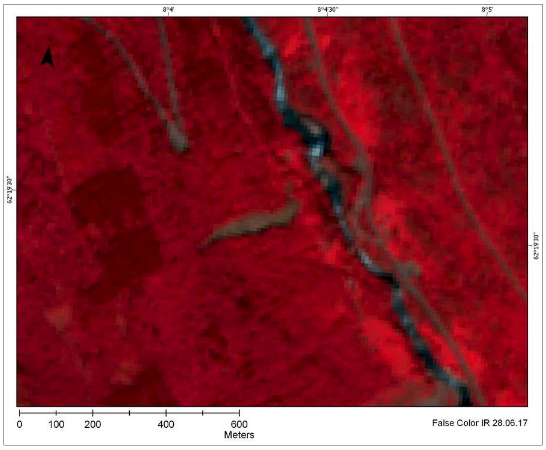

Figure C.38 - False color composite. Post-event data, Slettafossen
</td></tr>
</table>

<table>
<tr><td>Type</td><td colspan="4">Debris avalanche</td></tr>
<tr><td>Date</td><td colspan="4">09.06.2011</td></tr>
<tr><td>Area</td><td colspan="4">Rauma, Møre og Romsdal</td></tr>
<tr><td>Ref. ETRS89, UTM 33N</td><td>E: 142097</td><td colspan="3">N: 6929113</td></tr>
<tr><td rowspan="2">S2-data acquisition dates</td><td>Previsit:</td><td>Pre event:</td><td>Post event:</td><td>Revisit:</td></tr>
<tr><td>-</td><td>-</td><td>28.07.2017</td><td>-</td></tr>
<tr><td colspan="5">


Figure C.39 – Debris avalanche, Rødstøl. From (Åndalsnes Avis, 2011), Photo by L. Smisethjell

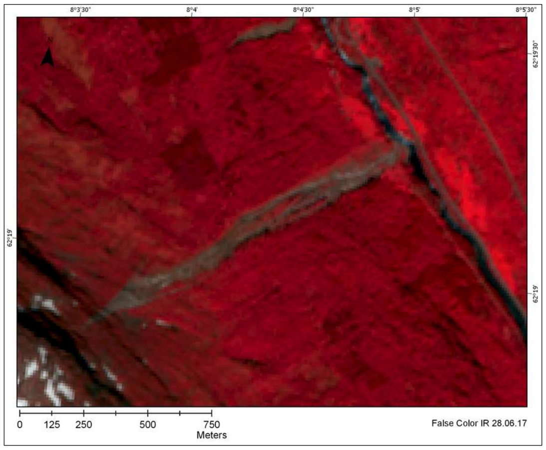

Figure C.40 - False color composite. Post-event data, Rødstøl
</td></tr>
</table>

Two events classified as debris avalanches in regObs. The two events occurred on the same slope, with approximately 6 years in between. The Rødstøl debris avalanche occurred in early summer 2011, and the Slettafossen debris avalanche occurred in spring 2017, roughly 600 meters north of the Rødstøl event.

Satellite data is available from 7 days prior to the date of occurrence of the Slettafossen debris avalanche. The post-event data is available from 70 days after the date of occurrence. There are large seasonal variations between the two datasets, where the pre-event data has a lot of snow cover. The post-event data has less snow cover and greener vegetation. The Rødstøl event is shown in the post-event data.

The meteorological conditions prior to the Slettafossen and Rødstøl event can be seen below.

Figure C.41 - Weekly precipitation and snowmelt time series for the Slettafossen excact location. (Screenshot from xgeo.no, captured 13.04.2018)

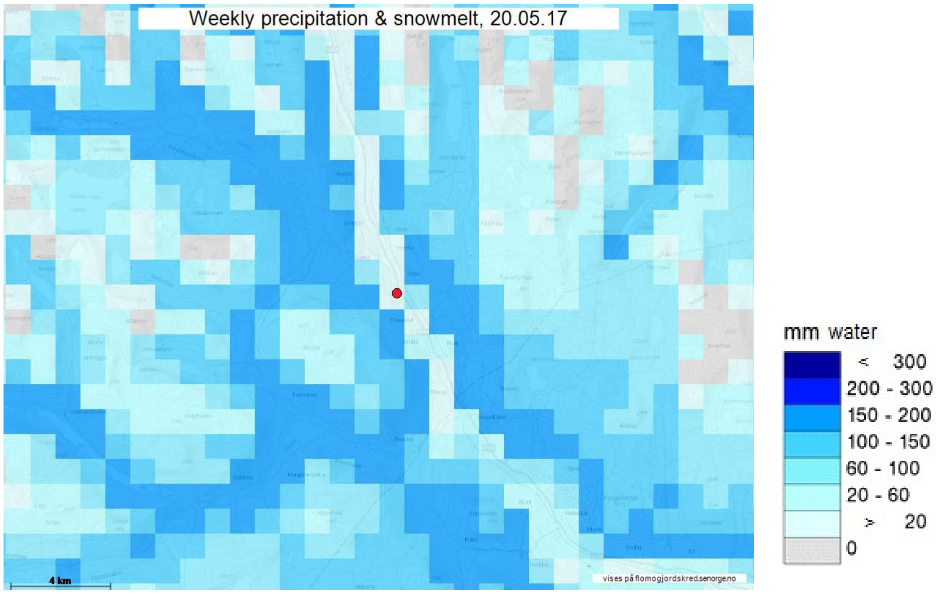

Figure C.42 - Combined precipitation and snowmelt for Slettafossen area (Screenshot from xgeo.no, captured 13.04.2018)

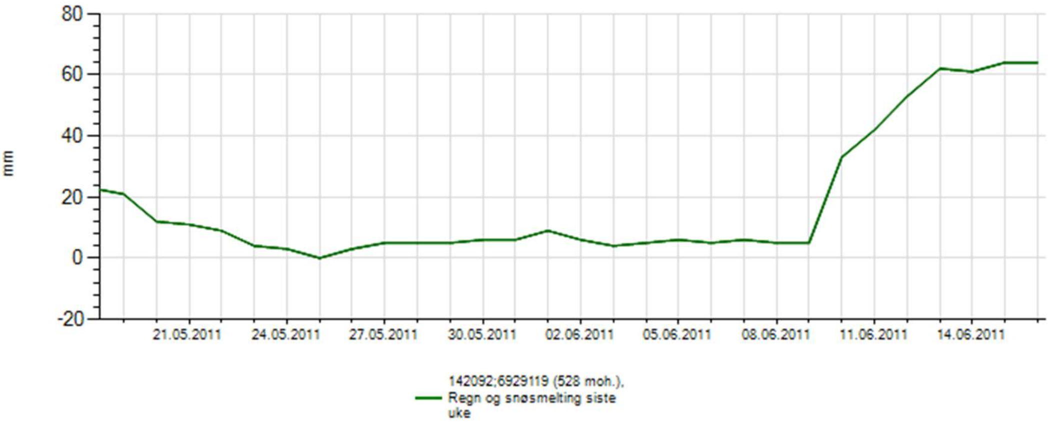

Figure C.43 - Weekly precipitation and snowmelt time series for the Rødstøl excact location. (Screenshot from xgeo.no, captured 13.04.2018)

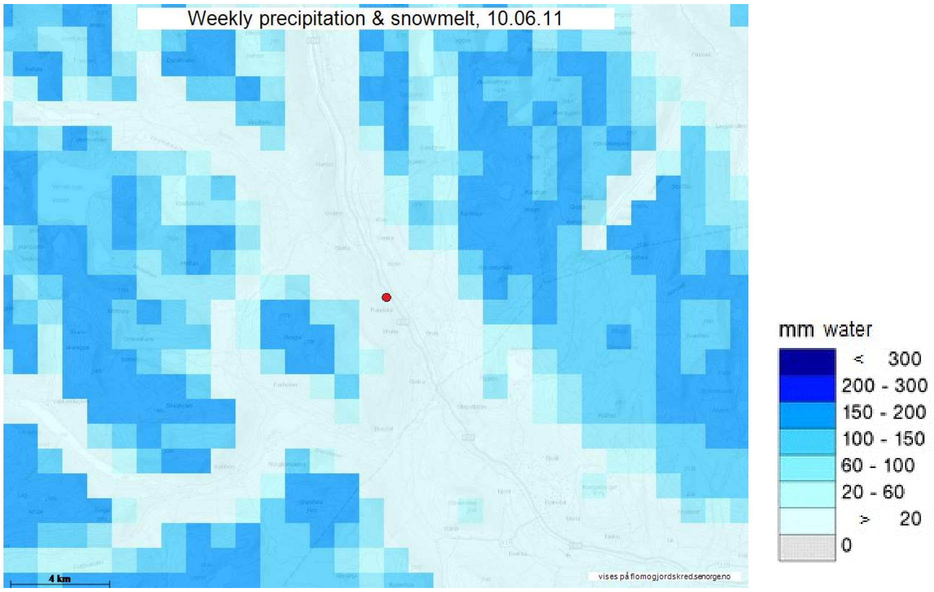

Figure C.44 - Combined precipitation and snowmelt for Slettafoss/Rødstøl area (Screenshot from xgeo.no, captured 13.04.2018)

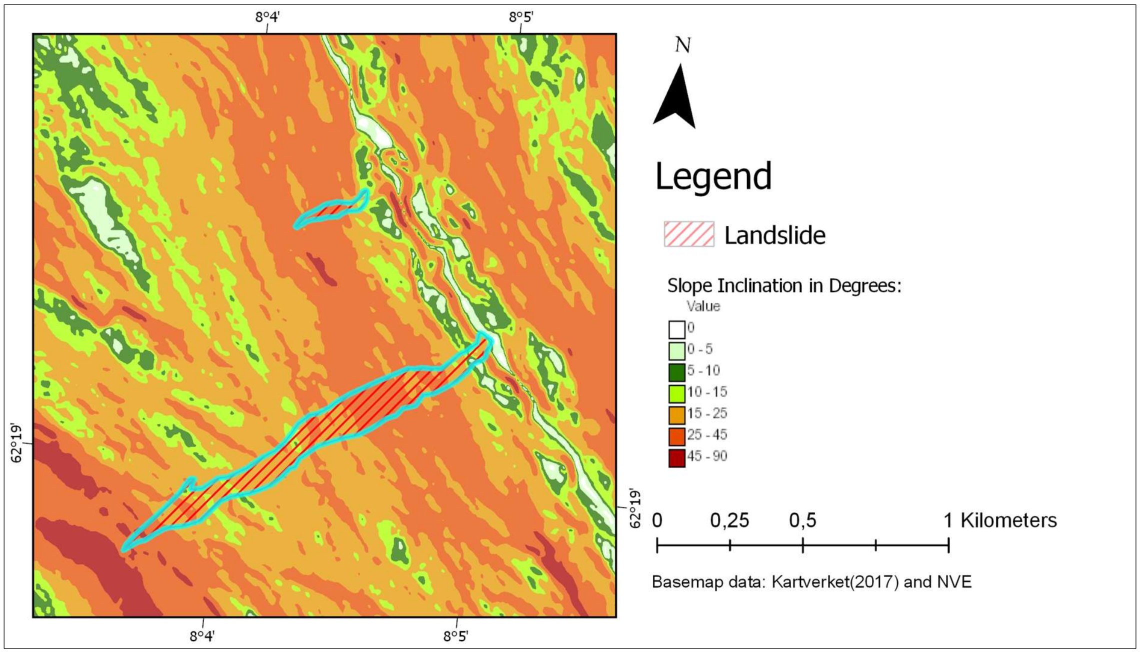

Figure C.45 – Inclination, Slettafossen and Rødstøl

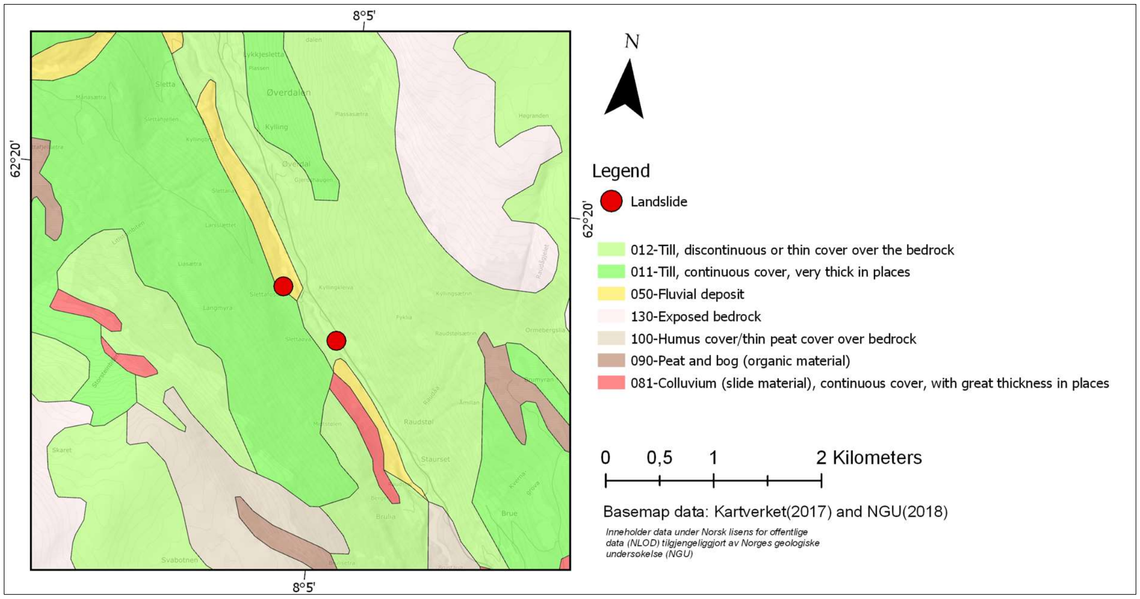

Figure C.46 - Quaternary geology, Slettafossen, and Rødstøl

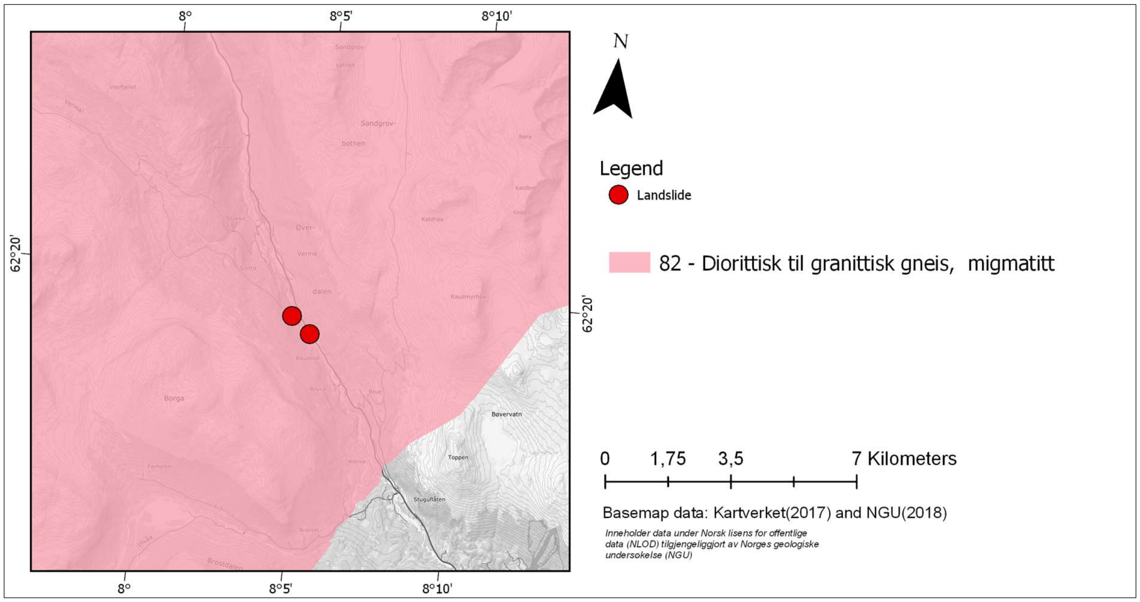

Figure C.47 – Geology, Slettafossen, and Rødstøl

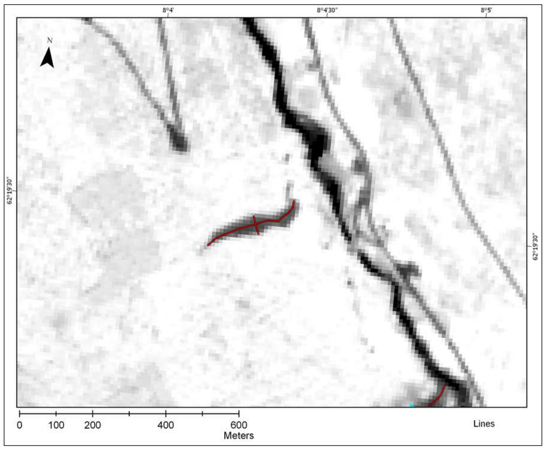

Figure C.48 – Line sections, Slettafossen

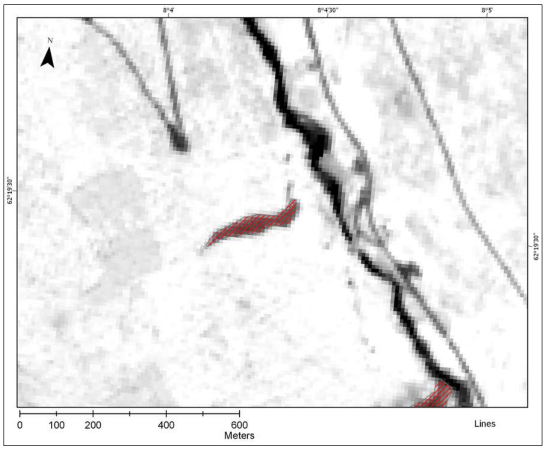

Figure C.49 - Polygon, Slettafossen

<u>The geometry of the Slettafossen landslide</u>

Area of polygon	8 764	m^2	*(1)*
Perimeter of polygon	607	m	*(2)*
Length of centerline	285	m	*(3)*
Length of wide line	55	m	*(4)*
Length of narrow line	33	m	*(5)*
Area/Perimeter	14.4		*(1) / (2)*
Length/Widest width	5.2		*(3) / (4)*
Length/Narrowest width	1.7		*(4) / (5)*

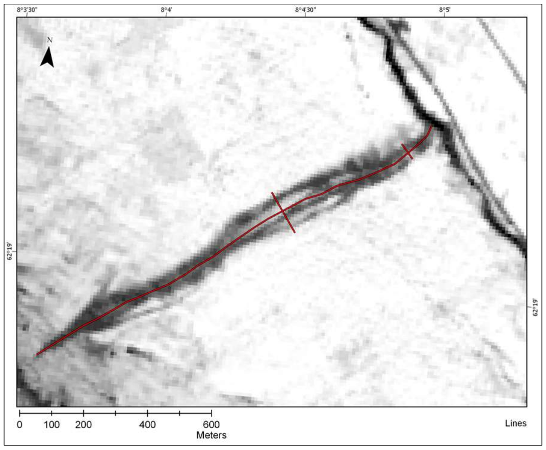

Figure C.50 – Line sections, Rødstøl

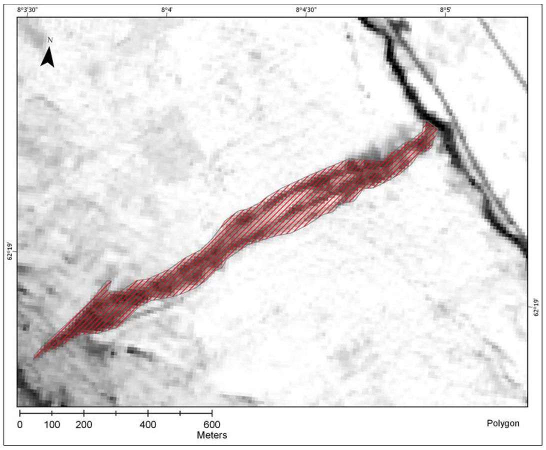

Figure C.51 - Polygon, Rødstøl

The geometry of Rødstøl landslide

Area of polygon	128 414	m^2	*(1)*
Perimeter of polygon	3 126	m	*(2)*
Length of centerline	1 441	m	*(3)*
Length of wide line	146	m	*(4)*
Length of narrow line	58	m	*(5)*
Area/Perimeter	41.1		*(1) / (2)*
Length/Widest width	9.9		*(3) / (4)*
Length/Narrowest width	24.8		*(4) / (5)*

C.1.6 Event 6 – Kråkagjelet

<table>
<tr><td>Type</td><td colspan="4">Debris flow</td></tr>
<tr><td>Date</td><td colspan="4">19.05.2017</td></tr>
<tr><td>Area</td><td colspan="4">Aurland, Sogn og Fjordane</td></tr>
<tr><td>Ref. ETRS89, UTM 33N</td><td>E: 87781</td><td colspan="3">N: 6772220</td></tr>
<tr><td rowspan="2">S2-data acquisition dates</td><td>Previsit:</td><td>Pre event:</td><td>Post event:</td><td>Revisit:</td></tr>
<tr><td>18.08.15</td><td>06.05.2017</td><td>22.08.2017</td><td>-</td></tr>
<tr><td colspan="5">


Figure C.52 - Picture of the Kråkagjelet debris flow. Photo: Bergens tidende, from (NVE, 2017b).

Figure C.53 - Natural color composite, Kråkagjelet post-event data
</td></tr>
</table>

Landslide classified as debris flow in regObs. There is little information regarding the event. The landslide is mentioned as *"50 meters wide rock avalanche"* in the media (See link in regObs registration 128325). From the figure C.52. the displaced material looks to contain material from the course fractions, as well as fines. The material blocked a popular hiking path.

Pre-event data is acquired 13 days prior to the date of occurrence, and the post-event data is acquired 95 days after the date of occurrence. There are large seasonal variations between the two datasets. Snow cover and early spring conditions predominate the pre-event data, while the post-event data has little snow and green vegetation. The previsit data is acquired with similar conditions as the post-event data.

Meteorological data from the area suggest wet conditions leading up to the debris flow, due to snow melt and precipitation as indicated in the data below. A Precipitation, snowmelt and temperature time series are shown in figure C.54. Accumulated snowmelt and precipitation for the 7 preceding days are shown in figure C.55. The time series is obtained from www.xgeo.no, with data provided from NVE and met.no. The spatial reference is given in UTM 33N coordinates in the figures.

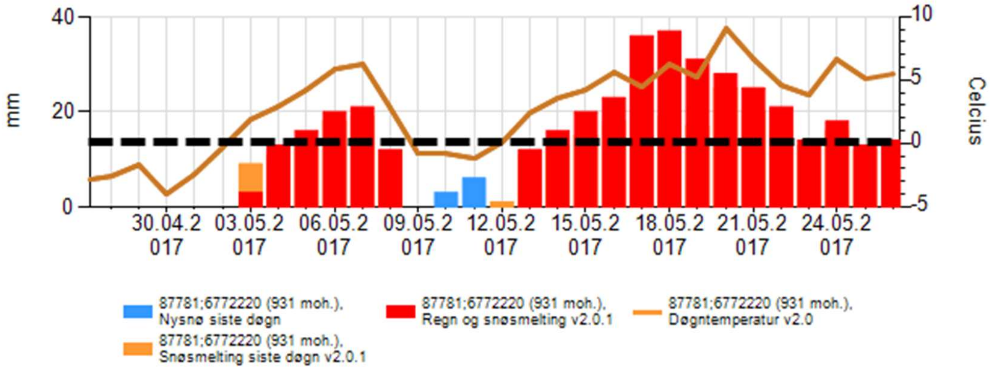

Figure C.54 - Meteorolgical conditions time series in the Kråkagjelet area. (Screenshot from xgeo.no, captured 21.04.18)

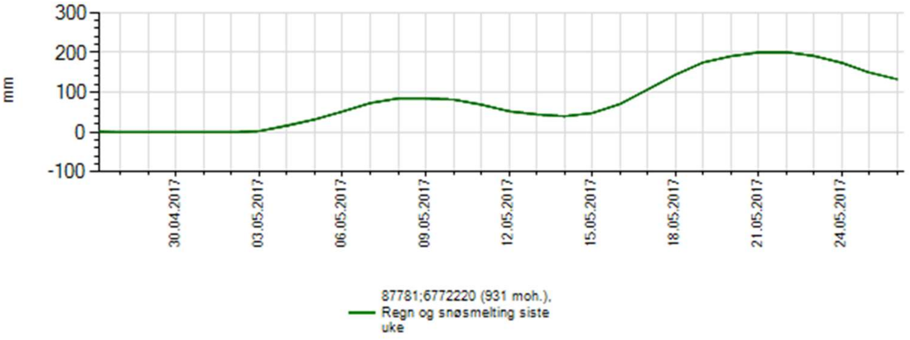

Figure C.55 - Weekly snowmelt & precipitation in the Kråkagjelet area. (Screenshot from xgeo.no, captured 21.04.18)

The debris flow occurred in a steep south-facing slope. A distinct stream gully can be seen in topographic maps of the debris flow location. The slope inclination is shown in the figure below.

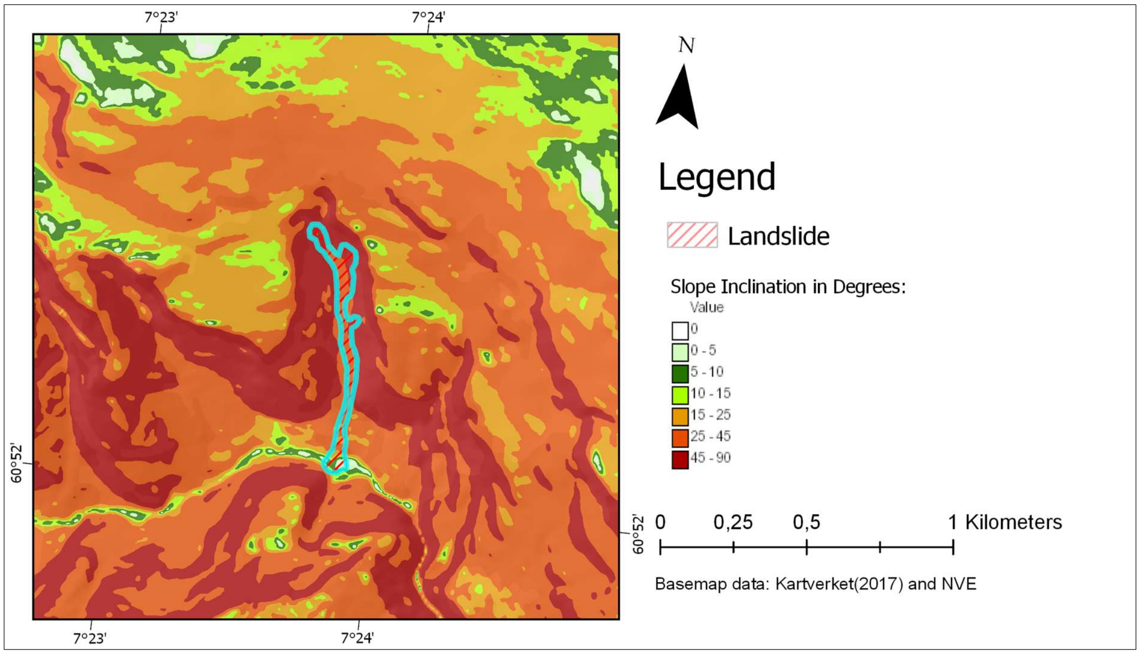

Figure C.56 - Inclination, Kråkagjelet

The soil cover characteristics of the area are predominated by exposed bedrock, with surrounding deposits of colluvium, and weathered material and some deposits of moraine material. The location of the debris flow is between two classifications; exposed bedrock and colluvium (slide material).

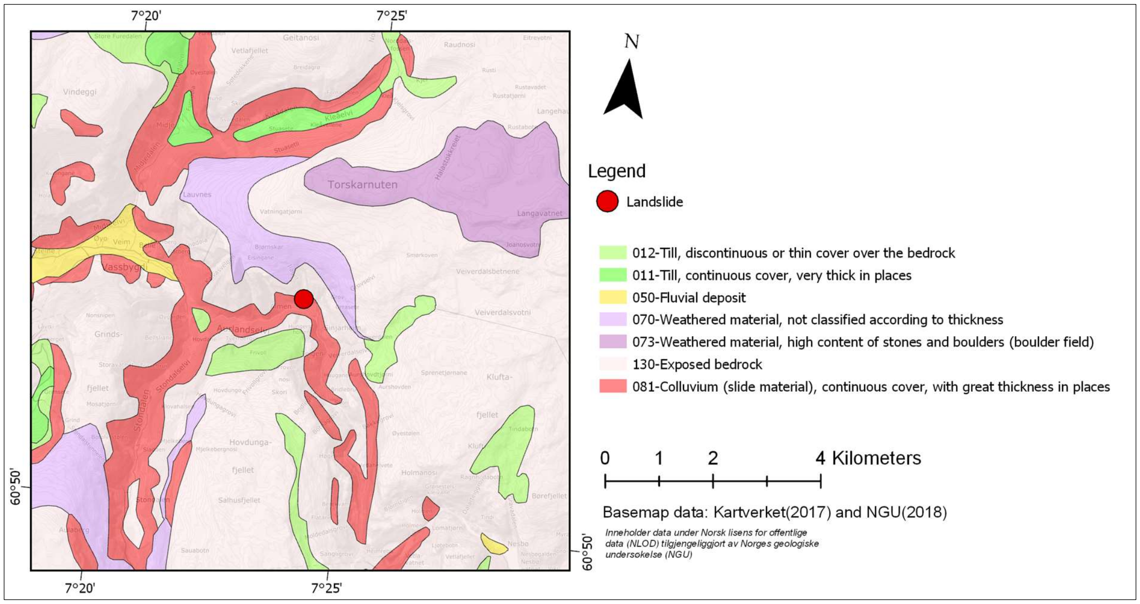

Figure C.57 - Quaternary geology, Kråkagjelet

The geology of the area is given in the figure below.

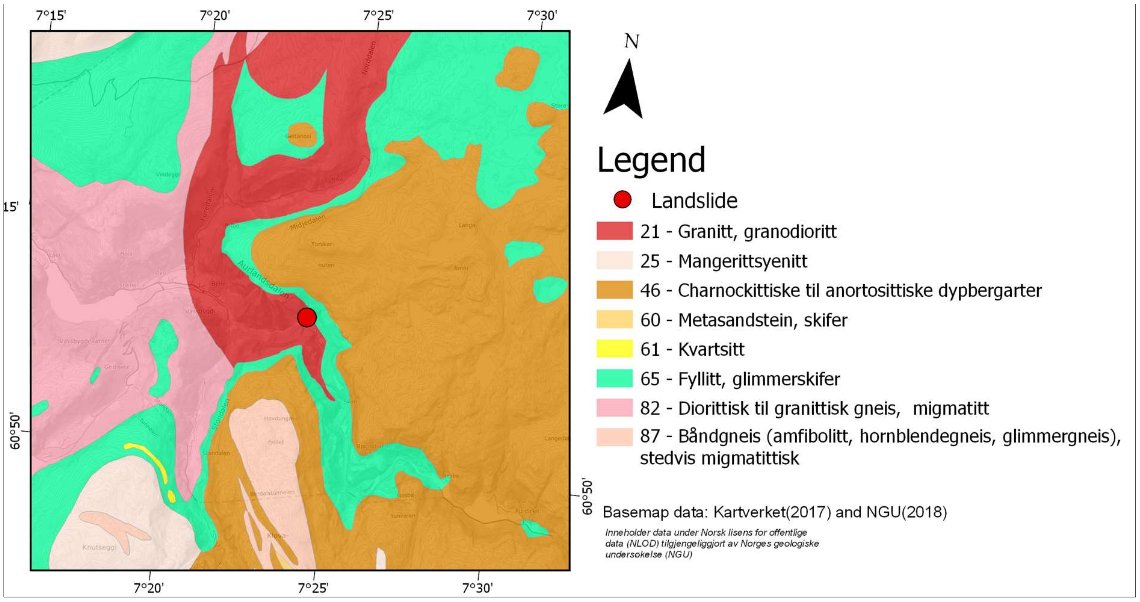

Figure C.58 -Geology, Kråkagjelet

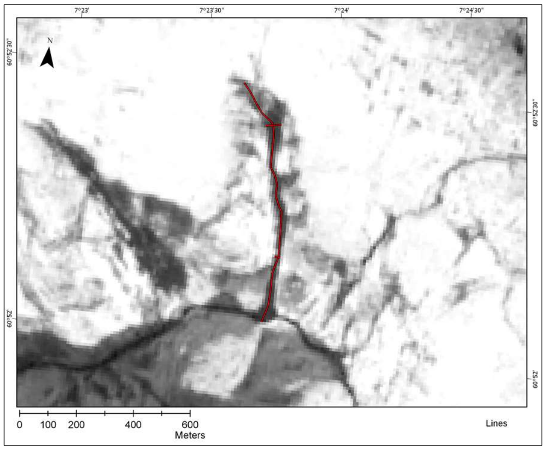

Figure C.59 – Line sections, Kråkagjelet

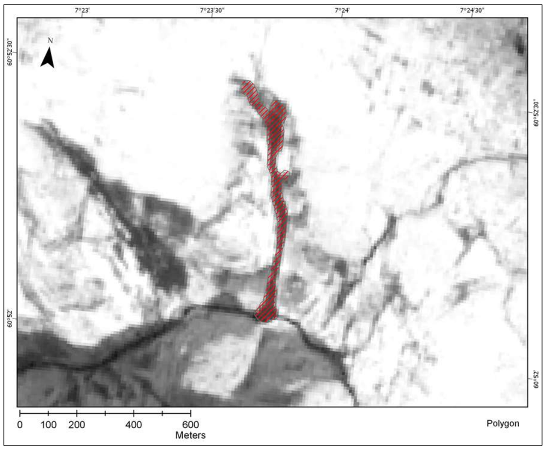

Figure C.60 - Polygon, Kråkagjelet

The geometry of the Rødstøl landslide

Area of polygon	37 569	m^2	*(1)*
Perimeter of polygon	2 047	m	*(2)*
Length of centerline	893	m	*(3)*
Length of wide line	56	m	*(4)*
Length of narrow line	21	m	*(5)*
Area/Perimeter	18.4		*(1) / (2)*
Length/Widest width	15.9		*(3) / (4)*
Length/Narrowest width	42.5		*(4) / (5)*

C.1.7 Event 7 – Spandsdalen

Type	Debris avalanche			
Date	15.06.2017			
Area	Lavangen, Troms			
Ref. ETRS89, UTM 33N	E: 619037	N: 7624840		
S2-data acquisition dates	Previsit:	Pre event:	Post event:	Revisit:
	23.07.2016	12.06.2017	22.07.2017	-

Figure C.61 – Aerial photography of the Spansdalen debris avalanche. From (Kristofers, 2017).

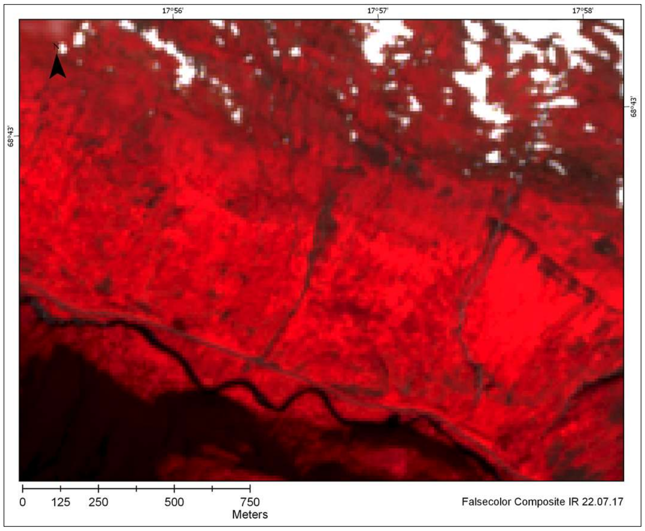

Figure C.62 – False color composite, Spansdalen post-event data

Landslide classified as a debris avalanche in regObs. The debris avalanche occurred in the summer season, in the northern part of Norway. (Kristofers, 2017) describes the normal meteorological conditions leading up the event, but a large amount of water inflow to the terrain, due to snowmelt. The debris avalanche initiated at the top of the slope, ca. 600 m.a.s.l. About 2/3 of the displaced material came to a rest at about 500 m.a.s.l, while the rest of the material was transported to the foot of the slop along a gully stream (Kristofers, 2017). A motor highway is situated at the foot of the slope.

The satellite data is acquired from 3 days prior and 40 days later than the date of occurrence. Although the data is acquired close to the event, there are large seasonal variations between the two datasets. The previsit data from 2016 has similar conditions as the pre-event data.

The meteorological data does not show significant amounts of precipitation leading up to the event. The temperature has a significant prior to the event, possibly causing more snowmelt, although not recorded in the data. A snowmelt and temperature time series are shown in figure C.63. Accumulated snowmelt and precipitation for the 7 preceding days are shown in figure C.64. The time series is obtained from www.xgeo.no, with data provided from NVE and met.no. The spatial reference is given in UTM 33N coordinates in the figures.

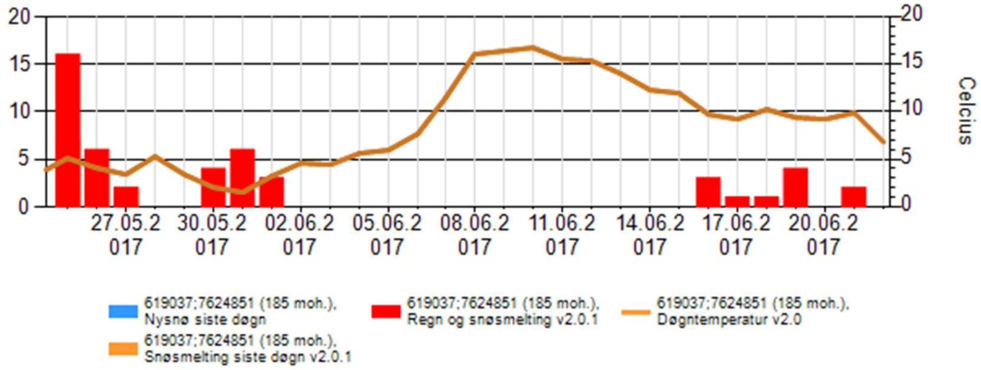

Figure C.63 - Meteorological conditions in the Spansdalen area. (Screenshot from xgeo.no, captured 21.04.18)

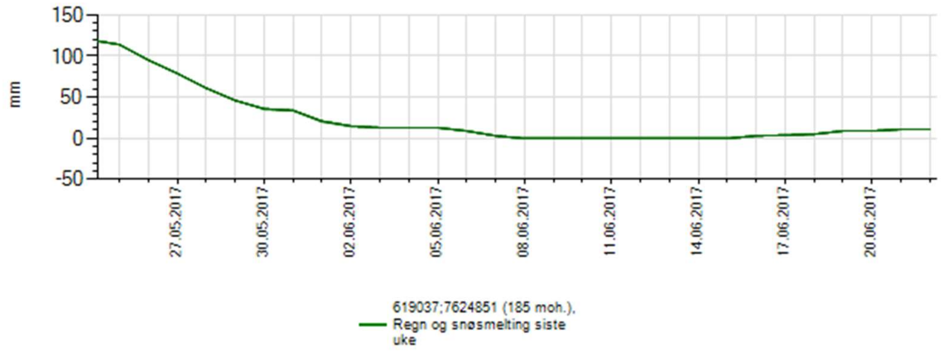

Figure C.64 - Weekly snowmelt & precipitation in the Spansdalen area. (Screenshot from xgeo.no, captured 21.04.18)

The debris avalanche occurred in a south-southwest facing slope, inclined 25-45 degrees.

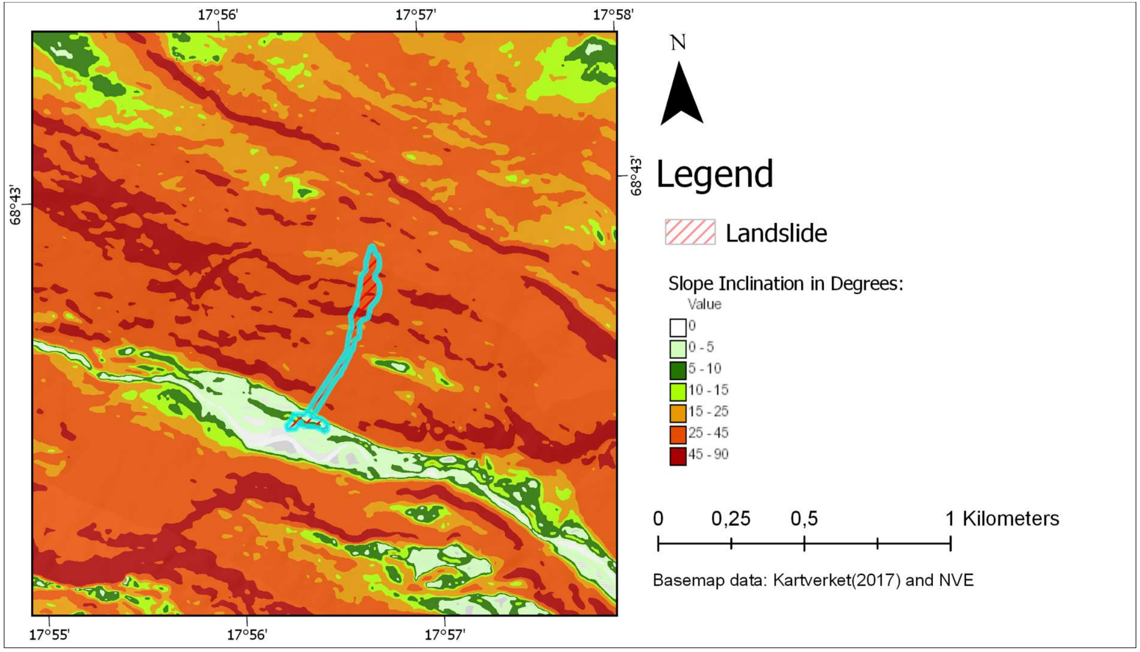

Figure C.65 - Inclination, Spansdalen

The quaternary geology of the area is given in the figure below.

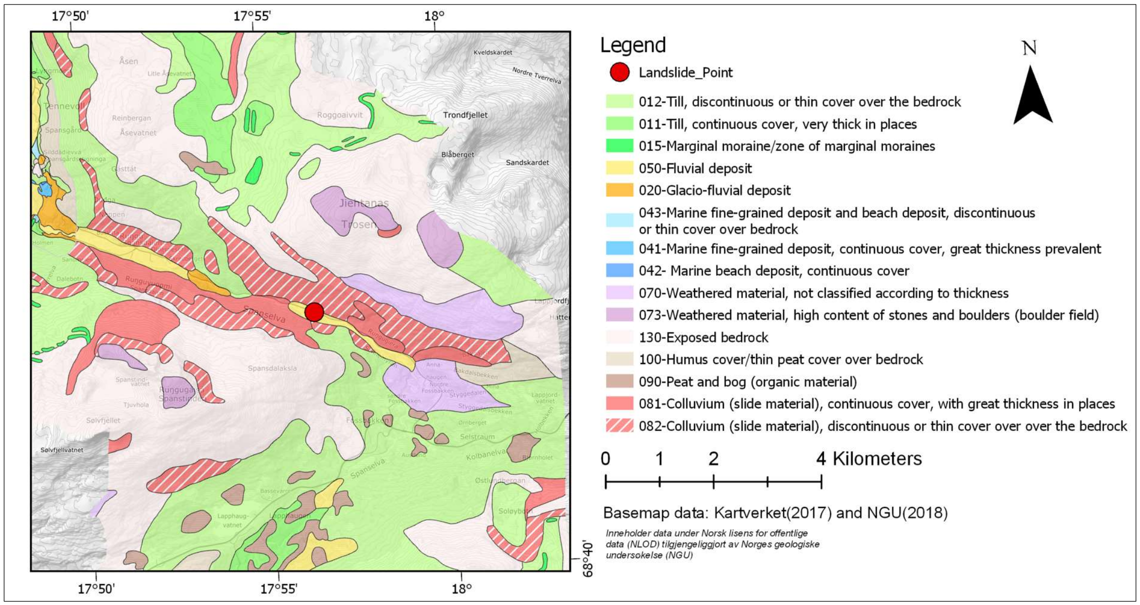

Figure C.66 - Quaternary geology, Spansdalen

The geology of the area is given below.

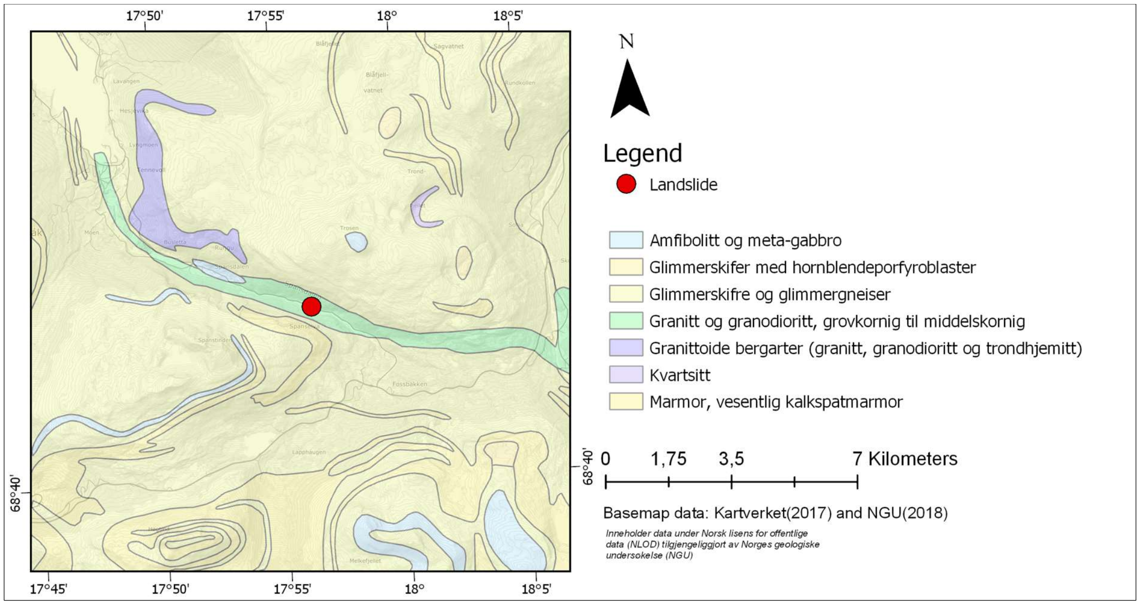

Figure C.67 - Geology, Spansdalen

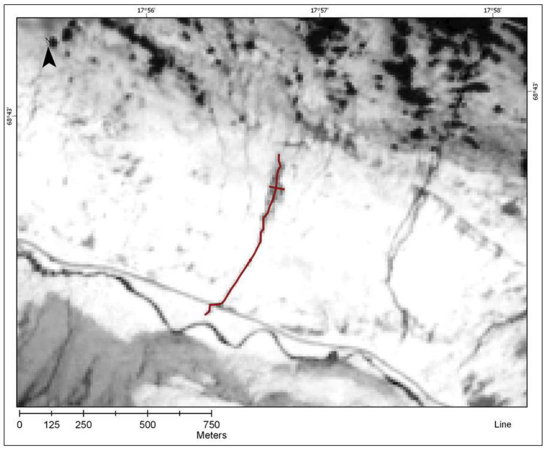

Figure C.68 – Line sections, Spansdalen

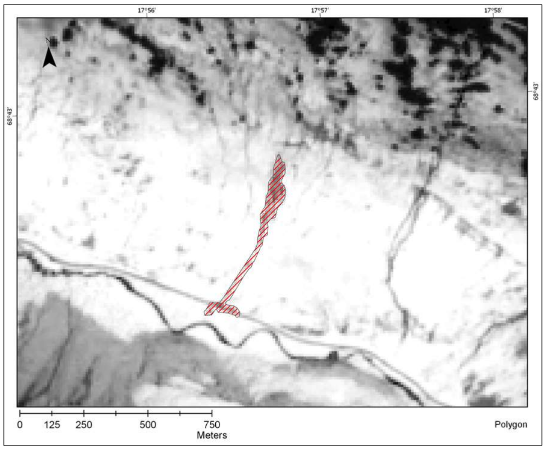

Figure C.69 - Polygon, Spansdalen

Geometry of landslide

Area of polygon	26 300	m^2	*(1)*
Perimeter of polygon	1 677	m	*(2)*
Length of centerline	741	m	*(3)*
Length of wide line	62	m	*(4)*
Length of narrow line	12	m	*(5)*
Area/Perimeter	14.1		*(1) / (2)*
Length/Widest width	12.0		*(3) / (4)*
Length/Narrowest width	61.8		*(4) / (5)*

C.1.8 Event 8 – Selskreda

<table>
<tr><td>Type</td><td colspan="4">Debris flow</td></tr>
<tr><td>Date</td><td colspan="4">24.07.2017</td></tr>
<tr><td>Area</td><td colspan="4">Nesset, Møre og Romsdal</td></tr>
<tr><td>Ref. ETRS89, UTM 33N</td><td>E: 152446</td><td colspan="3">N: 6942625</td></tr>
<tr><td rowspan="2">S2-data acquisition dates</td><td>Previsit:</td><td>Pre event:</td><td>Post event:</td><td>Revisit:</td></tr>
<tr><td>-</td><td>21.07.2017</td><td>26.07.2017</td><td>22.08.2017</td></tr>
<tr><td colspan="5">
Figure C.70 - Picture of displaced material on road. Courtesy of Statens Vegvesen.</td></tr>
<tr><td colspan="2">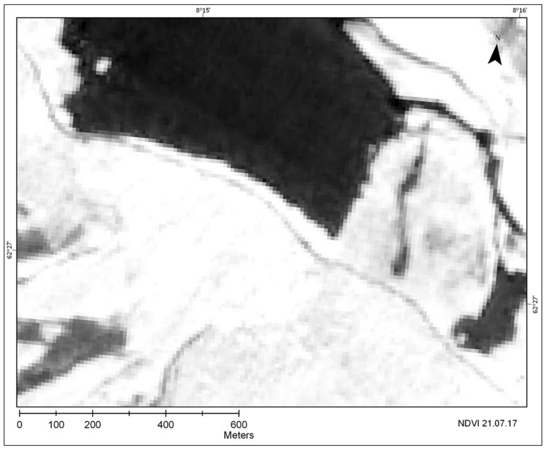
Figure C.71 – NDVI image of Selskreda. Pre-event data.</td><td colspan="3">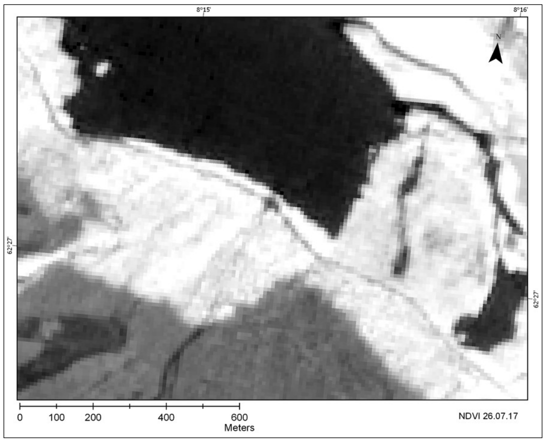
Figure C.72 – NDVI image of Selskreda, Post-event data.</td></tr>
</table>

Landslide classified as debris flow in regObs. The event is poorly documented. The slope is situated next to a low traffic road, where the picture above is taken from. The displaced material looks to contain large amounts of water. The debris flow has followed a stream gully, before accumulating a small debris around the crossing road, as indicated at the NDVI images above. The landslide has not affected the surrounding vegetation significantly, other than the small debris fan at the foot of the slope. The stream gully can be detected in the NDVI image, but it is not detectable in color composites.

The satellite data is acquired 3 days prior, and 2 days after the date of occurrence. The post-event data has poor lighting conditions and cloud cover. A thin cloud cover is situated above the area of interest and affects the color composite images. The debris flow is detectable in NDVI images. The revisit data has cloud free conditions. The gully stream is not detectable in the revisit data, the small debris fan is.

Meteorological conditions leading up to the debris flow are shown below. Precipitation, snowmelt and temperature are shown in figure C.73. Accumulated snowmelt and precipitation for the 7 preceding days are shown in figure C.74. The time series is obtained from www.xgeo.no, with data provided from NVE and met.no. The spatial reference is given in UTM 33N coordinates in the figures.

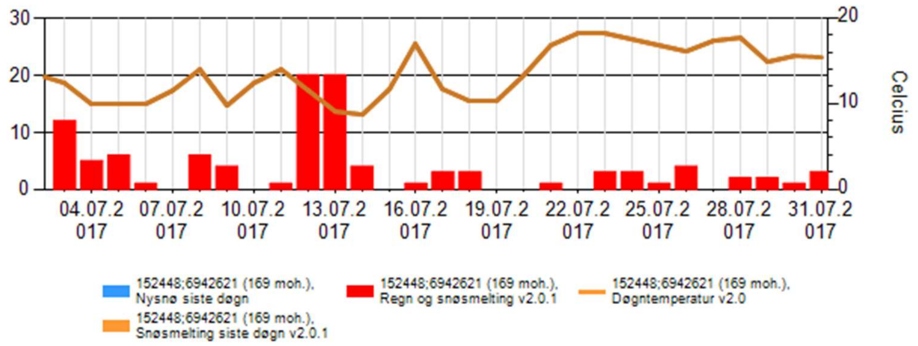

Figure C.73 - Meteorological conditions in the Selskreda area. (Screenshot from xgeo.no, captured 21.04.18)

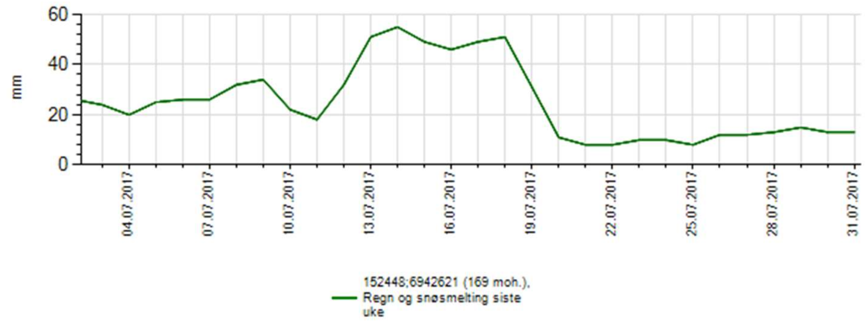

Figure C.74 - Weekly snowmelt & precipitation in the Selskreda area. (Screenshot from xgeo.no, captured 21.04.18)

The debris flow occurred in a north-northeast facing slope. The slope is inclined between 15-25 degrees and flattening out at the toe.

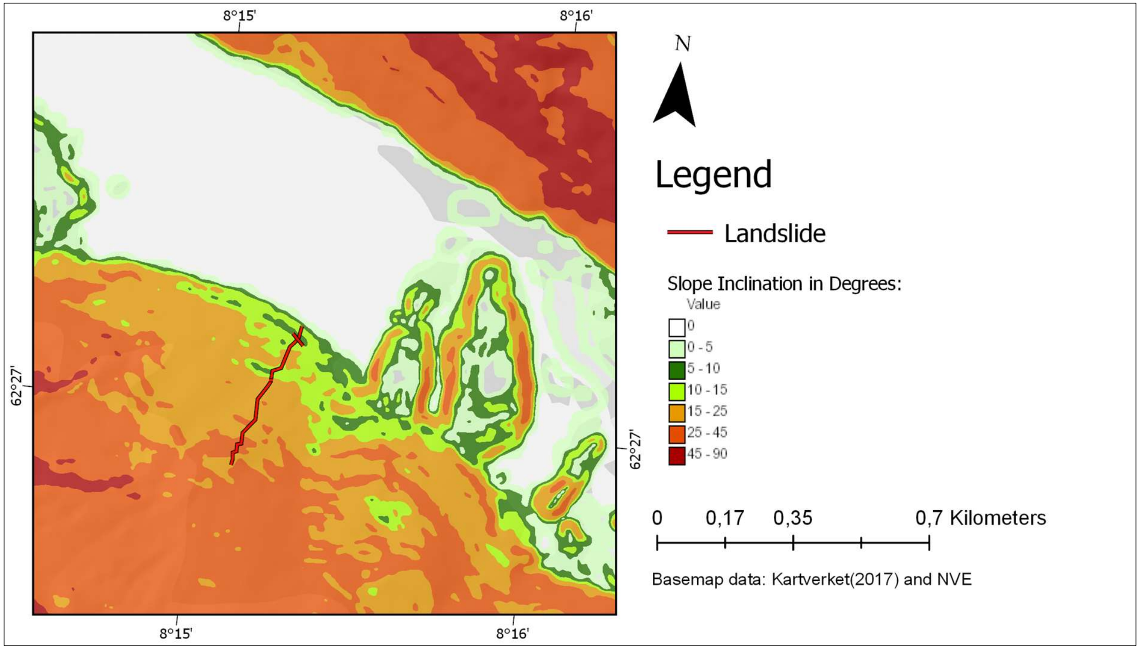

Figure C.75 - Inclination, Selskreda

The quaternary geology and geological settings for the area are shown in the figures below.

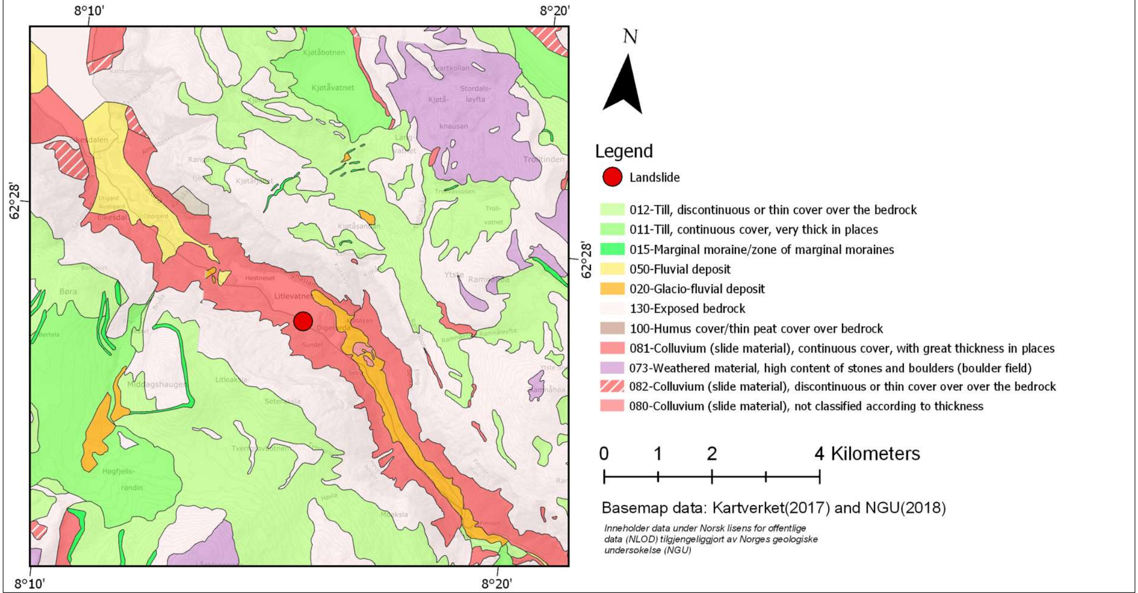

Figure C.76 - Quaternary geology, Selskreda

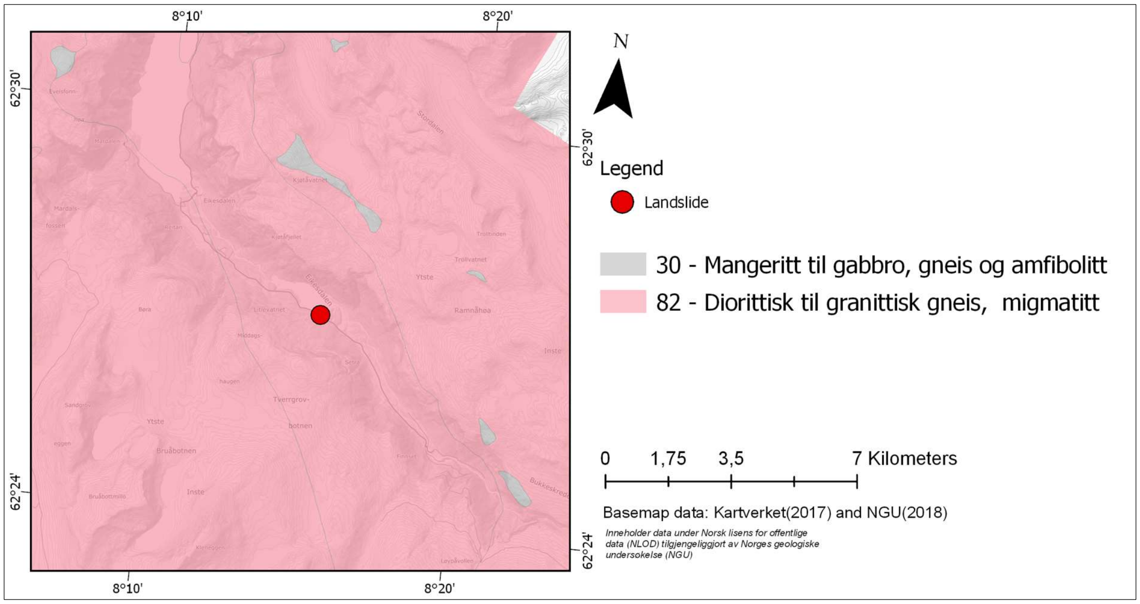

Figure C.77 - Geology, Selskreda

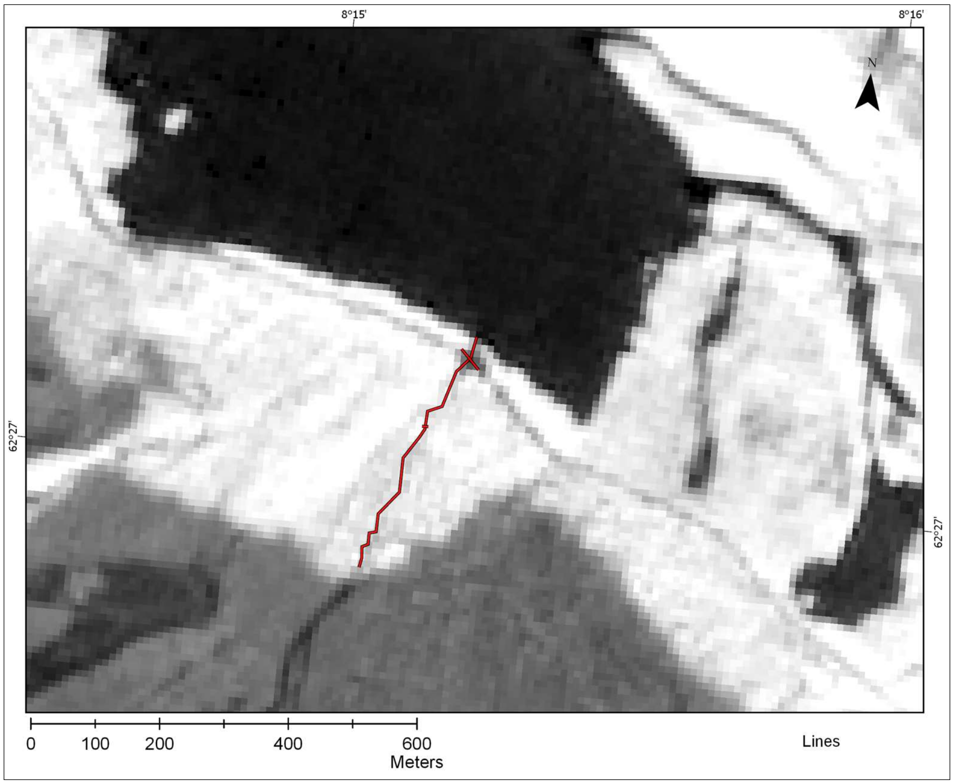

Figure C.78 – Line sections, Selskreda

Geometry of landslide

Area of polygon	-	m²	*(1)*
Perimeter of polygon	-	m	*(2)*
Length of centerline	431	m	*(3)*
Length of wide line	42	m	*(4)*
Length of narrow line	10	m	*(5)*
Area/Perimeter	.		*(1) / (2)*
Length/Widest width	35.9		*(3) / (4)*
Length/Narrowest width	43.1		*(4) / (5)*

C.1.9 Event 10 – Tokke

Type	Debris flow			
Date	02.10.2017			
Area	Tokke, Telemark			
Ref. ETRS89, UTM 33N	E: 94984	N: 6616064		
S2-data acquisition dates	Previsit:	Pre event:	Post event:	Revisit:
	-	16.09.2017	06.10.2017	-
 **Figure C.79 - Natural color composite, post-event data Tokke**				

Landslide event classified as debris flow in regObs, with the following description: The event blocked a 70 meter stretch of a nearby road. The material was entrained from roughly 200 meters upslope. A small river runs at the location of the debris flow. The displaced material can be seen in the picture above.

Pre-event data is aquired 16 days prior to the date of occurence. The post-event data is acquired 4 days after the date of occurence. Meteorological data shows a peak in close to the date of occurrence. Snowmelt, precipitation and temperature are shown in figure C.80. Accumulated snowmelt and precipitation for the 7 preceding days are shown in figure C.81. The time series is obtained from www.xgeo.no, with data provided from NVE and met.no. The spatial reference is given in UTM 33N coordinates in the figures.

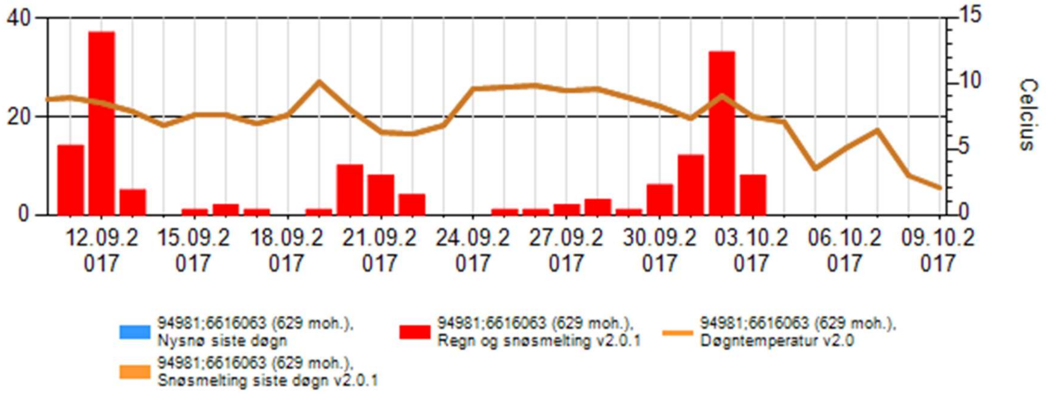

Figure C.80 - Meteorological conditions in the Tokke area. (Screenshot from xgeo.no, captured 21.04.18)

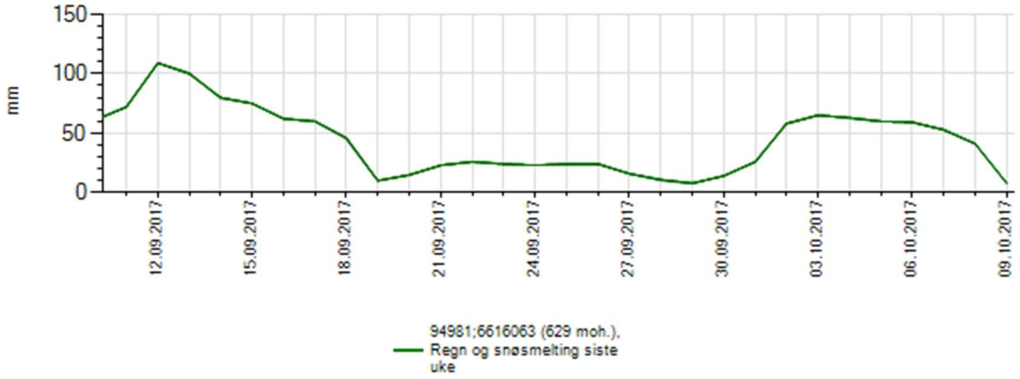

Figure C.81 - Weekly snowmelt & precipitation in the Tokke area. (Screenshot from xgeo.no, captured 21.04.18)

The debris flow has occurred in an east-facing. The inclination at the area of initiation is between 15-25 degrees, whereas the lower 2/3 of the landslide scar is situated between 5-10 degrees.

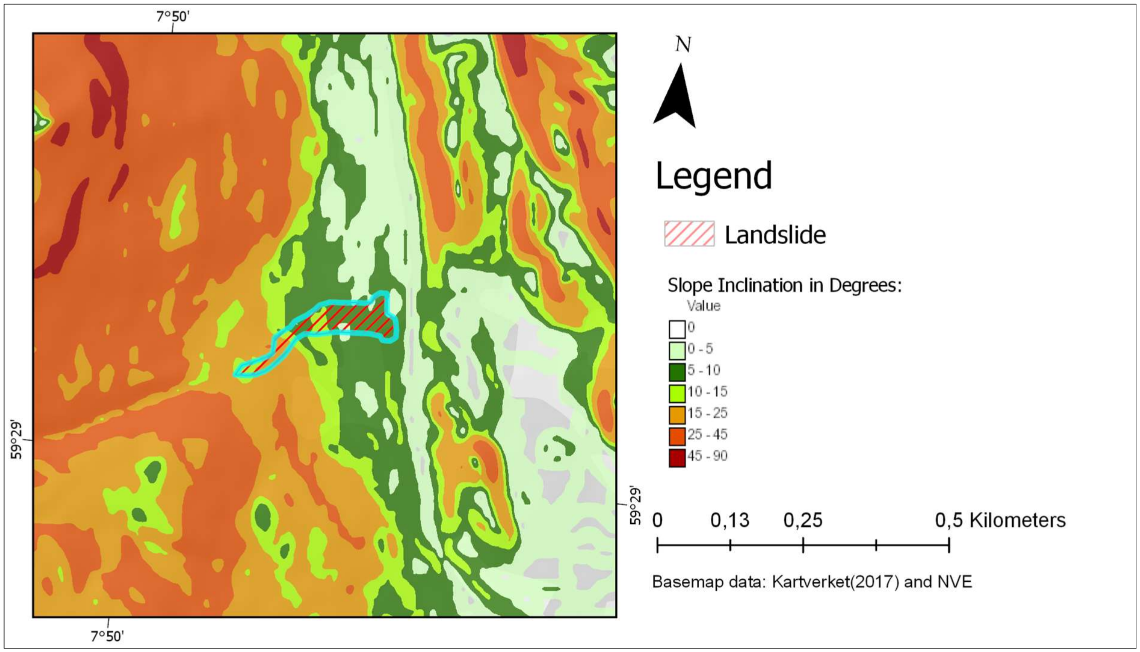

Figure C.82 - Inclination, Tokke

The soil cover and geology in the Tokke area are shown in the figures below.

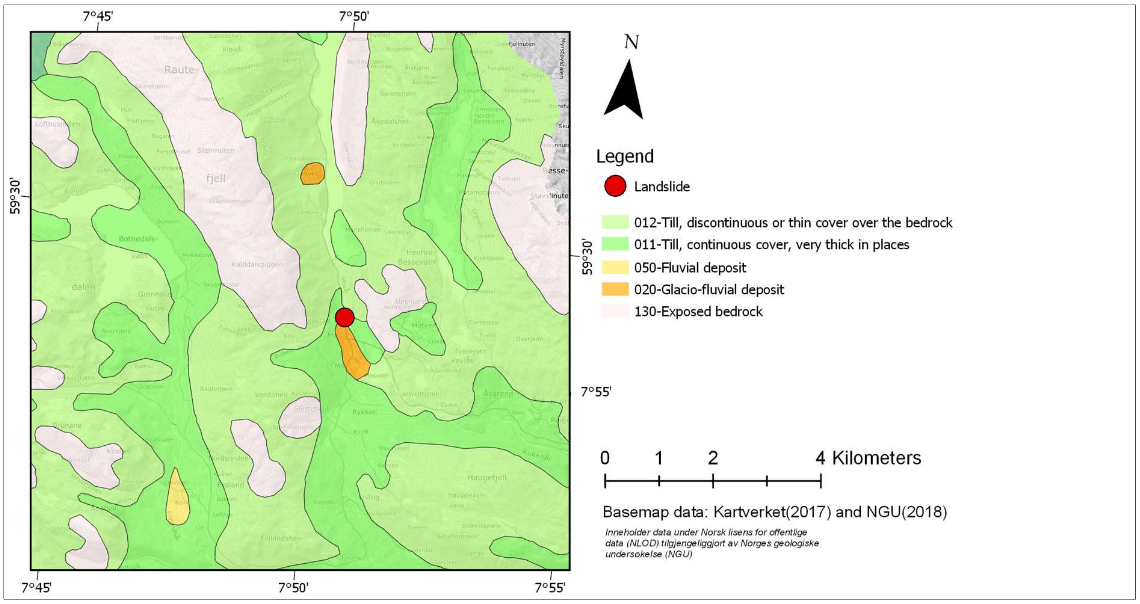

Figure C.83 - Quaternary geology, Tokke

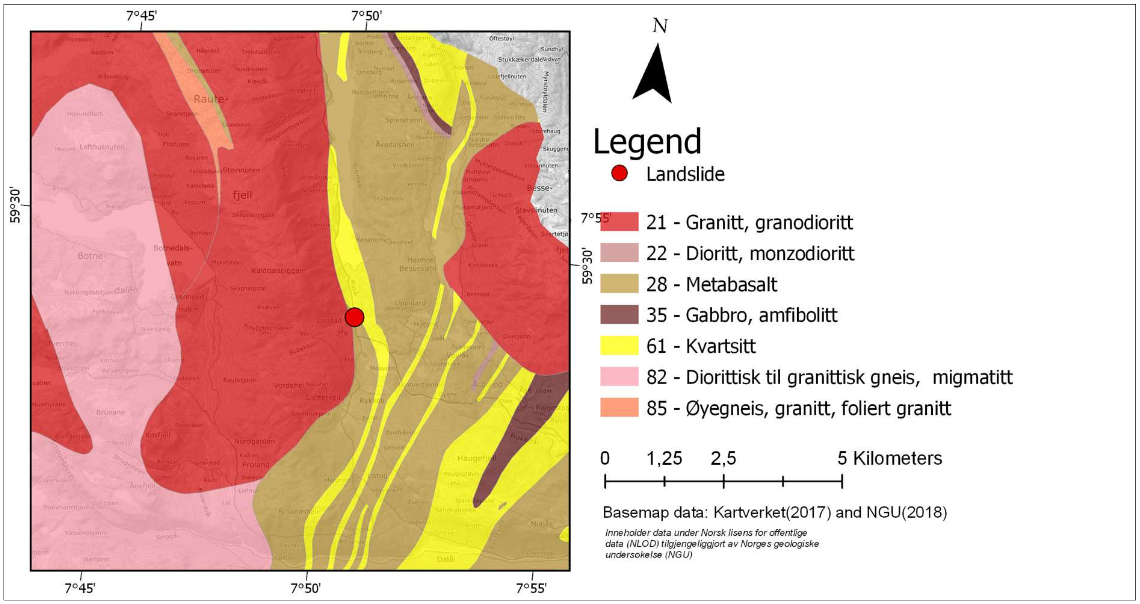

Figure C.84 - Geology, Tokke

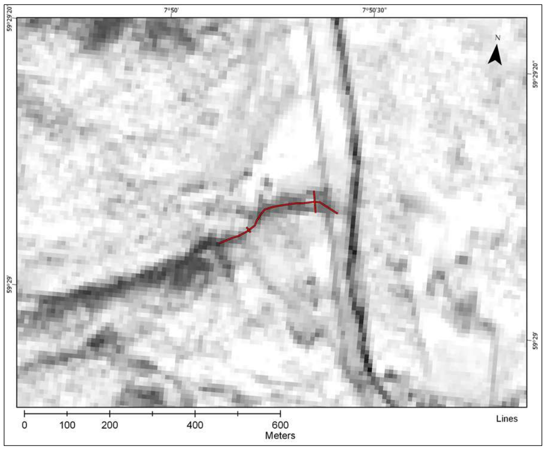

Figure C.85 – Line sections, Tokke

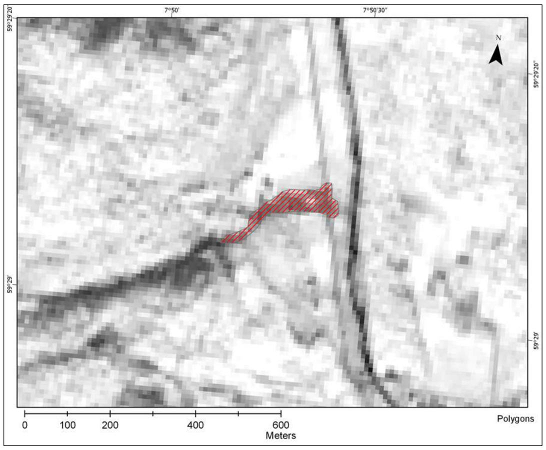

Figure C.86 - Polygon, Tokke

Geometry of landslide

Area of polygon	11 437	m^2	*(1)*
Perimeter of polygon	717	m	*(2)*
Length of centerline	319	m	*(3)*
Length of wide line	53	m	*(4)*
Length of narrow line	16	m	*(5)*
Area/Perimeter	16.0		*(1) / (2)*
Length/Widest width	6.0		*(3) / (4)*
Length/Narrowest width	20.0		*(4) / (5)*

C.1.10 Event 11 – Krundalen

<table>
<tr><td>Type</td><td colspan="4">Debris avalanche</td></tr>
<tr><td>Date</td><td colspan="4">05.07.2015</td></tr>
<tr><td>Area</td><td colspan="4">Luster, Sogn og Fjordane</td></tr>
<tr><td>Ref. ETRS89, UTM 33N</td><td>E: 89269</td><td colspan="3">N: 6857894</td></tr>
<tr><td rowspan="2">S2-data acquisition dates</td><td>Previsit:</td><td>Pre event:</td><td>Post event:</td><td>Revisit:</td></tr>
<tr><td>-</td><td>-</td><td>18.08.2015</td><td>06.06.2016</td></tr>
<tr><td colspan="5">


Figure C.87 – Debris avalanche in Luster. From (NVE, 2015)
</td></tr>
<tr><td colspan="5">
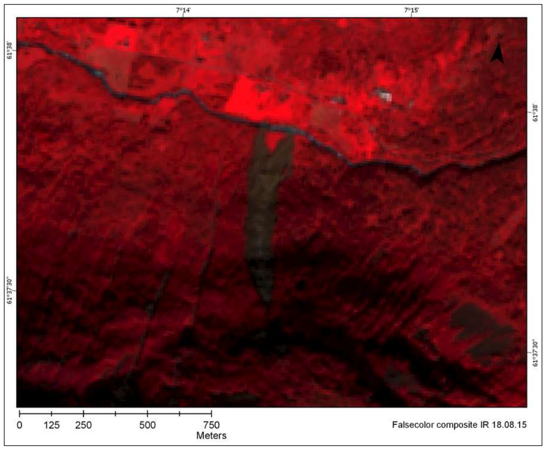

Figure C.88 – False color composite, Krundalen post-event data.
</td></tr>
</table>

Landslide classified as debris avalanche in regObs. The event is reported by the news, as a local farmer lost sheep and outhouses to the debris avalanche. The event occurred mid-summer 2015 and was presumably initiated by a rockfall striking the saturated soil (From event description in www.skredregistrering.no)

Satellite data is available 44 days after the date of occurrence. Sentinel-2 data prior to the landslide is not available, as it the satellite became operational in mid-summer 2015. Revisit data is available from mid-summer 2016, with somewhat better lighting conditions, due to shorter shadows from the surrounding landscape.

Meteorological data does show relatively little water inflow prior to the debris avalanche. Snowmelt, precipitation and temperature are shown in figure C.89. Accumulated snowmelt and precipitation for the 7 preceding days are shown in figure C.90. The time series is obtained from www.xgeo.no, with data provided from NVE and met.no. The spatial reference is given in UTM 33N coordinates in the figures.

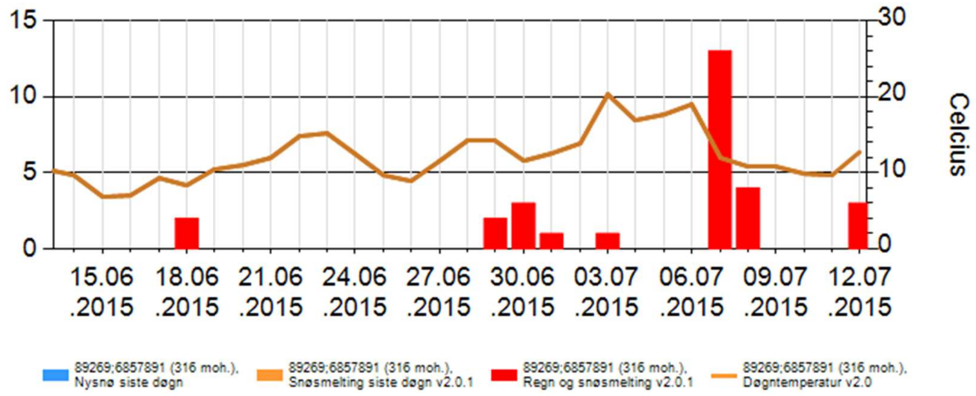

Figure C.89 - Meteorological conditions in the Krundalen area. (Screenshot from xgeo.no, captured 15.05.18)

Figure C.90 - Weekly snowmelt & precipitation in the Krundalen area. (Screenshot from xgeo.no, captured 15.05.18)

The debris avalanche occurred in a north-facing slope. The inclination is between 25-45 degrees in the area of initiation, the mid-section between 15-25 degrees and the toe of the landslide scar is relatively flat.

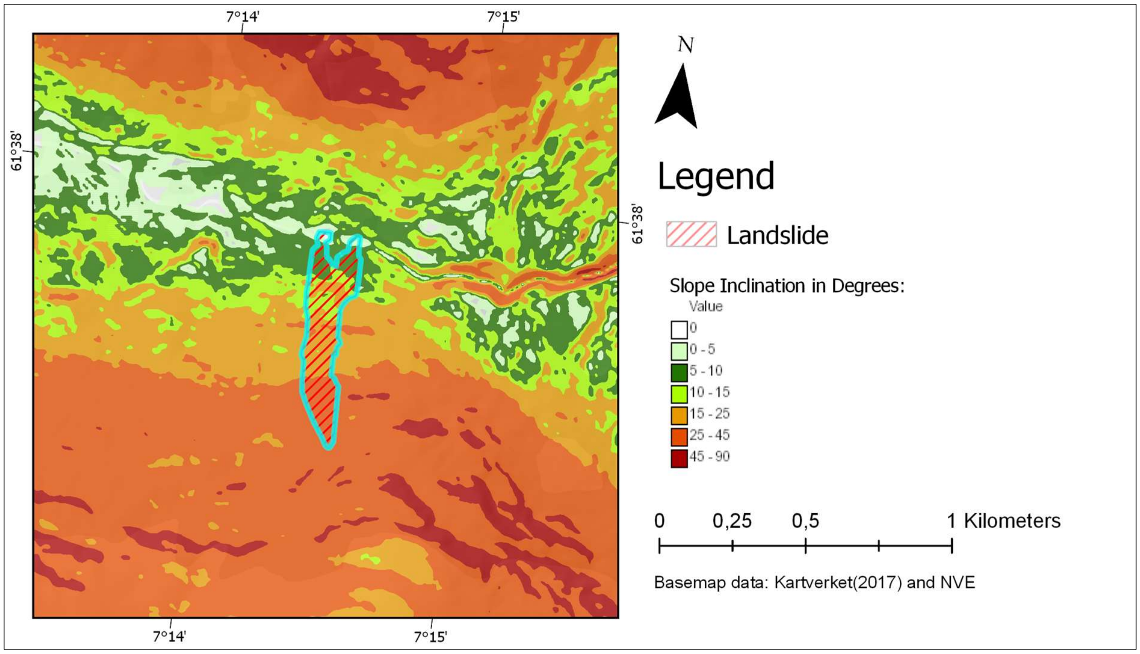

Figure C.91 - Inclination, Krundalen

The quaternary geology of the area is shown in the figure below.

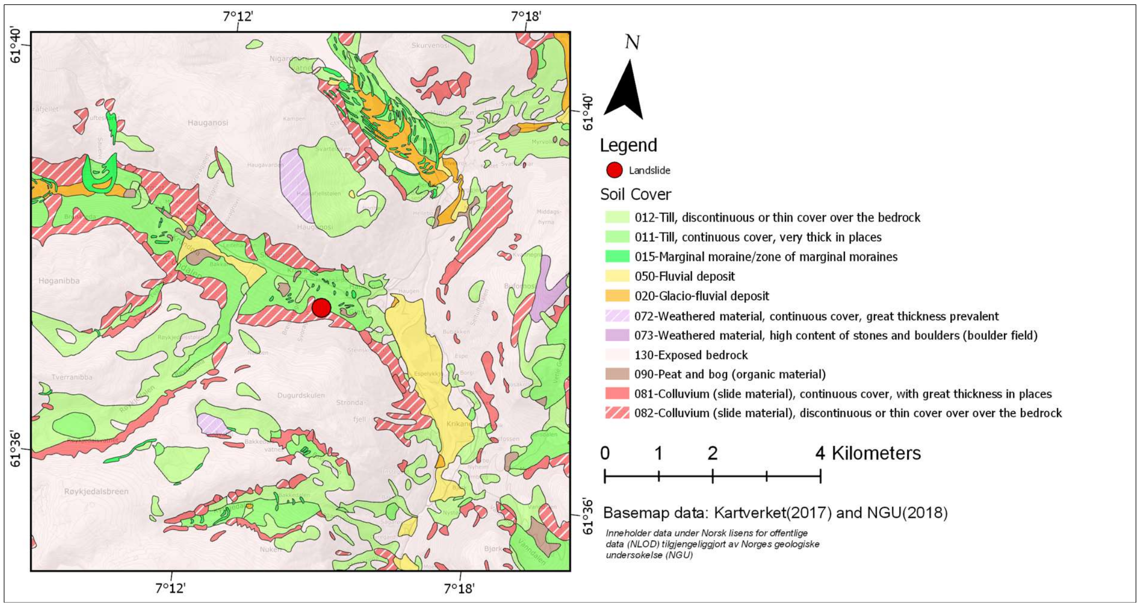

Figure C.92 - Quaternary geology, Krundalen

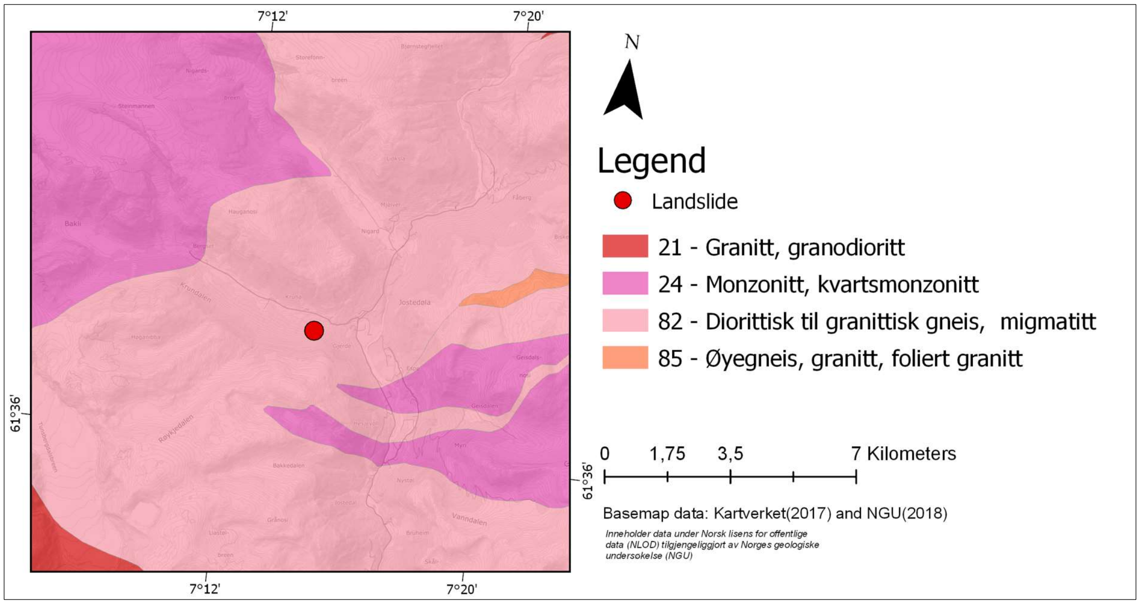

Figure C.93 - Geology, Krundalen

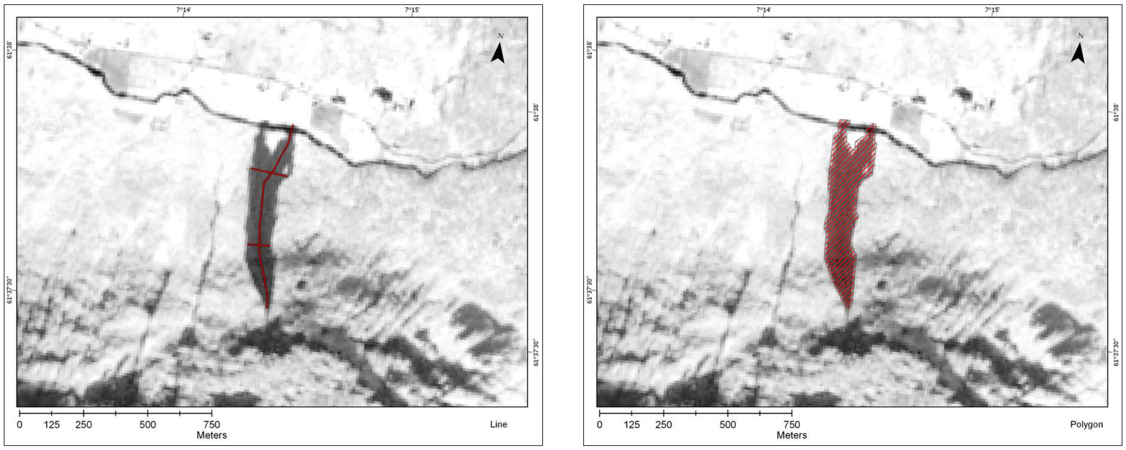

Figure C.94 – Line sections, Krundalen

Figure C.95 - Polygon, Krundalen

Geometry of landslide

Area of polygon	80 417	m^2	*(1)*
Perimeter of polygon	1 896	m	*(2)*
Length of centerline	752	m	*(3)*
Length of wide line	148	m	*(4)*
Length of narrow line	89	m	*(5)*
Area/Perimeter	42.4		*(1) / (2)*
Length/Widest width	5.1		*(3) / (4)*
Length/Narrowest width	8.4		*(4) / (5)*

C.2 Possibly Detected Landslides

C.2.1 Event 12 - Bjerkadalen

Type	Debris avalanche			
Date	26.01.2017			
Area	Hemnes, Nordland			
Ref. ETRS89, UTM 33N	E: 451347	N: 7337775		
S2-data acquisition dates	Previsit:	Pre event:	Post event:	Revisit:
	-	25.10.2016	15.02.2017	20.07.2017

Figure C.96 – Bjerkadalen debris avalanche. Photo: (Statens Vegvesen, 2017)

Figure C.97 – Shaved vegetation, Bjerkadalen debris avalanche. Photo: (Statens Vegvesen, 2017)

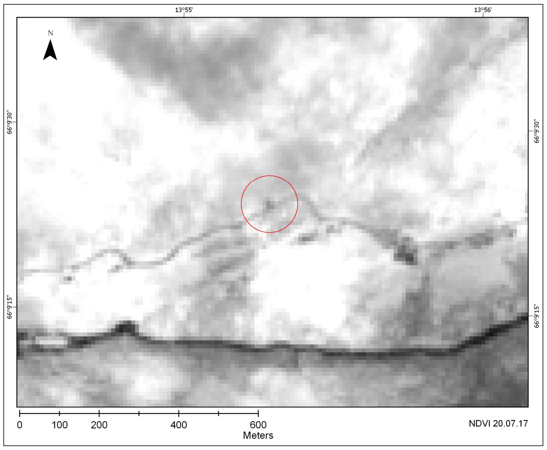

Figure C.98 – NDVI image of the Bjerkadalen area. The presumed landslide circled in red.

The landslide is classified as a debris avalanche in regObs. The event occurred in the winter season and has removed vegetation and snow cover from the slope. The size of the landslide is not reported. The width of material covering the road is estimated as 15 meters wide, using the road as a 5 m reference. The length is difficult to estimate from the pictures.

Pre-event satellite data is acquired 93 days prior to the date of occurrence. The post-event data is acquired 20 days after the event. The two datasets have large seasonal variations and different lighting conditions. No landslide activity is detected in the post-event data. The post-event data has poor lighting conditions in the area of interest due to shadows from the surrounding terrain(from the opposite side of the valley). Revisit data is acquired from the following summer, with better lighting conditions, and greener vegetation. The revisit data show three pixels with less vegetation than the surrounding pixels at the reported location, possibly due to landslide activity.

The meteorological conditions leading up to the event were wet, as indicated in the figures below. Accumulated precipitation and snowmelt for the 7 preceding days are registered to 244 mm.

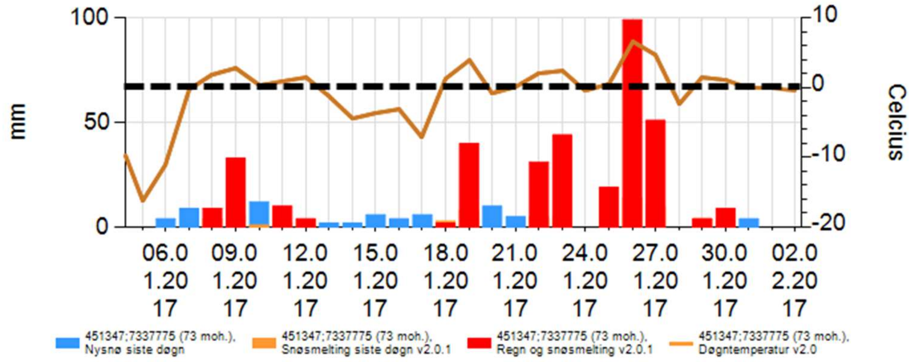

Figure C.99 - Meteorolgical conditions time series in the Bjerkadalen area. (Screenshot from xgeo.no, captured 21.05.2018)

Figure C.100 - Weekly snowmelt & precipitation in the Bjerkadalen area. (Screenshot from xgeo.no, captured 21.05.18)

The reported location lies on the boundary between a large fluvial deposit, and weathered material. The slope is facing south-east, with varying inclination. The top half of the slope is inclined 15-25 degrees, before flattening out towards the foot of the slope.

C.2.2 Event 13 - Sulitjelma

Type	*Possible* Debris avalanche			
Date	02.05.2017			
Area	Fauske, Nordland			
Ref. ETRS89, UTM 33N	E: 451347	N: 7337775		
S2-data acquisition dates	Previsit:	Pre event:	Post event:	Revisit:
	-	29.04.2017	09.05.2017	

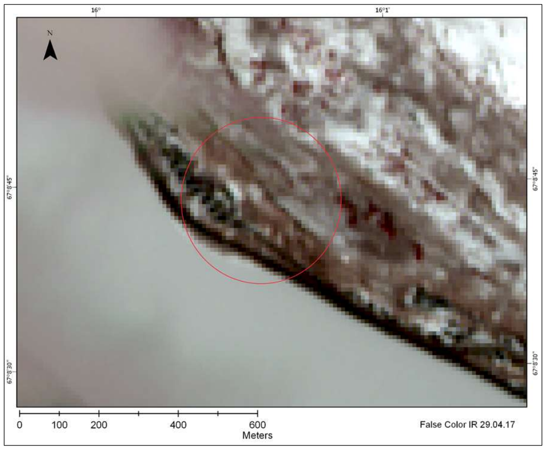

Figure C.101 Pre-event, false color composite Sulitjelma

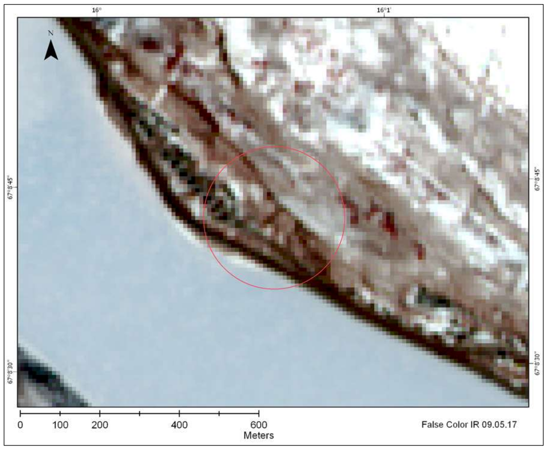

Figure C.102 - Post-event, false color composite Sulitjelma. The presumed landslide circled in red.

Figure C.103 – Sulitjelma event. Photo: Linn Normann Godtfredsen/Saltenposten (NVE, 2017a)

The event is classified as a debris avalanche in regObs. The regObs registration reports a probable initiation from a rock fall. The event occurred in spring. The area has still a lot of snow.

The satellite data is obtained close to the date of occurrence. The pre-event data is acquired 3 days prior to the event, and the post-event data is acquired 7 days after the event. The lighting conditions appear similar in the two datasets. Some variations due to snowmelt can be seen in the two datasets. The presumed landslide is not at the reported coordinates, but at the location of the red and green flag in regObs registration 126553 (coordinates not specified). A narrow cluster of around 10-12 pixels with less snow can be seen in the post-event data, at the presumed landslide location, resembling that of the picture in the local news report. It is not known if the change in spectral reflectance is due to landslide activity, or simply snow melt. The meteorological conditions leading up to the event were wet. Accumulated snowmelt and precipitation for the 7 preceding days close to the reported coordinates are reported in *xgeo.no* to be 60 mm.

The assumed event occurred in a southwest-facing slope, with an average inclination between 25-45 degrees. The quaternary geology of the area is characterized by a large deposit of weathered material, with elements of colluvium, exposed bedrock, and humus.

C.2.3 Event 14 –Byrkjedal

Type	Debris avalanche			
Date	02.10.2017			
Area	Gjesdal, Rogaland			
Ref. ETRS89, UTM 33N	E: -3207	N: 6549591		
S2-data acquisition dates	Previsit:	Pre event:	Post event:	Revisit:
	-	23.09.2017	23.10.2017	-

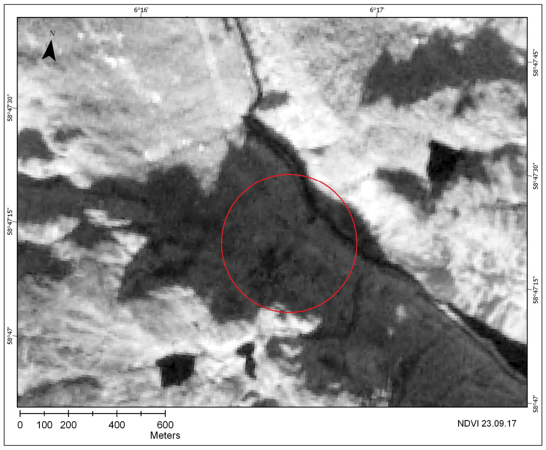

Figure C.104 – Pre-event NDVI image of the Byrkjedal area.

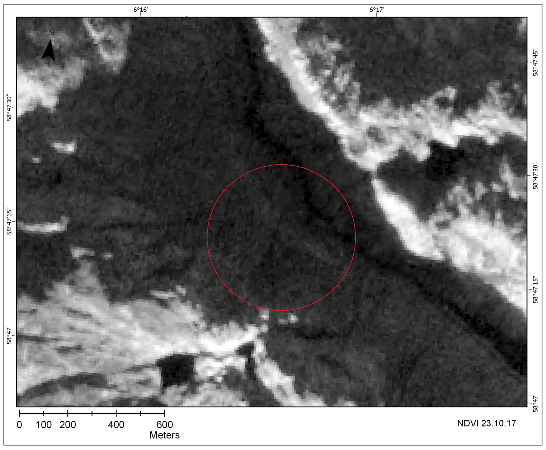

Figure C.105 – Post-event NDVI image of the Bjerkadalen area. The presumed landslide circled in red.

The event is classified as a debris avalanche in regObs. A local news report has described the landslide as 10 meters wide and 50 meters long (Link in regObs). It occurred in autumn.

The satellite data is acquired 9 days prior to the event and 21 days after the event. The lighting conditions vary between the two datasets with longer shadows in the post-event data. A narrow strip of pixels with lower NDVI values can be seen in the post-event data, maybe due to shaved vegetation from landslide activity. A significant shadow-effect distorts the data and makes it uncertain to interpret. The meteorological conditions leading up to the event were extremely wet. Accumulated snowmelt and precipitation for the 7 preceding days close to the reported coordinates are reported in *xgeo.no* to be 243 mm.

The landslide occurred in a steep northeast facing slope, with an inclination between 25-45 degrees. The quaternary geology is the same as in event 2 and 3.

C.3 Undetected Events

Name / Type	Beiarn / Debris flow			
Date	11.07.2015			
Area	Beiarn, Nordland			
Ref. ETRS89, UTM 33N (Reported location)	E: 483056	N: 7406592		
S2-data acquisition dates	Previsit:	Pre event:	Post event:	Revisit:
	-	-	15.08.2015	-

Type and possible trigger:

Event classified as debris flow, possibly initiated by a slush flow. The meteorological conditions leading up to the event were wet. Accumulated snowmelt and precipitation for the 7 preceding days close to the reported coordinates are reported in *xgeo.no* to be 175 mm.

Satellite data:

Pre-event data not available. Sentinel-2 data does not exist prior to July 2015. Post-event of good with good lighting conditions acquired 35 days after the date of occurrence.

Geometry/size:

The landslide is reported to have occurred in a north-northwest facing slope. The average inclination of the reported location is between 15-25 degrees (ref. NVE map data). The size of the landslide is in regObs described to be 100 meters wide and 900 meters long.

Quaternary geology and geological conditions (ref. NGU map data):

The quaternary geology at the reported location is classified as a continuous cover of till. The area is characterized by deposits of moraine material and exposed bedrock. There is also smaller deposits of colluvium and fluvial material. A large deposit of weathered material if following the bottom of the *Beiarn* valley. The geology is characterized by gneiss-type of rock and a biotite shale.

Possible causes why the landslide is undetected in S2-data:

The reported size of the landslide is large enough for the landslide to be detected. The landslide is not visually detected in color-composites or NDVI imagery. The Beiarn valley area in the satellite data has several features with little or no vegetation, which may have been caused by landslide activity. The exact location of the debris flow is unknown – The registered coordinates are reported to have an accuracy of +/- 1 km – which make the debris flow event difficult to delineate in an area with similar looking features. A change detection technique could possibly have been useful to detect “new” features in the terrain. It is possible that all the debris flow material followed an existing gully into the river at the valley floor, making minimal alterations in the surrounding terrain. The regObs report states that all the material from the debris flow went into the Beiarn river.

Name / Type	Raudskredbekken / Debris flow			
Date	05.12.2015			
Area	Ullensvang, Hordaland			
Ref. ETRS89, UTM 33N (Reported location)	E: 32023	N: 6702194		
S2-data acquisition dates	Previsit:	Pre event:	Post event:	Revisit:
	-	18.08.15	14.02.16	13.06.2016

Type and possible trigger:

Event classified as debris flow, possibly initiated by a slush flow. The meteorological conditions leading up to the event were wet. Accumulated snowmelt and precipitation for the 7 preceding days close to the reported coordinates are reported in *xgeo.no* to be 145 mm.

Satellite data:

Satellite data acquired close to the date of occurrence is not available. Pre-event data is acquired from 109 days before the event, and the post-event data 71 days after. There are large seasonal variations between the two datasets. The revisit data acquired in 2016 have similar conditions as the pre-event data.

Geometry/size:

The debris flow is reported to have occurred in an east facing slope. The top half of the slope has an inclination of 25-45 degrees, and the bottom inclines 15-25 degrees (ref. NVE map data). The size of the debris flow is unknown.

Quaternary geology and geological conditions (Ref. NGU map data):

The area is characterized by exposed bedrock. There is also smaller deposits of colluvium and fluvial material. Some moraine material is also found in the vicinity of the reported location. The geology at the reported location is classified as *"Metaandesitt, metadacitt og litt metabasalt, stedvis migmatittisk"*.

Possible causes why the landslide is undetected in S2-data:

A clearly defined gully stream can be detected at the reported location in the S2-data. There is also evidence of a debris fan at the foot of the gully stream, next to the crossing road at the foot of the slope. There is, however, no detectable alteration in the gully stream or surrounding terrain features in the three datasets. A change detection technique would not have detected any significant variation between the datasets. A picture from an NRK news report (link in regObs) shows the debris fan crossing the road. Satellite data from sooner after the event could possibly have detected the debris fan, depending on its size and if it altered vegetated terrain.

Name / Type	Reinåa / Debris avalanche			
Date	05.12.2016			
Area	Meråker, Trøndelag			
Ref. ETRS89, UTM 33N (Reported location)	E: 329768	N: 7040444		
S2-data acquisition dates	Previsit:	Pre event:	Post event:	Revisit:
	-	07.11.16	15.02.2017	-

Type and possible trigger:

The event is classified as a debris avalanche. The maximum accumulated snowmelt and precipitation for the 7 preceding days at the reported coordinates are reported in *xgeo.no* to be 78 mm. SVV reports large amounts of precipitation two days prior to the event, as well as high temperatures and wind which caused snowmelt (Frekhaug, 2016).

Satellite data:

Pre-event data is acquired 28 days prior to the event, and the post-event data 72 days after. The two datasets have small seasonal variations. The amount of snow cover and vegetation greenness appears roughly the same. The low winter sun causes long shadows, and the area of interest have different lighting conditions – The reported coordinates are shadowed in the pre-event data and on the shadow border in the post-event data, causing difficult lighting conditions for comparison.

Geometry/size:

The debris avalanche has occurred on steep west-southwest facing slope, with an inclination of 39 degrees (Frekhaug, 2016). The debris avalanche was roughly 20 meters wide, and the amount of material cleaned from the nearby road was estimated to 600 m^3 (Frekhaug, 2016). The debris avalanche has removed large trees.

Quaternary geology (From NGUs map data):

The reported coordinates lie on an intersection between *"Marine fine-grained deposit and beach deposit, discontinuous or thin cover over bedrock"*, *"fluvial deposit"* and *"glaciofluvial deposit.*

Possible causes why the landslide is undetected in S2-data:

The seasonal conditions make the interpretation more difficult due to the low sun and long shadows. The spectral signature from vegetation is less distinct, and not as "helpful". The event is probably too small to be detected.

Name / Type	Jølster / Debris avalanche			
Date	08.12.2016			
Area	Jølster, Sogn og Fjordane			
Ref. ETRS89, UTM 33N (Reported location)	E: 31549	N: 6850364		
S2-data acquisition dates	Previsit:	Pre event:	Post event:	Revisit:
	-	03.11.16	23.03.17	-

Type and possible trigger:

The event is classified as a debris avalanches. The maximum accumulated snowmelt and precipitation for the 7 preceding days close to the reported coordinates are reported in *xgeo.no* to be 153 mm.

Satellite data:

Pre-event data is acquired from 35 days prior to the event, and the post-event data 105 days after. The post-event data has more snow cover than the pre-event data. The lighting conditions of the data are influenced by the season and terrain, with long shadows.

Geometry/size:

The Hyestranda event has occurred in a north facing slope, inclined 15-25 degrees (ref. NVE map data). The width of the slide is reported by NRK to be 10 m wide (link in regObs).

Quaternary geology and geological conditions (Ref. NGU map data):

A large deposit of moraine material surrounds the area of the reported coordinates.

Possible causes why the landslide is undetected in S2-data:

The two datasets have large seasonal variations, making change detection and interpretation of terrain features difficult. The size of the landslide is likely to be too small.

Name / Type	Hyestranda & Ommedal / Debris avalanche			
Date	30.12.2016			
Area	Gloppen, Sogn og Fjordane			
Ref. ETRS89, UTM 33N (Reported locations)	E: 30495 & 21026	N: 6886478 & 6874308		
S2-data acquisition dates	Previsit:	Pre event:	Post event:	Revisit:
	-	03.11.16	23.03.17	-

Type and possible trigger:

Two events classified as debris avalanches, occurring in the same area on the same date. The meteorological conditions leading up to the event were wet. Accumulated snowmelt and precipitation for the 7 preceding days close to the reported coordinates are reported in *xgeo.no* to be 152 and 200 mm.

Satellite data:

Pre-event data is acquired from 57 days prior to the event, and the post-event data 83 days after. The post-event data has more snow cover than the pre-event data. The lighting conditions of the data are influenced by the season and terrain, with long shadows.

Geometry/size:

The Hyestranda event has occurred in a steep north-northeast facing slope, with the top half inclined 45-90 degrees, and the bottom half 25-45 degrees (ref. NVE map data). The Ommedal event occurred in a south-west facing slope, most of the slope inclining 25-45 degrees. The size of the events is unknown, but they have been reported to close a stretch of road with a length of 10-50 meters and 50-100 meters respectively.

Quaternary geology and geological conditions (Ref. NGU map data):

The area around Hyestranda is classified as *humus cover/thin peat cover over bedrock.* The area surrounding the Ommedal event is classified as colluvium and fluvial deposits. The Gloppen area is characterized by large amounts of exposed bedrock, till and colluvium deposits, with some glaciofluvial and fluvial deposits.

Possible causes why the landslide is undetected in S2-data:

Clearly defined gully streams can be detected at the reported locations in the S2-data. The events should possibly be classified as debris flows. Pictures from regObs show a small debris fan of coarse material (cobble/gravel) accumulated on a road, as well as a large amount of water. By using the road as a reference, the debris fan is possibly around 10 meters wide, and too small to be detected in S2-data. The Ommedal event looks to have material which has shaved or covered vegetation, as seen in the regObs pictures. The extent of the displaced material is possibly too narrow, but cannot be determined from the pictures. The seasonal variations and the long shadows make change detection and interpreting terrain features from the individual datasets difficult.

Name / Type	Falla / Debris avalanche			
Date	20.01.2017			
Area	Surnadal, Møre og Romsdal			
Ref. ETRS89, UTM 33N (Reported location)	E: 183744	N: 6978059		
S2-data acquisition dates	Previsit:	Pre event:	Post event:	Revisit:
	-	17.11.16	16.04.2017	-

Type and possible trigger:

The event is classified as a debris avalanche. The maximum accumulated snowmelt and precipitation for the 7 preceding days at the reported coordinates are reported in *xgeo.no* to be 101 mm.

Satellite data:

Pre-event data is acquired from 64 days prior to the event, and the post-event data 86 days after. The two datasets have large seasonal variations with respect to lighting conditions, snow cover, and vegetation.

Geometry/size:

The debris avalanche has occurred on a small north-northwest facing slope. The average inclination of the slope is interpreted from NVEs inclination data to be roughly 15-25 degrees. The size of the landslide is unknown. A picture in the local newspaper shows the landslide scar (link in regObs), but the size is difficult to estimate. Vegetation is removed due to the displaced material.

Quaternary geology and geological conditions (ref. NGU map data):

The reported coordinates lie on an intersection between *"Marine fine-grained deposit, continuous cover, great thickness prevalent"*, *"fluvial deposit"*, *"exposed bedrock"* and *"colluvium, slide material"*.

Possible causes why the landslide is undetected in S2-data:

The two datasets have large seasonal variations, making change detection and interpretation of terrain features difficult. The size of the landslide is likely to be too small.

Name / Type	Ávžejávri / Debris avalanche			
Date	08.06.2017			
Area	Kautokeino, Finnmark			
Ref. ETRS89, UTM 33N (reported locations)	E: 825987	N: 7752075		
S2-data acquisition dates	Previsit:	Pre event:	Post event:	Revisit:
	-	27.05.2017	09.06.2017	-

Type and possible trigger:

Event classified as debris avalanche. The meteorological conditions leading up to the event were wet. Accumulated snowmelt and precipitation for the 7 preceding days at the reported coordinates are reported in *xgeo.no* to be 161 mm.

Satellite data:

The satellite data is acquired close to the data of occurrence. The pre-event data is acquired 12 days prior to the event. The post-event data is acquired 1 day after the event. The pre-event data has more snow cover and some cloud cover. The area of interest is cloud free. The lighting conditions appear similar between the two datasets for the area of interest.

Geometry/size:

The debris avalanche occurred in a west-southwest facing slope, with varying inclination. The peak inclination is between 25-45 degrees, and gradually flattening out towards the foot of the slope. The size is unknown. The widest width is estimated to be 20 m and the length of the landslide scar to be 30-40 meters using the truck in the regObs pictures as a 7m reference.

Quaternary geology (ref. NGU map data):

The area is predominated by large deposits of moraine material, with elements of glaciofluvial deposits and exposed bedrock.

Possible causes why the landslide is undetected in S2-data:

The event occurred in late spring, in the Northernmost part of the country. The spring season at the location starts late, and the satellite data reflects this. The spring thaw is occurring at the time, and a difference in snow cover can be seen between the two datasets. There is little green vegetation at the reported location, which can also be seen on the pictures in regObs. The displaced material has altered the terrain, but it is possible that the spectral signature of the displaced mass is too similar to the surrounding terrain. The size of the event should, in theory, be large enough to detect, but is maybe in the lower boundary, especially if there is no clear spectral signature from the landslide.

Name / Type	Setesdalsveien / Debris avalanche			
Date	30.09.2017			
Area	Kristiansand, Aust-Agder			
Ref. ETRS89, UTM 33N (Reported location)	E: 84709	N: 6473561		
S2-data acquisition dates	Previsit:	Pre event:	Post event:	Revisit:
	-	22.08.17	16.10.17	-

Type and possible trigger:

The event occurred after a big flood event in southern Norway, in the start of October 2017.

Satellite data:

Pre-event data is acquired 8 days prior to the event, and the post-event data 16 days after. The two datasets have similar seasonal conditions. The two datasets have somewhat different lighting conditions due to atmospheric effects.

Geometry/size:

The debris avalanche has occurred in a small depression, between housing areas. The slope is facing southeast, with an inclination of 15-25 degrees. The size is not reported, and difficult to estimate from the available pictures.

Quaternary geology (ref. NGU map data):

The slope is classified as a fluvial deposit, with a small deposit of glaciofluvial material close by. The area is characterized by large humus covered areas, with elements of fluvial, glaciofluvial and moraine material.

Possible causes why the landslide is undetected in S2-data:

The size of the landslide is believed to be too small. The area of the landslide has elements of vegetation and infrastructure which complicate the satellite data interpretation. The area of interest appears to be shadowed in the post-event data.

Name / Type	Saga / Debris avalanche			
Date	02.10.2017			
Area	Vennesla, Aust-Agder			
Ref. ETRS89, UTM 33N (Reported location)	E: 85672	N: 6475590		
S2-data acquisition dates	Previsit:	Pre event:	Post event:	Revisit:
	-	12.08.17	06.10.17	-

Type and possible trigger:

The event occurred after a big flood event in southern Norway, around the start of October 2017.

Satellite data:

Pre-event data is acquired 55 days prior to the event, and the post-event data 4 days after. The two datasets have similar seasonal conditions. The two datasets have different lighting conditions, possibly due to atmospheric effects.

Geometry/size:

The debris avalanche occurred on a gentle northwest facing slope. The larger part of the slope has an inclination between 10-15 degrees, with a small peak area inclined 15-25 degrees.

Quaternary geology (ref. NGU map data):

The reported coordinates are between a moraine deposit and a fluvial deposit. The size of the landslide is unknown. From regObs pictures, it seems to have shaved vegetation. The size is difficult to estimate from the pictures.

Possible causes why the landslide is undetected in S2-data:

The size of the landslide is possibly too small. The area of the landslide has elements of vegetation and infrastructure which complicate the satellite data interpretation.

Name / Type	Luster / Multiple debris flows			
Date	02.10.2017			
Area	Luster, Sogn og Fjordane			
Ref. ETRS89, UTM 33N (Reported locations)	E: 104227 105424 106008 112582	N: 6836862 (1) 6837850 (2) 6838378 (3) 6841895 (4)		
S2-data acquisition dates	Previsit:	Pre event:	Post event:	Revisit:
	-	23.09.17	09.10.17	-

Type and possible trigger:

Multiple events classified as debris flows, occurring in the same area at the same date. The maximum accumulated snowmelt and precipitation for the 7 preceding days at the reported coordinates are reported in *xgeo.no* to be 50 mm for all locations. RegObs registrations describe intense precipitation and river flooding prior to the events. Events (1)-(3) occurred along the *Lustrafjord,* event (4) occurred just northeast of the fjord, in *Fortunsdalen.*

Satellite data:

Pre-event data is acquired 9 days prior to the day of occurrence. Post-event data is acquired 7 days after. There is little variation between the two datasets at the areas of interest. The shadows are somewhat longer in the post-event data.

Geometry/size:

Debris flows (1)-(3) occurred in a steep northwest-facing slope. Roughly 50 % of the slope has an inclination of 45-90 degrees and the other half 25-45 degrees. The size of the debris flows is unknown. The removed material from the road from the event (2) is estimated to 1500 m^3 by the contractor (see comment in regObs). Pictures from regObs show a substantial amount of material accumulated in debris fans, possibly 20+ meters wider using the road as a reference. The exact location of the event (4) is not known, but the reported location lies in a steep northwest facing slope, with the same characteristics as mentioned above. No photos or description of magnitude is available.

Quaternary geology (ref. NGU map data):

The reported coordinates are all positioned in colluvium deposits. The quaternary geology of the area is characterized mostly by exposed bedrock, deposits of weathered material and colluvium.

Possible causes why the landslide is undetected in S2-data:

All events are situated in steep northwest facing slopes, resulting in shadowing from the terrain. The satellite data is acquired close to the date of occurrence, but the debris flows are possibly too small to have been detected. It is unknown how much vegetation that has been removed, or if the events have altered the terrain significantly. The area is believed to be exposed to frequent debris flow activity (portals have been constructed to shield the road + many regObs observations nearby) – The displaced material from these events may possibly not alter “fresh” terrain, but terrain originating from previous debris flow activity.

C.4 References

FRANK, E., SIRI, E. & CAMILLA, B. 2015. Nattoget Bergen-Oslo passerte en knapp time tidligere: Bergensbanen i løse luften. *VG*. Available: https://www.vg.no/nyheter/innenriks/i/xLP2G/nattoget-bergen-oslo-passerte-en-knapp-time-tidligere-bergensbanen-i-loese-luften [Accessed 08.04.2018].

FREKHAUG, M. H. 2016. Notat: E14 Reinåa. Statens Vegvesen.

KRISTOFERS, J. 2017. Notat: Jordskred i Spansdalen, Fv. 84. Statens Vegvesen.

NVE. 2015. *regObs registration 65514* [Online]. Available: http://www.regobs.no/Registration/65514 [Accessed 15.05.2018].

NVE. 2017a. *regObs registration 126553* [Online]. Available: http://www.regobs.no/Registration/126553 [Accessed 21.05.2018].

NVE. 2017b. *regObs registrering 128325* [Online]. Available: http://www.regobs.no/Registration/128325 [Accessed 21.04.18].

NVE. 2017c. *regObs registrering 128393* [Online]. Available: http://www.regobs.no/Registration/128393 [Accessed 13.04.2018].

RESE, S. W. 2016. Notat Fv. 45 Hunnedalsveien, Mjåland. Multiconsult.

STATENS VEGVESEN. 2015. *regObs registrering 66293* [Online]. Available: http://www.regobs.no/Registration/66293 [Accessed 08.04.2018].

STATENS VEGVESEN. 2016. *regObs registrering 100133* [Online]. Available: http://www.regobs.no/Registration/100133 [Accessed 12.04.2018].

STATENS VEGVESEN. 2017. *regObs registrering 120366* [Online]. Available: http://www.regobs.no/Registration/120366 [Accessed 21.05.2018].

ÅNDALSNES AVIS. 2011. *200 meter bredt jordras øverst i Romsdalen* [Online]. Available: https://www.andalsnes-avis.no/nyheter/article347475.ece [Accessed 13.04.2018].

D. APPENDIX D – Spectral Signatures

The spectral signature of all detected events are examined along a transect. The transects is manually lineated and is placed as a centerline in the detected events. The reflectance from the VNIR-bands, and values from resulting NDVI and ratios are given in the following chapters. The location of the pixels with their corresponding numbers are given in the images as a reference. It should be noted that the NDVI is given it same plot as the reflectance of the VNIR-bands and is derived from the NIR and red bands.

D.1 Event 1 – Lindelia

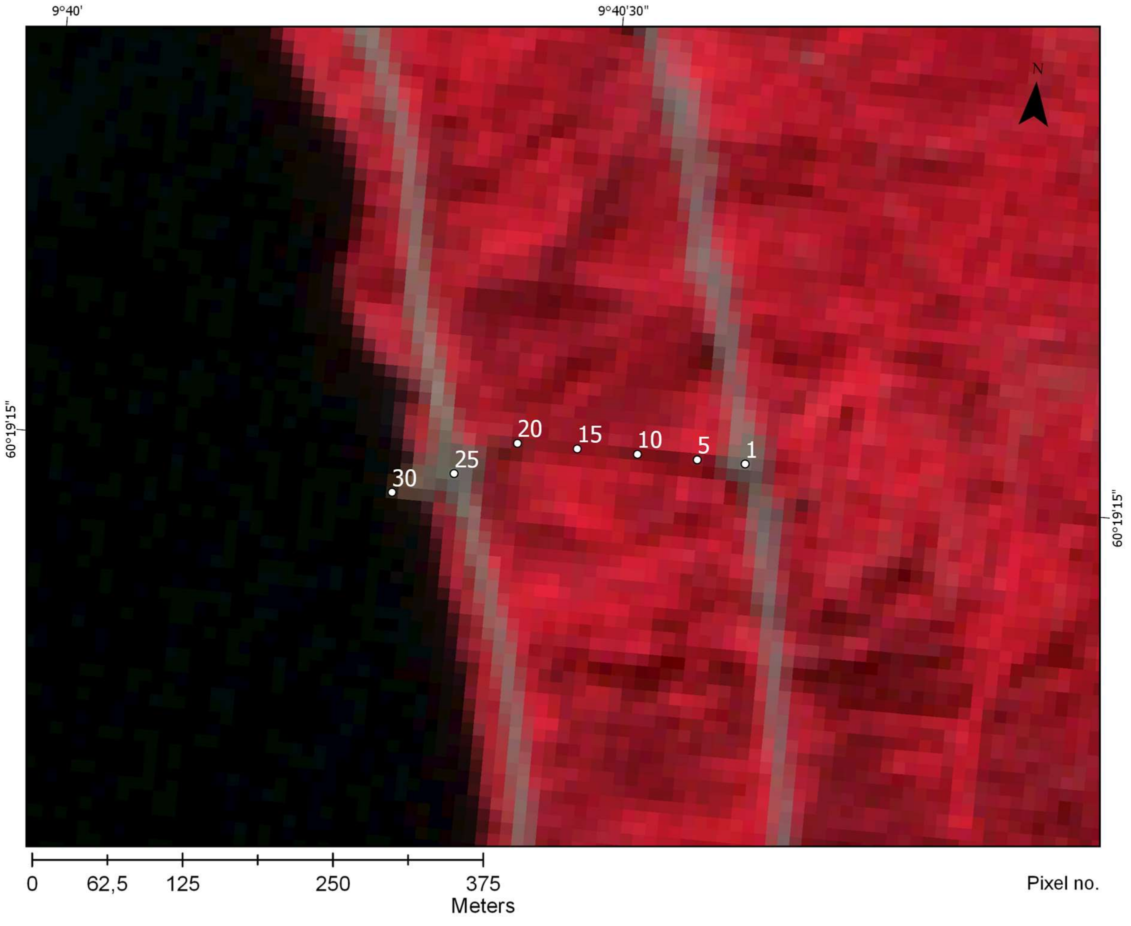

The transect is manually lineated from an NDVI image of the post-event data. Pixel 1 is starting at the Bergensbanen railroad. The transect crosses the road at ca. pixel 25. The displaced material ends up in the lake Krøderfjorden. The narrow section between pixels 3-23 has an NDVI ranging from 0.60 - 0.72, indication large amounts of vegetation. The NDVI is the lowest in the start of the transect, and where it crosses the road. The pixels 26-30 has a specific signature and should be considered representative for the landslide.All NDVI-ratios vary between: 0.57 – 3.84 The RGB-ratios vary from 0.85 – 1.01. The NIR-ratios vary from 1.27 – 1.54

D.1.1 VNIR & NDVI

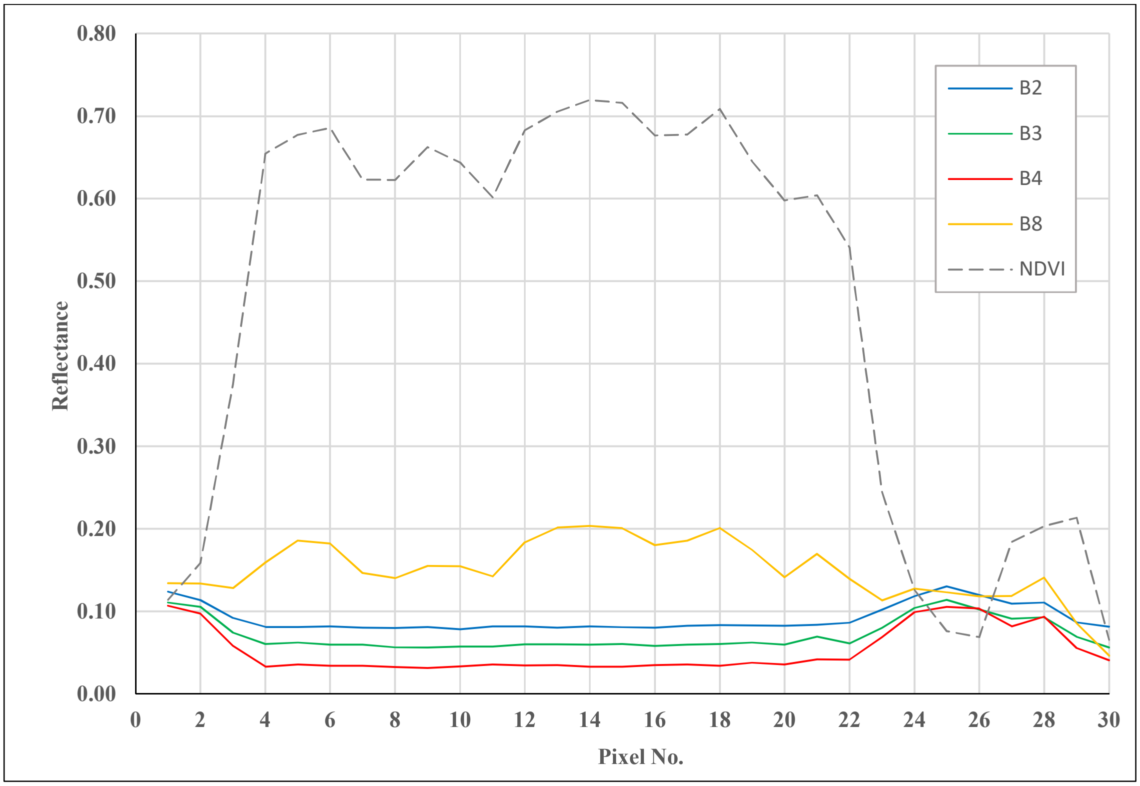

D.1.2 NIR- & RGB-ratios

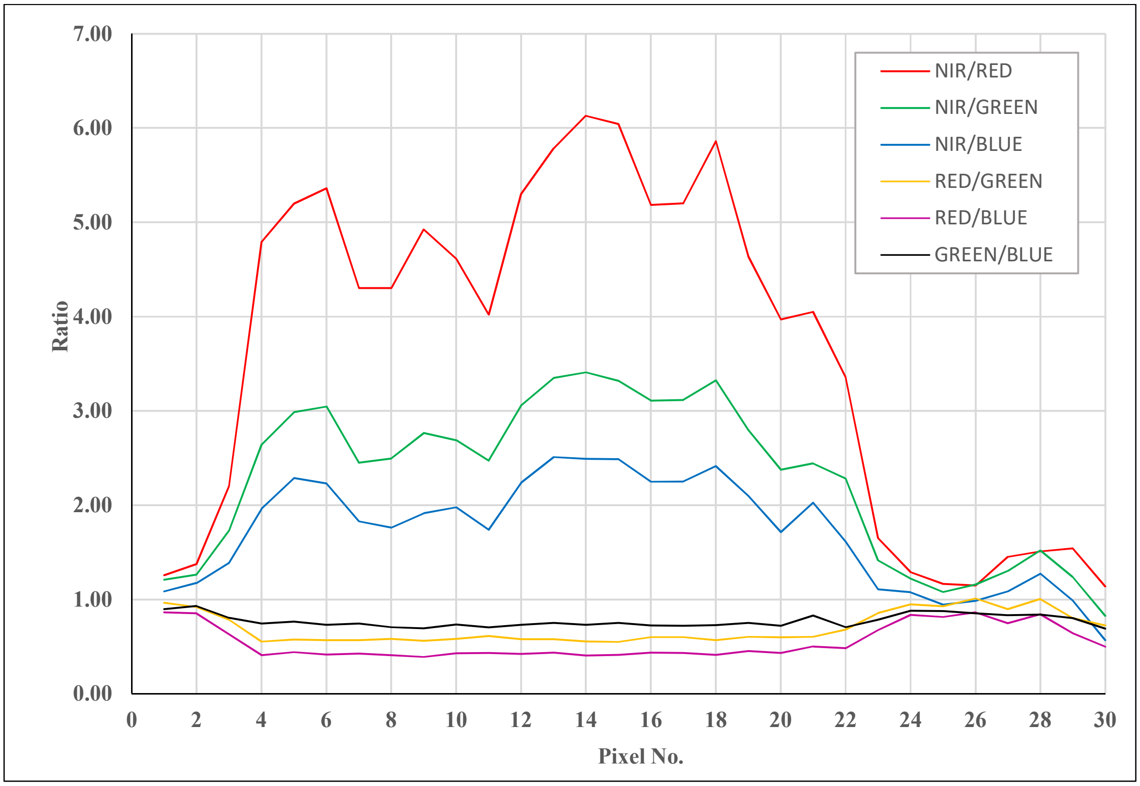

D.1.3 NDVI-ratios

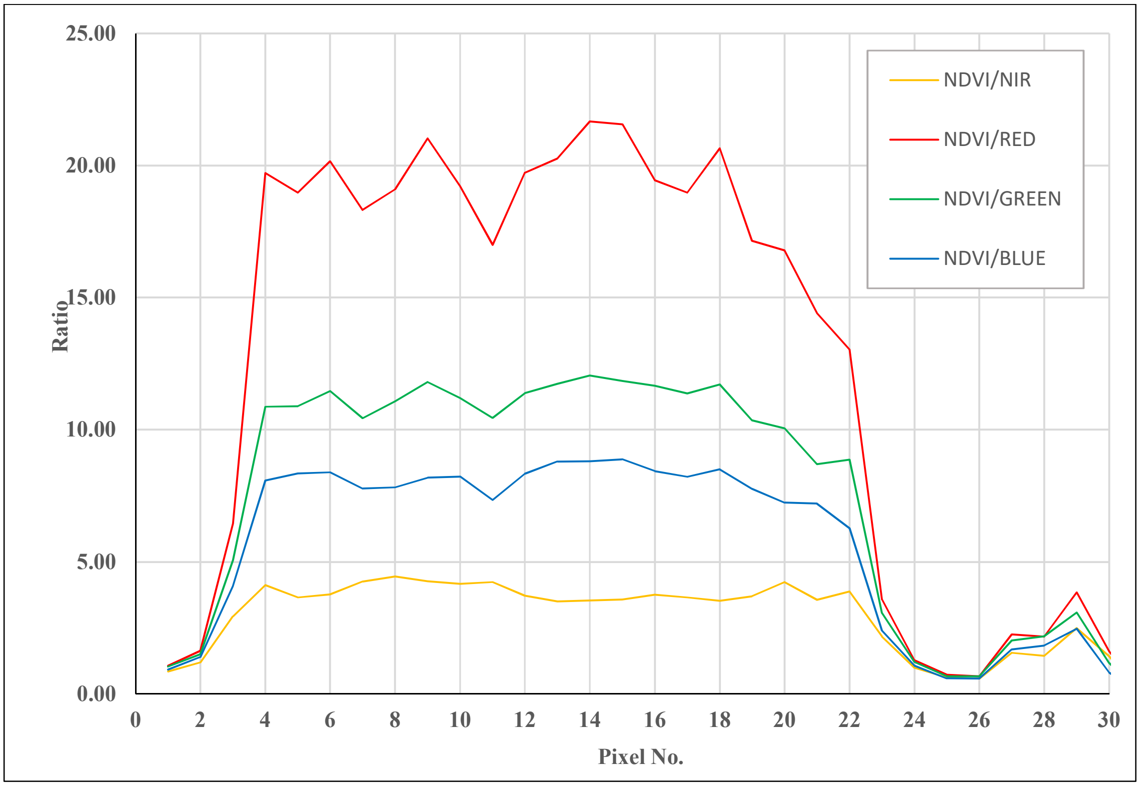

D.2 Event 2 – Hunnedalen

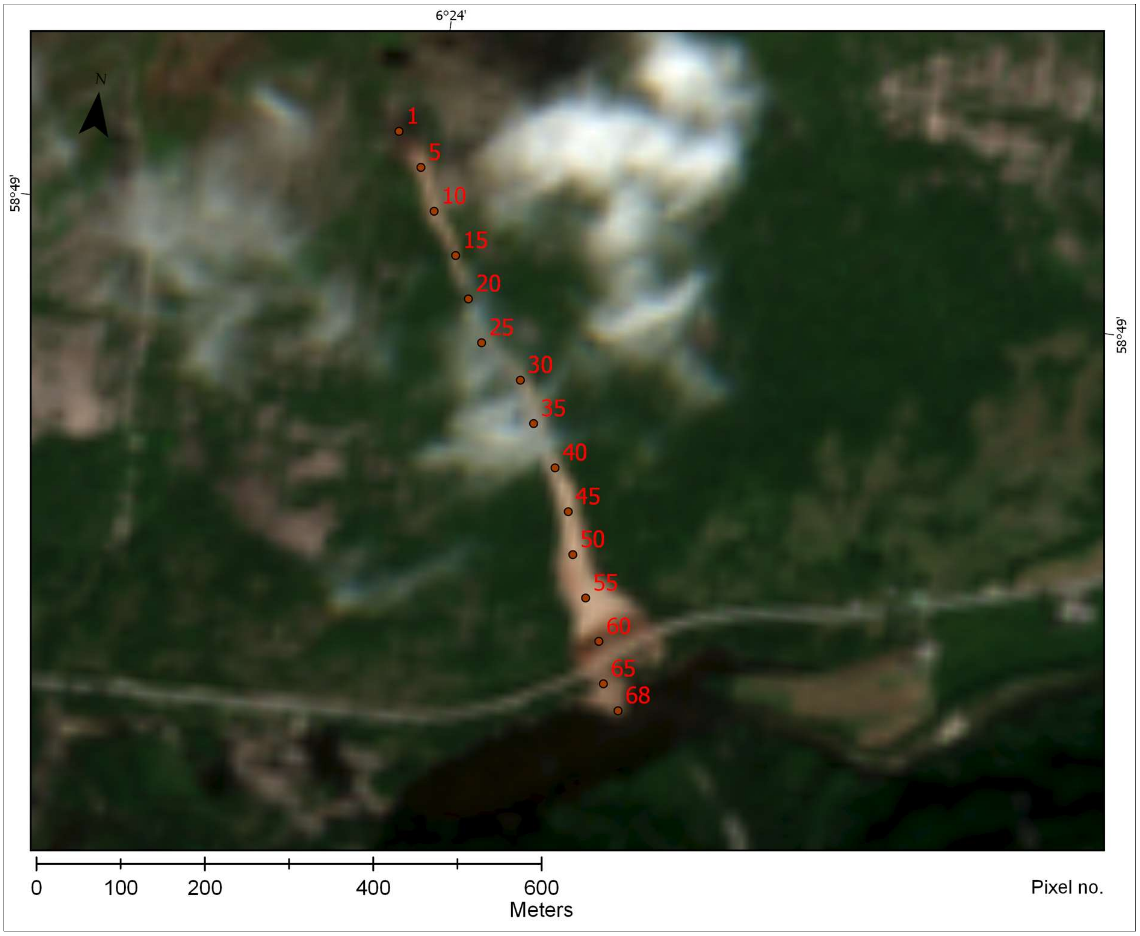

The debris flow follows gully stream ca. first 40 pixels, before widening out into debris fan. A thin cloud cover influence the pixels 20-40. This section also appear to be the narrowest part. It is uncertain if the high NDVI values in this section is solely due to vegetative cover, or cloud influenced values. Some variation can be seen around pixel 60 as darker brown pixels in the NCC, possibly due to the clean-up process of removing material from the road. The road intersects at pixel 62-63. The most representative landslide pixels are considered to be the sections 1-20 (1) and 20-68 (2):

NDVI varying from 0.18 – 0.43 in the section (1), and the NDVI is below 0.20 the entire section (2).

NIR reflectance is fluctuating around 0.3 in the “brightest” pixels (#40-58), while dropping to 0.17 at the browner pixels (#60). The visible bands show the same trend, and have relative little variation. The green and blue band have approximately the same reflectance, yielding a GREEN/BLUE-ratio fluctuating around 1.0

The NIR-ratios vary from 1.19 – 2.28, and the RGB ratios range 0.83 – 1.31.

D.2.1 VNIR & NDVI

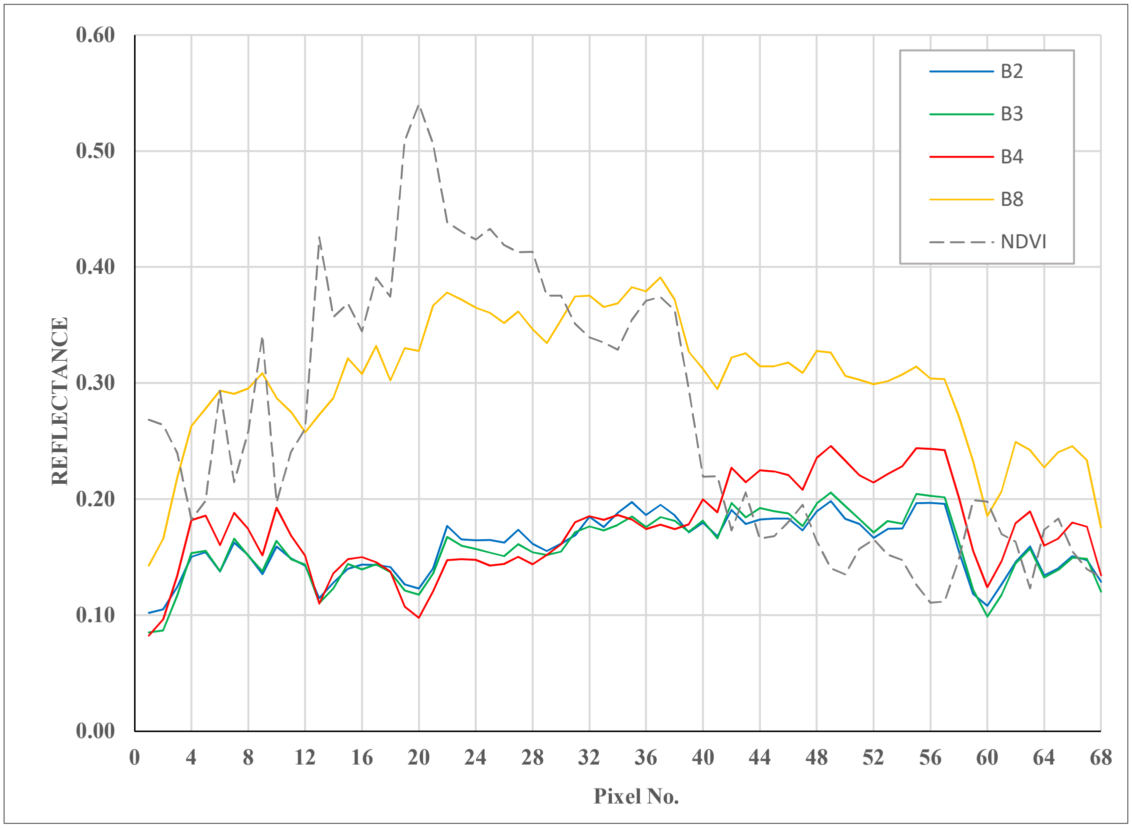

D.2.2 NIR- & RGB-ratios

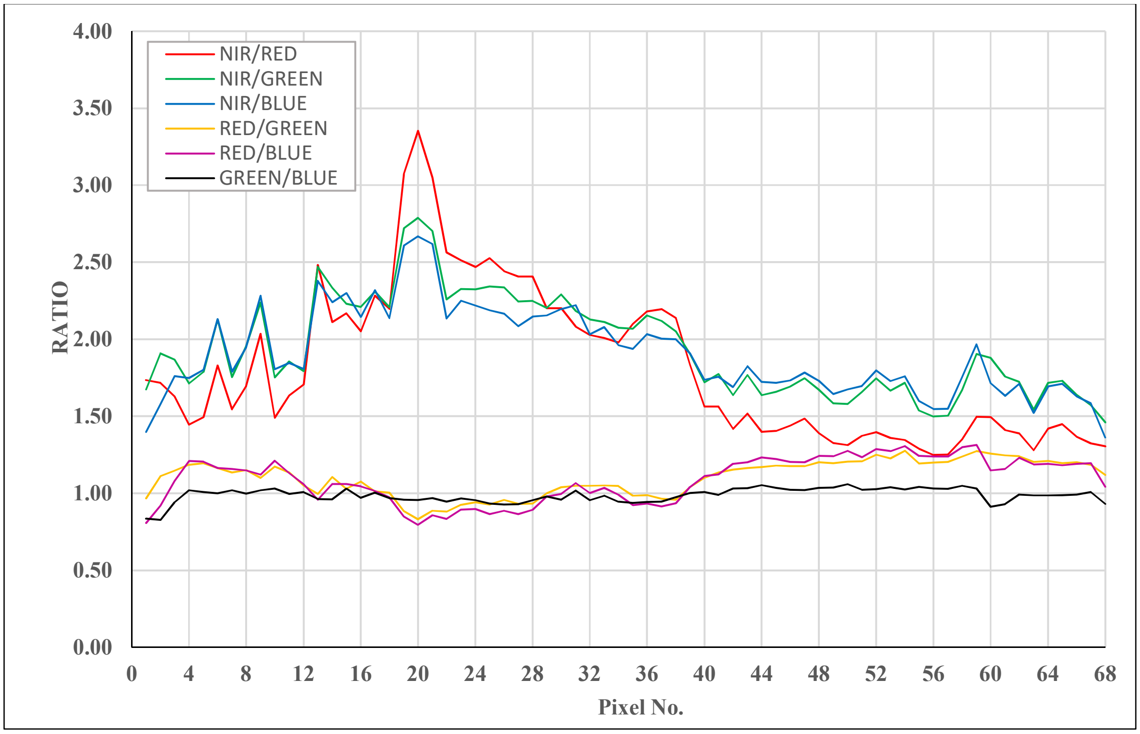

D.2.3 NDVI-ratios

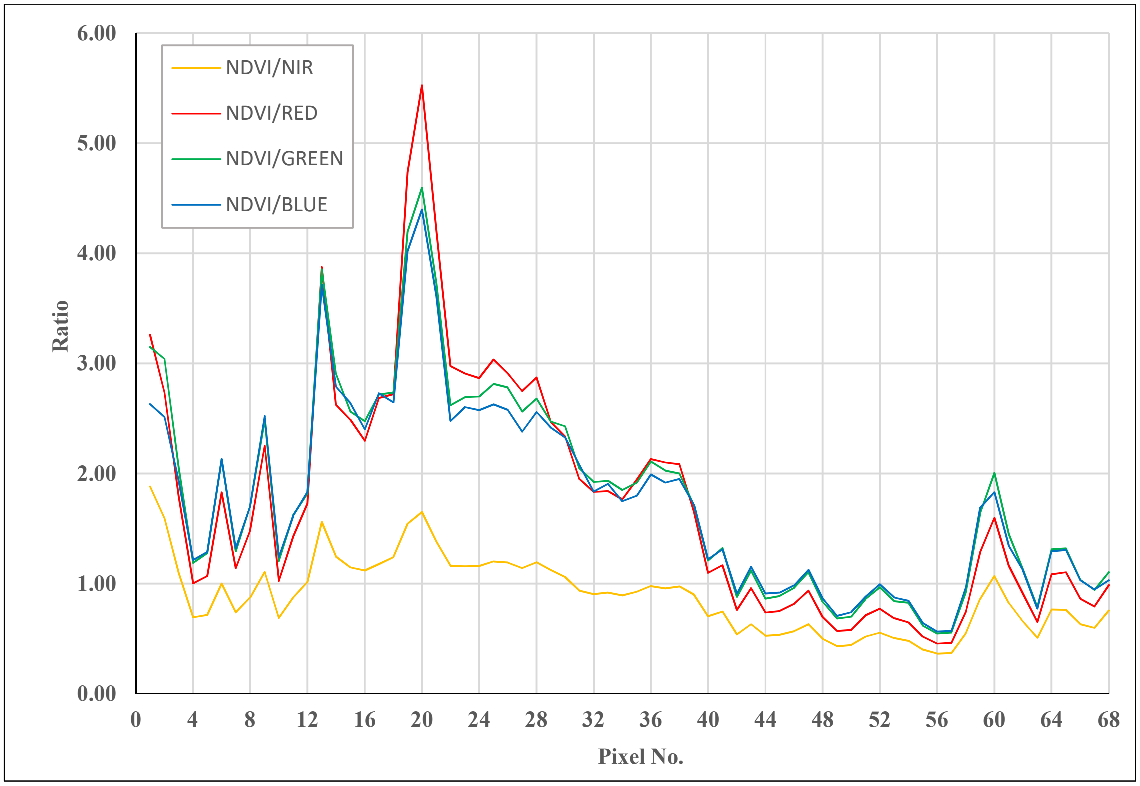

D.3 Event 3 – Kommedal

A relatively small event, with some uncertainty regarding if the first few pixels are due to landslide activity. The landslide is roughly 3 pixels at its widest.

The transect has a large span in the NDVI signature, possibly due to the fact that it is a small feature in the satellite data. The pixels 6-14 shows clearest signature of least vegetation. The VNIR-bands show little variation.

The RGB-ratios are all below 1.0.

The NDVI-ratios vary between 5.16 – 1.52 between pixels 6-14, and peaks at almost 17.0 in the most vegetated part of the transect.

The NIR-ratios vary from almost 1.3 to almost 5.0.

D.3.1 VNIR & NDVI

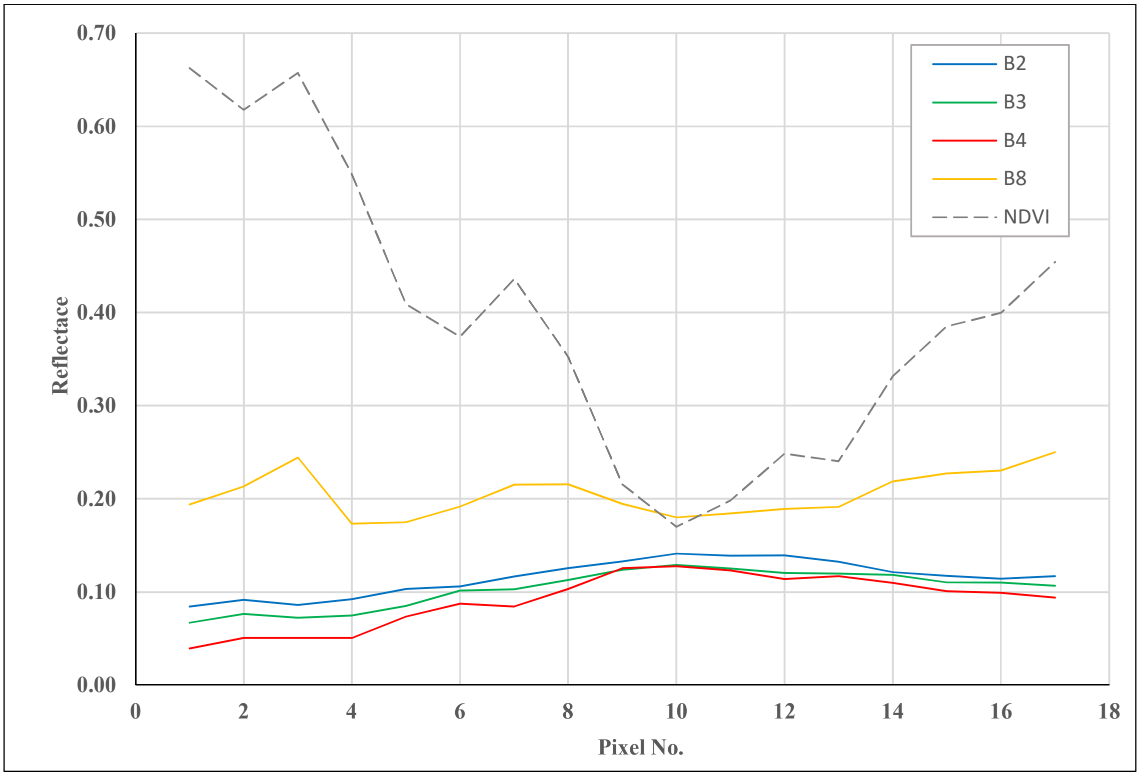

D.3.2 NIR- & RGB-ratios

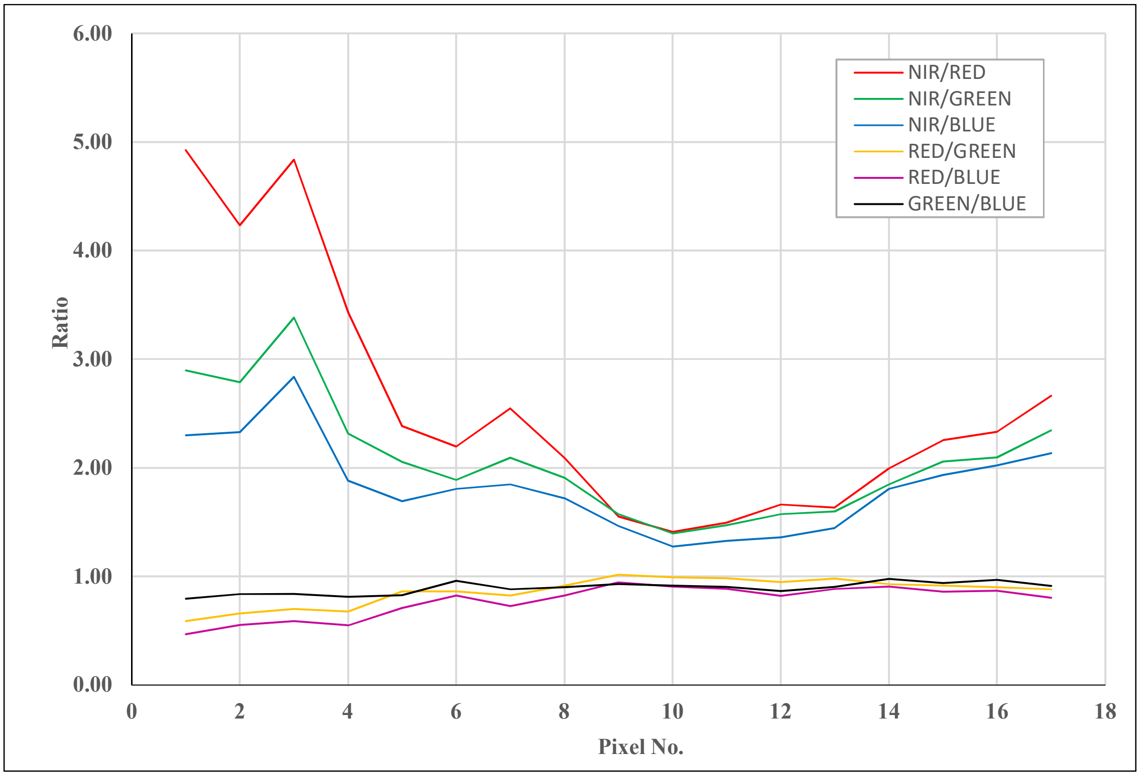

D.3.3 NDVI-ratios

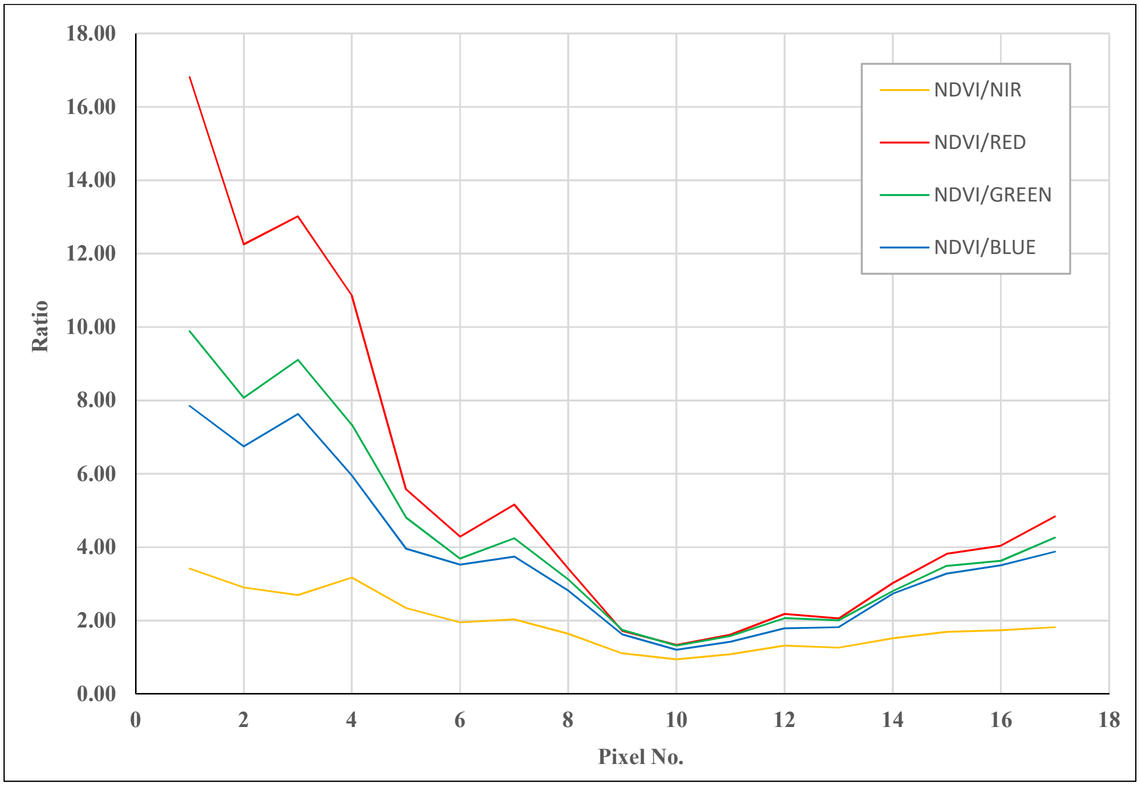

D.4 Event 4 – Øksland

Parts of the landslide area is somewhat shadowed. The landslide is v-shaped – The landslide scar is approximately 1 pixel wide from pixels 1-7. The transect end at the end of the road.

The first 8-10 pixels of the transect is more influenced by vegetation, than the remainder. The wider part of the landslide has an NDVI below or equal to 0.21.

The RGB-bands have an almost constant reflectance along the transect. The NIR band show relatively little variance, ranging from 0.03 – 0.09.

The RGB-ratios are all below 1.0.

The NIR-ratios vary from almost 3.2 – 0.5.

The NDVI-ratios vary between 1.7 – 0.5 from pixel 8 and out. The NIR/RED peaks at roughly 18.0 in the most vegetated part of the transect, not surprisingly as these are the components of the NDVI, and are bands sensitive to the spectral signature of vegetation.

D.4.1 VNIR & NDVI

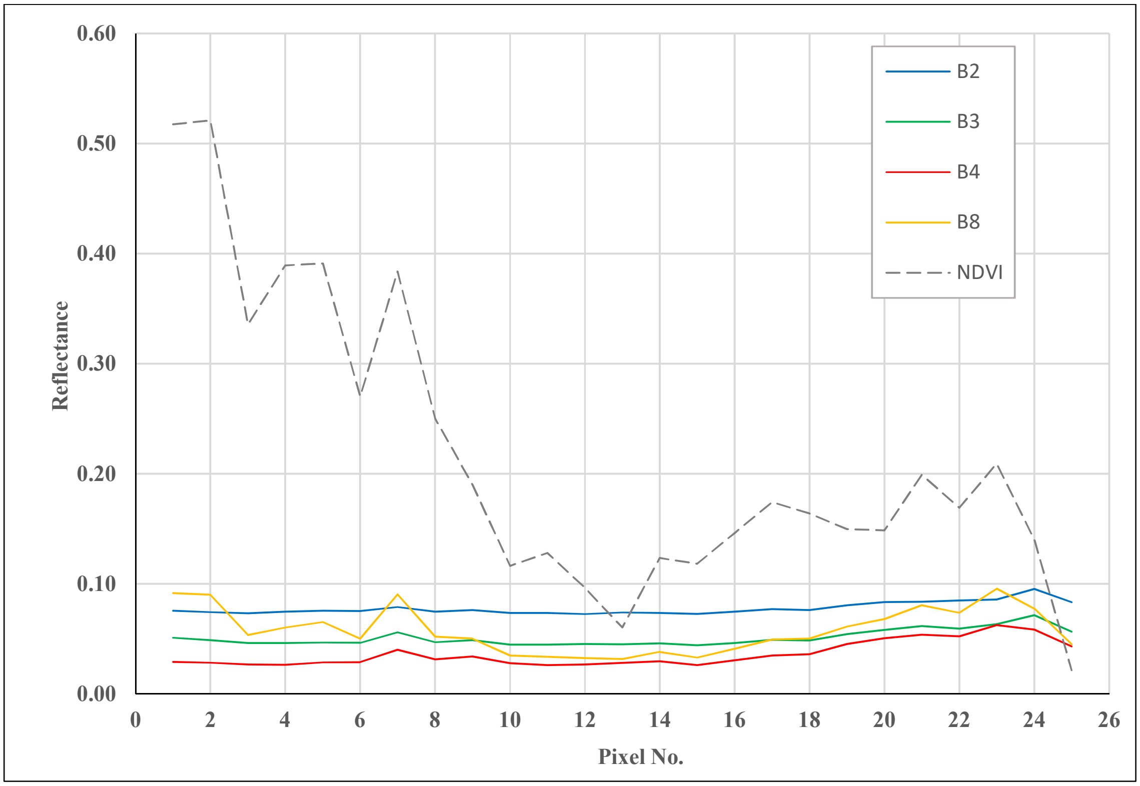

D.4.2 NIR- & RGB-ratios

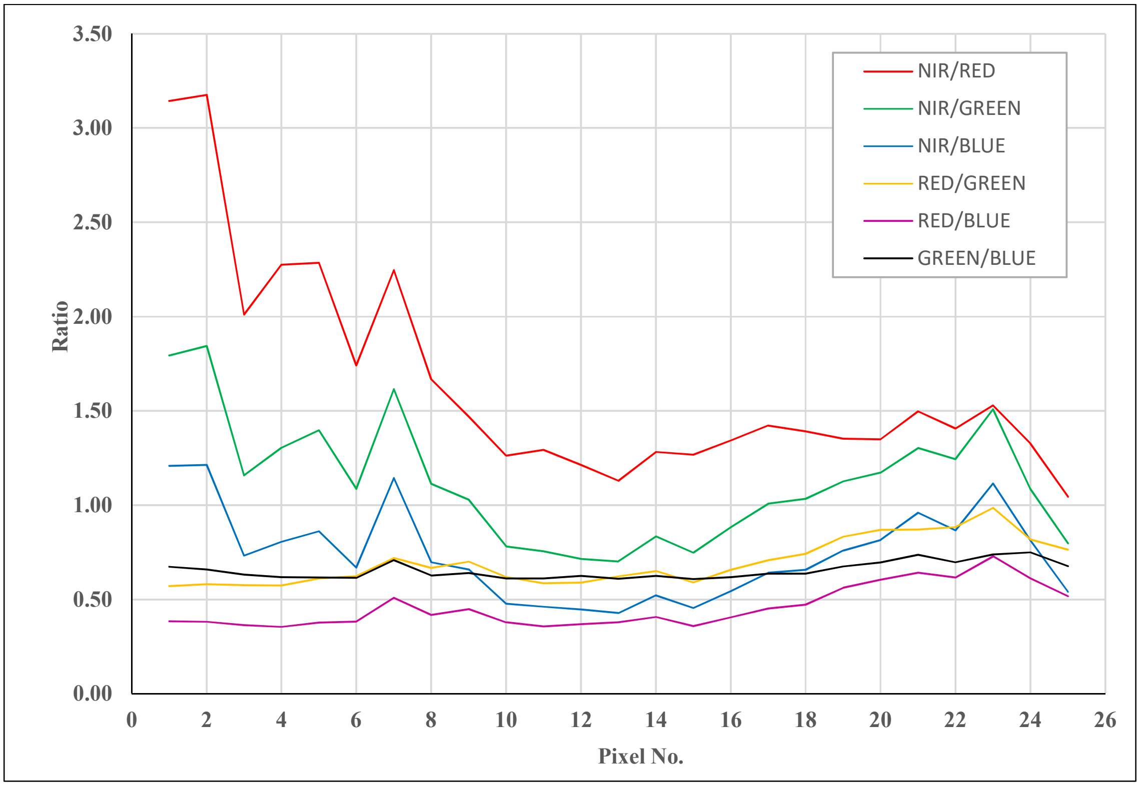

D.4.3 NDVI-ratios

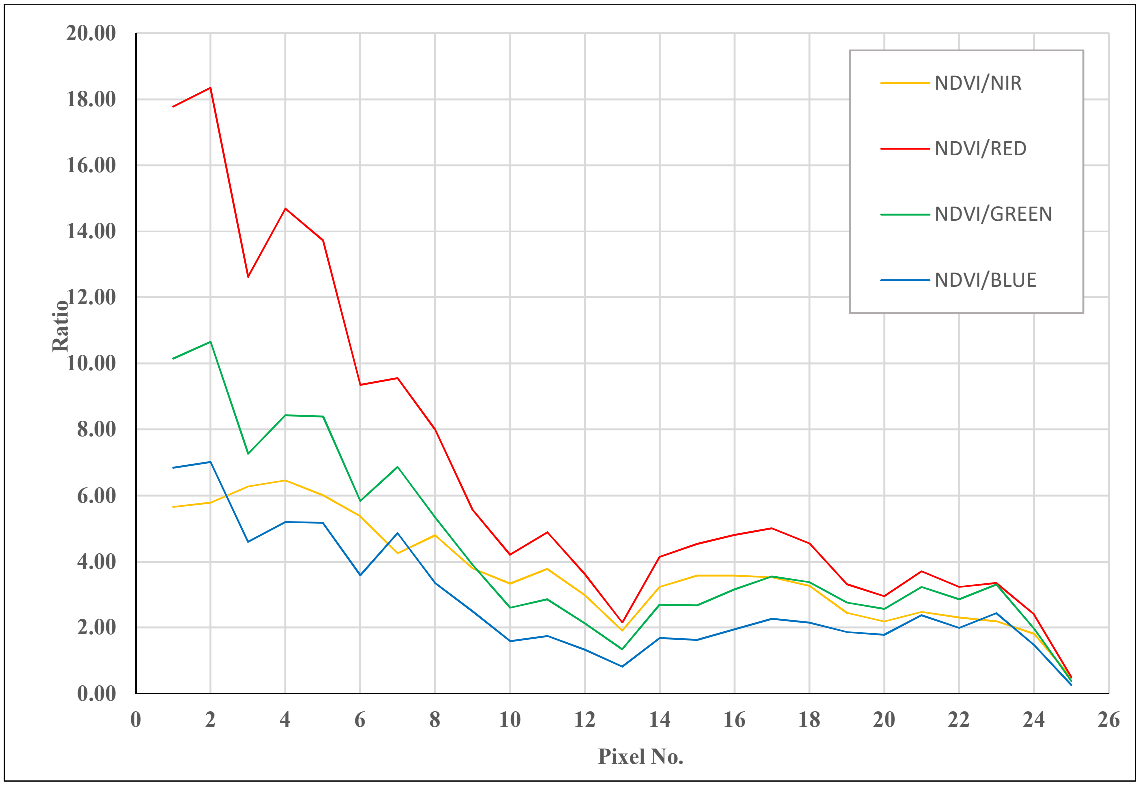

D.5 Event 5 – Slettafossen

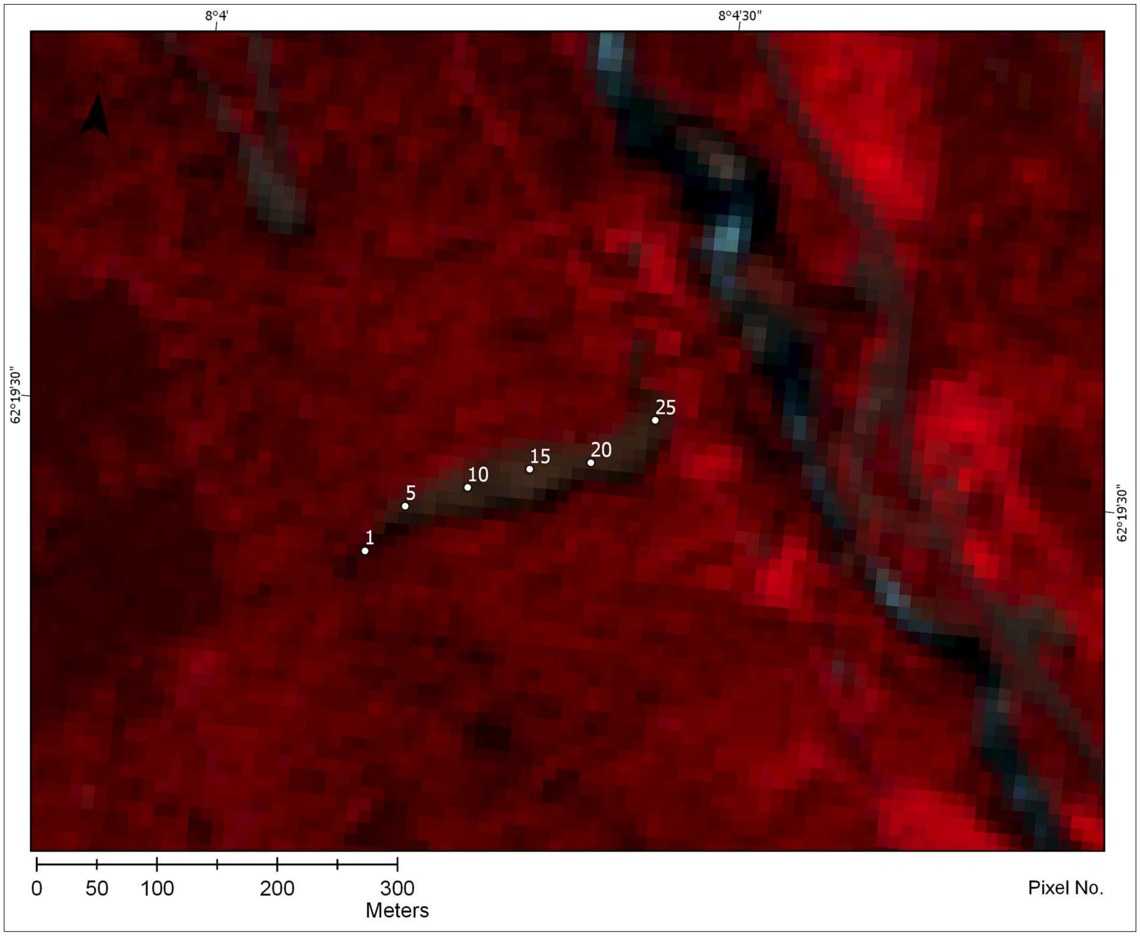

V-shaped landslide scar, with plenty of surrounding vegetation. The landslide is roughly 8 pixels wide at widest. No infrastructure or special features appear to affect the landslide-area.

The "main" (pixel #6-24) body has an NDVI less than 0.20. The NDVI peaks at the start and end of the transect, possibly due to the narrow shape in the start, and that the transects slightly extends the landslide scar.

The RGB-bands have slightly higher values in the pixel range 6-24, varying from 0.11 – 0.16. The NIR-band fluctuates more than the RGB-bands, but doesn't vary more than from 0.13 – 0.20.

The RGB-ratios are fluctuating around 1.0.

The NIR-ratios are fluctuating around 1.5, in the section #6-24.

The NDVI-ratios correlates to the NDVI, resulting in values around 1.5 in the #6-24 section, and peaks in the areas affected by vegetation.

D.5.1 VNIR & NDVI

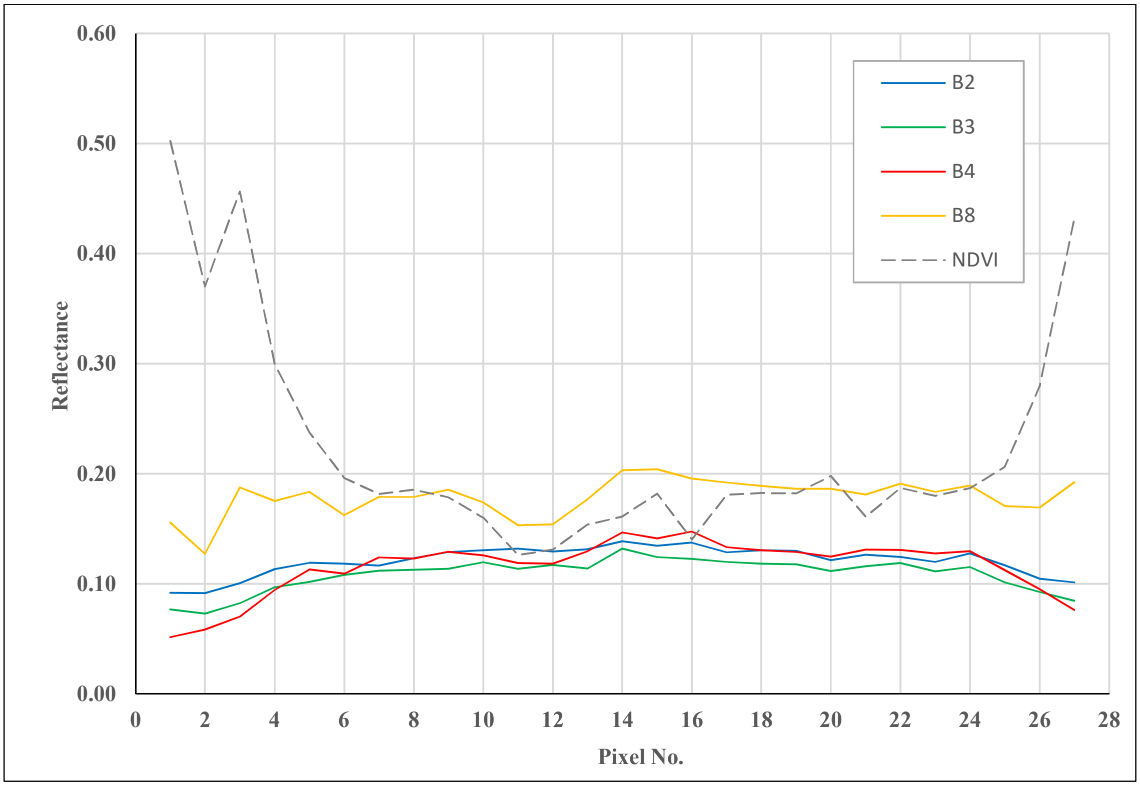

D.5.2 NIR- & RGB-ratios

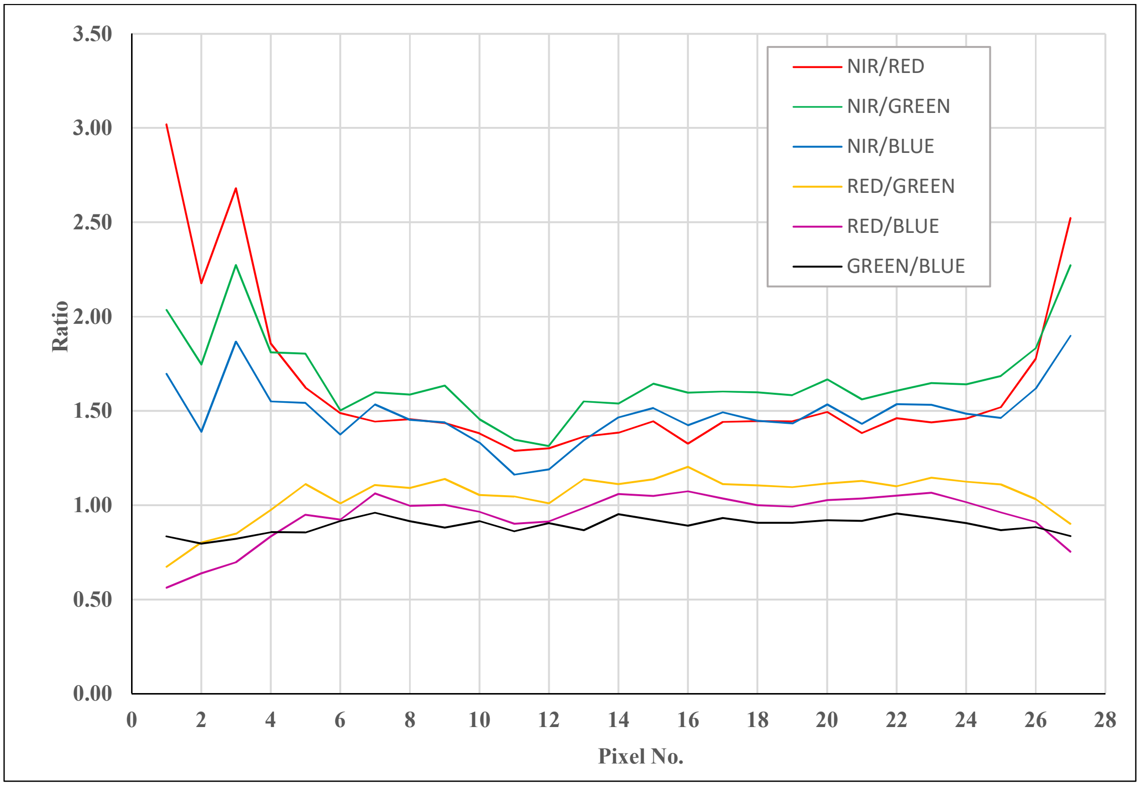

D.5.3 NDVI-ratios

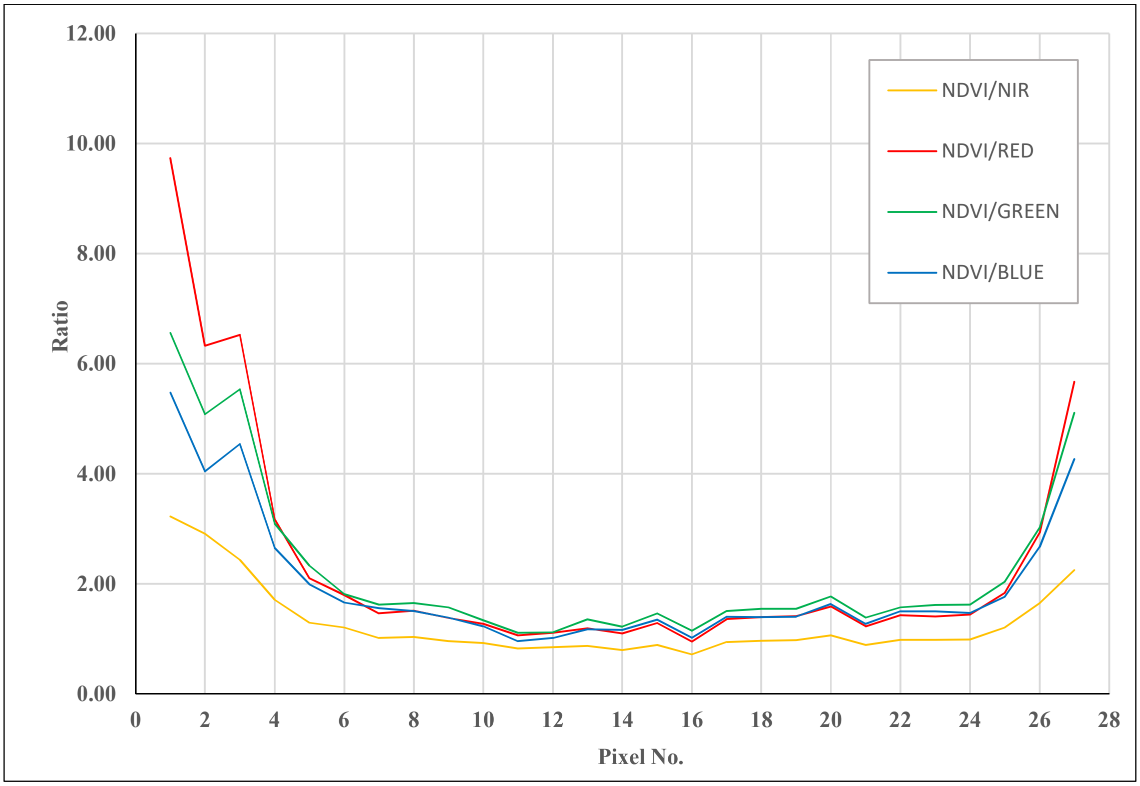

D.6 Event 6 – Kråkagjelet

The debris flow has followed a distinct gully in a steep mountain slope. The debris flow is relatively thin along the entire gully – Roughly between 3-6 pixels wide – before widening into a small fan at the foot of the slope. The fan has covered a river running at the valley floor.

The NDVI varies from 0.06 – 0.32. The NIR reflectance lies between 0.15 and 0.20 for the larger part of the transect. The RGB-bands have similar reflectance, ranging from 0.12 – 0.15 for the most part of the transect.

The RGB-ratios are fluctuating just below 1.0.

The NIR-ratios are fluctuating between 1.0 - 1.5, from pixel 12 and onwards.

The NDVI-ratio varies roughly from 0.5 – 4.0

D.6.1 VNIR & NDVI

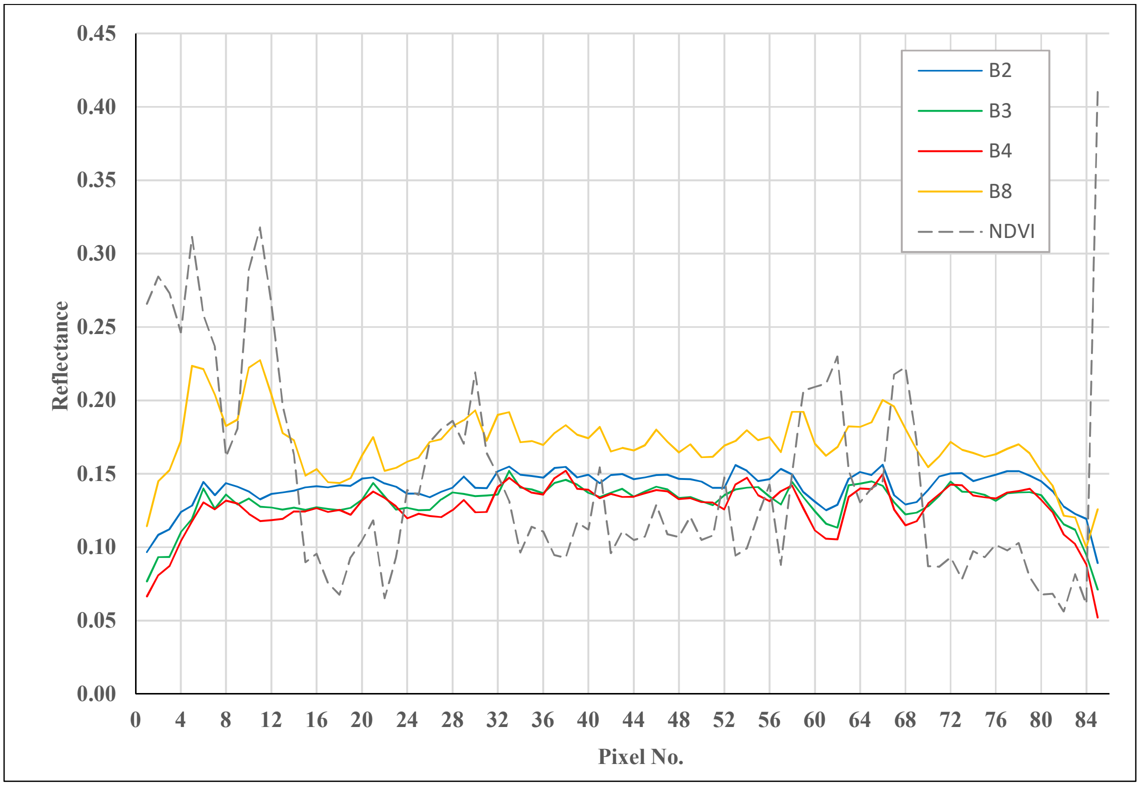

D.6.2 NIR- & RGB-ratios

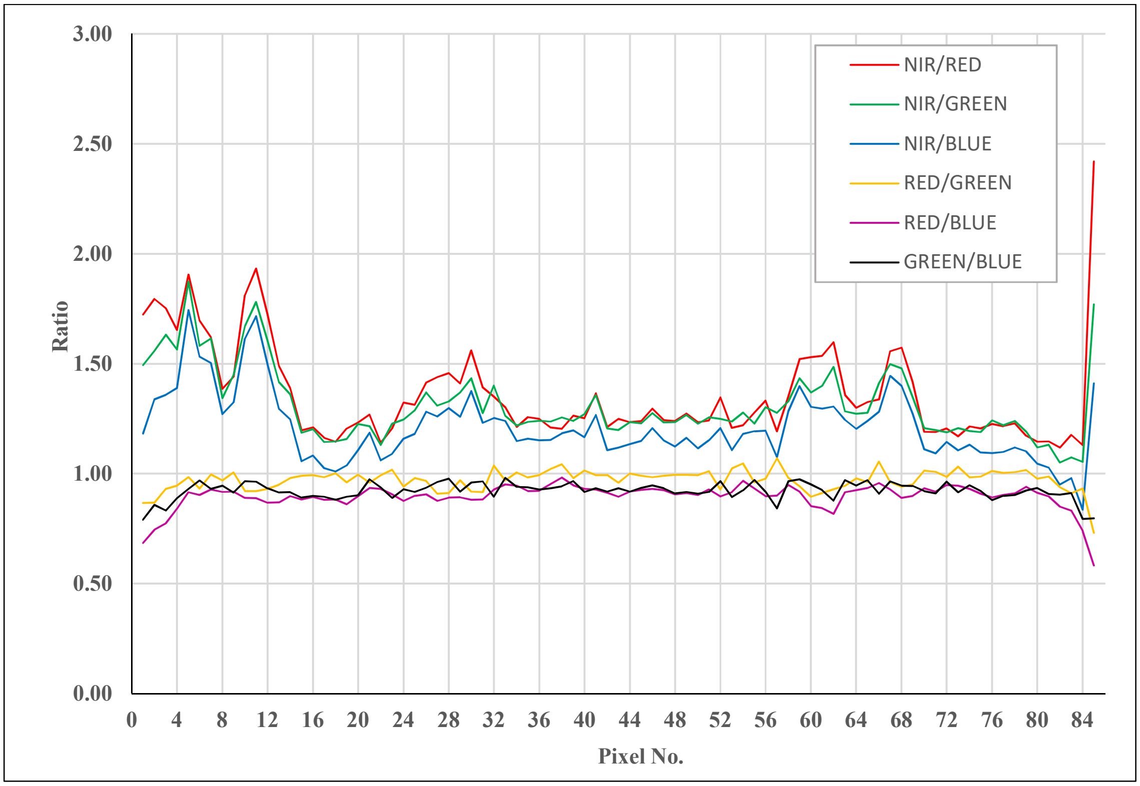

D.6.3 NDVI-ratios

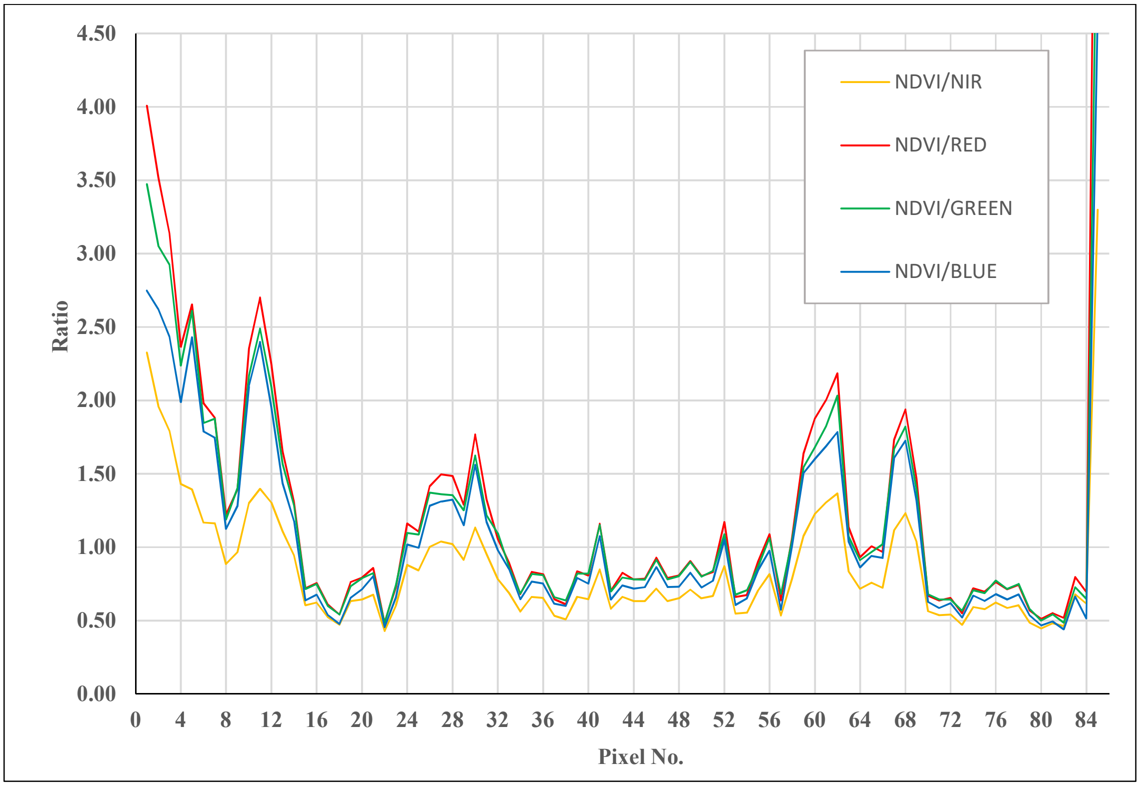

D.7 Event 7 – Spansdalen

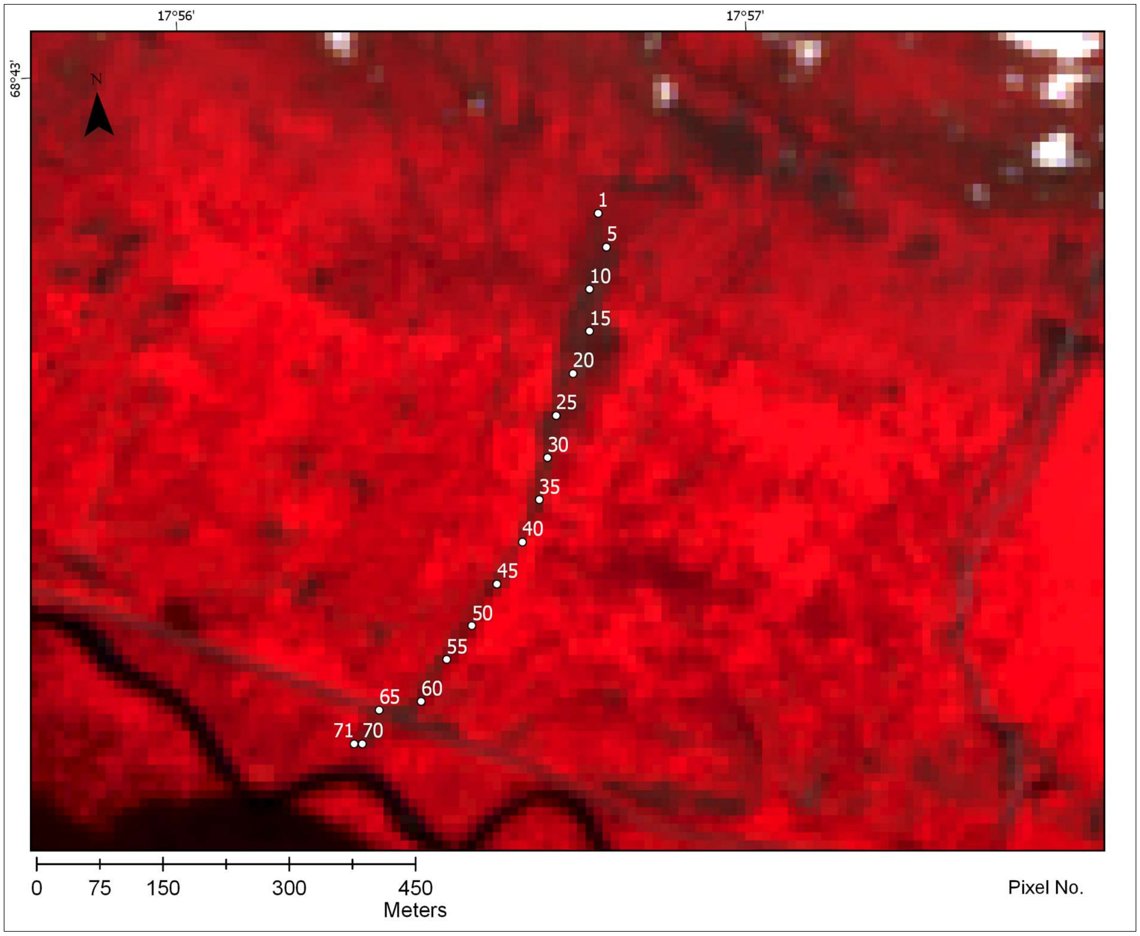

Shallow landslide, with a wider landslide scar at the top part of the slope, before possibly following a stream gully. The widest section is ranging from pixel 10-25. The narrowest section from 35-60, roughly 1-2 pixels wide. The transect crosses a road at pixel 65. The pixels 65-71 are downslope from the road.

The slope is vegetated, and the narrow sections show clear signs of being a highly vegetated. The NDVI varies from 0.22 to 0.81 along the transect.

The NIR bands follow the same tendency as the NDVI band, but with another magnitude, varying from 0.21 – 0.46 along the transect. The RGB-bands have a relatively constant reflectance along the transect, fluctuating around 0.10.

The RGB-ratios are fluctuating just below 1.0.

The NIR-ratios are fluctuating between 1.5 – 9.6.

The NDVI/NIR-ratio has a relative constant value around 2.0, while the other ratios fluctuate significantly more.

D.7.1 VNIR & NDVI

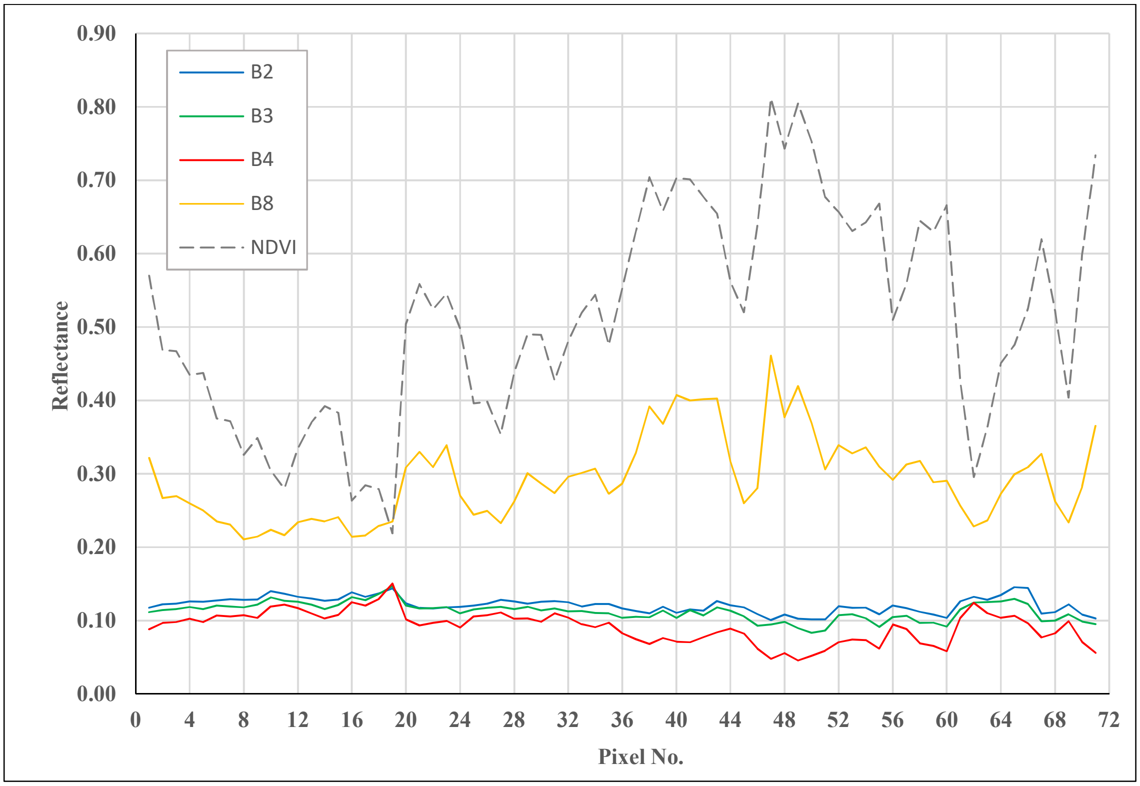

D.7.2 NIR- & RGB-ratios

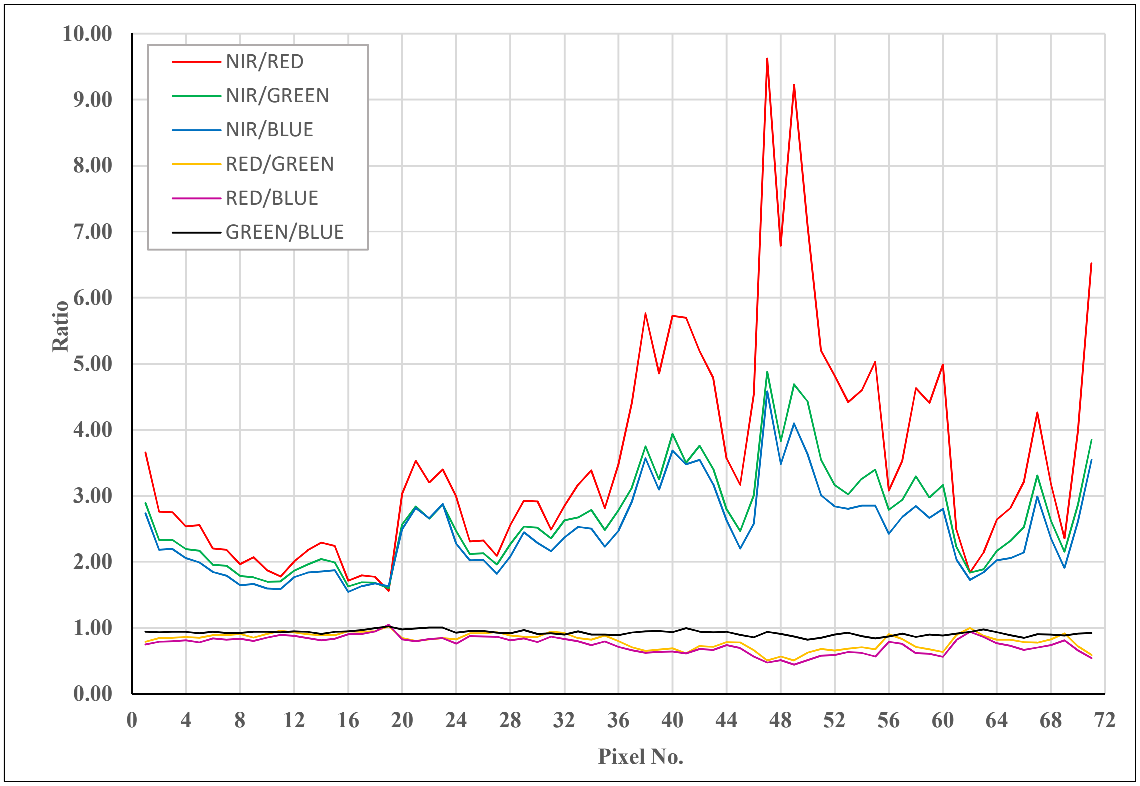

D.7.3 NDVI-ratios

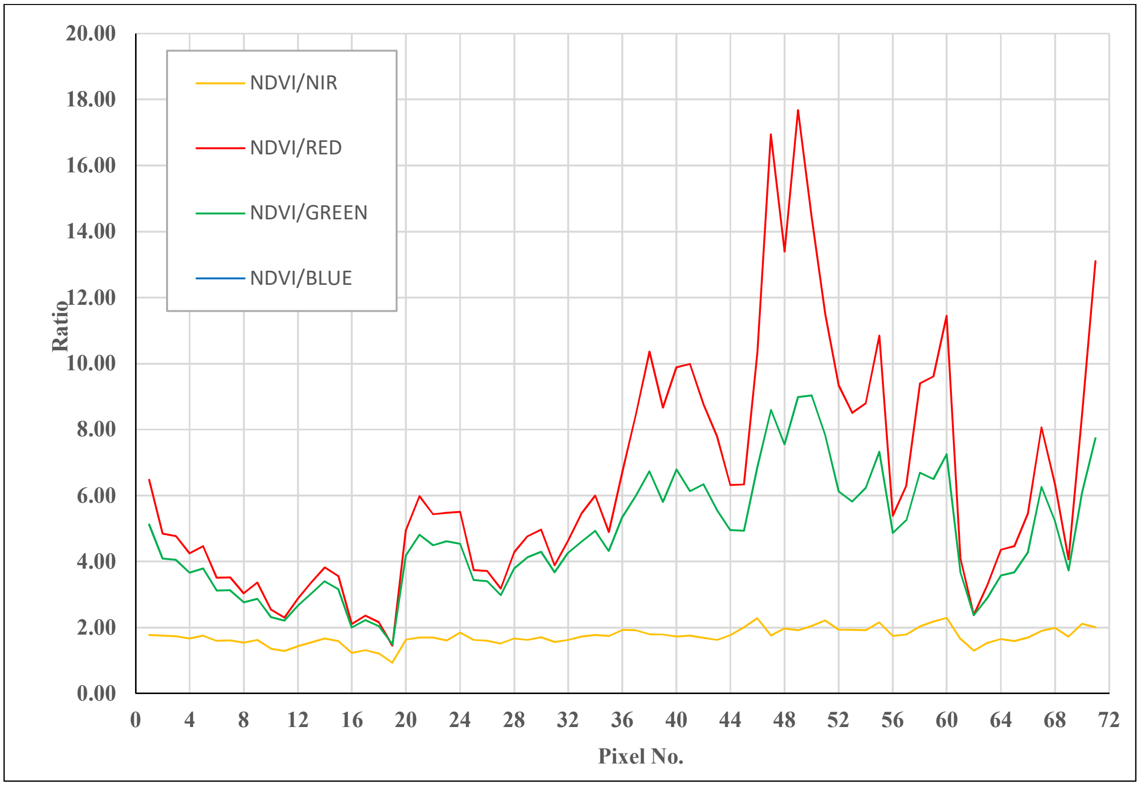

D.8 Event 8 – Selskreda

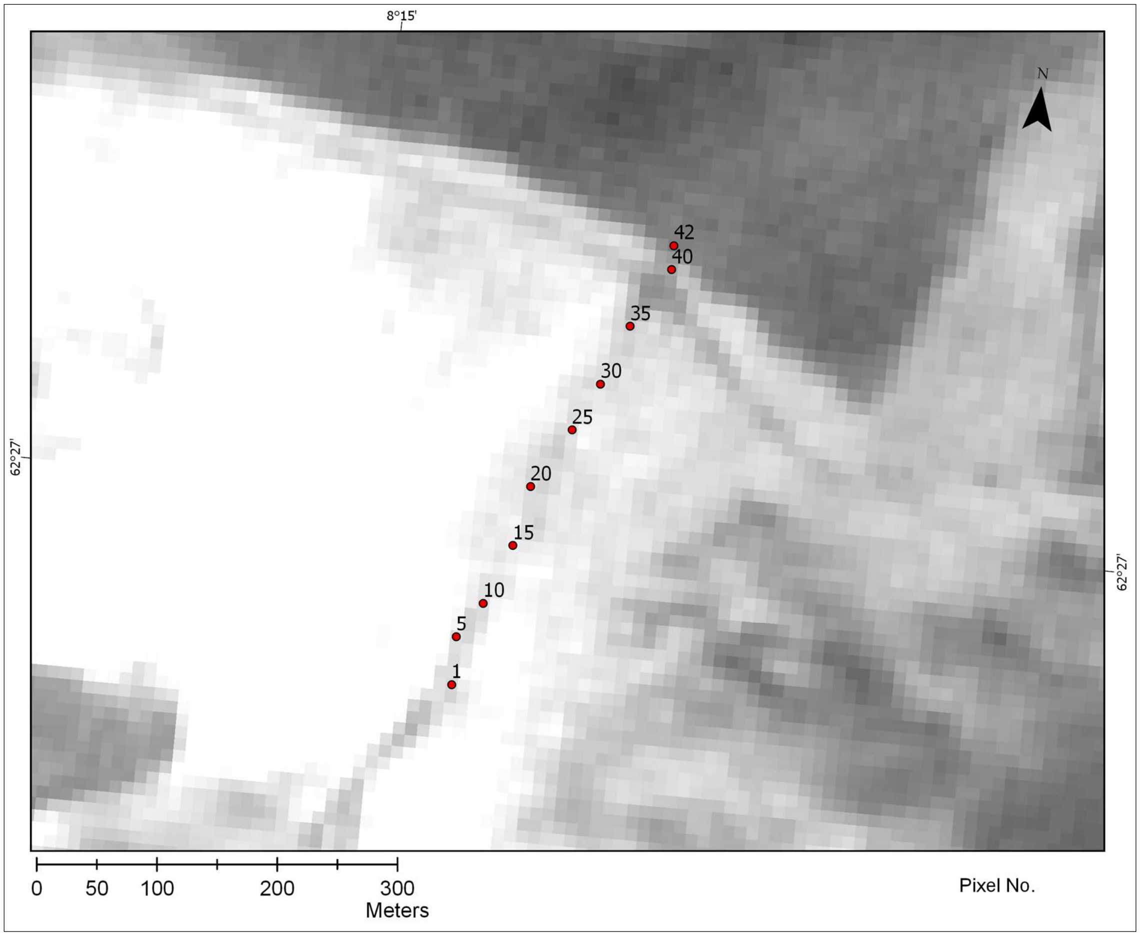

The area of interest is covered by a thin cloud cover, and difficult to delineate in color composites. The debris flow event is barely visible in NDVI-image. B8 seems least affected by thin cloud cover. B2-B4 seems to mostly reflect clouds. Transect cross the road at pixel 37.

Reflectance values seem to be affected to a large extent by the atmospheric effects. The spectral signatures and ratios are shown below, but are disregarded for further analysis and discussion with respect to its spectral signature.

D.8.1 VNIR & NDVI

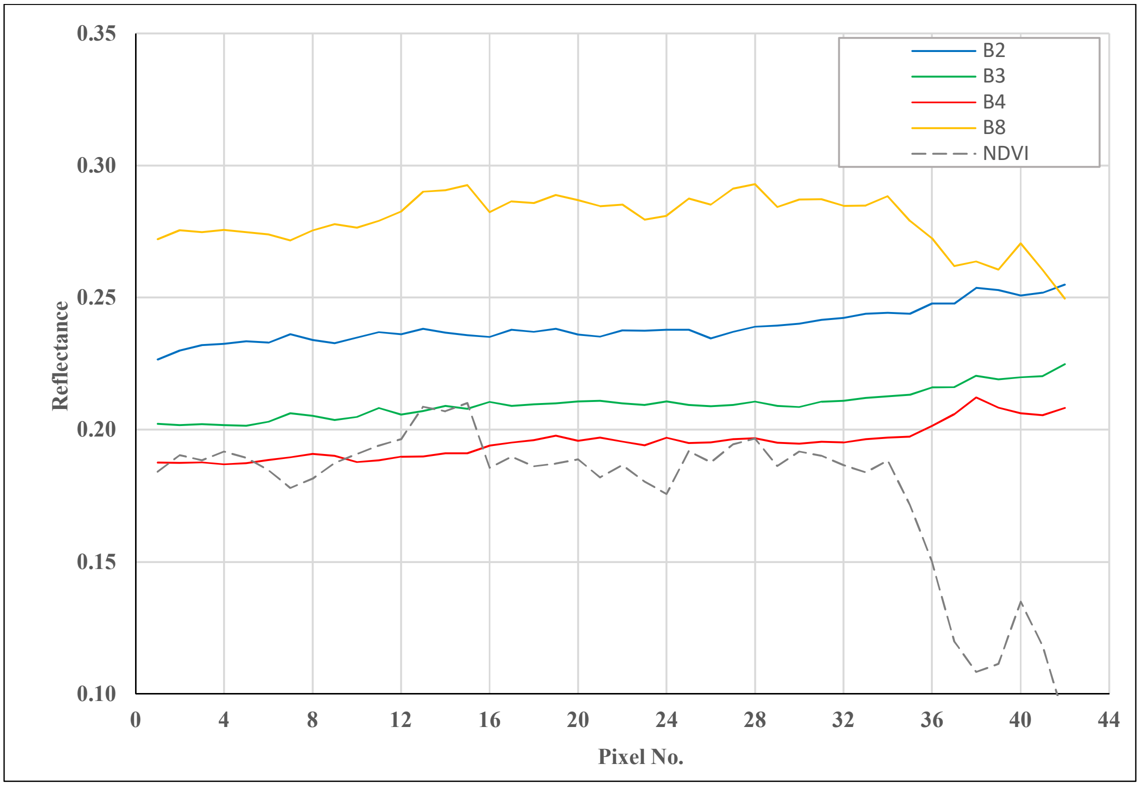

D.8.2 NIR- & RGB.ratios

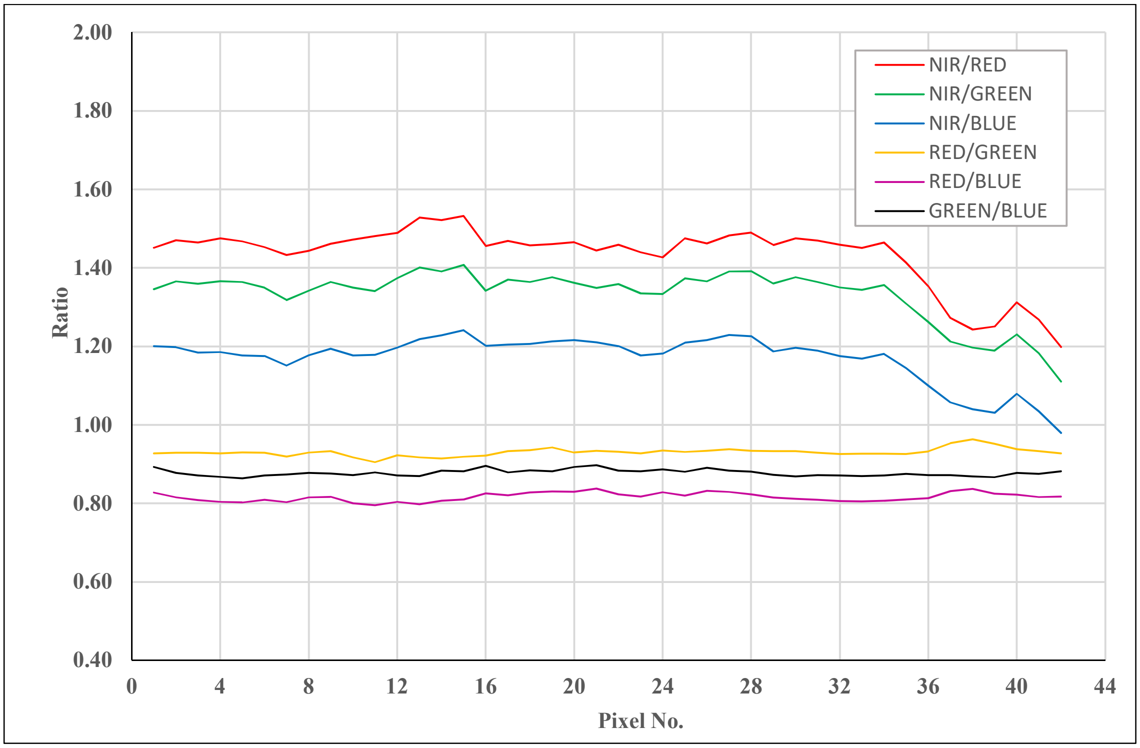

D.8.3 NDVI-ratios

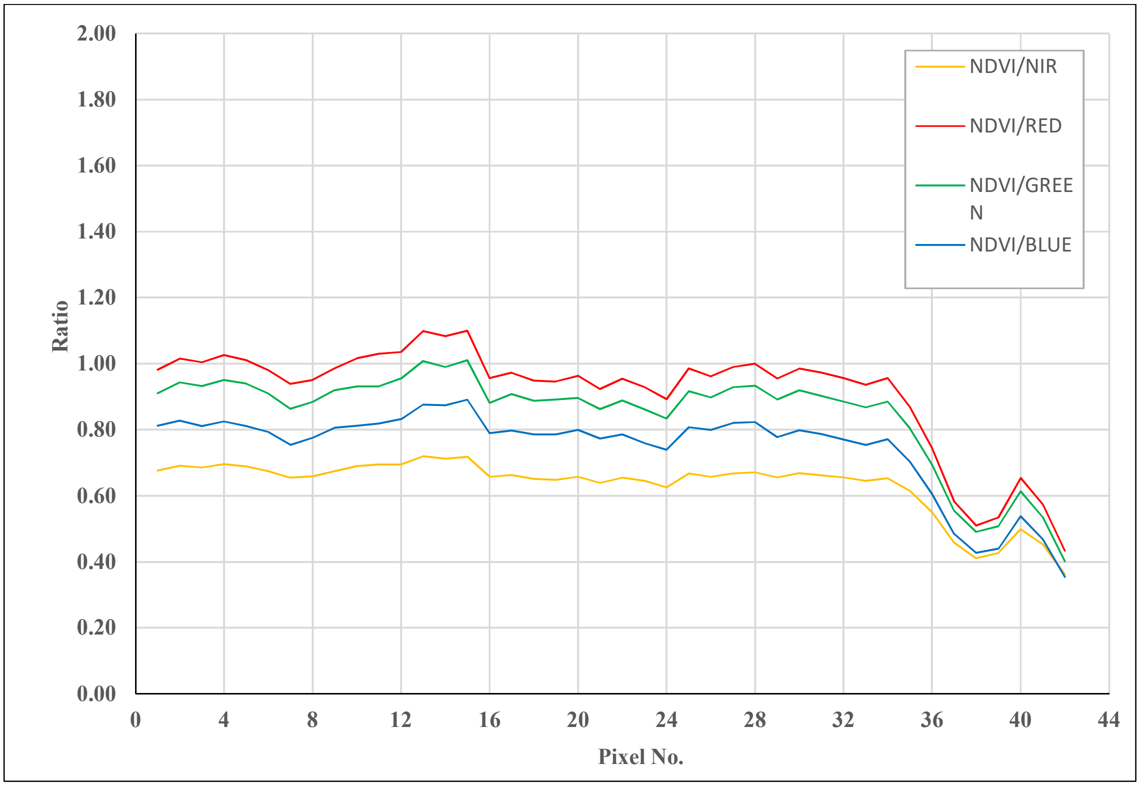

D.9 Event 9 – Tokke

The pixels 1-12 is the narrowest part of the detected landslide, roughly 1-2 pixels wide. The displaced material seems to have spread out on relatively flatland, and a“islands” of vegetation can be spotted in the NCC close to pixel 25. The transect crosses a road pixel #27-28.

The NDVI is varying from negative values, to a peak value of 0.48. The negative value indicate a waterbody or very wet conditions. The NDVI is for the most part below 0.20, but at the before mentioned spot of vegetation has its peak value. The NIR-band fluctuates around 0.10 the first 20 pixels, before increasing towards the end of the transect. The RGB-bands fluctuates around 0.10.

The RGB-ratios are fluctuating around 1.0.

The RED/GREEN-ratio (~1.0) is higher than the GREEN/BLUE and RED/BLUE ratios (~0.75).

The NDVI-ratios are relatively similar, ranging from 0.5 to 6.8.

D.9.1 VNIR & NDVI

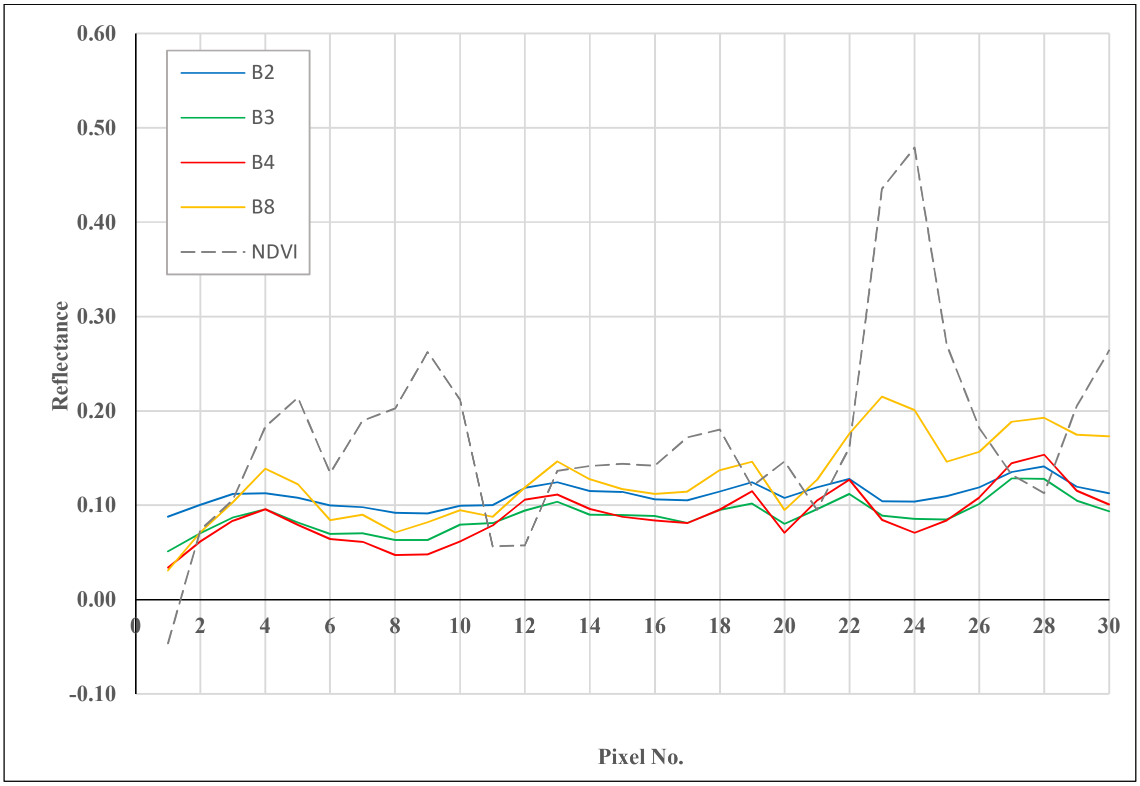

D.9.2 NIR- & RGB-ratios

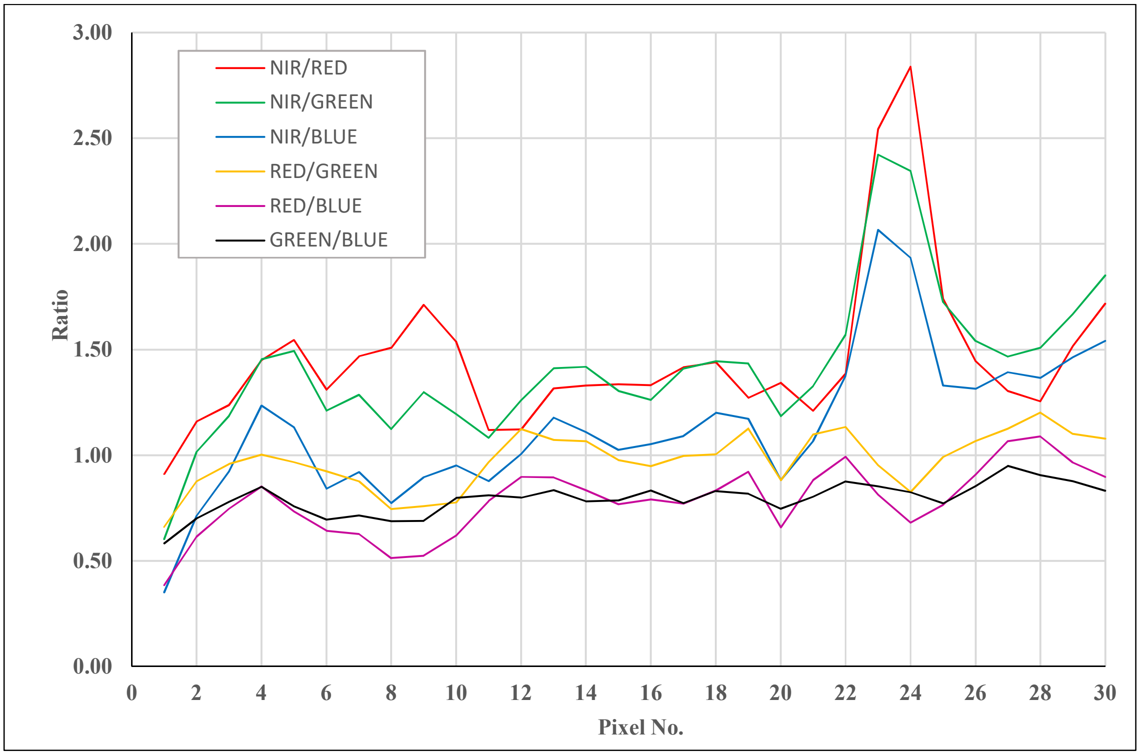

D.9.3 NDVI-ratios

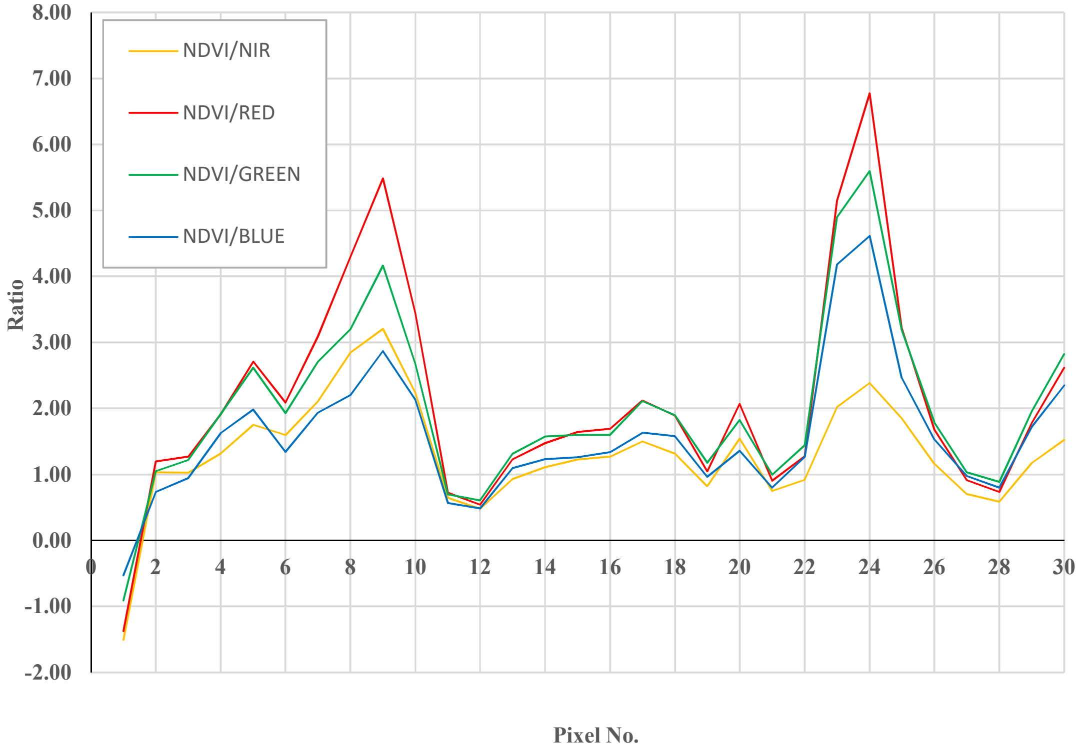

D.10 Event 10 – Rødstøl

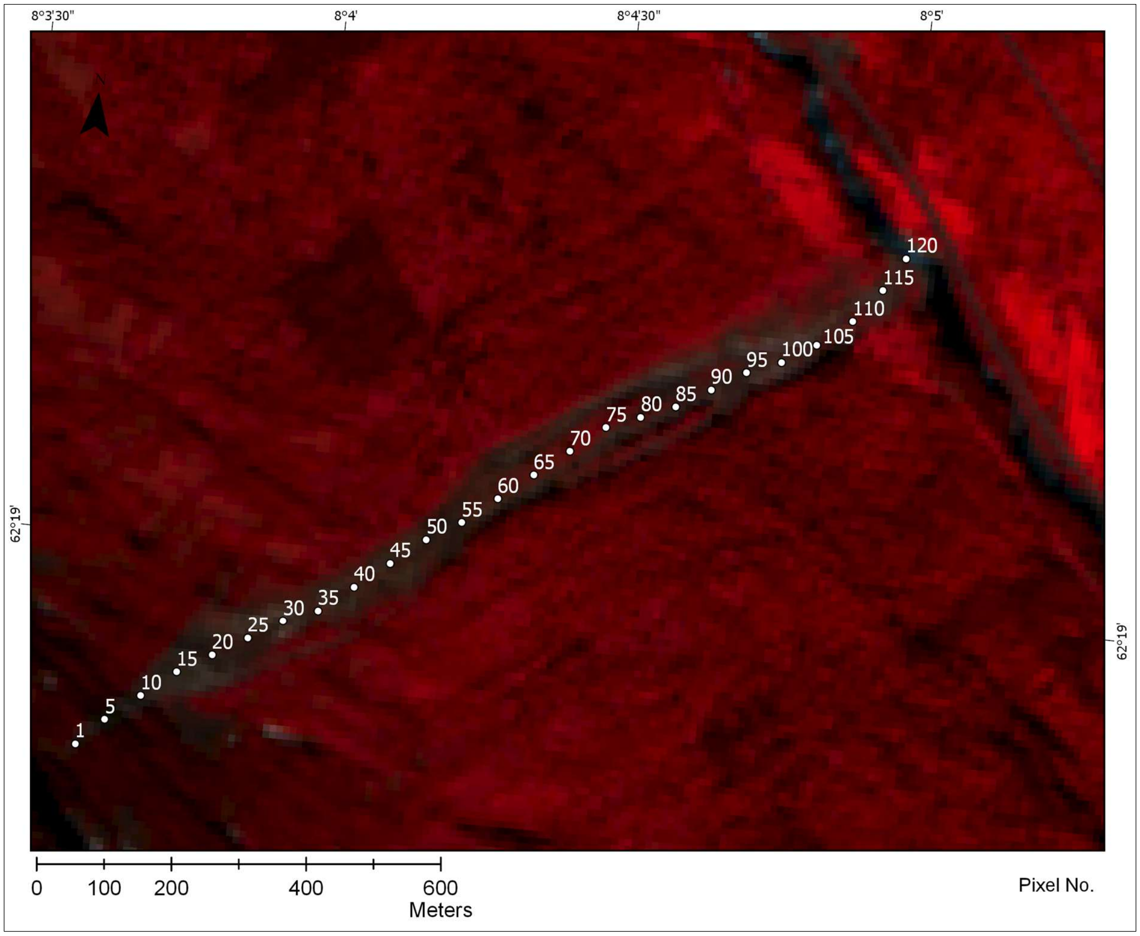

The Rødstøl debris avalanche is a large event occurring in 2011. The spectral reflectance below is derived from a dataset acquired in 2017. Possibly re-vegetated areas can be seen in the landslide scar, approximately ranging from pixel 60-90. The transect ends in a river in the valley-floor.

The NDVI along the transect is relatively spikey. The peak values appear at the abovementioned vegetated areas. The NDVI signature along the major part of the transect is fluctuating between 0.10 and 0.30.

The RGB-bands fluctuate around 0.10, while the NIR-bands appear to be sensitive to the vegetation.

The RGB-ratios are fluctuating around and just below 1.0.

The NIR-ratios follow the same tendency as the NDVI, but with values ranging from 0.8 – 4.2.

The NDVI/NIR-ratio is less sensitive than the other NDVI-ratios.

D.10.1 VNIR & NDVI

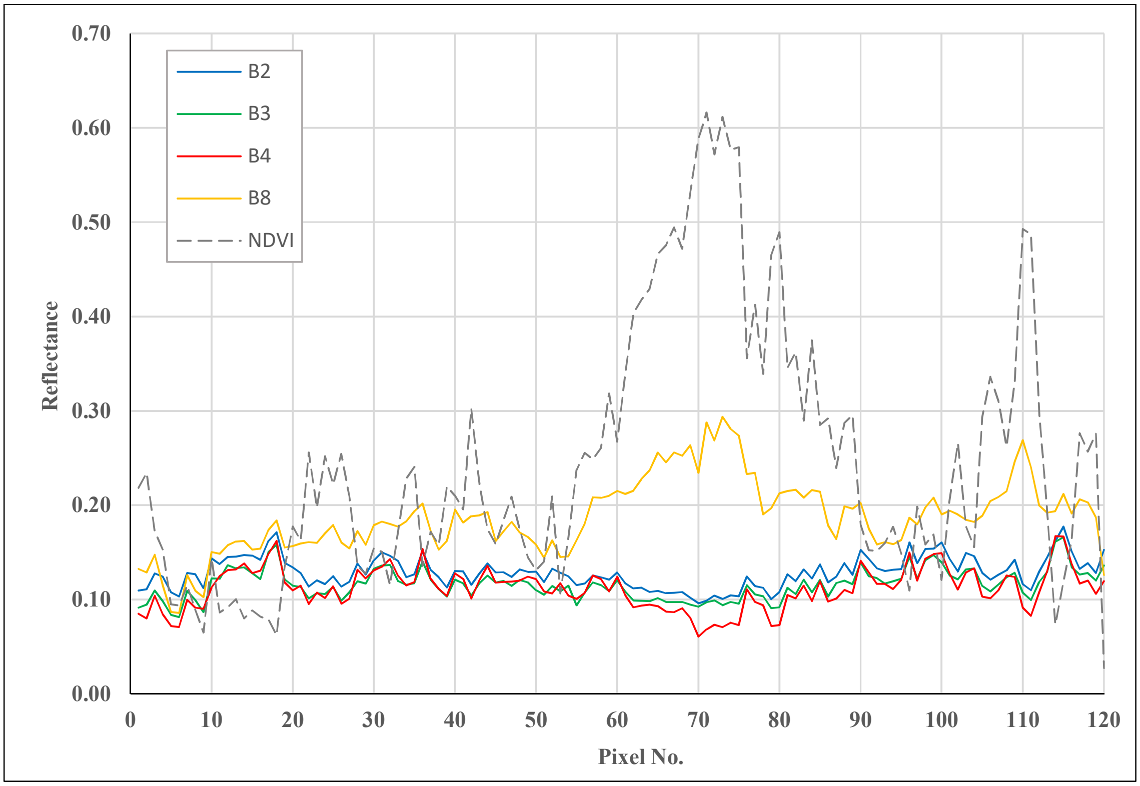

D.10.2 NIR- & RGB-ratios

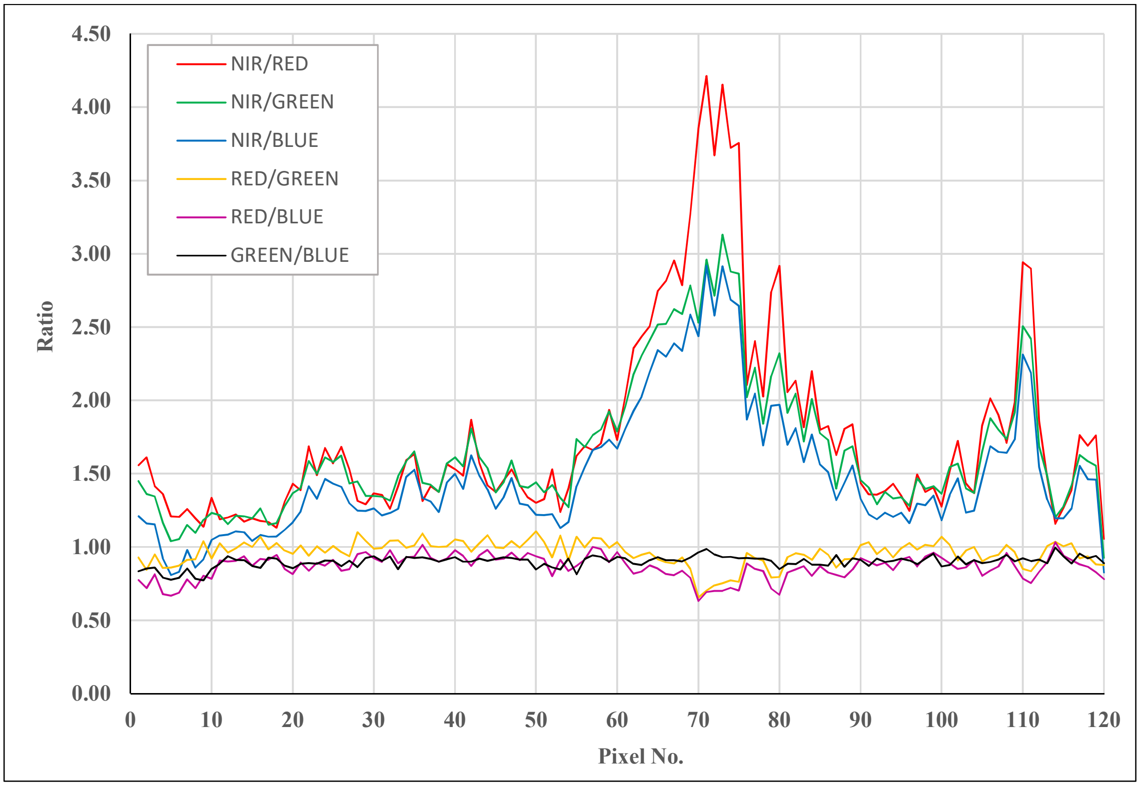

D.10.3 NDVI-Ratios

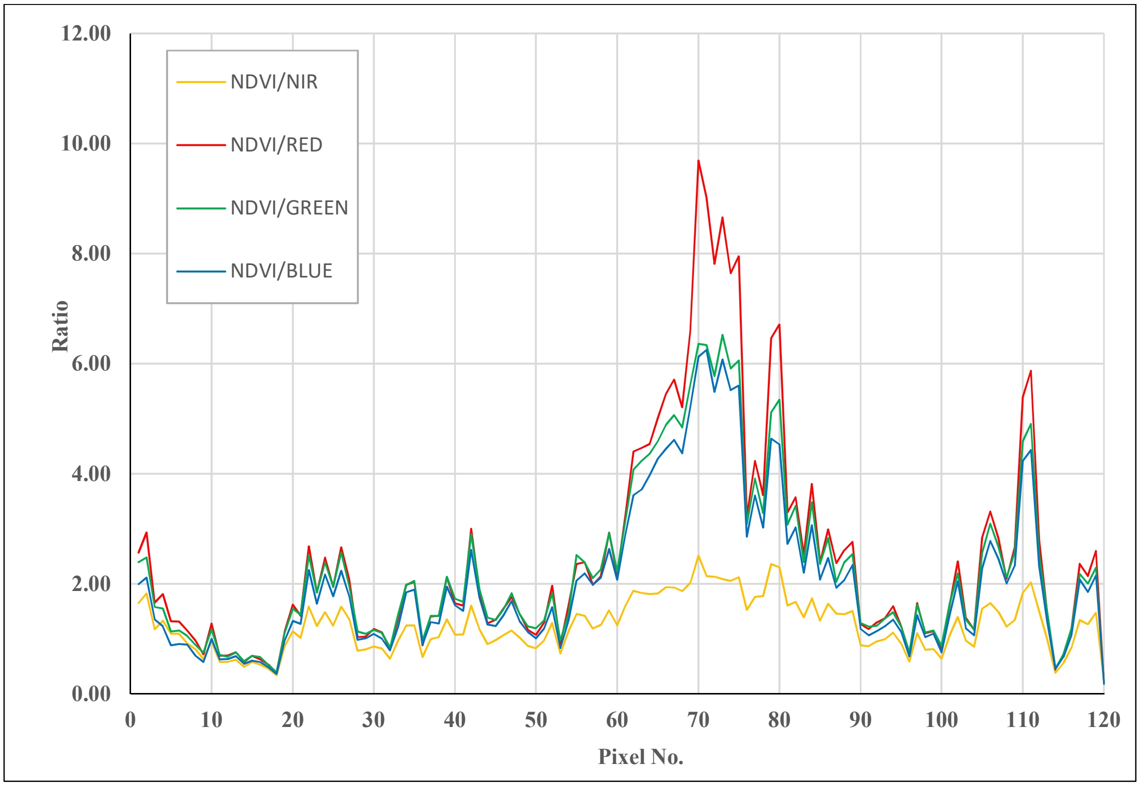

D.11 Event 11 – Krundalen

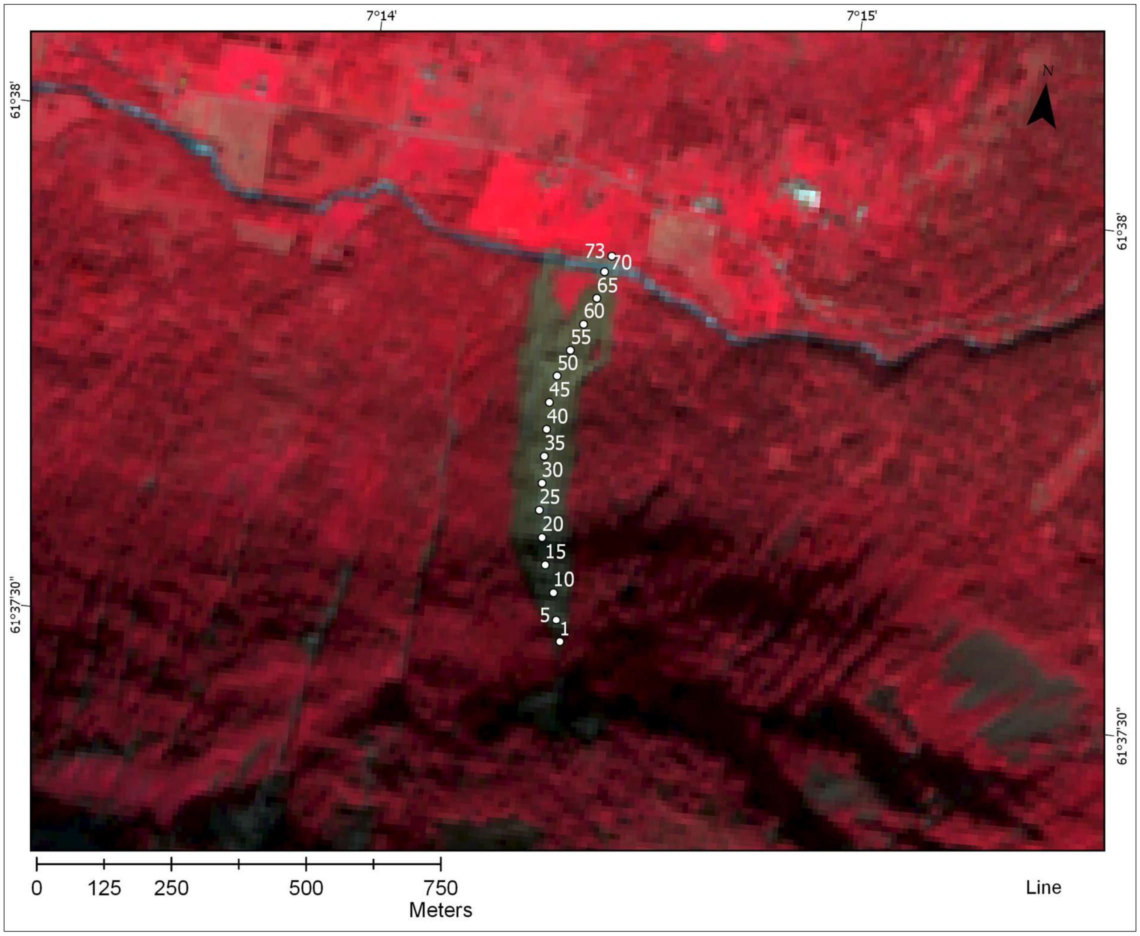

The landslide scar is V-shaped, and relatively large with roughly 15 pixels at the widest section. The transect follows the rightmost path, where the displaced material splits up at the foot of the slope. The transect ends in the river at the valley floor.

The NDVI along the transect is low, mostly below ~0.15 before increasing to around 0.20 towards the foot of the slope. The VNIR-values is also relatively small, with minor fluctuations.

The RGB-ratios are fluctuating just below 1.0, and the NIR-ratios ranging from roughly 1.0 to 1.5.

The major part of the NDVI-ratios are relatively similar, ranging from 0.5 to 2.5.

D.11.1 VNIR & NDVI

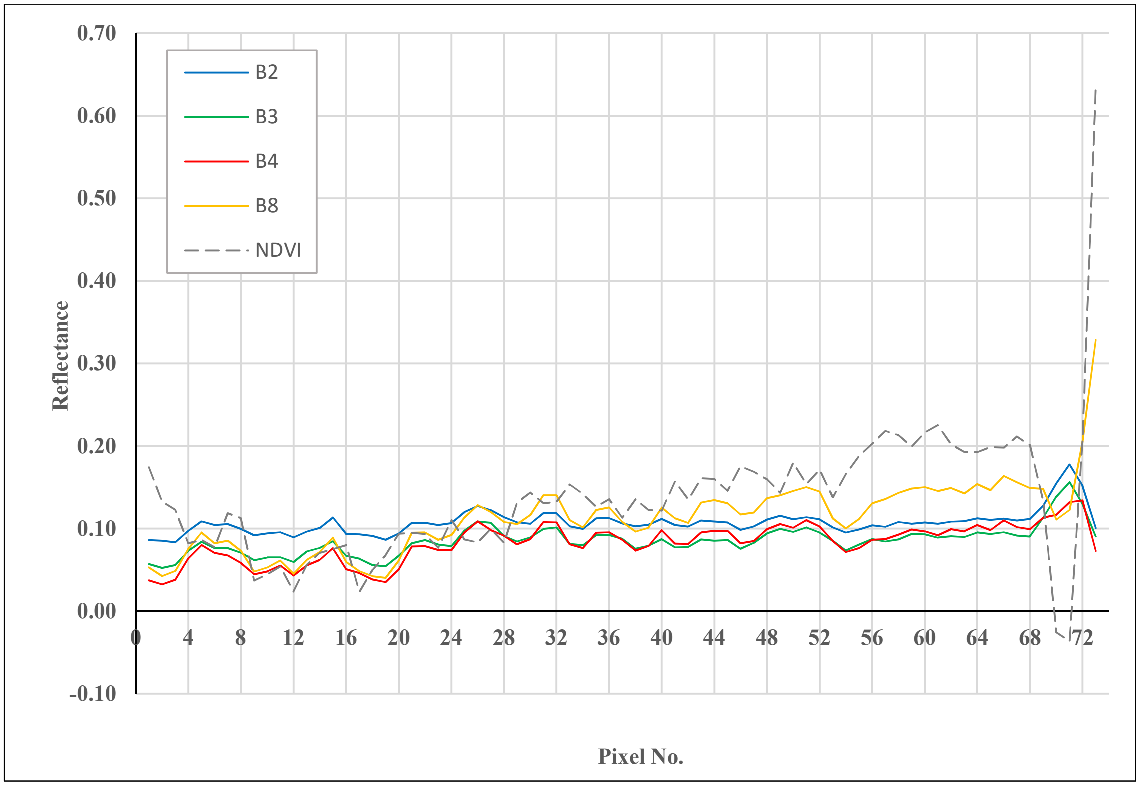

D.11.2 NIR- & RGB-ratios

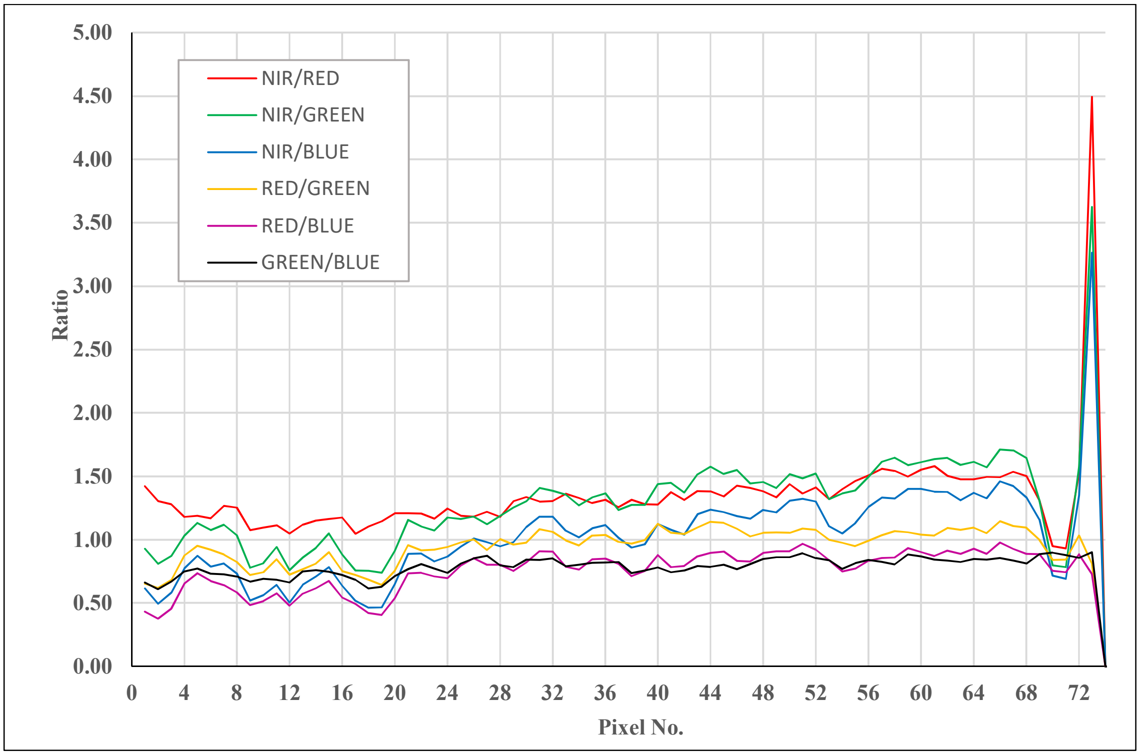

D.11.3 NDVI-ratios

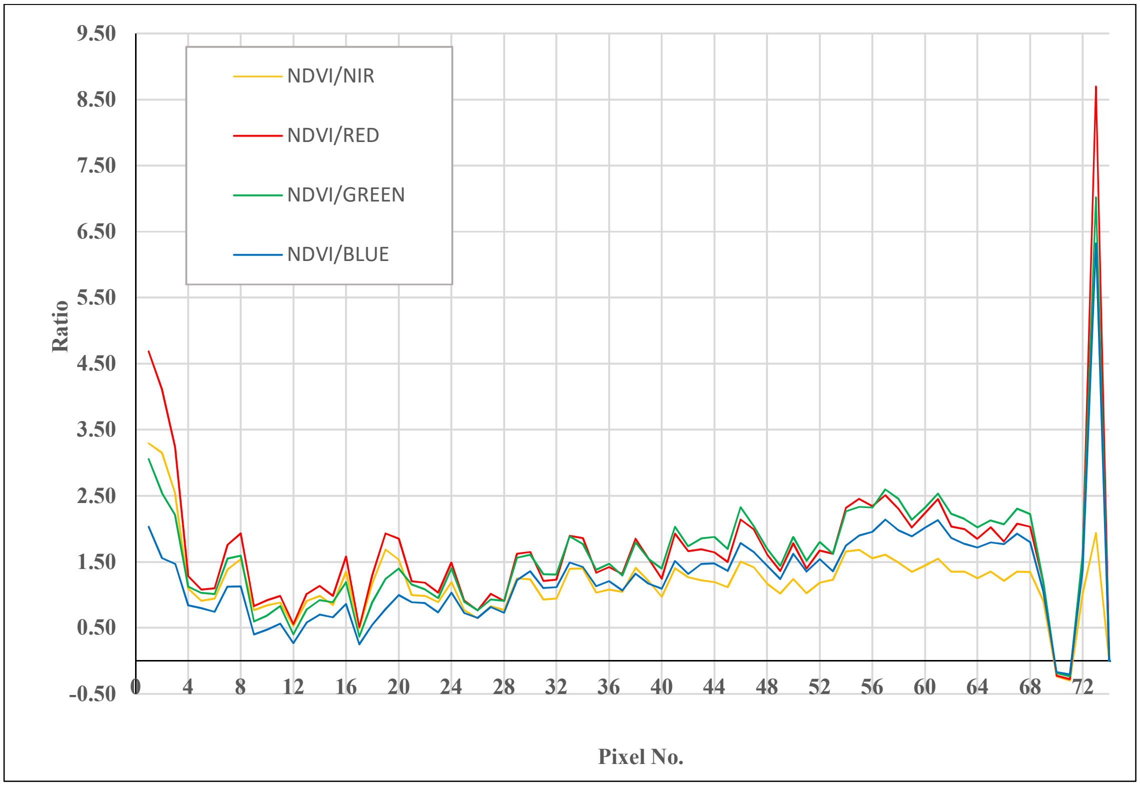

E. APPENDIX E – Change Detection Signatures

The change in the spectral signature between two, or three datasets acquired at different points in time are examined below. The detected events with available S2-data acquired prior to, and later than the date of occurrence are investigated. The change in spectral reflectance are for some events calculated with three datasets to inspect how seasonal and atmospheric variations influence the results. Color composites/NDVI-images are given for all datasets, put chronologically, starting with the oldest dataset.

The change in spectral reflectance, NDVI and ratios are given in the graphs below. The values are derived from the same transects as in APPENDIX D – spectral signature. The pixel location and corresponding number is given in all images for reference. The solid lines are values derived from datasets acquired at times closest to the event. Dashed lines are values from datasets acquired at a different time, but possibly with more similar conditions.

The following values have been calculated, where t_1 denotes a time prior to the landslide, and t_2 denotes a time after the landslide, and the $B^{\#}$ refers to a specific Sentinel-2 band. The bands 2, 3, 4, and 8 are used in the calculations.

Difference:

$$B_{t_1}^{\#} - B_{t_2}^{\#}$$

$$NDVI_{t_1} - NDVI_{t_2}$$

Ratio:

$$\frac{B_{t_1}^{\#}}{B_{t_2}^{\#}}$$

$$\frac{NDVI_{t_1}}{NDVI_{t_2}}$$

Normalized Difference Ratio (NDR):

$$\frac{B_{t_1}^{\#} - B_{t_2}^{\#}}{B_{t_1}^{\#} + B_{t_2}^{\#}}$$

$$\frac{NDVI_{t_1} - NDVI_{t_2}}{NDVI_{t_1} + NDVI_{t_2}}$$

E.1 Event 1 – Lindelia

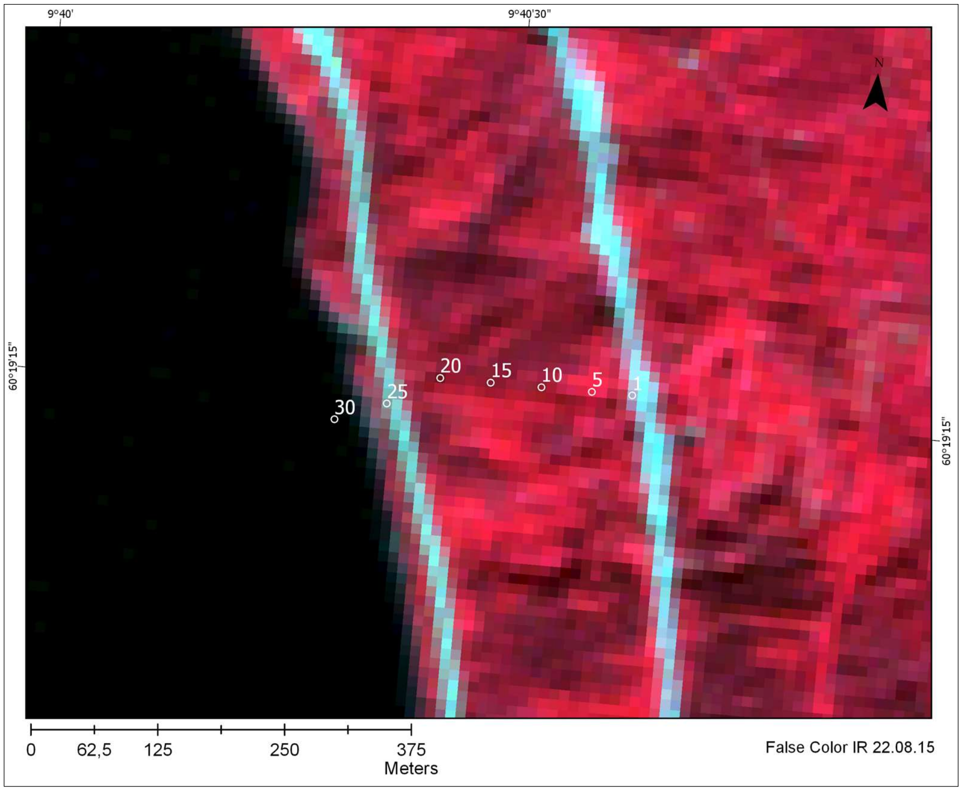

False Color IR 22.08.15

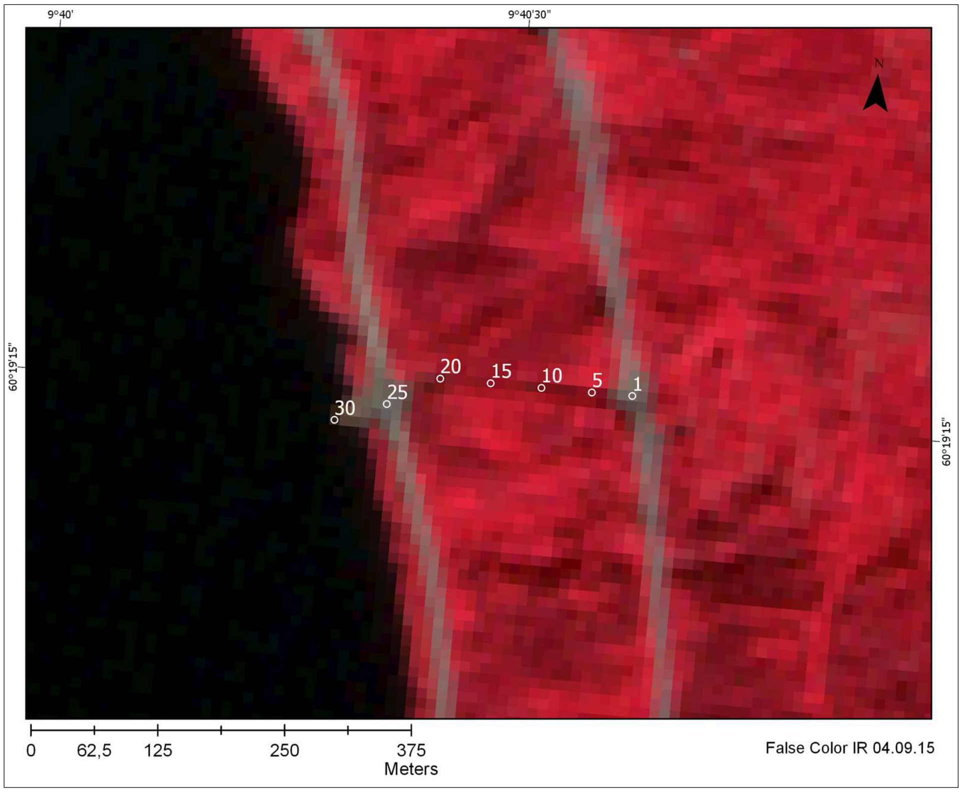

False Color IR 04.09.15

E.1.1 Difference

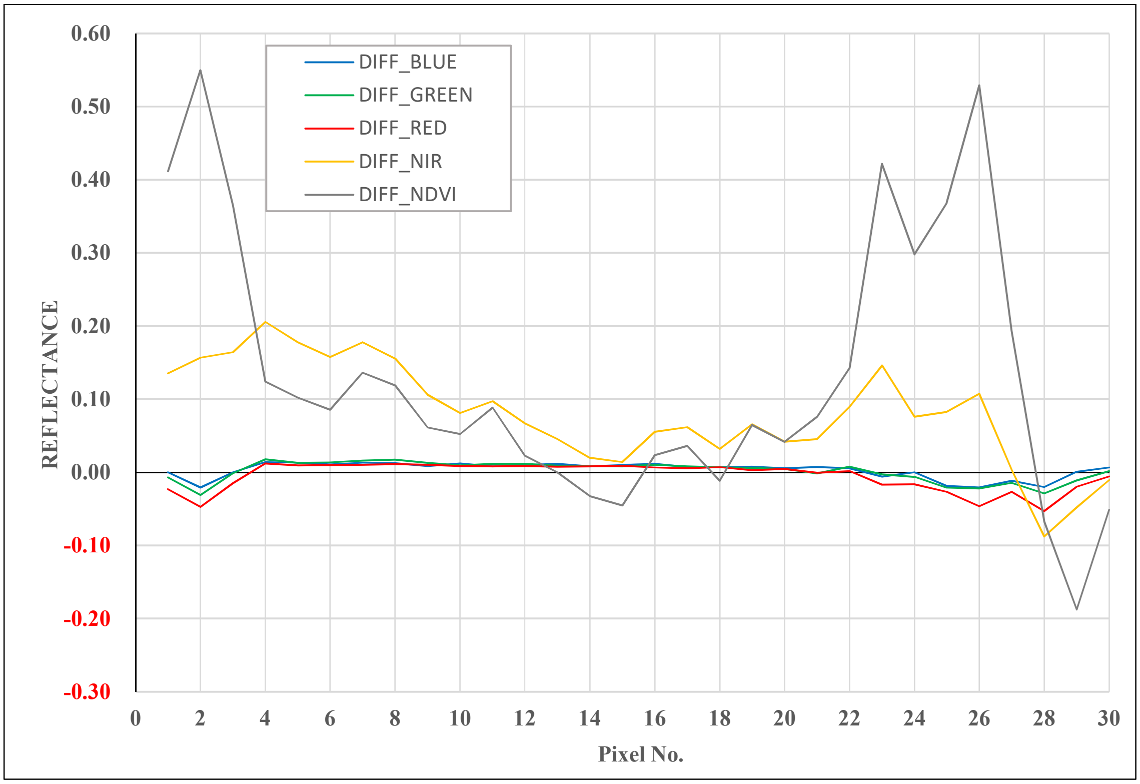

E.1.2 Ratios

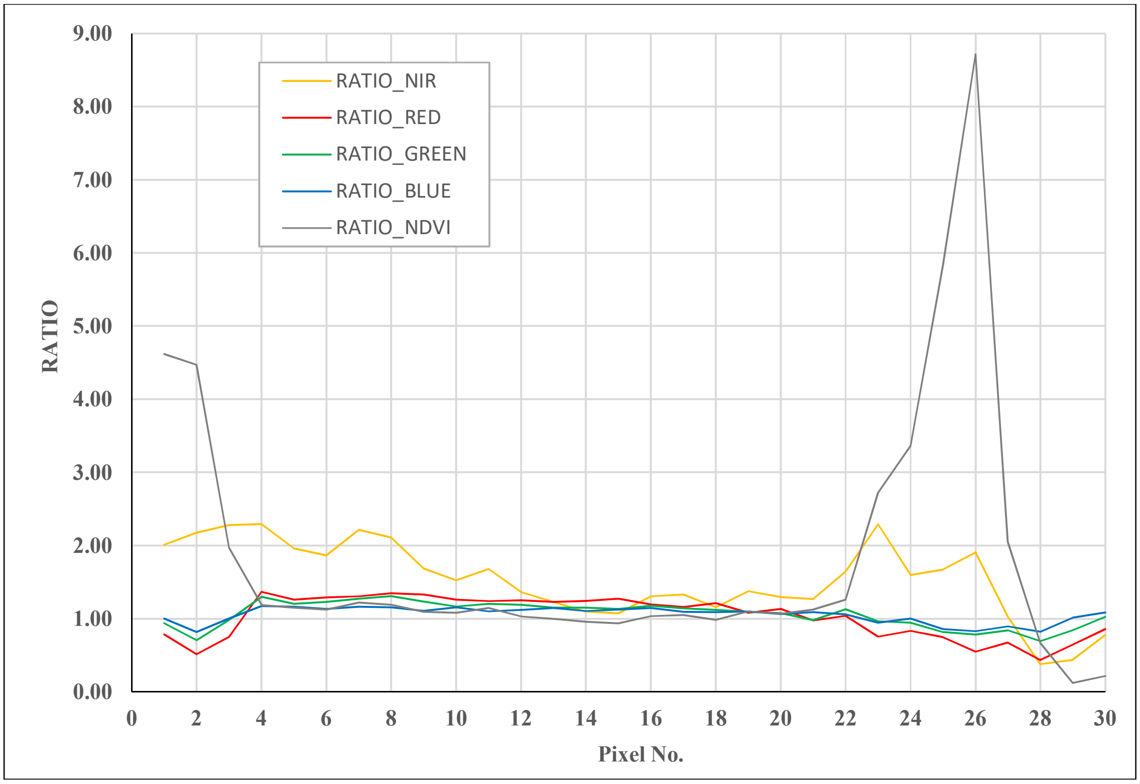

E.1.3 Normalized difference ratios

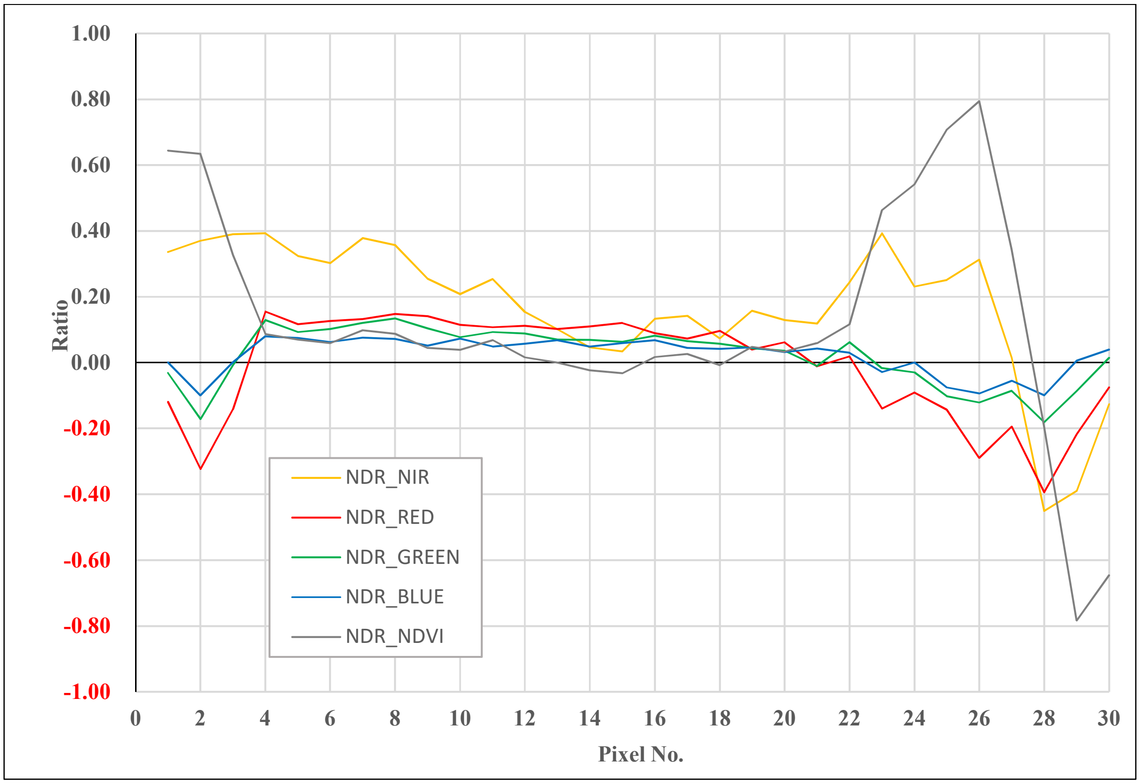

The two datasets are acquired within a relative show time interval. No significant seasonal variations appears to affect the images. The lighting conditions differ slightly between the two datasets, possibly due to atmospheric effects.

Little change can be observed between the RGB-bands. The largest change can be identified in the start and end of the transect, where the landslide is most distinct. The peak change in NDVI is 0.55, and in the NIR-band 0.21. The negative values in the end are probably due to the lake.

The RGB-ratios fluctuate around 1.0, while the NIR-ratio are slightly higher in the areas with the most change in vegetation. The NDVI-ratio peaks at 8.7.

The RGB-ratios are fluctuating around and just below 1.0.

The NDR-ratios have the same tendency as the ratios, but with a different scale.

E.2 Event 2 – Hunnedalen

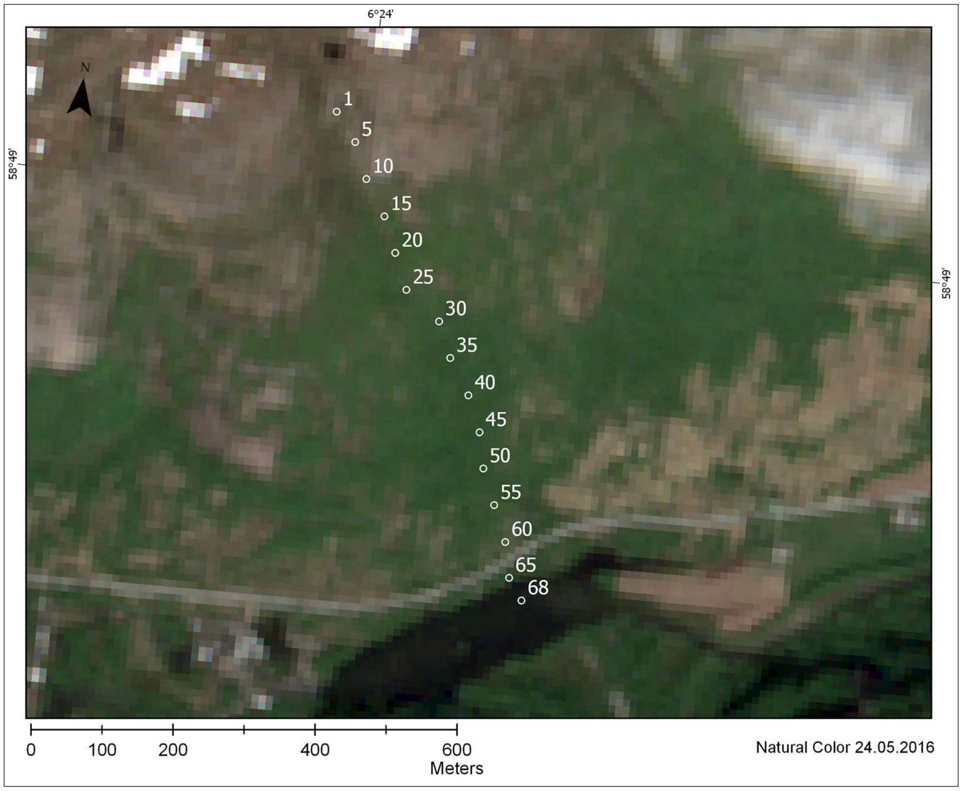

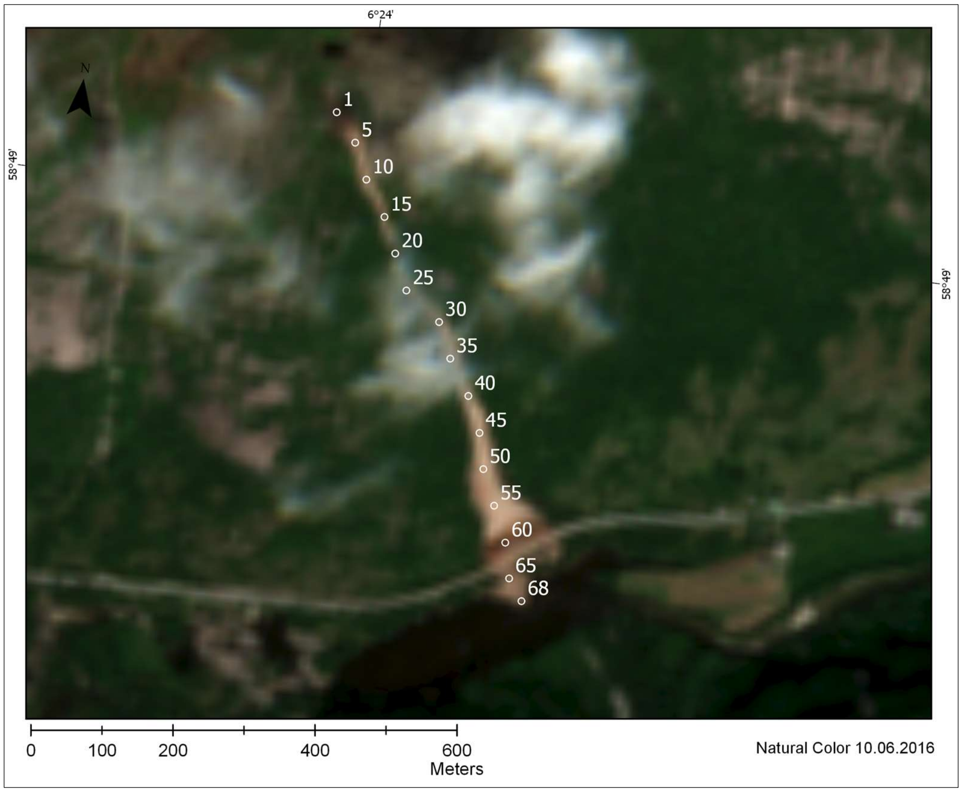

E.2.1 Difference

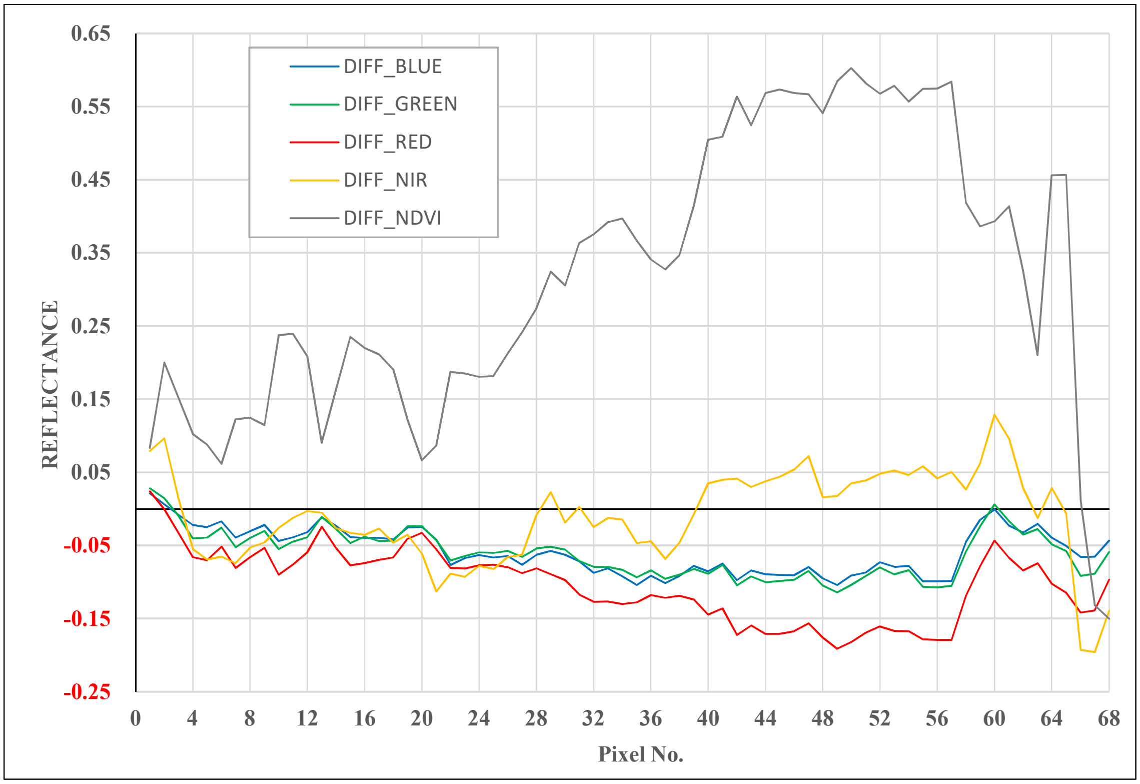

E.2.2 Ratios

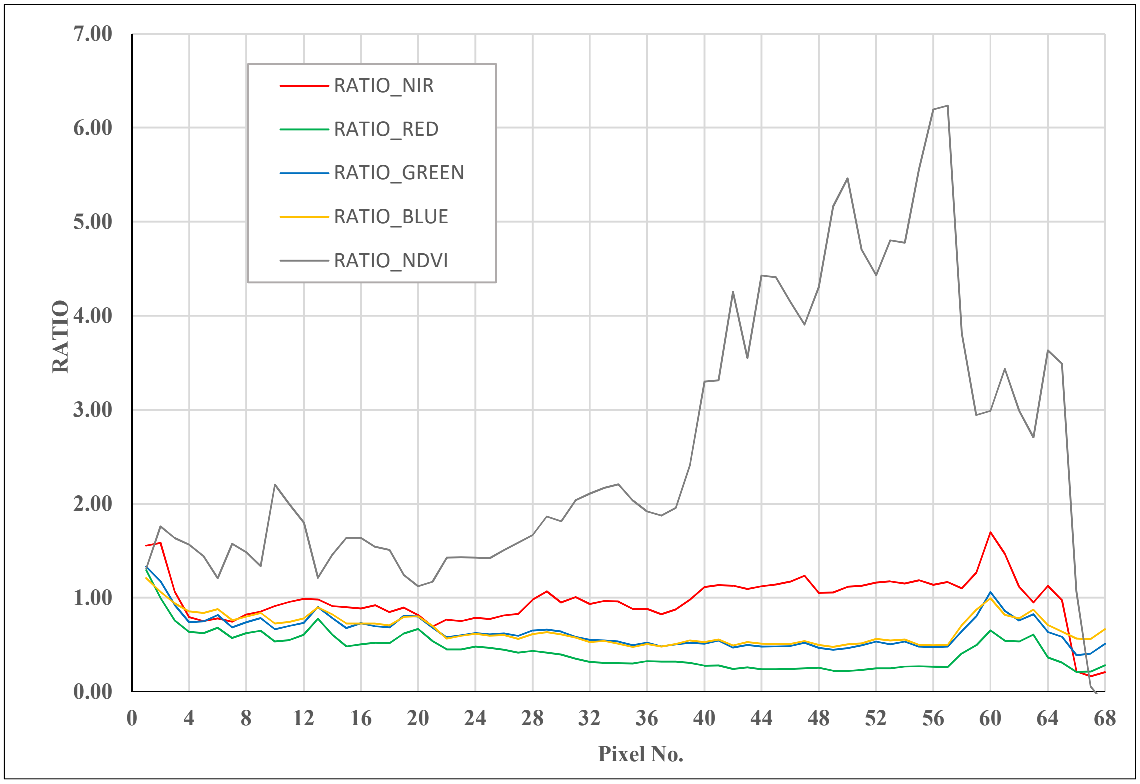

E.2.3 Normalized difference ratios

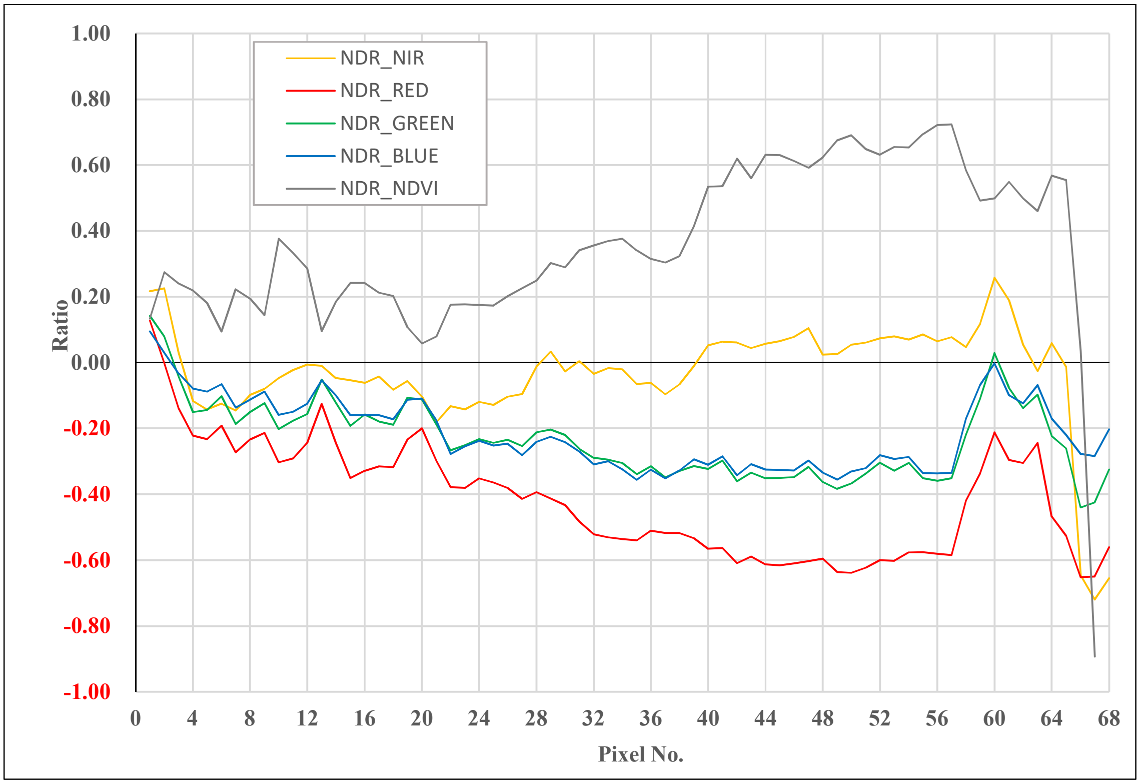

The conditions between the two datasets are fairly similar, except some clouds influencing the area of interest from ca. pixel 20-40.

The debris fan, (pixels ~50-68) yields the largest difference, with a change in NDVI around 0.55. A small change in the NIR-band, with around 0.05. The RGB-bands have a negative value in this section, meaning that the spectral reflectance from the visible bands have a greater magnitude from the landslide material, than the previously vegetated slope.

E.3 Event 3 –Kommedal

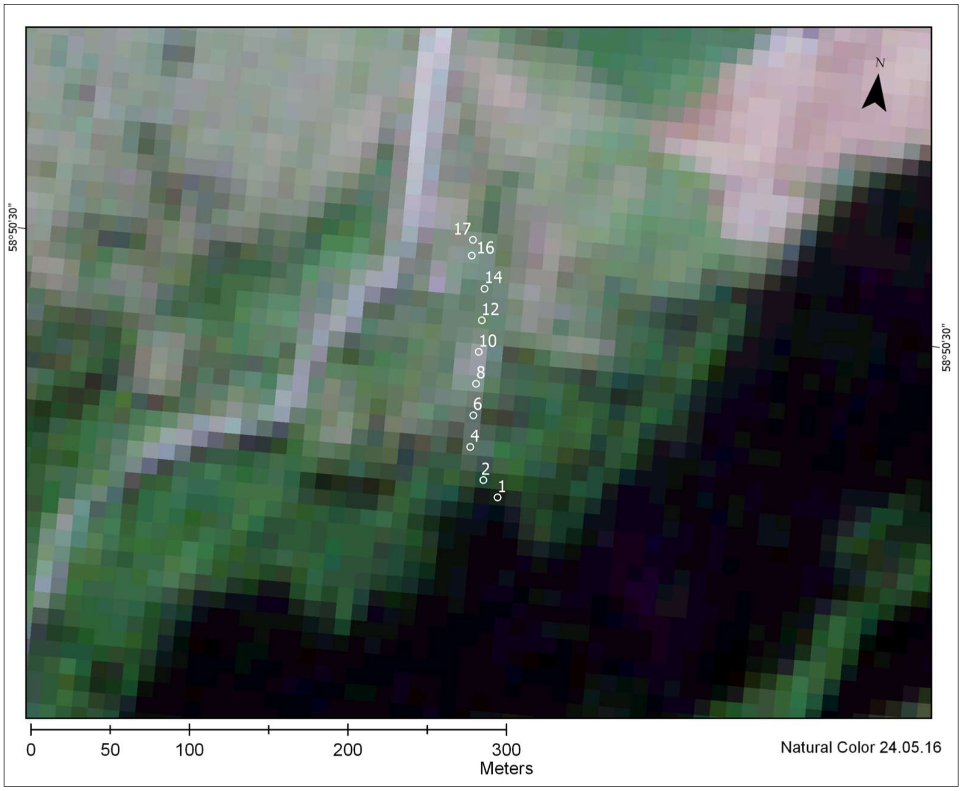

E.3.1 Difference

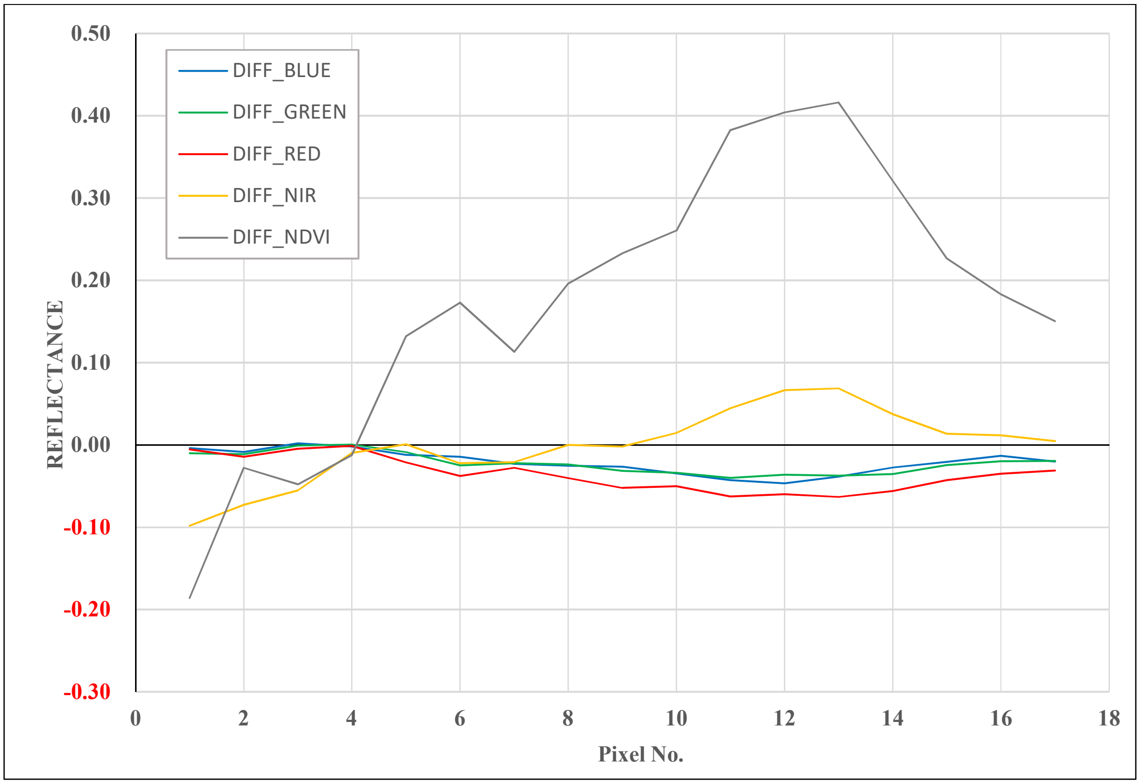

E.3.2 Ratios

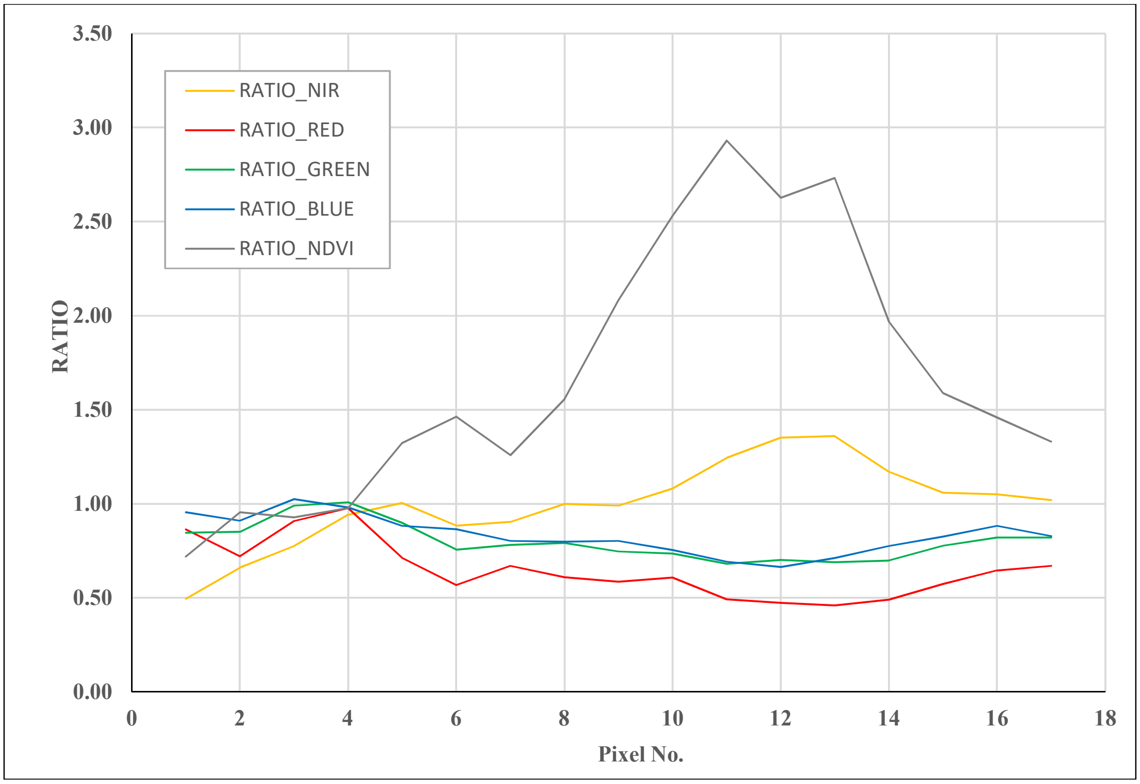

E.3.3 Normalized difference ratio

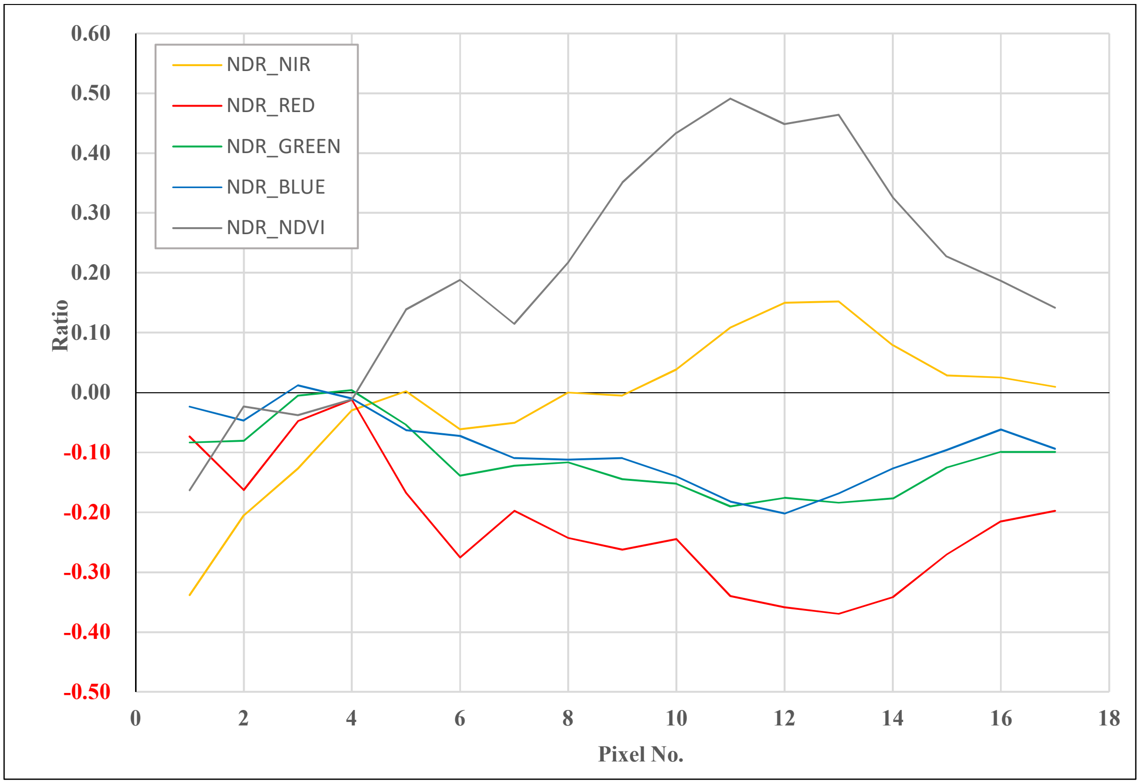

The event is detected in the same dataset as event #2. The two datasets have similar seasonal and atmospheric conditions.

The landslide is relatively small, but a distinct change in spectral reflectance can be observed. From pixels 10-14, the change in vegetation peaks at 0.42. The NIR-bands have a difference of 0.07, while the RGB-bands have a negative change of around 0.05. Minor changes can be observed from the narrower part of the landslide.

E.4 Event 4 – Øksland

Natural Color Composite 06.06.16

Natural Color Composite 04.09.16

Three datasets from the same area is examined. The *pre-event* (06.06.16) and *post-event* (04.09.16) data are acquired at the start of summer and the start of fall. Minor seasonal variations can be observed between the images. The landslide scar is somewhat influenced by shadowing from the nearby terrain in the post event data. All data derived from these datasets are represented with **solid lines.**

The *pre-event* (06.06.16) and *revisit* (23.07.17) data are acquired from the start and middle of summer. The vegetation appear greener in the revisit data, and the landslide scar is not influenced by shadows. The landslide scar appear to have a different color in the NCC, possibly related to water content, or weathering. All data derived from these datasets are represented with **dashed lines.**

The difference in NDVI is approximately equal for both comparisons. The NIR-bands show the same trend, but with roughly 10 percentage points difference between the post-event and revisit data. The RGB-bands appear to have a large intensity in the revisit data, where the landslide scar is brighter.

E.4.1 Difference

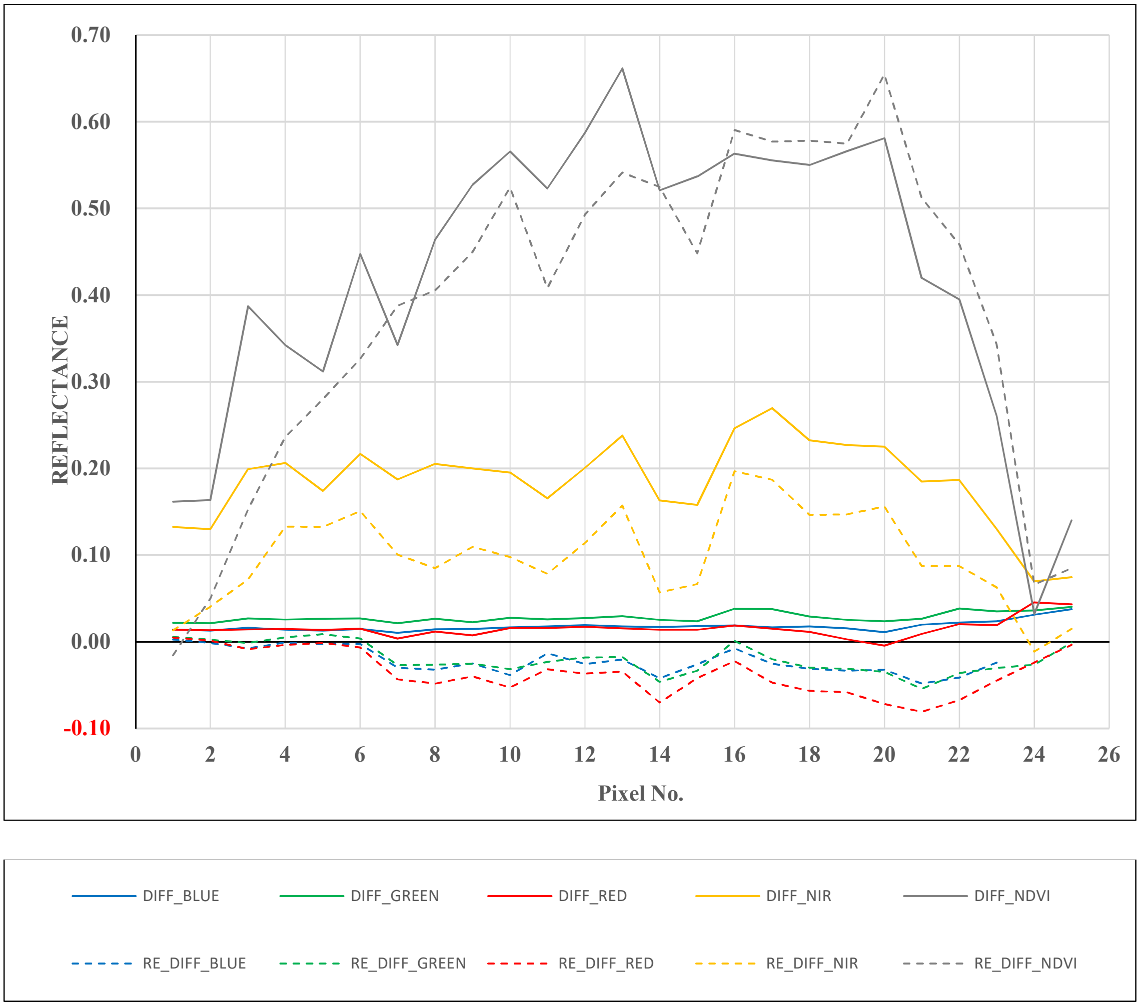

E.4.2 Ratios

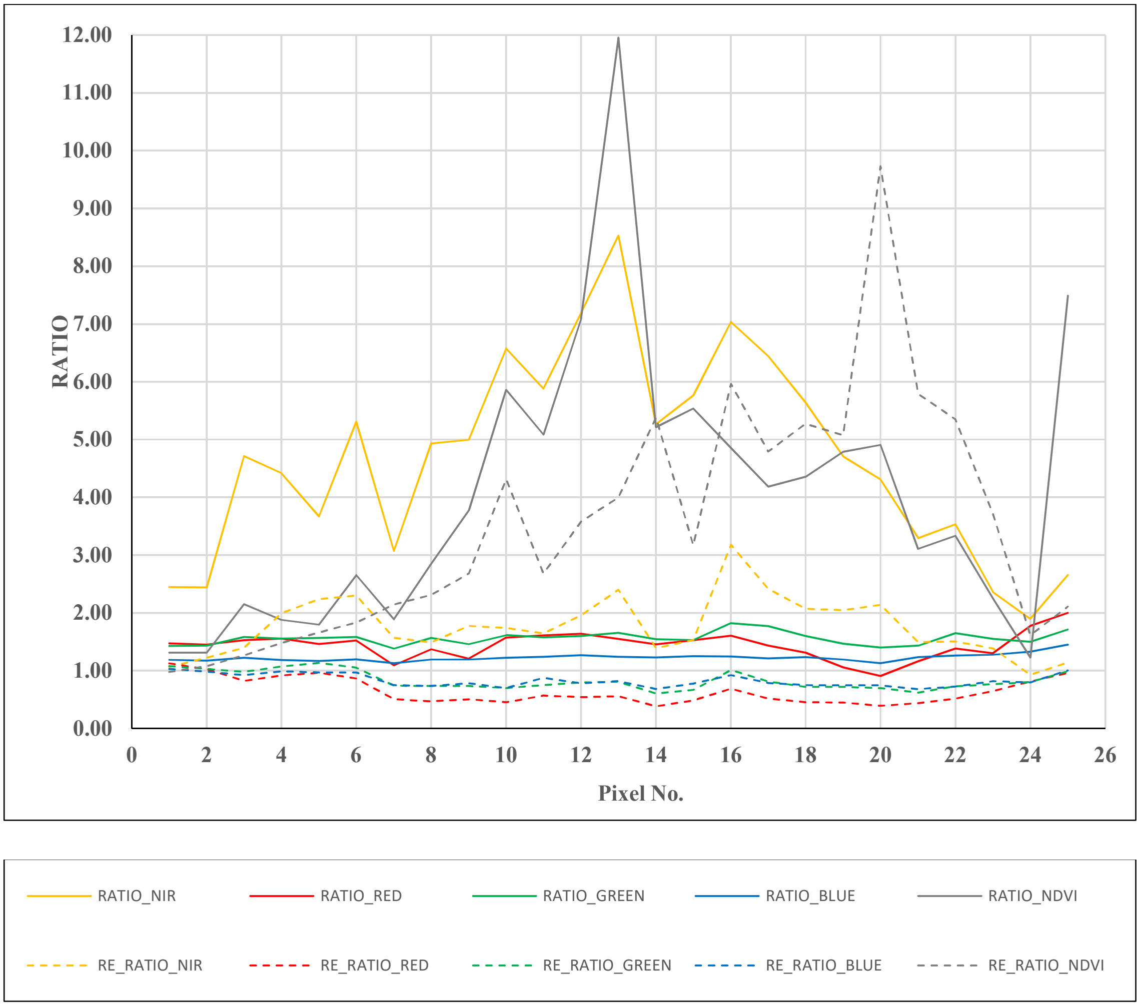

RATIO
12.00
11.00
10.00
9.00
8.00
7.00
6.00
5.00
4.00
3.00
2.00
1.00
0.00
0
2
4
6
8
10
12
14
16
18
20
22
24
26
Pixel No.
RATIO_NIR
RATIO_RED
RATIO_GREEN
RATIO_BLUE
RATIO_NDVI
RE_RATIO_NIR
RE_RATIO_RED
RE_RATIO_GREEN
RE_RATIO_BLUE
RE_RATIO_NDVI

E.4.3 Normalized difference ratios

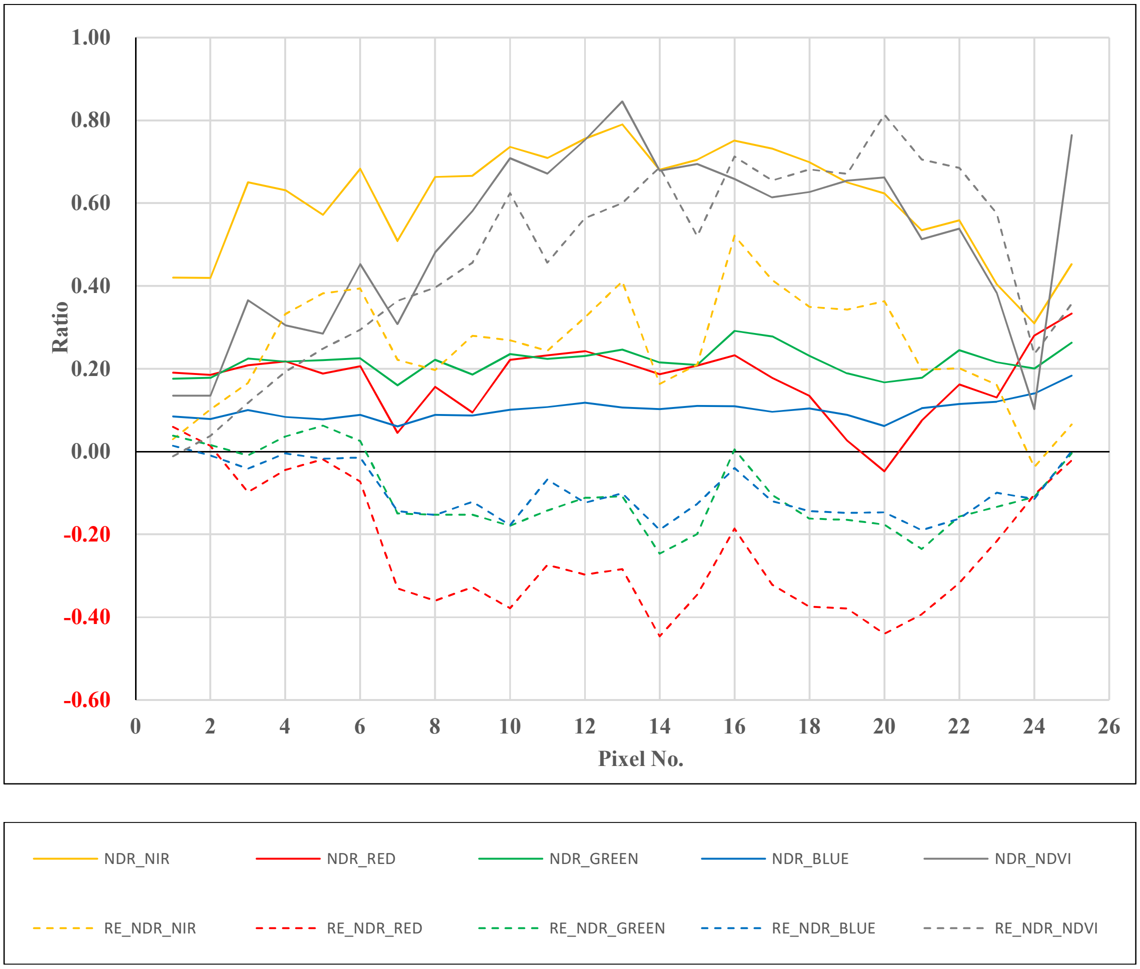

E.5 Event 5 – Slettafoss

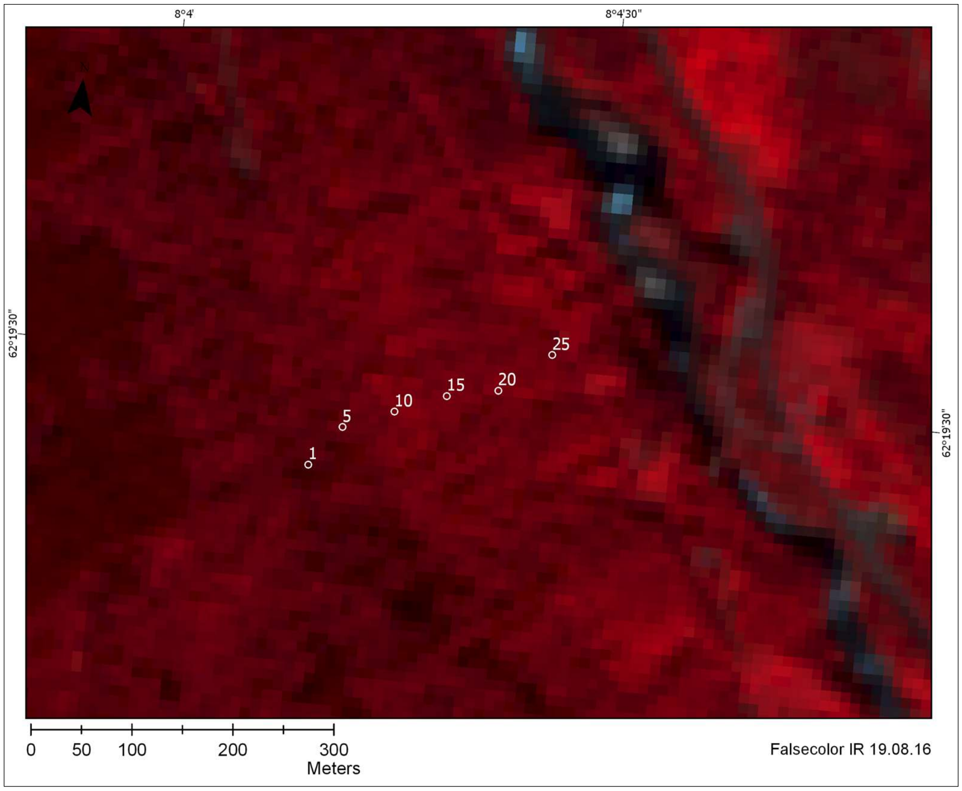

Falsecolor IR 19.08.16

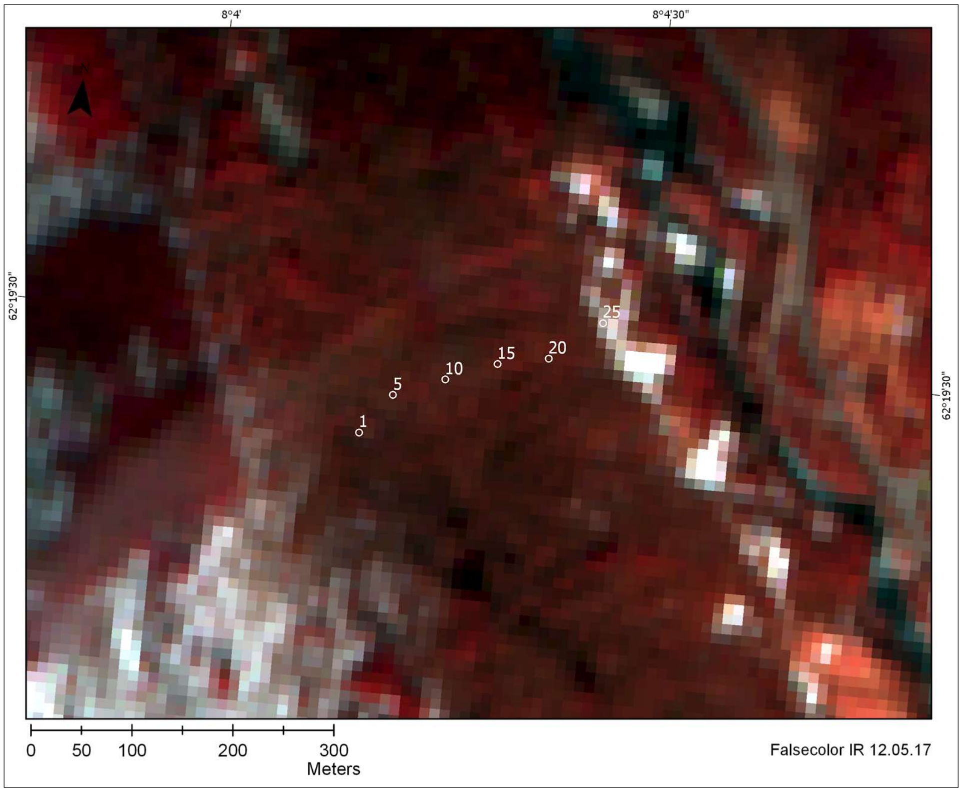

Falsecolor IR 12.05.17

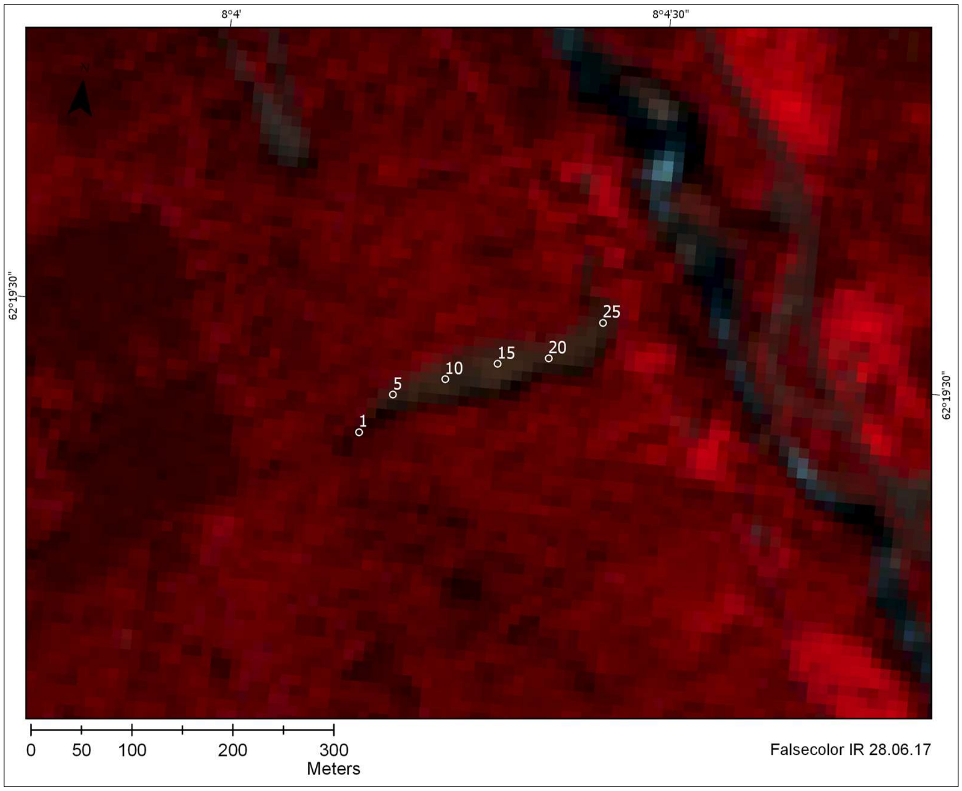

Three datasets from the same area is examined. The *pre-event* (12.05.17) and *post-event* (28.06.17) data are acquired at early spring, and mid-summer. Seasonal variations can be observed between the images in the form of difference in green vegetation (Not as bright red-color in falsecolor IR composite) and some snow. All data derived from these datasets are represented with **solid lines.**

The *previsit* (19.08.16) and *post-event* (28.06.17) data are acquired from the same time of the season, with a one-year interval. The seasonal and atmospheric conditions appear to be the same in the two datasets. All data derived from these datasets are represented with **dashed lines.**

E.5.1 Difference

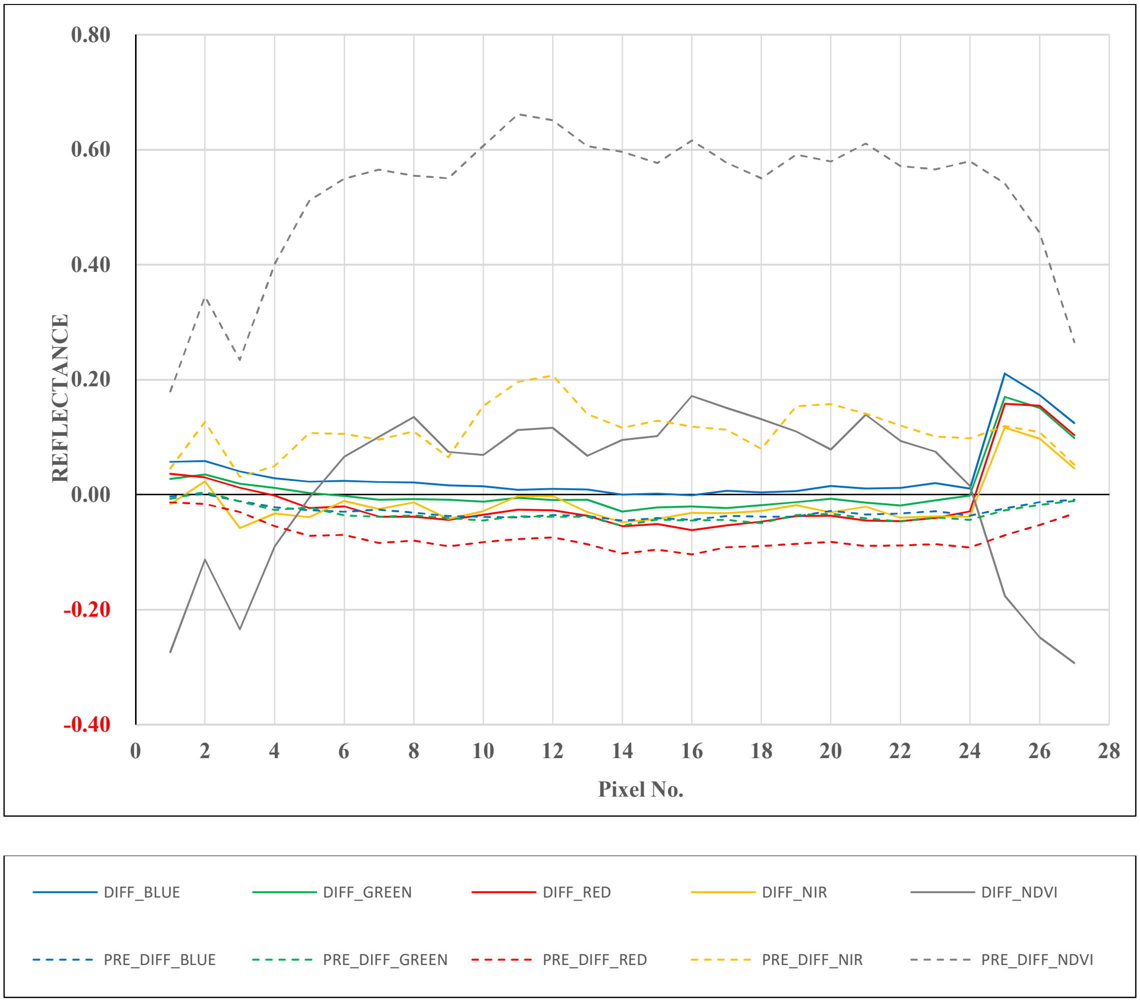

E.5.2 Ratios

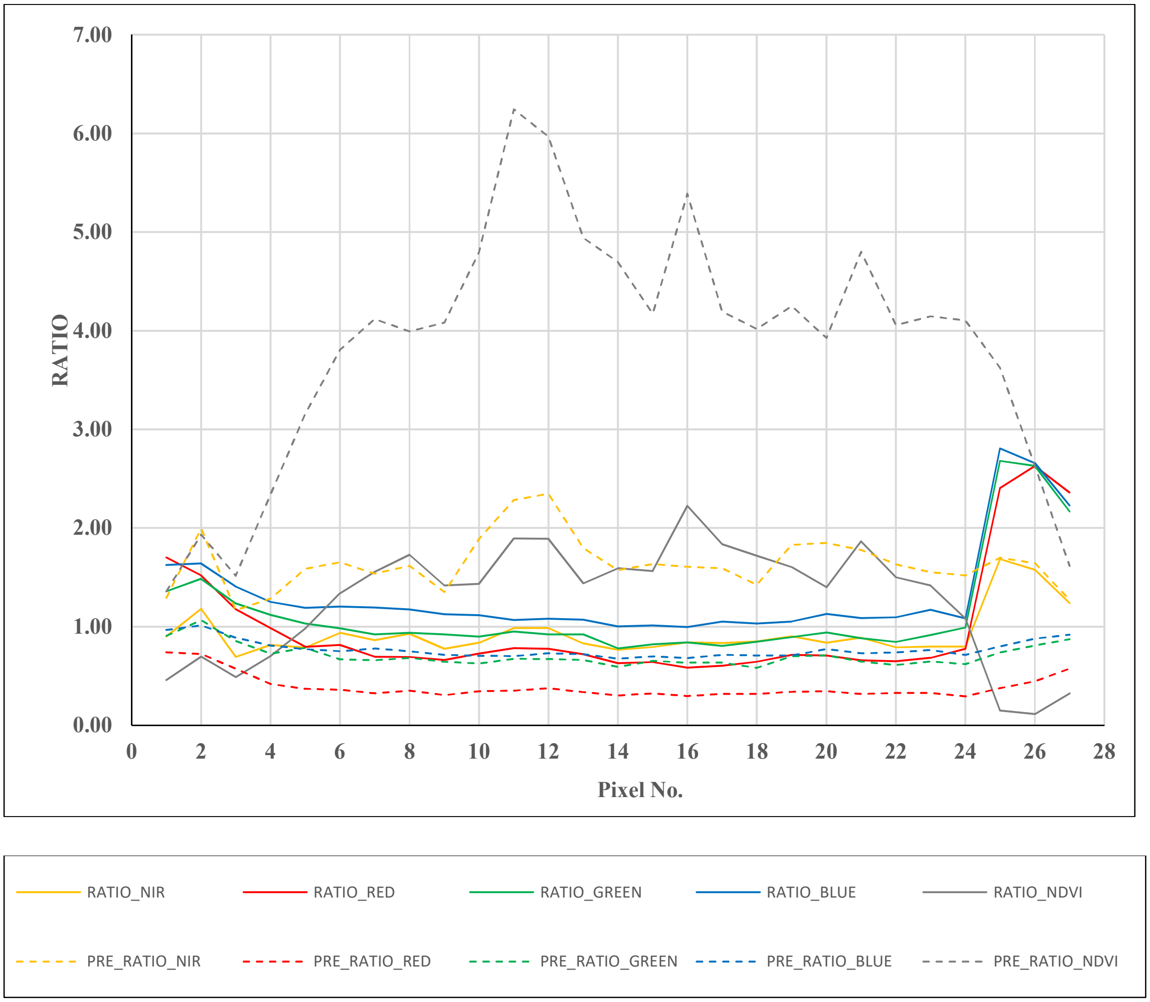
7.00
6.00
5.00
4.00
3.00
2.00
1.00
0.00
RATIO
0
2
4
6
8
10
12
14
16
18
20
22
24
26
28
Pixel No.
RATIO_NIR
RATIO_RED
RATIO_GREEN
RATIO_BLUE
RATIO_NDVI
PRE_RATIO_NIR
PRE_RATIO_RED
PRE_RATIO_GREEN
PRE_RATIO_BLUE
PRE_RATIO_NDVI

E.5.3 Normalized difference ratios

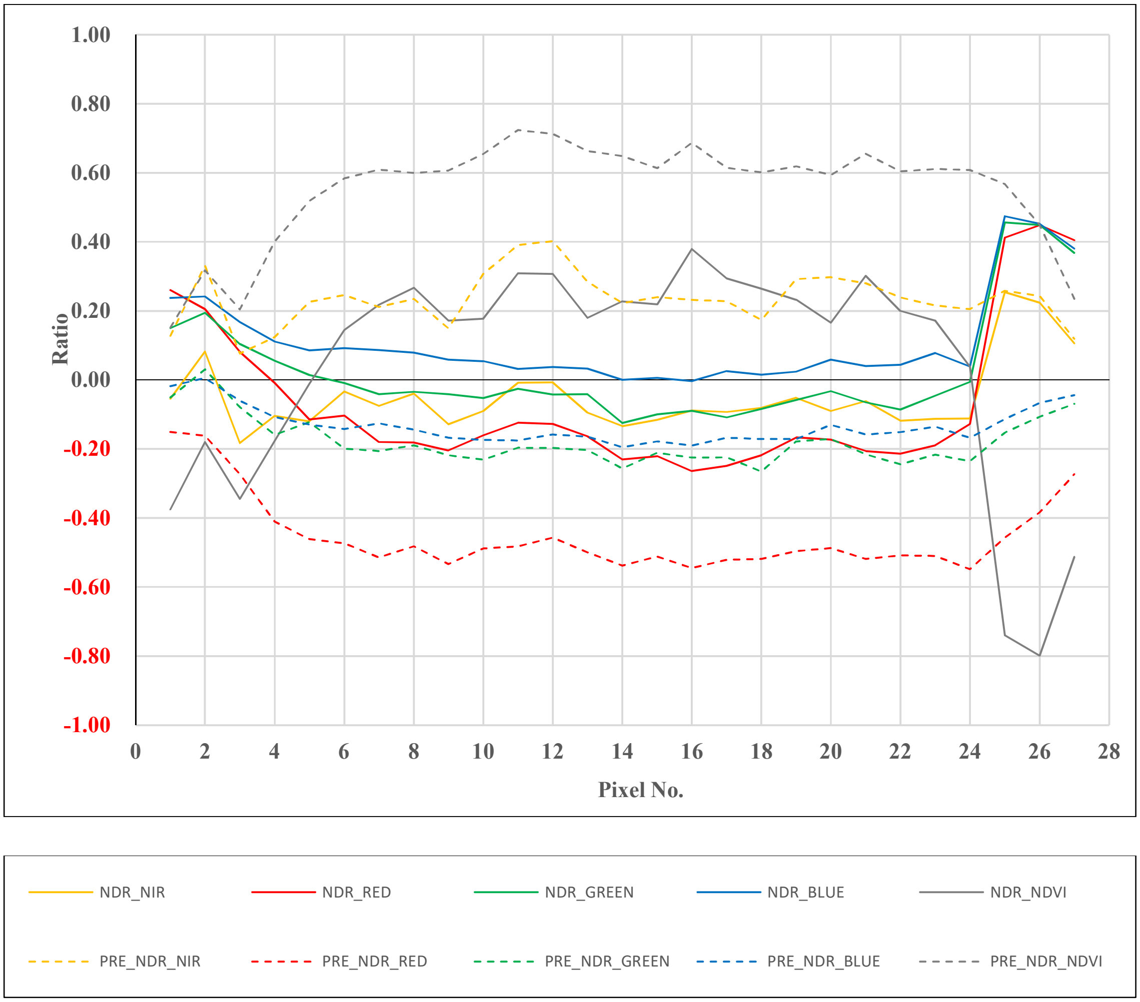

E.6 Event 6 – Kråkagjelet

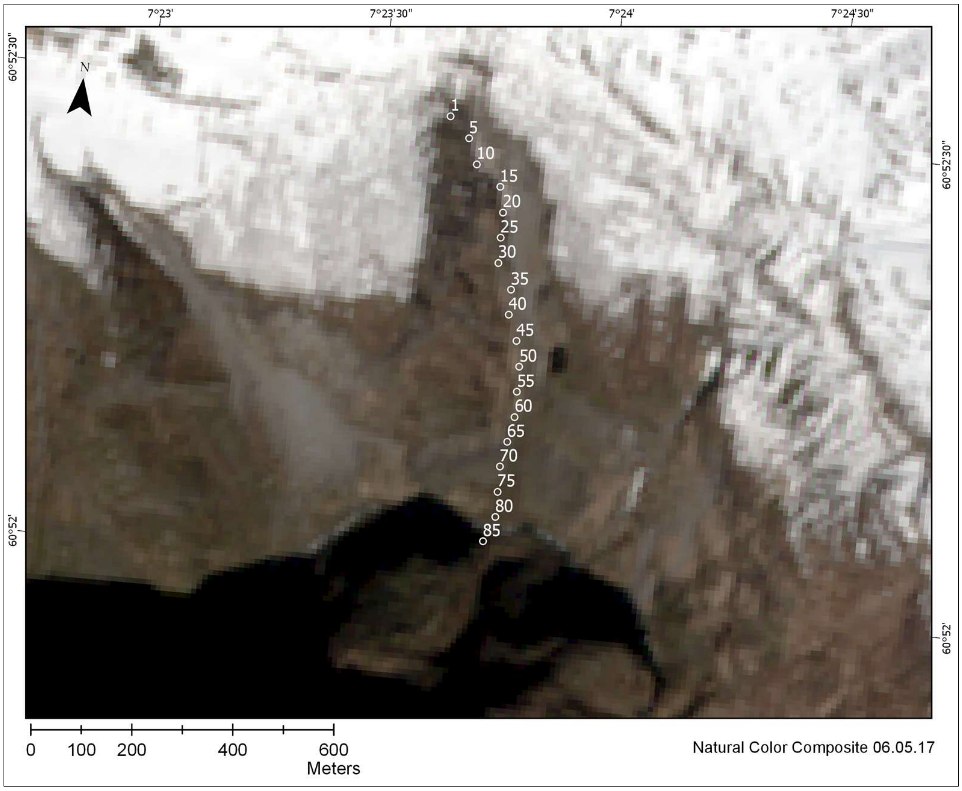

Three datasets from the same area is examined. The *pre-event* (06.05.17) and *post-event* (22.08.17) data are acquired at the end of spring and the end of summer. Seasonal variations can be observed between the images in the form of difference in vegetative condition and snow cover. All data derived from these datasets are represented with **solid lines.**

The *pre-visit* (18.08.15) and *post-event* (22.08.17) data are acquired from the same time of the season, with a two-year interval. The seasonal and atmospheric conditions appear to be more similar in the two datasets. All data derived from these datasets are represented with **dashed lines.**

Less variance is observed in the difference between the pre-event and post-event data, probably due to the seasonal conditions. The change in NDVI is less than 0.10 for the majority of the section, peaking at 0.28. The difference in the NIR-bands follow the same tendency, but with less magnitude. A larger variance is observed in the change between the previsit and pre-event data .

E.6.1 Difference

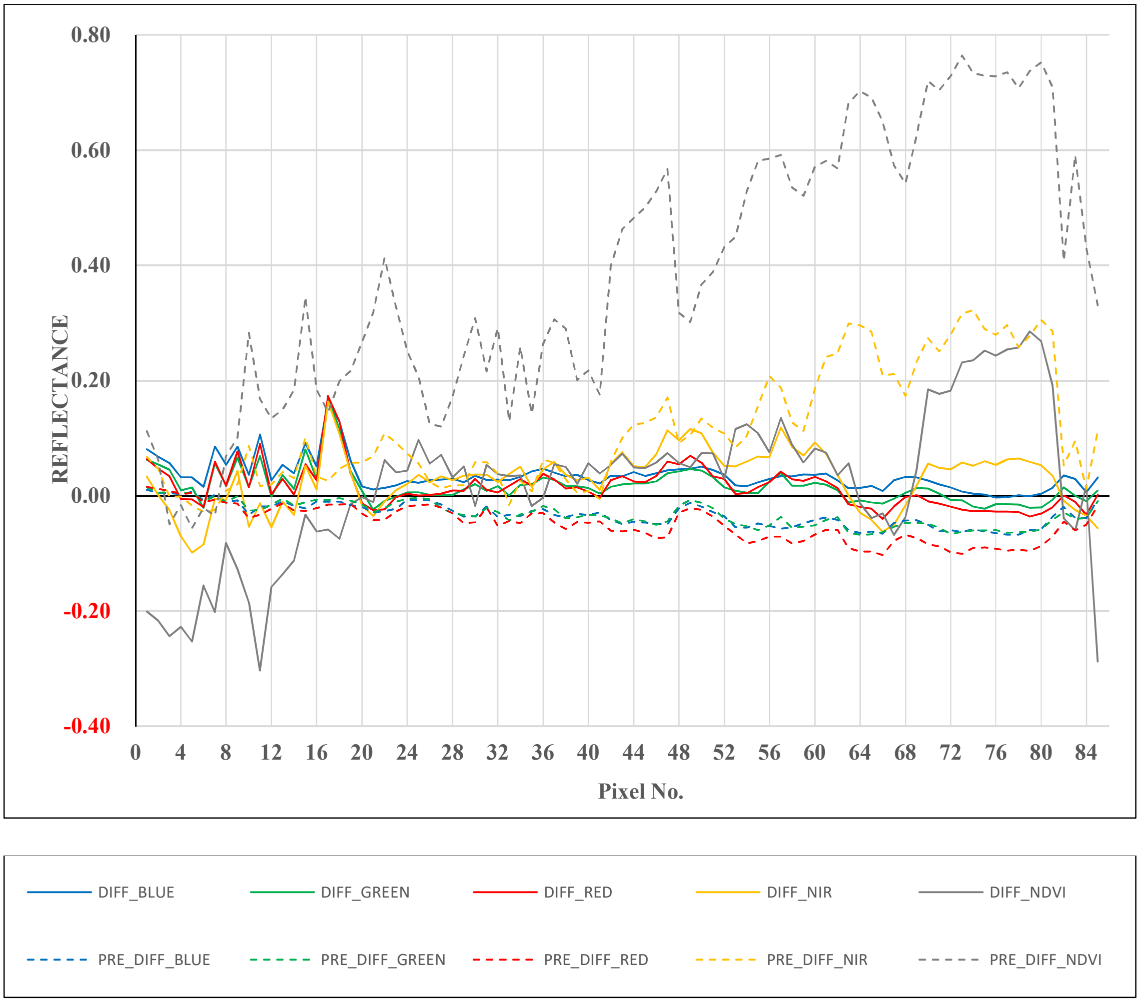

E.6.2 Ratios

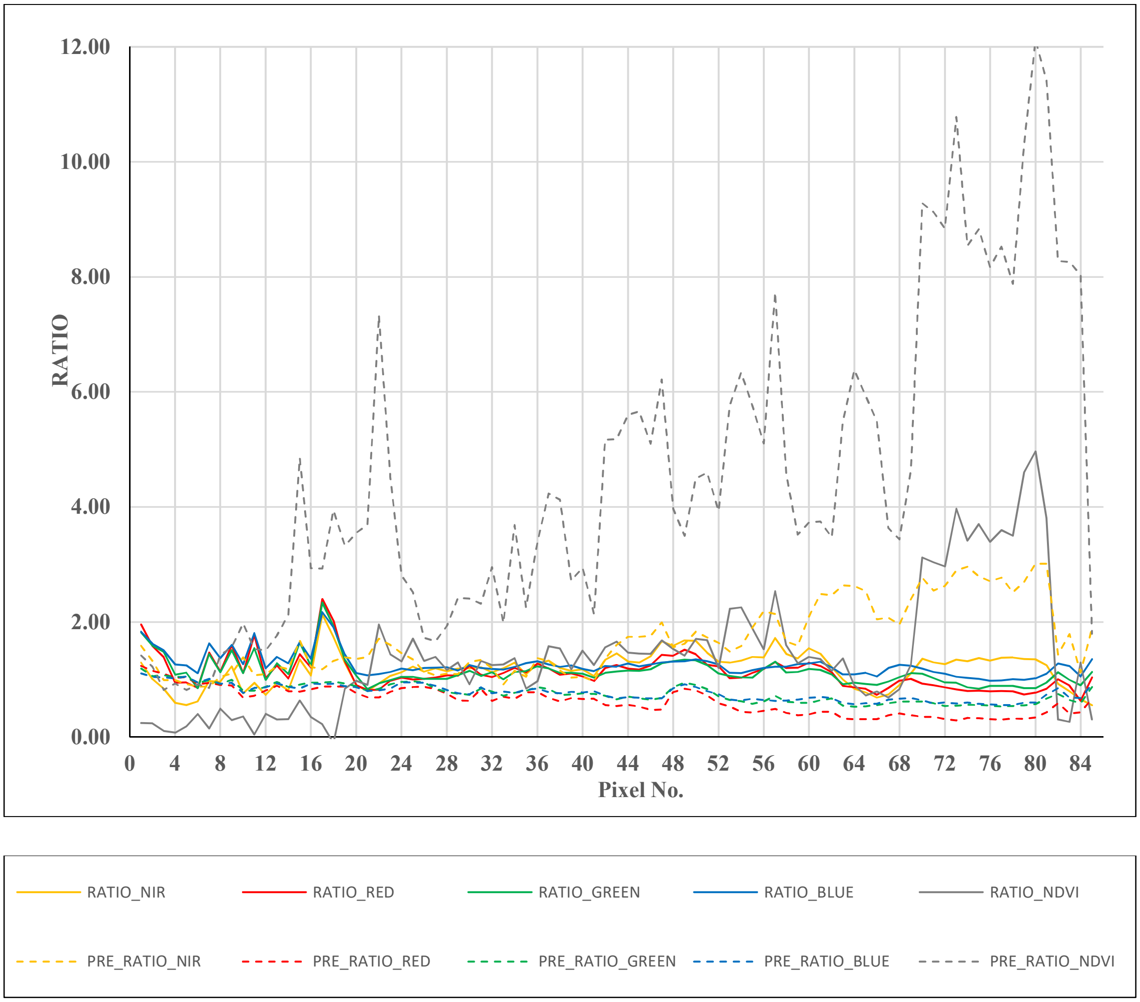
12.00
10.00
8.00
6.00
4.00
2.00
0.00
RATIO
0
4
8
12
16
20
24
28
32
36
40
44
48
52
56
60
64
68
72
76
80
84
Pixel No.
RATIO_NIR
RATIO_RED
RATIO_GREEN
RATIO_BLUE
RATIO_NDVI
PRE_RATIO_NIR
PRE_RATIO_RED
PRE_RATIO_GREEN
PRE_RATIO_BLUE
PRE_RATIO_NDVI

E.6.3 Normalized difference ratios

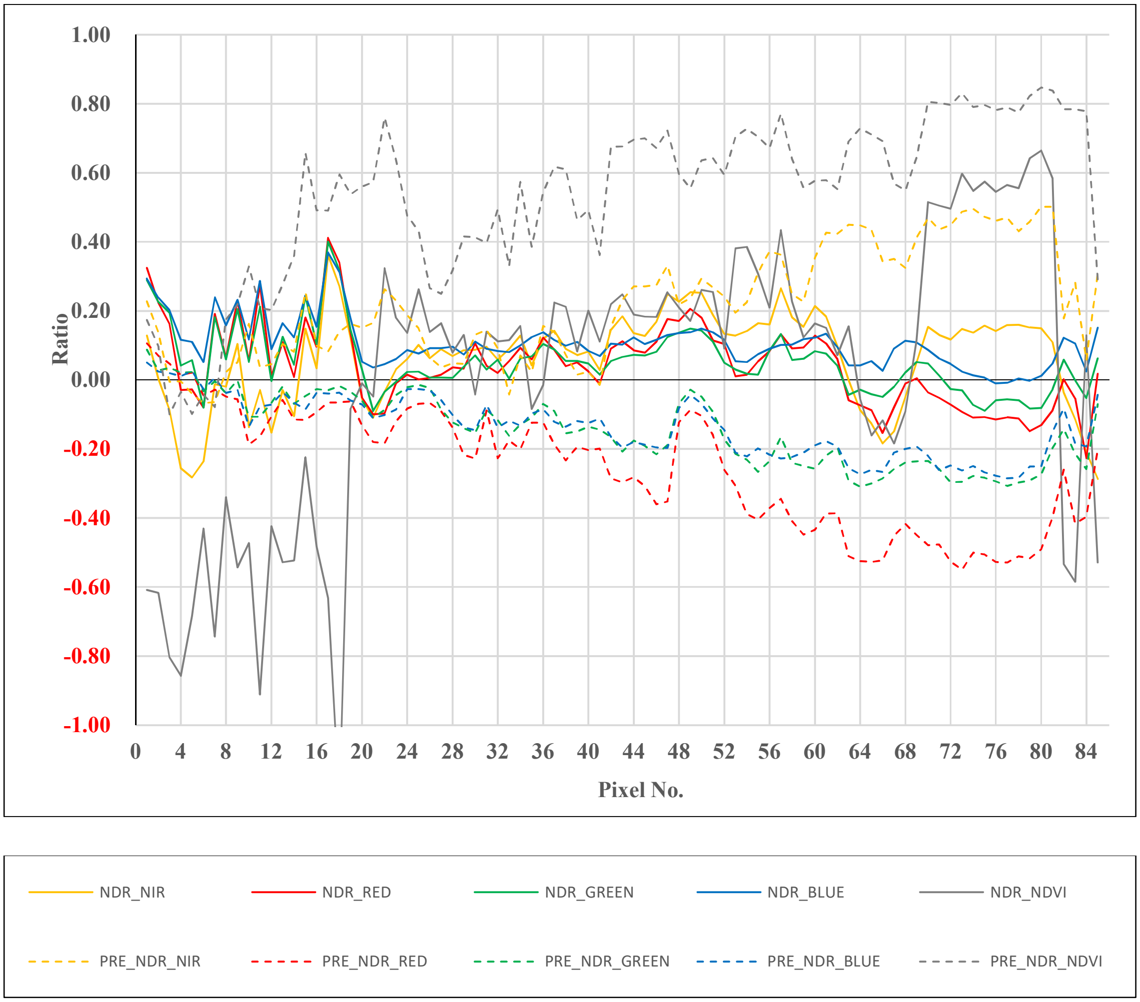

E.7 Event 7 –Spansdalen

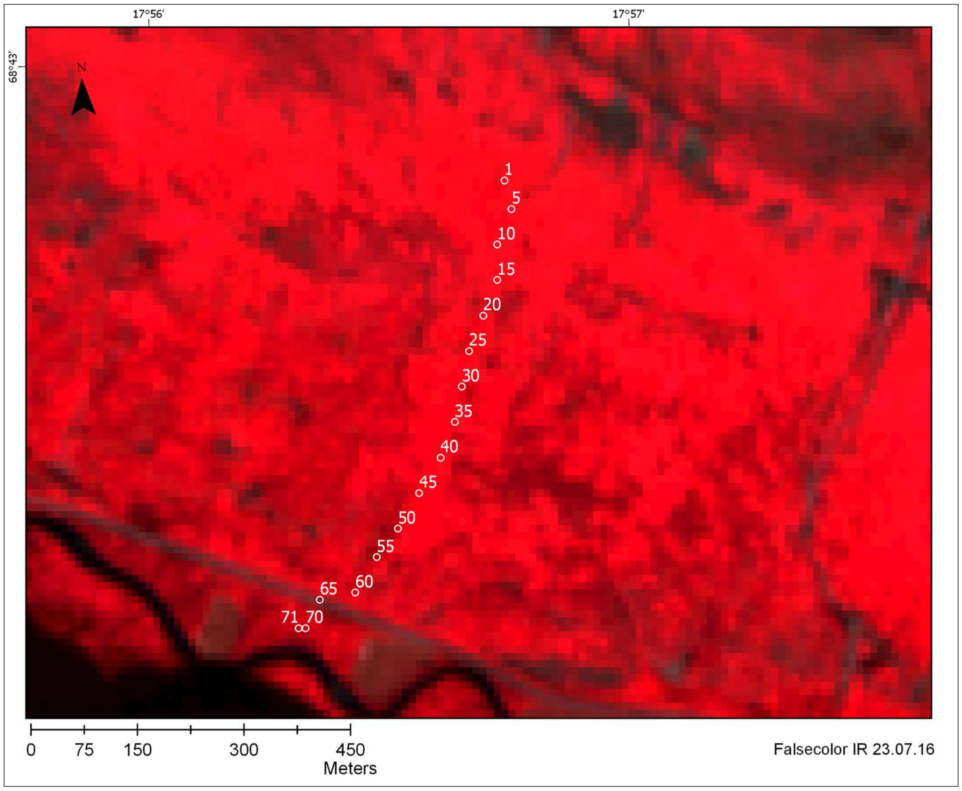

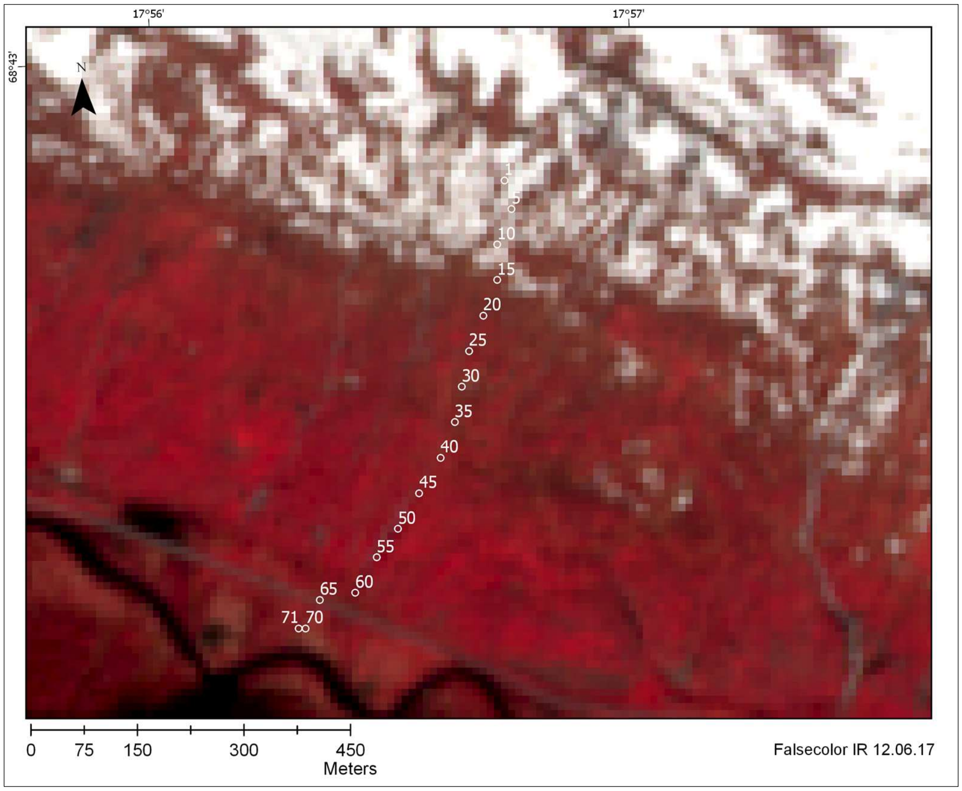

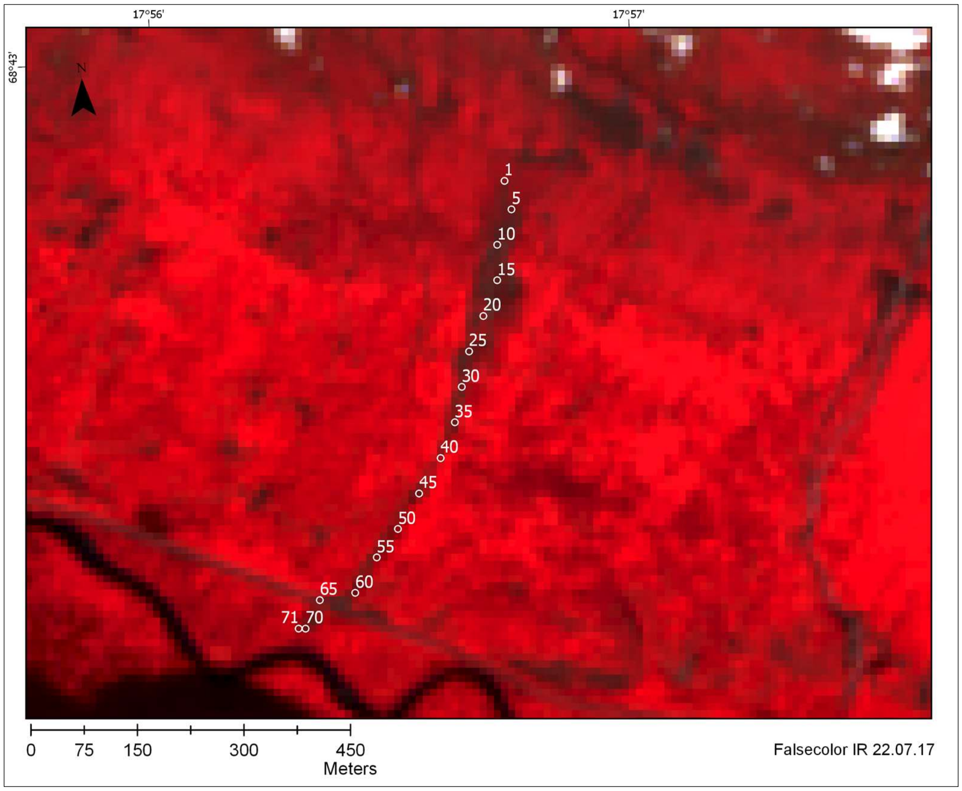

Three datasets from the same area is examined. The *pre-event* (12.06.17) and *post-event* (22.07.17) data are acquired at the start and the end of summer. Seasonal variations can be observed between the images in the form of difference in vegetative condition and snow cover. All data derived from these datasets are represented with **solid lines.**

The *pre-visit* (23.07.16) and *post-event* (22.07.17) data are acquired from the season, with a one-year interval. The seasonal and atmospheric conditions appear to be more similar in the two datasets. All data derived from these datasets are represented with **dashed lines.**

The seasonal variations affect the change detection between the pre-event and post-event data. The snow cover at the start of the transect result in a large change in the RGB-bands, as well as a negative change in the NDVI. The narrow section seem to have more vegetation in the post-event data, than prior to the landslide, due to a more lush valley side.

The change detection between the previsit and post-event data show more logical observations, with less vegetation along the entire transect, and generally low change in the RGB-bands, similar to what is observed in the other events.

E.7.1 Difference

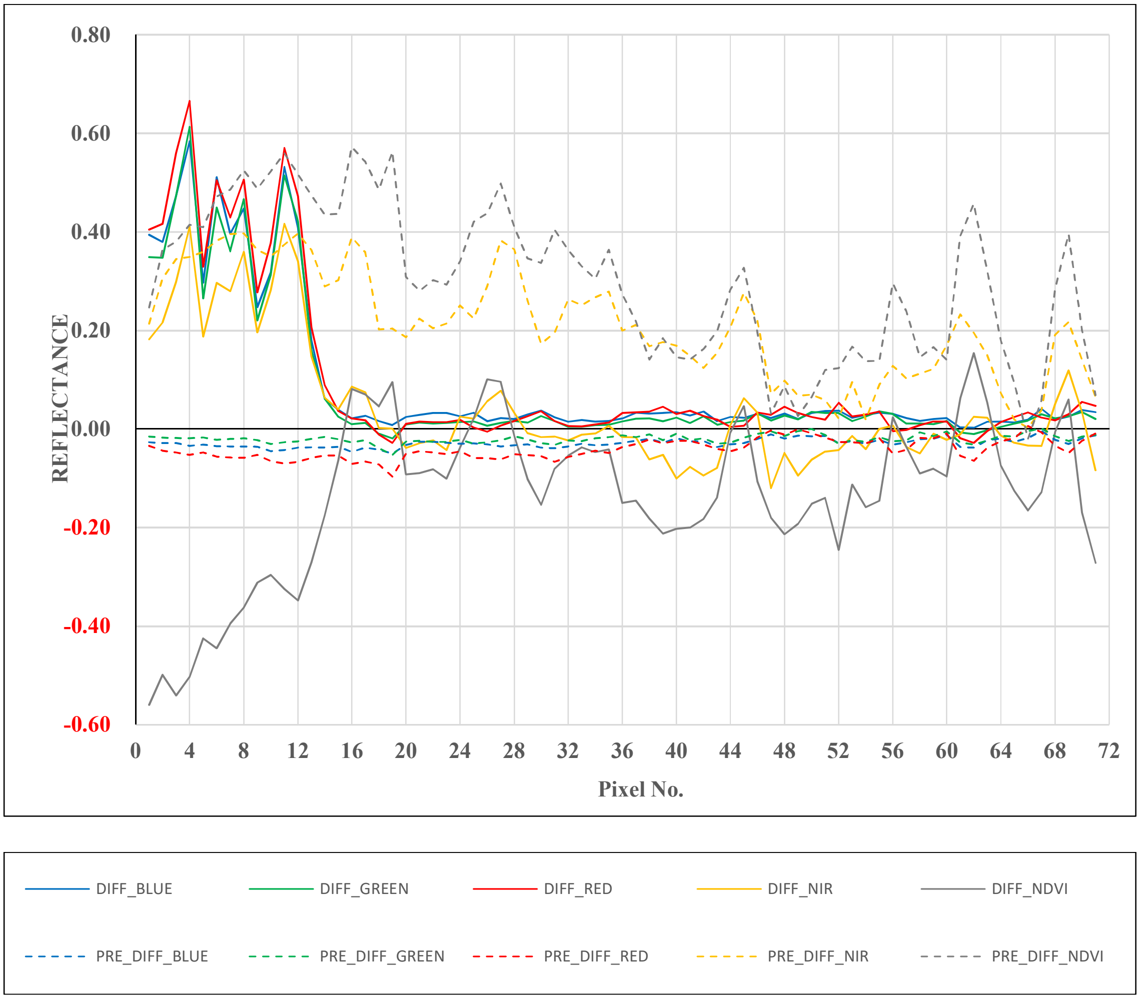

E.7.2 Ratios

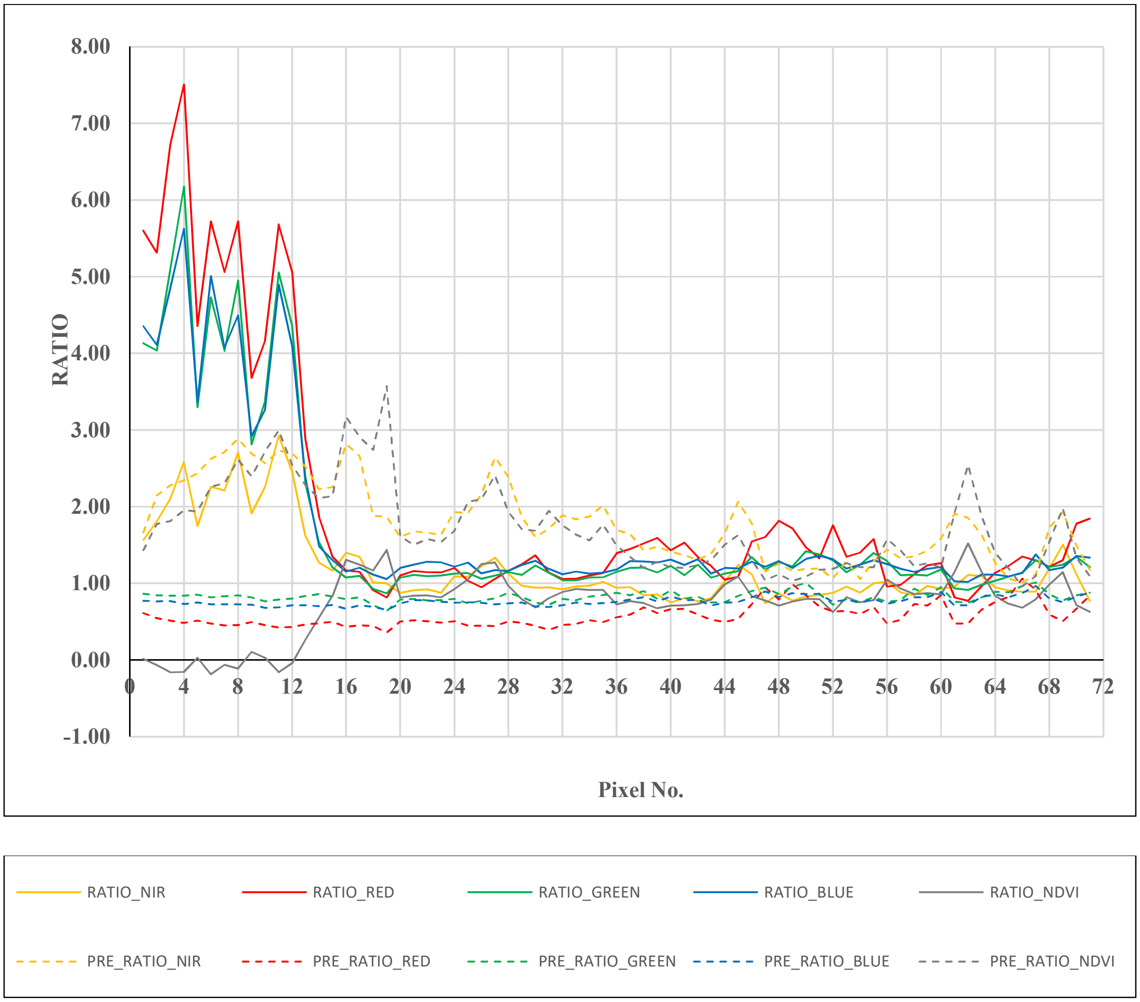

8.00
7.00
6.00
5.00
4.00
3.00
2.00
1.00
0.00
-1.00
RATIO
0
4
8
12
16
20
24
28
32
36
40
44
48
52
56
60
64
68
72
Pixel No.
RATIO_NIR
RATIO_RED
RATIO_GREEN
RATIO_BLUE
RATIO_NDVI
PRE_RATIO_NIR
PRE_RATIO_RED
PRE_RATIO_GREEN
PRE_RATIO_BLUE
PRE_RATIO_NDVI

E.7.3 Normalized difference ratios

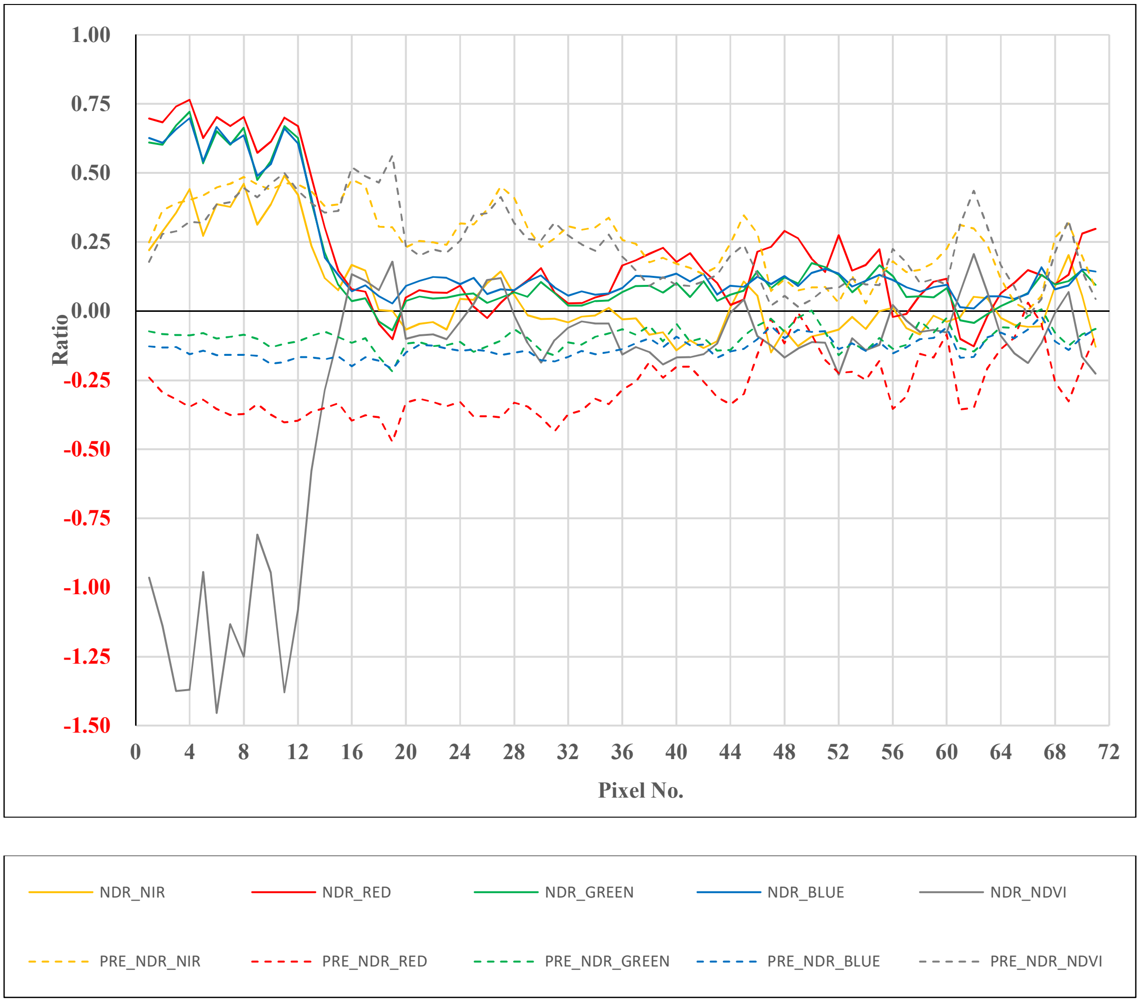

E.8 Event 8 – Selskreda

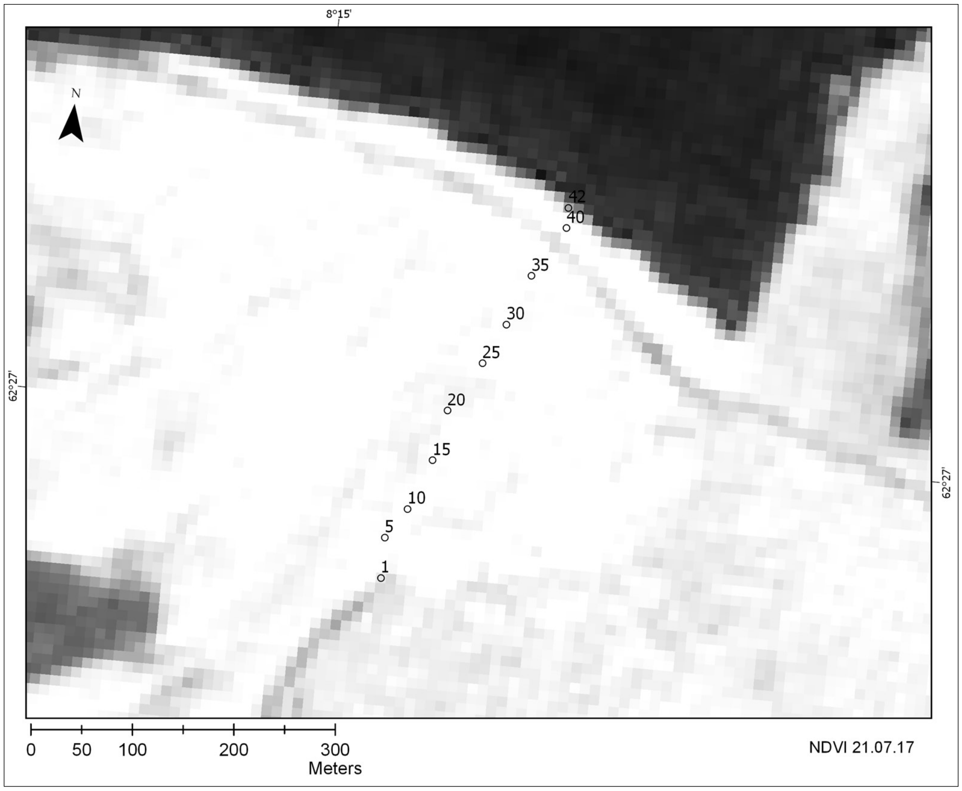

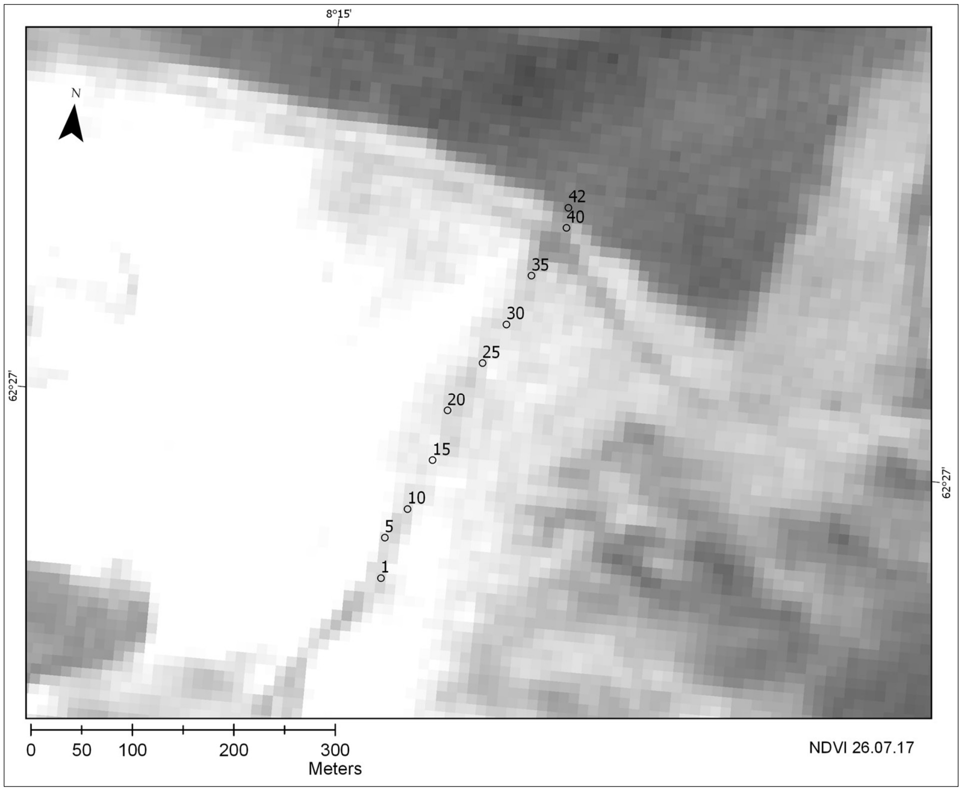

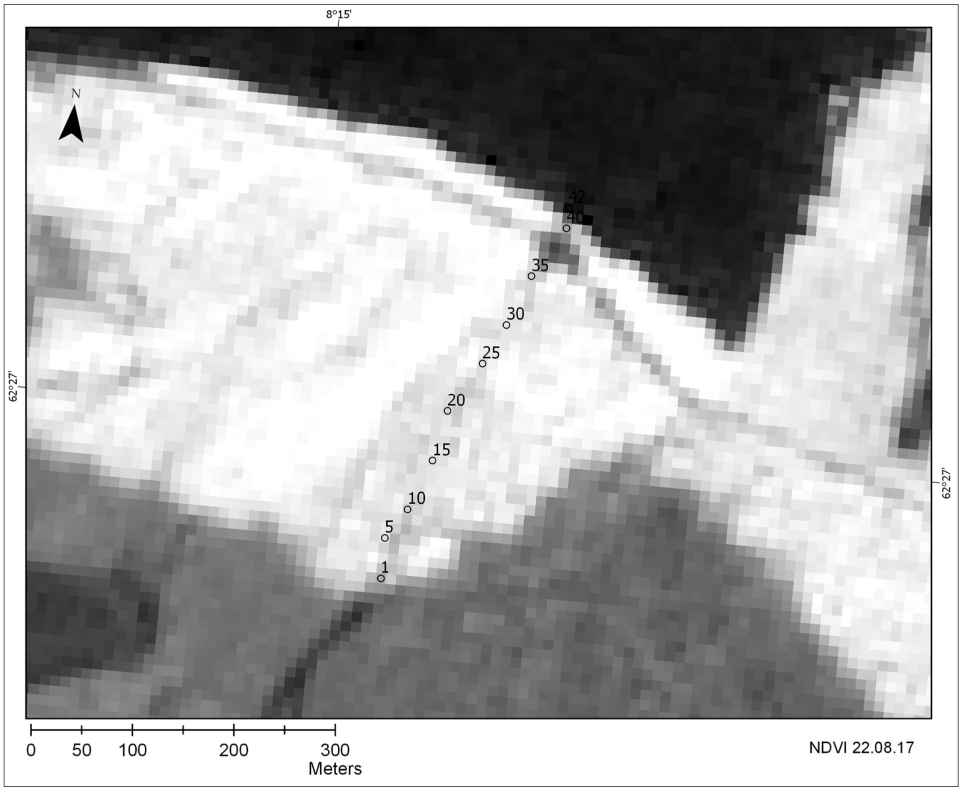

Three datasets from the same area is examined. The *pre-event* (21.07.17) and *post-event* (26.07.17) data are acquired with a 6-day time interval. Atmospheric variations can be observed between the as the post-event data has thin clouds covering the area of interest. All data derived from these datasets are represented with **solid lines.**

The *pre-event* (21.07.17) and *revisit* (22.08.17) data appear to have more similar atmospheric conditions. Some seasonal variation can be observed, regarding a longer shadow influencing the slope in the post event data. All data derived from these datasets are represented with **dashed lines.**

Acticity from the debris flow can be observed in the post-event data, the spectral signature from the transect is believed to be influenced by the atmospheic effects. The spectral reflectance derived from these datasets are disregarder for further consideration.

Small changes can be observed along the first 30 pixels of the transect, in both NDVI and the NIR-bands. The small debris fan accumulated around the road at the end of the transect result in distinct changes, similar to what has been observed in the other events.

E.8.1 Difference

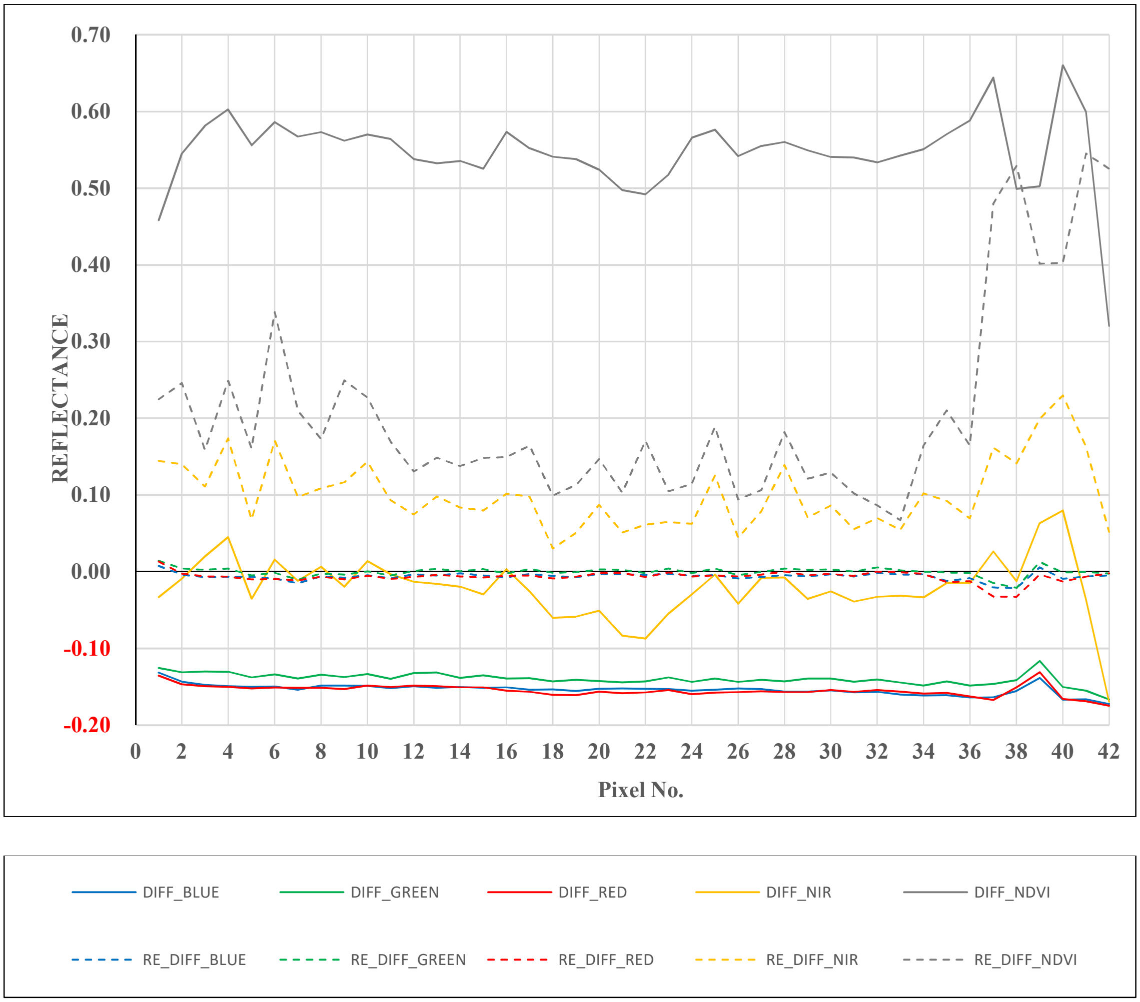

E.8.2 Ratios

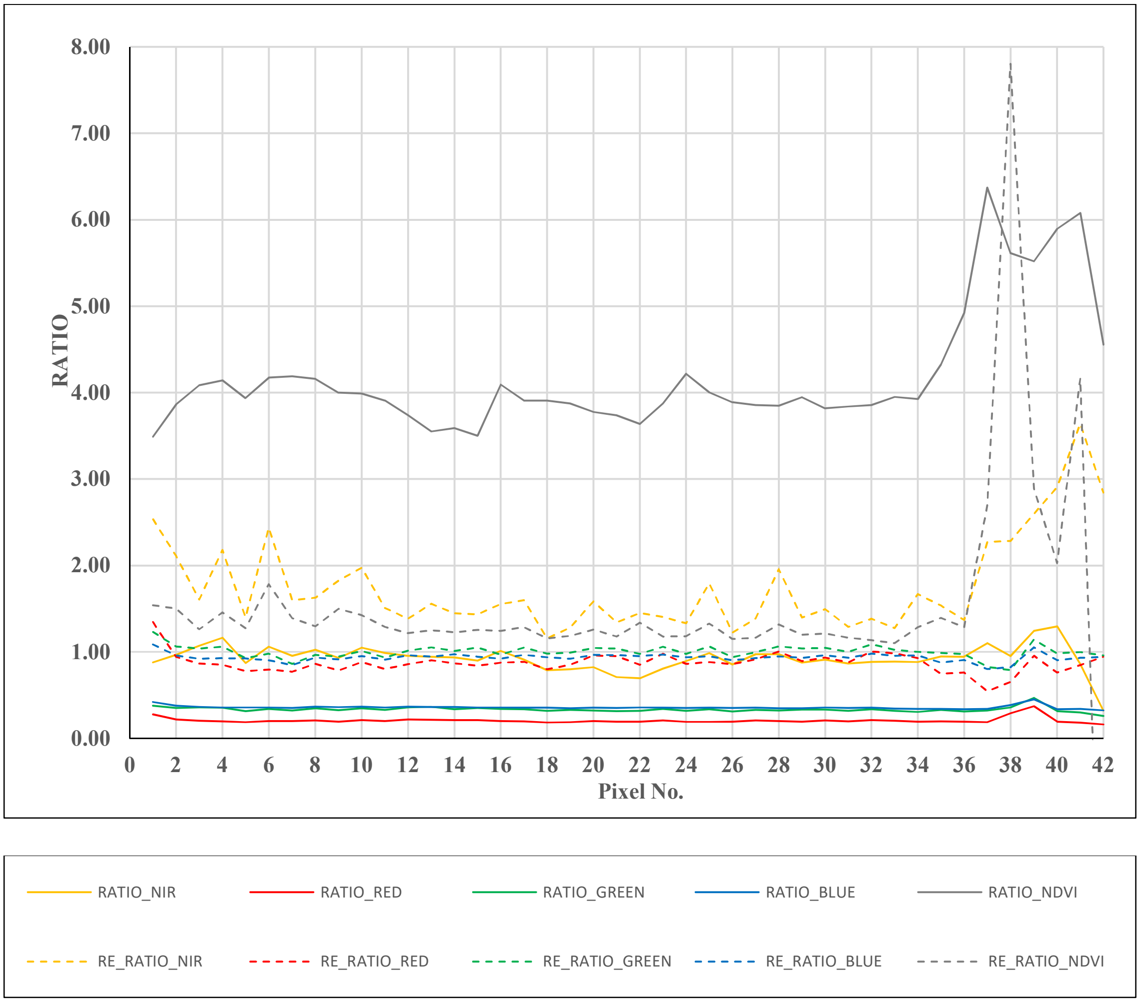
8.00
7.00
6.00
5.00
4.00
3.00
2.00
1.00
0.00
RATIO
0
2
4
6
8
10
12
14
16
18
20
22
24
26
28
30
32
34
36
38
40
42
Pixel No.
RATIO_NIR
RATIO_RED
RATIO_GREEN
RATIO_BLUE
RATIO_NDVI
RE_RATIO_NIR
RE_RATIO_RED
RE_RATIO_GREEN
RE_RATIO_BLUE
RE_RATIO_NDVI

E.8.3 Normalized difference ratios

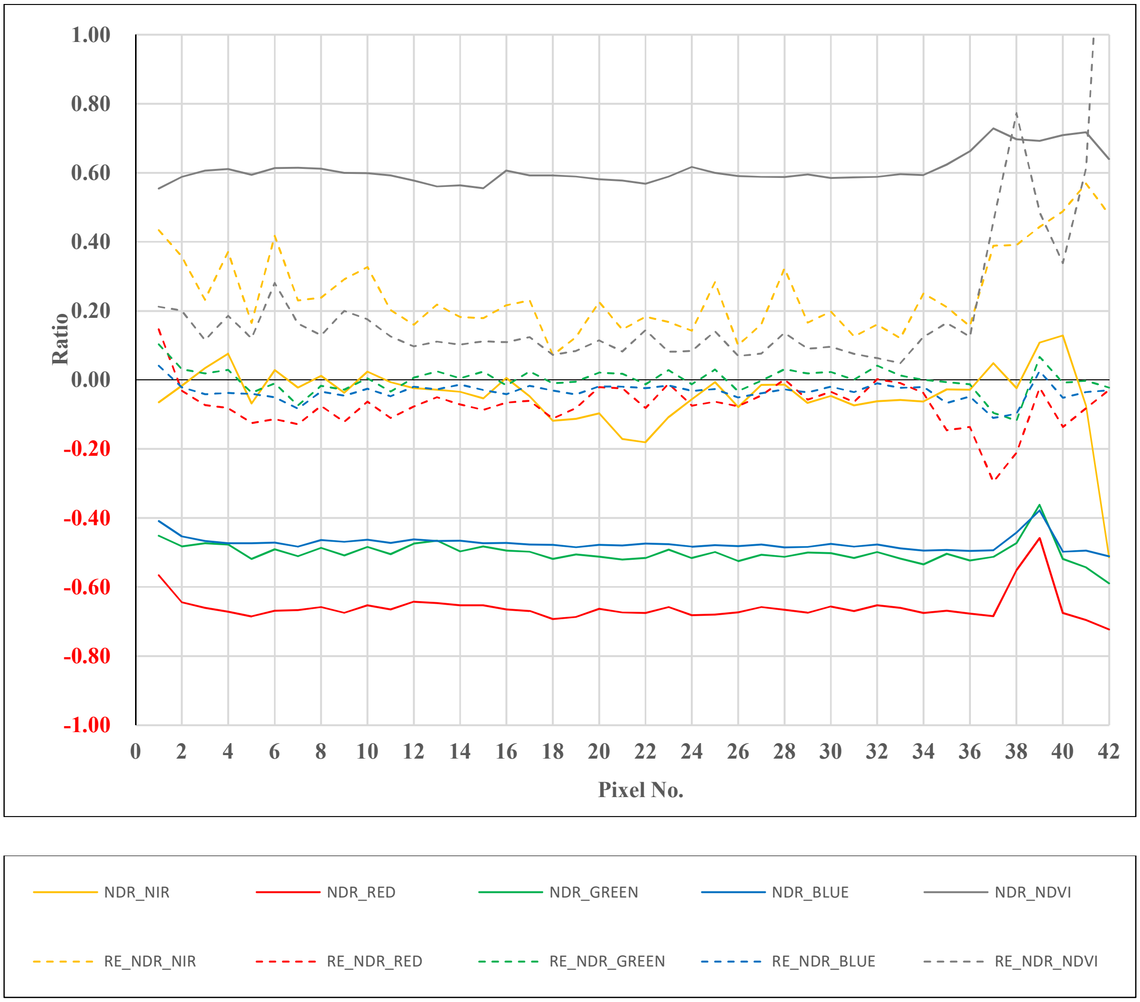

E.9 Event 9 – Tokke

Natural Color Composite 16.09.17

Natural Color Composite 06.10.17

E.9.1 Difference

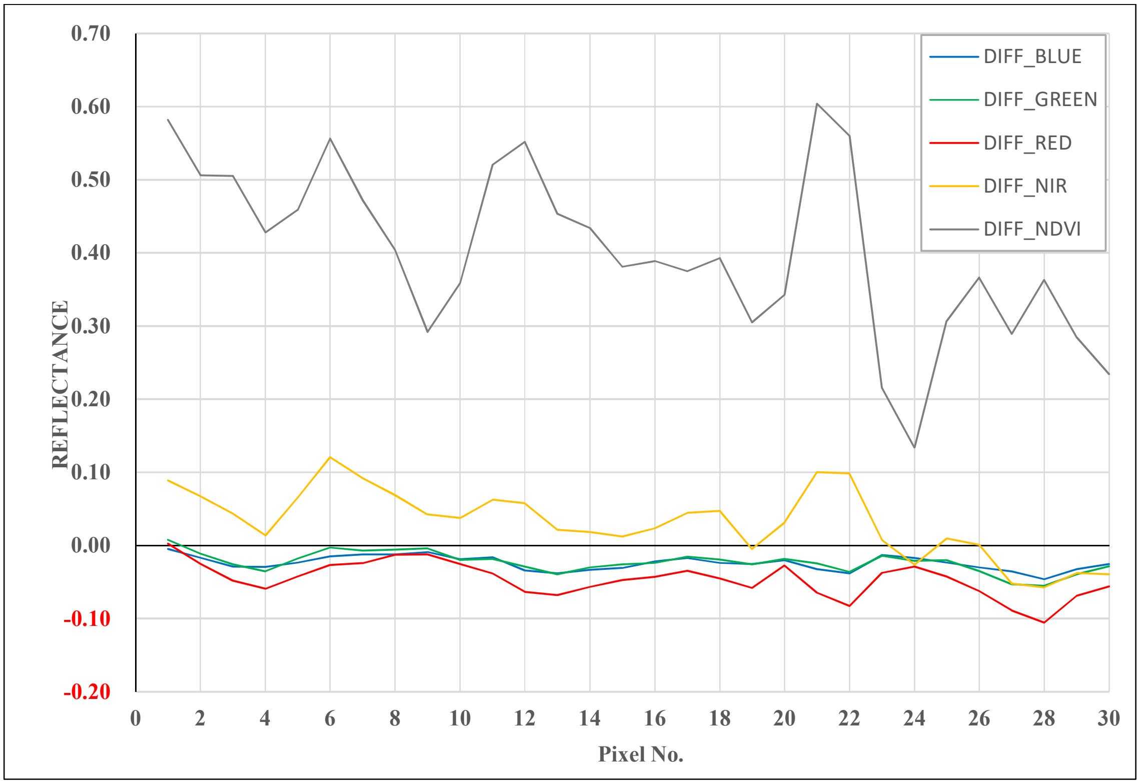

E.9.2 Ratios

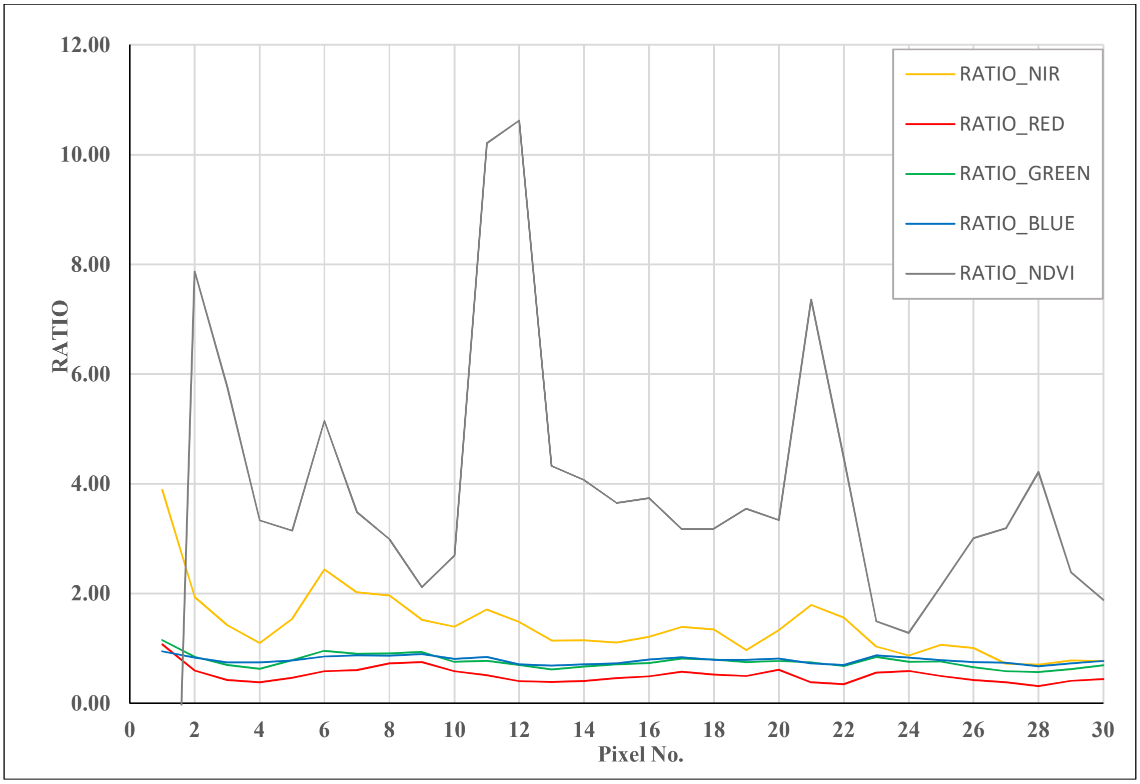

E.9.3 Normalized difference ratios

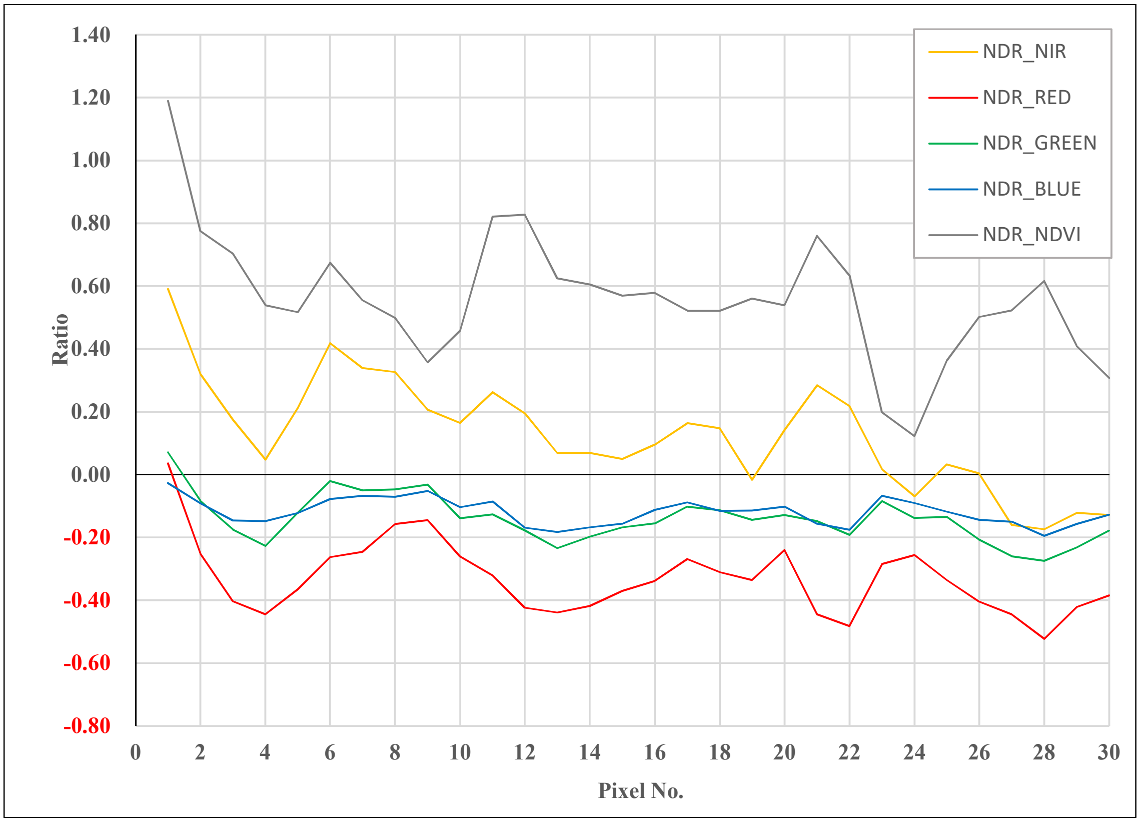

The two datasets are acquired within a relative show time interval. No significant seasonal variations appears to affect the images. The lighting conditions differ slightly between the two datasets, possibly due to atmospheric effects.

A significant change in vegetation can be observed along the transect, and minor negative changes in the RGB-bands.

F. APPENDIX F – Normalized Signatures

The VNIR-spectral signatures and VNIR-change detection signatures are normalized with respect to their length and compared in the figures below. Reflectance is given on the ordinate and the %-length of the landslide on the abscissa. 0 % represents the start of the transect, and 100 % at the end

VNIR BANDS

Event 1 Lindelia

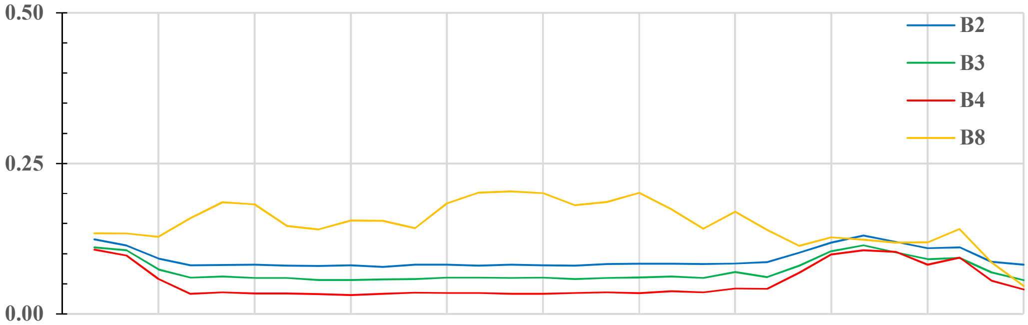

Event 2 Hunndedalen

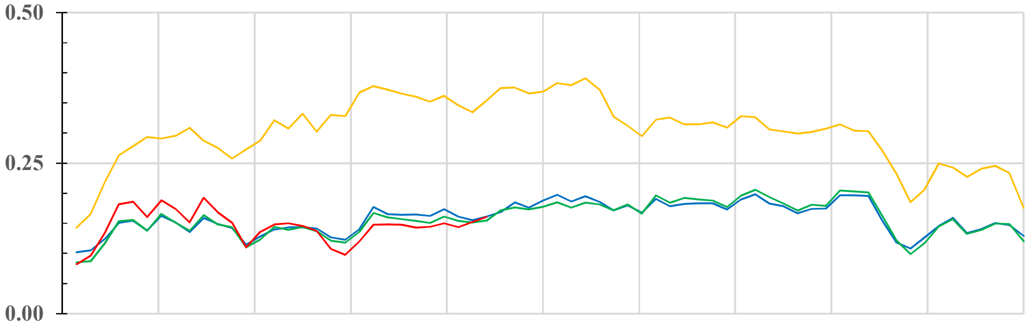

Event 3 Kommedal

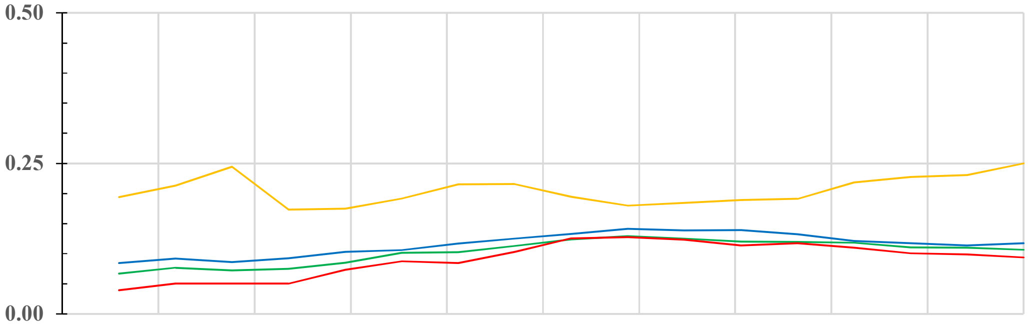

Event 4 Øksland

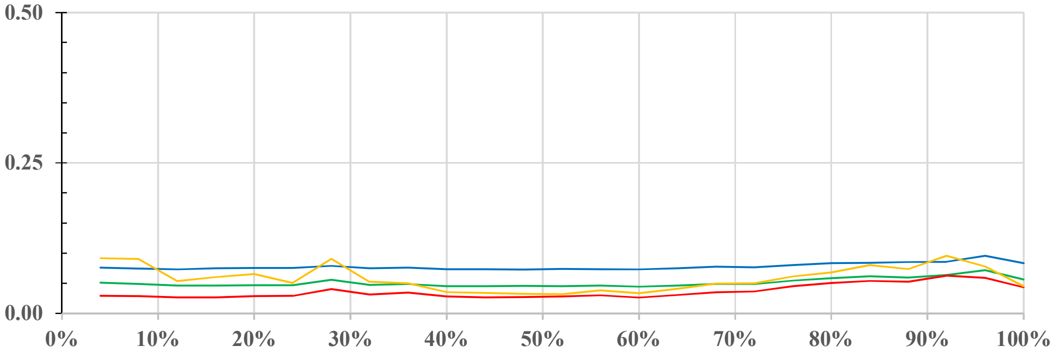

VNIR BANDS

Event 5 Slettafossen

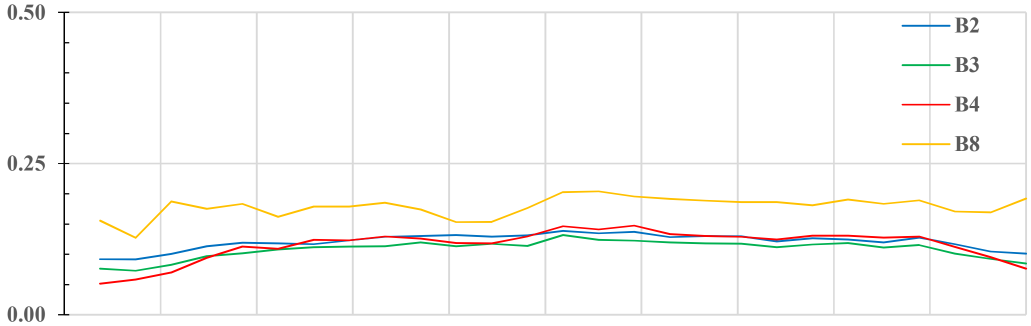

Event 6 Kråkagjelet

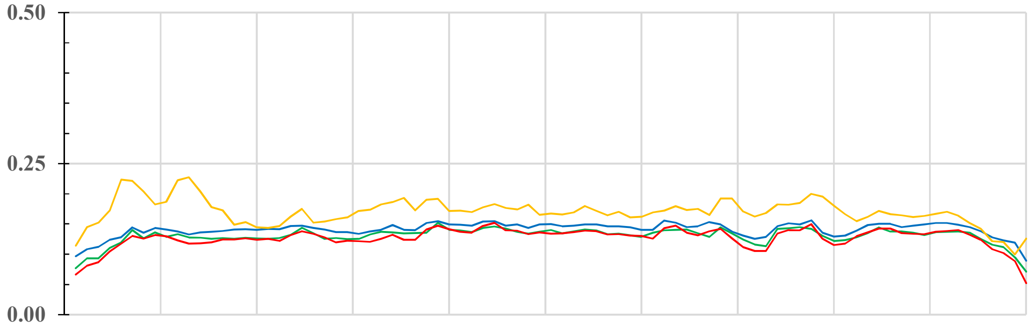

Event 7 Spansdalen

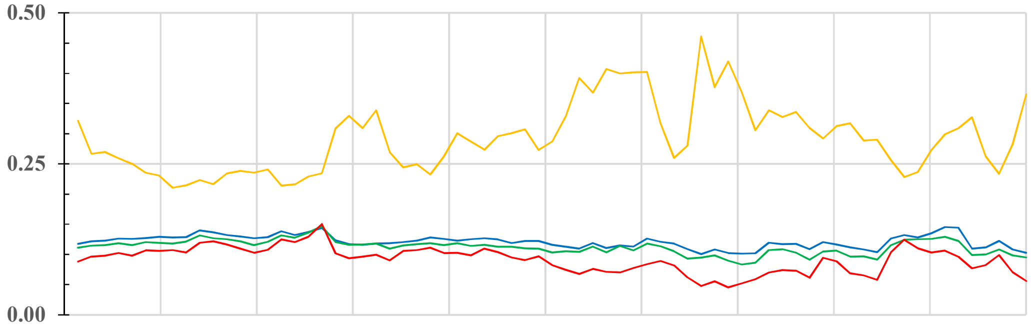

Event 8 Selskreda

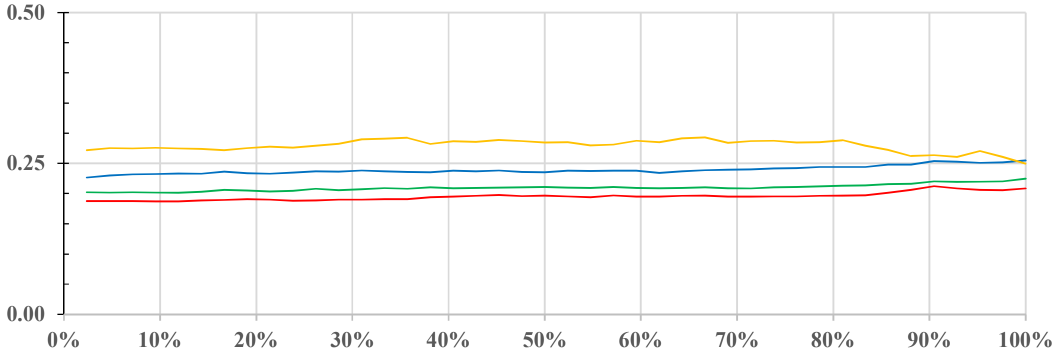

VNIR BANDS

Event 9 Tokke

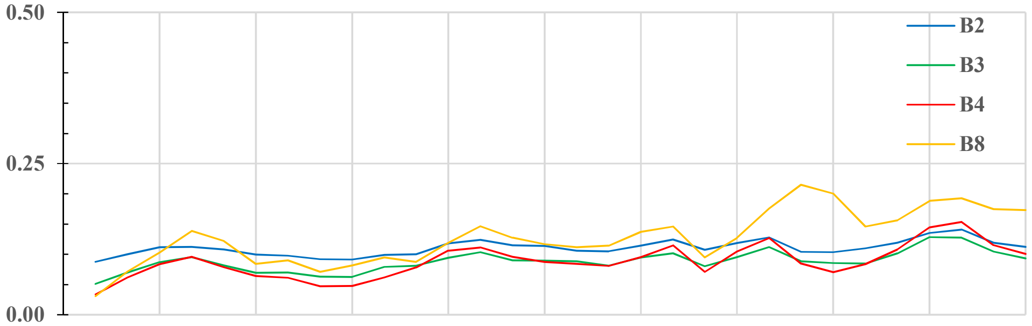

Event 10 Rødstøl

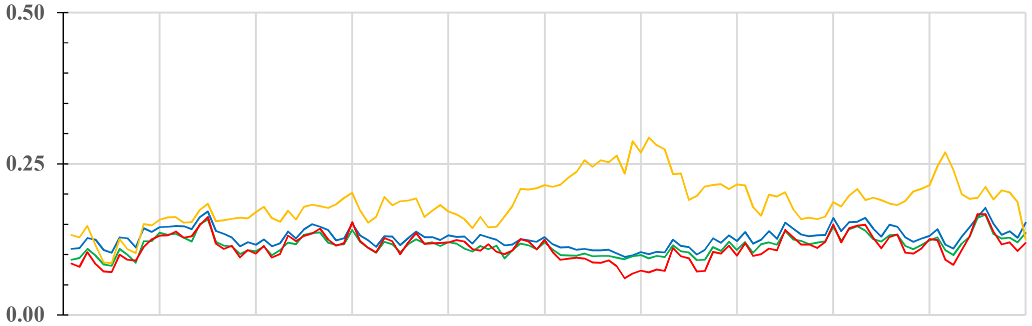

Event 11 Krundalen

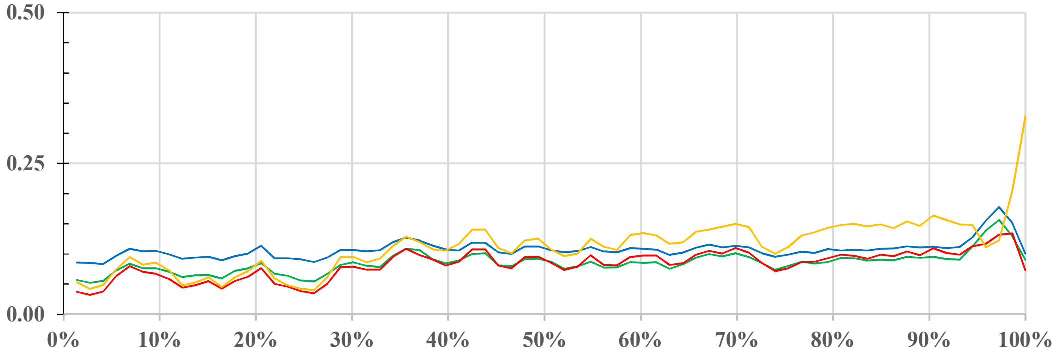

VNIR BANDS - DIFFERENCE

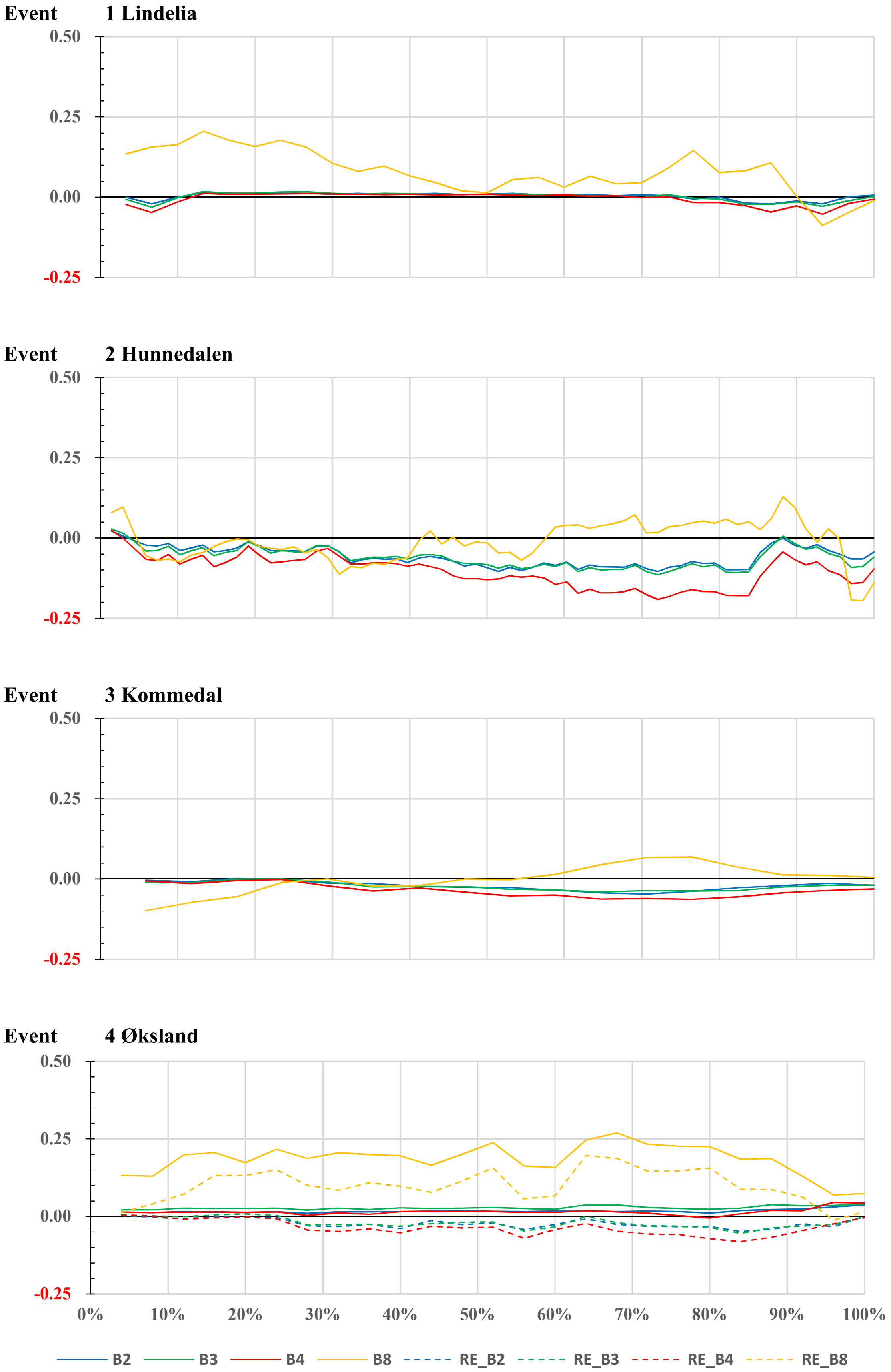

VNIR BANDS - DIFFERENCE

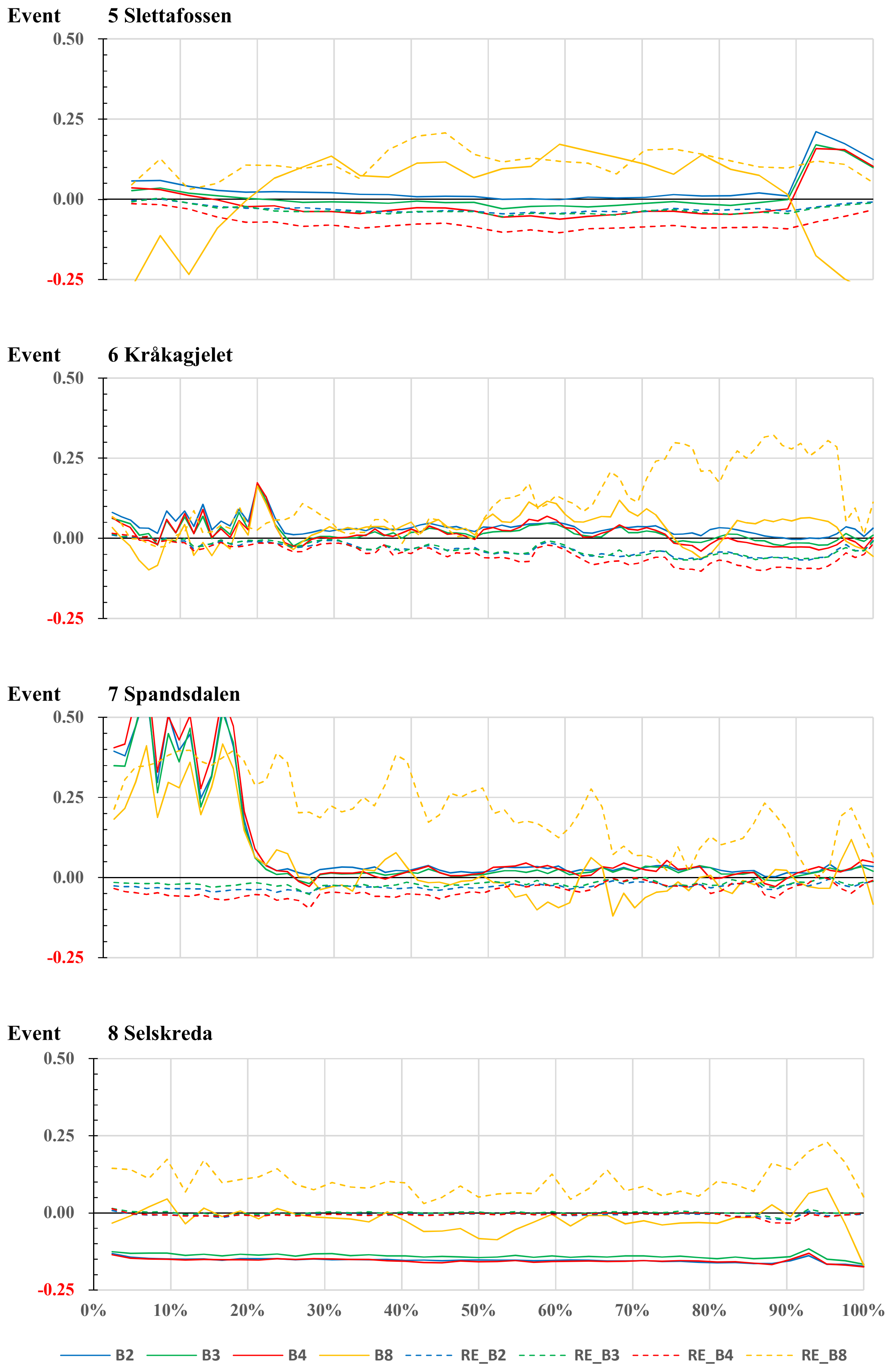

VNIR BANDS - DIFFERENCE

Event **9 Tokke**

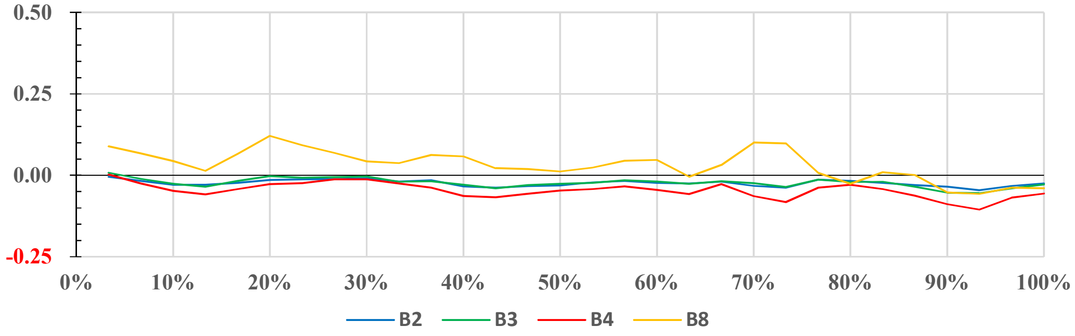

G. APPENDIX G – Transects

The data ID and coordinates of the transect pixels are given in the following chapter.

G.1 Lindelia

CRS	WGS 84/UTM ZONE 32N
Name	1 Lindelia

Pixel no.	Latitude	Longitude
1	60.3210156410236	9.6773690430311
2	60.3210165631287	9.6771880157228
3	60.3210174849874	9.6770069884026
4	60.3210184065996	9.6768259610705
5	60.3210193279654	9.6766449337266
6	60.3210202490848	9.6764639063708
7	60.3210211699577	9.6762828790032
8	60.3210220905842	9.6761018516237
9	60.3210230109642	9.6759208242323
10	60.3210239310978	9.6757397968291
11	60.3210248509849	9.6755587694141
12	60.3210257706255	9.6753777419873
13	60.3210266900198	9.6751967145486
14	60.3210276091676	9.6750156870980
15	60.3210285280689	9.6748346596357
16	60.3210294467238	9.6746536321615
17	60.3210303651322	9.6744726046755
18	60.3210312832942	9.6742915771777
19	60.3210322012098	9.6741105496680
20	60.3210331188789	9.6739295221466
21	60.3210340363015	9.6737484946133
22	60.3209451714433	9.6735656180199
23	60.3208563063308	9.6733827424201
24	60.3208572230075	9.6732017158452
25	60.3207683573908	9.6730188417242
26	60.3207692735713	9.6728378156225
27	60.3206804074505	9.6726549429803
28	60.3206813231348	9.6724739173518
29	60.3205924565099	9.6722910461884
30	60.3205933716980	9.6721100210332

G.2 Hunnedalen

CRS	WGS 84/UTM ZONE 32N
Name	2 Hunndedalen

pixel_no	latitude	longitude
1	58.8178345780528	6.3992263657624
2	58.8177483479238	6.3994060522149
3	58.8176621175370	6.3995857377758
4	58.8175758868923	6.3997654224452
5	58.8174861703964	6.3997721425347
6	58.8173964538987	6.3997788625832
7	58.8173102229683	6.3999585453873
8	58.8172205064549	6.3999652649079
9	58.8171307899398	6.3999719843873
10	58.8170445587235	6.4001516653262
11	58.8169548421927	6.4001583842777
12	58.8168686107046	6.4003380638382
13	58.8167788941580	6.4003447822618
14	58.8166926623982	6.4005244604439
15	58.8166064303805	6.4007041377345
16	58.8165167138042	6.4007108551434
17	58.8164304815148	6.4008905310557
18	58.8163407649228	6.4008972479367
19	58.8162545323615	6.4010769224707
20	58.8161648157538	6.4010836388239
21	58.8160750991444	6.4010903551360
22	58.8159888662973	6.4012700278049
23	58.8158991496722	6.4012767435892
24	58.8158129165534	6.4014564148798
25	58.8157231999125	6.4014631301363
26	58.8156369665219	6.4016428000486
27	58.8155507328735	6.4018224690695
28	58.8155542156502	6.4019954234028
29	58.8154679815002	6.4021750911275
30	58.8153817470924	6.4023547579608
31	58.8152955124269	6.4025344239026
32	58.8152057957022	6.4025411362385
33	58.8151195607649	6.4027208008022
34	58.8150298440244	6.4027275126103
35	58.8149401272823	6.4027342243774
36	58.8148538920593	6.4029138870762
37	58.8147641753014	6.4029205983156
38	58.8146779398066	6.4031002596362

39	58.8145882230330	6.4031069703478
40	58.8145019872665	6.4032866302903
41	58.8144122704772	6.4032933404742
42	58.8143260344390	6.4034729990386
43	58.8142397981430	6.4036526567116
44	58.8141500813240	6.4036593658811
45	58.8140603645033	6.4036660750095
46	58.8139706476809	6.4036727840970
47	58.8138809308567	6.4036794931434
48	58.8137946942471	6.4038591479783
49	58.8137049774073	6.4038658564970
50	58.8136152605656	6.4038725649747
51	58.8135255437223	6.4038792734115
52	58.8134358268772	6.4038859818072
53	58.8133495899540	6.4040656338041
54	58.8132598730932	6.4040723416721
55	58.8131736358983	6.4042519922910
56	58.8130873984456	6.4044316420186
57	58.8129976815551	6.4044383488723
58	58.8129114438307	6.4046179972219
59	58.8128217269246	6.4046247035480
60	58.8127320100168	6.4046314098332
61	58.8126422931072	6.4046381160773
62	58.8125525761959	6.4046448222804
63	58.8124628592828	6.4046515284426
64	58.8123766212309	6.4048311734678
65	58.8122869043021	6.4048378791023
66	58.8122006659785	6.4050175227496
67	58.8121109490340	6.4050242278565
68	58.8120247104387	6.4052038701259

G.3 Kommedalen

CRS	WGS 84/UTM ZONE 32N
Name	3 Kommedal

Pixel no.	Latitude	Longitude
1	58.8405054977126	6.3607782293803
2	58.8405916721704	6.3605983289964
3	58.8406778463698	6.3604184277196
4	58.8407675597203	6.3604115997652
5	58.8408572730690	6.3604047717689
6	58.8409469864159	6.3603979437310
7	58.8410366997612	6.3603911156512
8	58.8411264131046	6.3603842875297
9	58.8412161264464	6.3603774593664
10	58.8413058397863	6.3603706311614
11	58.8413955531246	6.3603638029146
12	58.8414852664611	6.3603569746260
13	58.8415749797958	6.3603501462957
14	58.8416646931288	6.3603433179236
15	58.8417544064600	6.3603364895097
16	58.8418405802306	6.3601565814815
17	58.8419302935459	6.3601497525376

G.4 Øksland

CRS WGS 84/UTM ZONE 32N
Name 4 Øksland

Pixel no.	Latitude	Longitude
1	61.2536040951010	5.8361903718856
2	61.2536893895954	5.8359952577969
3	61.2536850450433	5.8358091624889
4	61.2536807002361	5.8356230672400
5	61.2536763551738	5.8354369720502
6	61.2536720098564	5.8352508769195
7	61.2537573029771	5.8350557598974
8	61.2537529571336	5.8348696643567
9	61.2537486110349	5.8346835688750
10	61.2537442646811	5.8344974734525
11	61.2538295566993	5.8343023539662
12	61.2538252098193	5.8341162581337
13	61.2538208626842	5.8339301623603
14	61.2539061538709	5.8337350408790
15	61.2539018062096	5.8335489446955
16	61.2539870968360	5.8333538216884
17	61.2539827486485	5.8331677250949
18	61.2539784002059	5.8329816285607
19	61.2539740515082	5.8327955320856
20	61.2539697025554	5.8326094356696
21	61.2540549918080	5.8324143097292
22	61.2540506423290	5.8322282129033
23	61.2540462925949	5.8320421161365
24	61.2541315810161	5.8318469882011
25	61.2541272307557	5.8316608910244

G.5 Slettafossen

CRS	WGS 84/UTM ZONE 32N
Name	5 Slettafossen

Pixel no.	Latitude	Longitude
1	62.3241225378113	8.0699306321906
2	62.3242135777403	8.0701208089729
3	62.3243033274849	8.0701180355069
4	62.3243943671585	8.0703082139963
5	62.3244854065729	8.0704983936364
6	62.3244866959728	8.0706913462237
7	62.3244879851050	8.0708842988297
8	62.3245790237348	8.0710744808086
9	62.3245803123366	8.0712674340276
10	62.3246713504445	8.0714576177513
11	62.3246726385159	8.0716505715831
12	62.3246739263195	8.0718435254338
13	62.3247649636428	8.0720337114963
14	62.3247662509161	8.0722266659599
15	62.3248572877174	8.0724168537671
16	62.3248585744603	8.0726098088435
17	62.3249496107397	8.0727999983955
18	62.3249508969521	8.0729929540848
19	62.3249521828968	8.0731859097928
20	62.3249534685739	8.0733788655197
21	62.3249547539833	8.0735718212653
22	62.3250457889525	8.0737620143442
23	62.3251368236625	8.0739522085738
24	62.3252278581133	8.0741424039541
25	62.3253188923050	8.0743326004850
26	62.3254086421421	8.0743298394507
27	62.3254983919779	8.0743270783976

G.6 Kråkagjelet

CRS WGS 84/UTM ZONE 32N
Name 6 Kråkagjelet

Pixel no.	Latitude	Longitude
1	60.8748494982087	7.3942280179337
2	60.8747619503536	7.3944166204896
3	60.8746744022291	7.3946052220129
4	60.8745868538352	7.3947938225035
5	60.8744993051720	7.3949824219616
6	60.8744095596556	7.3949869280224
7	60.8743220107136	7.3951755259024
8	60.8742322651863	7.3951800313885
9	60.8741447159655	7.3953686276903
10	60.8740549704274	7.3953731326017
11	60.8739674209277	7.3955617273255
12	60.8738798711587	7.3957503210167
13	60.8738820666868	7.3959344104004
14	60.8737945163886	7.3961230025720
15	60.8737069658210	7.3963115937111
16	60.8736172202357	7.3963160958950
17	60.8735296693893	7.3965046854561
18	60.8734399237931	7.3965091870654
19	60.8733501781955	7.3965136886455
20	60.8732604325964	7.3965181901964
21	60.8731706869960	7.3965226917181
22	60.8730809413942	7.3965271932106
23	60.8729911957909	7.3965316946739
24	60.8729014501863	7.3965361961080
25	60.8728117045803	7.3965406975130
26	60.8727219589728	7.3965451988887
27	60.8726322133640	7.3965497002352
28	60.8725424677537	7.3965542015526
29	60.8724527221421	7.3965587028407
30	60.8723629765290	7.3965632040996
31	60.8722754252905	7.3967517855375
32	60.8721856796666	7.3967562862218
33	60.8720981281493	7.3969448660819
34	60.8720083825145	7.3969493661916
35	60.8719208307185	7.3971379444738
36	60.8718310850729	7.3971424440090
37	60.8717413394258	7.3971469435150
38	60.8716515937774	7.3971514429918
39	60.8715618481276	7.3971559424394

40	60.8714721024764	7.3971604418579
41	60.8713823568238	7.3971649412471
42	60.8712948047017	7.3973535152247
43	60.8712050590382	7.3973580140394
44	60.8711175066375	7.3975465864393
45	60.8710277609631	7.3975510846795
46	60.8709380152874	7.3975555828905
47	60.8708482696103	7.3975600810723
48	60.8707607169119	7.3977486508038
49	60.8706709712239	7.3977531484111
50	60.8705812255345	7.3977576459893
51	60.8704914798437	7.3977621435383
52	60.8704017341515	7.3977666410582
53	60.8703119884579	7.3977711385488
54	60.8702222427630	7.3977756360103
55	60.8701324970665	7.3977801334427
56	60.8700427513687	7.3977846308458
57	60.8699530056695	7.3977891282198
58	60.8698632599689	7.3977936255647
59	60.8697735142669	7.3977981228803
60	60.8696837685635	7.3978026201668
61	60.8695940228587	7.3978071174242
62	60.8695042771524	7.3978116146523
63	60.8694123385853	7.3976320480146
64	60.8693225928843	7.3976365457005
65	60.8692328471819	7.3976410433573
66	60.8691409083909	7.3974614787257
67	60.8690511626937	7.3974659768402
68	60.8689614169951	7.3974704749256
69	60.8688716712951	7.3974749729818
70	60.8687819255938	7.3974794710088
71	60.8686921798910	7.3974839690067
72	60.8686024341868	7.3974884669754
73	60.8685126884812	7.3974929649149
74	60.8684229427742	7.3974974628252
75	60.8683331970658	7.3975019607064
76	60.8682434513560	7.3975064585584
77	60.8681537056448	7.3975109563812
78	60.8680639599322	7.3975154541749
79	60.8679742142182	7.3975199519394
80	60.8678844685028	7.3975244496748
81	60.8677925295675	7.3973448928920
82	60.8677027838573	7.3973493910850
83	60.8676130381458	7.3973538892489

84	60.8675210989867	7.3971743344720
85	60.8674313532803	7.3971788330936

G.7 Spansdalen

CRS WGS 84/UTM ZONE 33N
Name 7 Spansdalen

Pixel no.	Latitude	Longitude
1	68.7149408319112	17.9454182702000
2	68.7148512648957	17.9454064515569
3	68.7147616978784	17.9453946330158
4	68.7146721308591	17.9453828145766
5	68.7145782696437	17.9456175087848
6	68.7144887026404	17.9456056895639
7	68.7144034297897	17.9453473598709
8	68.7143138627628	17.9453355418395
9	68.7142285894900	17.9450772152053
10	68.7141390224395	17.9450653983635
11	68.7140494553871	17.9450535816236
12	68.7139598883328	17.9450417649856
13	68.7138703212765	17.9450299484496
14	68.7137807542184	17.9450181320155
15	68.7136911871583	17.9450063156834
16	68.7136059133550	17.9447479975455
17	68.7135163462713	17.9447361824027
18	68.7134267791858	17.9447243673619
19	68.7133372120983	17.9447125524231
20	68.7132519378296	17.9444542395186
21	68.7131623707185	17.9444424257691
22	68.7130770960277	17.9441841159231
23	68.7129875288931	17.9441723033629
24	68.7128979617565	17.9441604909046
25	68.7128126866220	17.9439021852043
26	68.7127231194619	17.9438903739353
27	68.7126378439053	17.9436320712934
28	68.7125482767215	17.9436202612136
29	68.7124587095359	17.9436084512356
30	68.7123691423484	17.9435966413596
31	68.7122795751589	17.9435848315854
32	68.7121942991153	17.9433265352637
33	68.7121047319023	17.9433147266786
34	68.7120151646874	17.9433029181955
35	68.7119255974705	17.9432911098142

36	68.7118360302518	17.9432793015347
37	68.7117507537211	17.9430210115329
38	68.7116611864788	17.9430092044425
39	68.7115759095261	17.9427509174986
40	68.7114863422602	17.9427391115973
41	68.7114010648856	17.9424808277114
42	68.7113157871105	17.9422225457961
43	68.7112262197994	17.9422107421710
44	68.7111409416024	17.9419524633136
45	68.7110513742677	17.9419406608774
46	68.7109660956488	17.9416823850778
47	68.7108765282905	17.9416705838305
48	68.7107912492496	17.9414123110886
49	68.7107016818678	17.9414005110302
50	68.7106164024050	17.9411422413460
51	68.7105311225418	17.9408839736323
52	68.7105354097252	17.9406375046864
53	68.7104458422784	17.9406257078891
54	68.7103605616147	17.9403674441165
55	68.7102709941443	17.9403556485080
56	68.7101857130587	17.9400973877929
57	68.7101004315729	17.9398391290483
58	68.7100108640573	17.9398273357155
59	68.7099255821495	17.9395690800283
60	68.7098360146104	17.9395572878841
61	68.7097507322807	17.9392990352543
62	68.7097550171332	17.9390525745652
63	68.7097593016268	17.9388061137744
64	68.7097635857615	17.9385596528820
65	68.7097678695374	17.9383131918878
66	68.7097721529544	17.9380667307920
67	68.7096825852931	17.9380549447625
68	68.7095930176299	17.9380431588346
69	68.7095034499647	17.9380313730084
70	68.7094181652769	17.9377731300272
71	68.7094224478973	17.9375266726689

G.8 Selskreda

CRS	WGS 84/UTM ZONE 32N
Name	8 Selskreda

Pixel no.	Latitude	Longitude
1	62.4486474271543	8.2519080851808
2	62.4487371794540	8.2519058420639
3	62.4488269317526	8.2519035989318
4	62.4489166840499	8.2519013557843
5	62.4490064363460	8.2518991126216
6	62.4490074752587	8.2520928763766
7	62.4490972275576	8.2520906337794
8	62.4491869798552	8.2520883911670
9	62.4491880185067	8.2522821560990
10	62.4492777708071	8.2522799140521
11	62.4493675231063	8.2522776719900
12	62.4494572754043	8.2522754299126
13	62.4495480660993	8.2524669550908
14	62.4496388565318	8.2526584814306
15	62.4497286088341	8.2526562404692
16	62.4498193990069	8.2528477685365
17	62.4499091513107	8.2528455281255
18	62.4499989036132	8.2528432876991
19	62.4500886559146	8.2528410472576
20	62.4501784082147	8.2528388068007
21	62.4502681605136	8.2528365663286
22	62.4503589504378	8.2530280983859
23	62.4504487027382	8.2530258584642
24	62.4505394924027	8.2532173922491
25	62.4506302818047	8.2534089271958
26	62.4507200341094	8.2534066883902
27	62.4508097864129	8.2534044495693
28	62.4508995387152	8.2534022107331
29	62.4509903278629	8.2535937485388
30	62.4509913644405	8.2537875252112
31	62.4510811167482	8.2537852875065
32	62.4511719053711	8.2539768276360
33	62.4512616576804	8.2539745904817
34	62.4513514099885	8.2539723533122
35	62.4514421983543	8.2541638957351
36	62.4515319506639	8.2541616591160
37	62.4516227387701	8.2543532032666
38	62.4517135266138	8.2545447485792
39	62.4518032789276	8.2545425130764

40	62.4518940665116	8.2547340601167
41	62.4519838188269	8.2547318251644
42	62.4520735711411	8.2547295901969

G.9 Tokke

CRS WGS 84/UTM ZONE 32N
Name 9 Tokke

Pixel no.	Latitude	Longitude
1	59.4846337422520	7.8362675508027
2	59.4847250945119	7.8364409705183
3	59.4847266653456	7.8366174791843
4	59.4848180171445	7.8367909003239
5	59.4848195875072	7.8369674094967
6	59.4848211576316	7.8371439186887
7	59.4849125087368	7.8373173417398
8	59.4850038596135	7.8374907657274
9	59.4850952102619	7.8376641906515
10	59.4851849914881	7.8376611053702
11	59.4852763419123	7.8378345316799
12	59.4853661231414	7.8378314468284
13	59.4854574733414	7.8380048745237
14	59.4855488233130	7.8381783031556
15	59.4855503918144	7.8383548162284
16	59.4855519600776	7.8385313293204
17	59.4855535281024	7.8387078424316
18	59.4855550958890	7.8388843555620
19	59.4856464447016	7.8390577870804
20	59.4856480120172	7.8392343007175
21	59.4856495790947	7.8394108143738
22	59.4856511459338	7.8395873280494
23	59.4857424938199	7.8397607619668
24	59.4857440601881	7.8399372761490
25	59.4857456263180	7.8401137903504
26	59.4857471922097	7.8402903045709
27	59.4856589765557	7.8404698967148
28	59.4856605419653	7.8406464105054
29	59.4855723258166	7.8408260012635
30	59.4855738907441	7.8410025146242

G.10 Rødstøl

CRS WGS 84/UTM ZONE 32N
Name 10 Rødstøl

Min

Pixel no.	Latitude	Longitude
1	62.3138301450398	8.0611811890974
2	62.3139211968957	8.0613712745611
3	62.3140122484928	8.0615613611744
4	62.3141032998310	8.0617514489375
5	62.3141943509102	8.0619415378502
6	62.3142854017305	8.0621316279126
7	62.3143764522920	8.0623217191248
8	62.3144675025945	8.0625118114866
9	62.3144688029561	8.0627046994274
10	62.3145598527371	8.0628947935328
11	62.3146509022591	8.0630848887880
12	62.3147419515223	8.0632749851929
13	62.3147432508285	8.0634678749341
14	62.3148342995701	8.0636579730826
15	62.3149253480527	8.0638480723808
16	62.3149266465662	8.0640409633286
17	62.3150176945273	8.0642310643704
18	62.3150189925105	8.0644239559310
19	62.3151100399501	8.0646140587164
20	62.3152010871307	8.0648041626516
21	62.3152023843211	8.0649970554187
22	62.3152934309801	8.0651871610975
23	62.3152947276404	8.0653800544773
24	62.3153857737778	8.0655701618997
25	62.3154768196563	8.0657602704720
26	62.3154781155237	8.0659531650583
27	62.3155691608806	8.0661432753741
28	62.3156602059784	8.0663333868398
29	62.3156615010531	8.0665262826326
30	62.3157525456294	8.0667163958420
31	62.3157538401738	8.0669092922475
32	62.3158448842284	8.0670994072004
33	62.3158461782427	8.0672923042186
34	62.3159372217757	8.0674824209152
35	62.3159385152597	8.0676753185460
36	62.3160295582711	8.0678654369863
37	62.3161206010234	8.0680555565765
38	62.3161218937146	8.0682484554137
39	62.3162129359453	8.0684385767476

40	62.3163039779170	8.0686286992313
41	62.3163950196297	8.0688188228649
42	62.3163963112653	8.0690117235023
43	62.3164873524564	8.0692018488796
44	62.3165783933884	8.0693919754068
45	62.3166694340614	8.0695821030839
46	62.3167604744753	8.0697722319110
47	62.3167617647928	8.0699651349424
48	62.3168528046850	8.0701552655132
49	62.3169438443183	8.0703453972339
50	62.3170348836925	8.0705355301046
51	62.3170361729543	8.0707284349362
52	62.3171272118068	8.0709185695506
53	62.3172182504003	8.0711087053150
54	62.3173092887347	8.0712988422294
55	62.3173105769409	8.0714917488611
56	62.3174016147536	8.0716818875192
57	62.3174926523073	8.0718720273274
58	62.3175836896019	8.0720621682855
59	62.3176747266374	8.0722523103936
60	62.3176760135253	8.0724452194192
61	62.3177670500391	8.0726353632712
62	62.3178580862938	8.0728255082731
63	62.3179491222895	8.0730156544252
64	62.3179504081216	8.0732085652509
65	62.3180414435955	8.0733987131467
66	62.3181324788103	8.0735888621926
67	62.3182235137661	8.0737790123885
68	62.3182247985425	8.0739719250143
69	62.3183158329765	8.0741620769540
70	62.3184068671513	8.0743522300439
71	62.3184979010671	8.0745423842838
72	62.3184991847878	8.0747352987096
73	62.3185902181818	8.0749254546934
74	62.3186812513167	8.0751156118274
75	62.3187722841925	8.0753057701114
76	62.3187735668574	8.0754986863372
77	62.3188645992114	8.0756888463651
78	62.3188658813460	8.0758817632034
79	62.3189569131781	8.0760719249752
80	62.3189581947824	8.0762648424259
81	62.3189594761192	8.0764577598954
82	62.3190505071667	8.0766479240048
83	62.3190517879731	8.0768408420867

84	62.3191428184988	8.0770310079401
85	62.3191440987748	8.0772239266344
86	62.3192351287786	8.0774140942316
87	62.3193261585233	8.0776042629790
88	62.3193274380063	8.0777971828795
89	62.3194184672291	8.0779873533708
90	62.3194197461818	8.0781802738837
91	62.3195107748827	8.0783704461189
92	62.3195120533050	8.0785633672442
93	62.3196030814840	8.0787535412234
94	62.3196043593760	8.0789464629610
95	62.3196953870331	8.0791366386841
96	62.3196966643947	8.0793295610341
97	62.3197876915299	8.0795197385012
98	62.3197889683611	8.0797126614636
99	62.3198799949744	8.0799028406745
100	62.3198812712753	8.0800957642493
101	62.3199722973667	8.0802859452042
102	62.3200633231988	8.0804761273094
103	62.3200645987066	8.0806690520901
104	62.3201556240168	8.0808592359393
105	62.3201568989942	8.0810521613323
106	62.3202479237825	8.0812423469254
107	62.3203389483116	8.0814325336688
108	62.3204299725816	8.0816227215624
109	62.3204312465030	8.0818156487552
110	62.3205222702510	8.0820058383928
111	62.3206132937398	8.0821960291807
112	62.3207043169694	8.0823862211189
113	62.3207940670695	8.0823834846396
114	62.3208850900435	8.0825736782847
115	62.3209761127582	8.0827638730800
116	62.3210671352138	8.0829540690257
117	62.3211581574102	8.0831442661217
118	62.3212479075234	8.0831415318503
119	62.3213389294642	8.0833317306533
120	62.3214286795797	8.0833289969199

G.11 Krundalen

CRS WGS 84/UTM ZONE 32N
Name 11 Krundalen Max
Min

Pixel no.	Latitude	Longitude
1	61.6254580202591	7.2420871596250
2	61.6255477487312	7.2420820687909
3	61.6256350540455	7.2418884544897
4	61.6257247825056	7.2418833630428
5	61.6258145109643	7.2418782715621
6	61.6259042394217	7.2418731800476
7	61.6259915444254	7.2416795629186
8	61.6260812728708	7.2416744707913
9	61.6261710013147	7.2416693786301
10	61.6262607297573	7.2416642864352
11	61.6263480344504	7.2414706664784
12	61.6264377628810	7.2414655736705
13	61.6265274913102	7.2414604808289
14	61.6266172197379	7.2414553879535
15	61.6267045241205	7.2412617651688
16	61.6267942525363	7.2412566716804
17	61.6268839809508	7.2412515781583
18	61.6269712850331	7.2410579531247
19	61.6270610134356	7.2410528589896
20	61.6271507418367	7.2410477648208
21	61.6272380456189	7.2408541375382
22	61.6273277740081	7.2408490427564
23	61.6274175023959	7.2408439479408
24	61.6275072307822	7.2408388530913
25	61.6275969591671	7.2408337582081
26	61.6276866875506	7.2408286632910
27	61.6277764159327	7.2408235683401
28	61.6278661443133	7.2408184733554
29	61.6279558726925	7.2408133783369
30	61.6280456010702	7.2408082832846
31	61.6281353294465	7.2408031881985
32	61.6282250578215	7.2407980930785
33	61.6283147861949	7.2407929979248
34	61.6284045145670	7.2407879027372
35	61.6284942429376	7.2407828075158
36	61.6285839713067	7.2407777122606
37	61.6286736996745	7.2407726169716
38	61.6287634280408	7.2407675216487
39	61.6288531564057	7.2407624262921

40	61.6289428847691	7.2407573309016
41	61.6290326131311	7.2407522354773
42	61.6291223414917	7.2407471400192
43	61.6292120698509	7.2407420445273
44	61.6293017982086	7.2407369490016
45	61.6293915265649	7.2407318534420
46	61.6294812549198	7.2407267578487
47	61.6295709832732	7.2407216622215
48	61.6296607116252	7.2407165665605
49	61.6297504399758	7.2407114708656
50	61.6298425932046	7.2408949240331
51	61.6299323215613	7.2408898288160
52	61.6300244745546	7.2410732835860
53	61.6301142029175	7.2410681888468
54	61.6302063556754	7.2412516452193
55	61.6302960840445	7.2412465509579
56	61.6303858124121	7.2412414566627
57	61.6304779649420	7.2414249151494
58	61.6305676933159	7.2414198213320
59	61.6306598456102	7.2416032814213
60	61.6307495739903	7.2415981880818
61	61.6308417260491	7.2417816497738
62	61.6309314544353	7.2417765569122
63	61.6310236062586	7.2419600202067
64	61.6311133346510	7.2419549278230
65	61.6312030630420	7.2419498354055
66	61.6312952146373	7.2421333008144
67	61.6313849430344	7.2421282088748
68	61.6314746714301	7.2421231169014
69	61.6315643998244	7.2421180248942
70	61.6316541282172	7.2421129328532
71	61.6317438566086	7.2421078407784
72	61.6318360079989	7.2422913098369
73	61.6319257363964	7.2422862182400